Evaporites in Juventae Chasma – Mars

Leaching experiments and geochemical modeling

Dissertation

zur Erlangung des Doktorgrades in den Naturwissenschaften

Eingereicht am Fachbereich Geowissenschaften der Freien Universität Berlin

vorgelegt von

Dipl. Geol. Muna Al-Samir

Berlin, 2015

Erstgutachter: Prof. Dr. Alessandro Airo

Freie Universität Berlin
Fachbereich Geowissenschaften
Fachrichtung Tektonik und Sedimentologie

Gutachter: Prof. Dr. Ralf Jaumann

Freie Universität Berlin
Fachbereich Geowissenschaften
Fachrichtung Planetengeologie und Fernerkundung
und
Deutsches Zentrum für Luft-und Raumfahrt DLR e.V.
Institut für Planetenforschung, Abteilung Planetengeologie

Gutachter: Prof. Dr. Ekkehard Holzbecher

German University of Technology in Oman
Faculty of Science
Department of Applied GeoSciences

Tag der Disputation: 27. November 2015

Eidesstattliche Erklärung

Hiermit erkläre ich, die vorliegende Arbeit selbständig und nur unter Verwendung der angegebenen Quellen und Hilfsmittel erstellt zu haben.

Muna Al-Samir

Danksagung

Die vorliegende Arbeit wurde im Rahmen des von der Helmholtz-Gemeinschaft geförderten Projektes “Planetary Evolution and Life” am Deutschen Zentrum für Luft- und Raumfahrt e.V. (DLR) in Berlin-Adlershof und am Institut für Geologische Wissenschaften (Fachrichtung Planetologie und Fernerkundung) der Freien Universität Berlin angefertigt.

Mein besonderer Dank gilt Herrn Prof. Dr. Ralf Jaumann für die fachliche Betreuung über die Dauer der Dissertation. Ebenso danke ich vor allem Herrn Prof. Dr. Ekkehard Holzbecher, der als zweiter Gutachter tätig war, für seine hilfreichen Anmerkungen im Bereich der geochemischen Modellierungen.

Des Weiteren möchte ich mich recht herzlich bei all denjenigen bedanken, die zum Gelingen dieser Arbeit beigetragen haben. Allen voran bei Herrn Dr. Andreas Winkler und Prof. Dr. Stephan van Gasselt, die stets eine offene Tür und ein offenes Ohr für meine Fragen hatten und ohne die diese Arbeit nicht so hätte entstehen können. Danke auch an Frau Dr. Janice Bishop, die mir mit ihrer eigenen wissenschaftlichen Arbeit erst das Fundament für meine wissenschaftlichen Untersuchungen bereitete, für ihre Unterstützung, Inspiration und Beratung. Ich danke auch ausdrücklich Herrn Dr. Lorenz Wendt und Herrn Dipl. Geol. Sami Nabhan, die mir während zahlreicher Diskussionen aufgrund ihrer fachlichen Kompetenz Anregungen geben konnten. Auch möchte ich mich bei Herrn Dr. Thomas Kneissl für seine Hilfe mit ArcGis bedanken, sowie bei meinen Zimmergenossen und Freunden Dipl. Geol. Wilhelm Zuschneid und Dr. Patrick McGuire für ihre Geduld.

Großer Dank gilt auch meinem Partner Dipl. Geol. Christoph Groß, der mich stets liebevoll und unterstützend während der Jahre begleitet hat, wie im Übrigen auch meiner Familie, namentlich meiner Schwester Maha Dürr und meinem Neffen Louis, die mich schon seit Beginn meines Studiums stets zu motivieren wussten.

Mein Dank gilt auch den Mitarbeitern des Museums für Naturkunde Berlin (Leibniz-Institut für Evolutions- und Biodiversitätsforschung), namentlich Herrn Dr. Jörg Fritz und Herrn Dr. Ansgar Greshake für die Bereitstellung von Gesteins- und Mineralproben, sowie Herrn Dr. Rudolf Naumann vom Helmholtz-Zentrum Potsdam für die Analytik, als auch Herrn Stefan Ralew, von dem ich die Mars-Meteoritprobe Tissint bezog. Mein Dank geht auch an Herrn Dipl. Geol. Til Singhal von der Fugro Consult GmbH, Frau Dr. Musiol, Frau Dipl. Geogr. Heike Balthasar und Herrn Dipl. Geol. Moritz Liesegang und meinem lieben Kollegen und Freund Dipl. Geol. Cord Fenk.

Zuletzt möchte ich noch dem HRSC-Team für die Bereitstellung der von mir genutzten Bilddaten ausdrücklich danken.

Abstract

A new hypothesis of the formation and deposition of monohydrated and polyhydrated sulfates in Juventae Chasma as a result of evaporation processes was developed and tested in this thesis. Juventae Chasma, Mars, is an approximately 7 km deep basin located in close vicinity of Valles Marineris. It stretches for ~190 km east-west and ~270 km north-south and exhibits several light-toned interior layered deposits (ILD's). These deposits form four large and distinctive light-toned mounds referred to as mound A, B, C, and D, from south to north. The deposits, with thicknesses up to several kilometers, consist dominantly of Mg-, Fe-rich monohydrated sulfates at the base partly overlain by polyhydrated sulfates. Therefore, it is reasonable to assume that the precipitation was a result of evaporation processes related to chemical reactions of sulfate solutions with martian rocks.

In order to produce Mg, Na, K, Ca, Fe, and Al ion containing sulfate solutions as postulated for evaporation processes in Juventae Chasma the composition of ten Mars analog rock and mineral samples and the martian meteorite Tissint were mineralogically and geochemically examined. Subsequently, the samples were leached with pH 1.3 and pH 3 sulfuric acid solutions in order to simulate rock/fluid interactions similar to the martian crust which was altered by sulfur acidified waters. The resulting fluids were then analyzed and numerically evaporated at 25°C, 75°C, and between 100-200°C by using the Geochemist's Workbench™ software.

The results showed sulfate precipitations similar to those observed in Juventae Chasma and, for the first time, enabled the development of a paleolacustrine model of the Juventae basin including the evolution of the Maja Valles outflow system. The results indicate that sulfuric acid solutions were in contact with olivine minerals or olivine-bearing rocks such as komatiites or dunites on the surface of Mars at the time of the late Noachian/early Hesperian boundary. Simulated hydrothermal conditions were developed to explain the characteristic lithostratigraphy of polyhydrated sulfate precipitation above monohydrated sulfates in lake water large enough to fill Juventae Chasma and to form Maja Valles. The presence of a fracture system at the base of mound B, found during preparation of this study, supports this assumption. In summary, results from laboratory experiments and geochemical modeling were combined with image analyses at Juventae Chasma to create a geochemical scenario that explains the presence of the observed geological and mineralogical features in Juventae Chasma.

Zusammenfassung

Im Rahmen der hier vorliegenden Arbeit wurde eine neue Hypothese für die, auf Evaporationsprozessen basierende Entstehung und Ablagerung von monohydrierten und polyhydrierten Sulfaten im Juventae Chasma, Mars, entwickelt und getestet. Juventae Chasma ist ein, in enger Nachbarschaft zu Valles Marineris liegendes, etwa 7 km tiefes Becken. Es erstreckt sich mit ca. 190 km in Ost-West Richtung und mit etwa 270 km in Nord-Süd Richtung und offenbart mehrere geschichtete Ablagerungen (light-toned interior layered deposits/ILD's). Diese Ablagerungen formen vier charakteristische, große Berge mit hoher Albedo, die von Süd nach Nord als Mound A, B, C und D bezeichnet werden. Die Ablagerungen, mit Mächtigkeiten von mehreren Kilometern, bestehen an ihrer Basis hauptsächlich aus magnesium-und eisenreichen monohydrierten Sulfaten, die zum Teil mit polyhydrierten Sulfaten überdeckt sind. Aufgrund dessen ist die Annahme naheliegend, dass die Präzipitation als Ursache von Evaporationsprozessen in Verbindung mit chemischen Reaktionen von sulfathaltigen Lösungen mit dem Umgebungsgestein stattfand.

Um Mg-Na-K-Ca-Fe- und Al-haltige Sulfat-reiche Lösungen wie sie für die Evaporationsprozesse in Juventae Chasma postuliert werden herzustellen, wurden zehn Mars-analoge Gesteins- und Mineralproben, sowie Proben des Mars-Meteoriten Tissint mineralogisch und geochemisch untersucht. Anschließend wurden die Proben in einer pH 1,3 und pH 3 Schwefelsäure angelöst, um so Gesteins-Fluid Wechselwirkungen ähnlich der Alteration von Marskruste durch schwefelsaure Wässer zu simulieren. Die daraus resultierenden Fluide wurden danach analysiert und bei 25°C, 75°C und zwischen 100-200°C mittels des Computerprogramms Geochemist's Workbench™ numerische evaporiert.

Die Resultate zeigten Sulfatablagerungen, die denen im Juventae Chasma ähnlich sind, und ermöglichten zum ersten Mal die Entwicklung eines paläolakustrinen Modells, einschließlich der Entstehung des Maja Valles Abflusssystems. Die Resultate zeigen, dass schwefelsaure Lösungen im Kontakt mit Olivin-Mineralen oder Olivin-haltigen Gesteinen, wie z.B. Komatiiten oder Duniten auf der Marsoberfläche zur Zeit des späten Noachium/frühen Hesperium in Kontakt standen. Um die charakteristische Lithostratigraphie von präzipitierten, polyhydrierten Sulfaten oberhalb der monohydrierten Sulfate zu erklären, mussten hydrothermale Bedingungen geherrscht haben. Es zeigte sich, dass die dafür nötige Wassermenge groß genug war um Juventae Chasma zu füllen und Maja Valles zu formen. Die Anwesenheit eines Kluftsystems am Fuß des Mound B, das im Rahmen der Anfertigung dieser Arbeit entdeckt wurde, unterstützt die Annahme hydrothermaler Bedingungen. Insgesamt wurden die Resultate der Laborexperimente und der geochemischen Modellierungen mit den Bildanalysen von Juventae Chasma in Zusammenhang gebracht, um ein geochemisches Szenario zu entwerfen, das die Anwesenheit der geologischen und mineralogischen Besonderheiten im Juventae Chasma erklärt.

Contents

List of Figures

List of Tables

1. Introduction

1.1 Motivation and scope

The Compact Reconnaissance Imaging Spectrometer for Mars (CRISM) and the Visible and Infrared Mineralogical Mapping Spectrometer (OMEGA) discovered polyhydrated and monohydrated sulfate-rich deposits at various locations on Mars. These sulfate deposits with thicknesses up to several kilometers were identified and discussed by many authors (e.g. Gendrin, A. et al. 2005; Bibring et al., 2006; Bishop et al., 2009, and Noel et al., 2014) and consist dominantly of Mg-, Fe- and Ca-rich sulfates.

Some of these sulfate outcrops show interior layering, which leads to the assumption that their deposition is related to chemical reactions between aqueous solutions and the martian regolith followed by evaporation processes. Crater Size-Frequency Distribution (CSFD) measurements suggest that these materials may have been formed between 3.8 and 3.6 Ga ago at the late Noachian/early Hesperian boundary (Neukum et al., 2009; Gross et al., 2009).

Chemical reactions between aqueous sulfur-containing components and the martian regolith were potentially an important geochemical process on Mars because of the occurrence of kieserite ($MgSO_4 \cdot H_2O$) and other sulfates (e.g., Fe- and Ca sulfates) (Bishop et al., 2009; Wendt et al., 2009; Wendt, 2012; Noel et al., 2015).

Juventae Chasma is a closed-basin system with four distinct sulfate-bearing mounds separated from the Maja Valles outflow channel system only by a sill. That makes Juventae Chasma to a case study and a representative for other basins in the greater Valles Marineris region (Figure 1 and Figure 3). The mineral composition of these mounds has attracted the attention of many scientists because it still contains the information about a paleo-hydrogeological history. Based on spectral observations of Bishop et al. (2009), Wendt et al. (2009), Wendt (2012), and Noel et al. (2015) this study has the intention to fill in the gap regarding its geochemical and sedimentological evidence based on evaporitic processes to develop a reasonable paleolakustrine model and to contribute to the ongoing discussion about the origin of sulfate deposits on Mars.

The results, presented in this thesis, provide for the first time a reasonable scenario for the Juventae Chasma system, including the origin of Maja Vallis, the evolution of ILD formation, and also give an explanation for the characteristic lithostratigraphy of the sulfate deposits, based on experimental data.

How long these processes persisted cannot be answered adequately. However, it is assumable that the process of ILD formation is associated with minimum two flooding events in a relatively short period of a few years to a few thousand years.

1.2 The geology and mineralogy of Juventae Chasma in context with Valles Marineris

The formation of massive salt deposits generally requires basin morphologies as found at the Tularosa Basin (White Sands, New Mexico; Langford, 2003) or the Zechstein Basin (northern Germany; Walter, 1995). A basin must be largely separated from the open ocean by a system of barriers to prohibit an unhindered exchange of sea water into the basin. Certain climate conditions must prevail such that a large amount of water can evaporate. The subsidence of the basin floor is another requirement for massive evaporite deposition, whether by synsedimentary subsidence or syntectonic sedimentation. The initial depth of the basin does not necessarily correspond to the subsequently occurring layer thicknesses (Füchtbauer, 1988).

These requirements appear to have occurred at Juventae basin on Mars, which hosts multiple large sulfate deposits (e.g., Catling, 2006; Bishop, 2009; Sowe, 2009; Wendt, 2009).

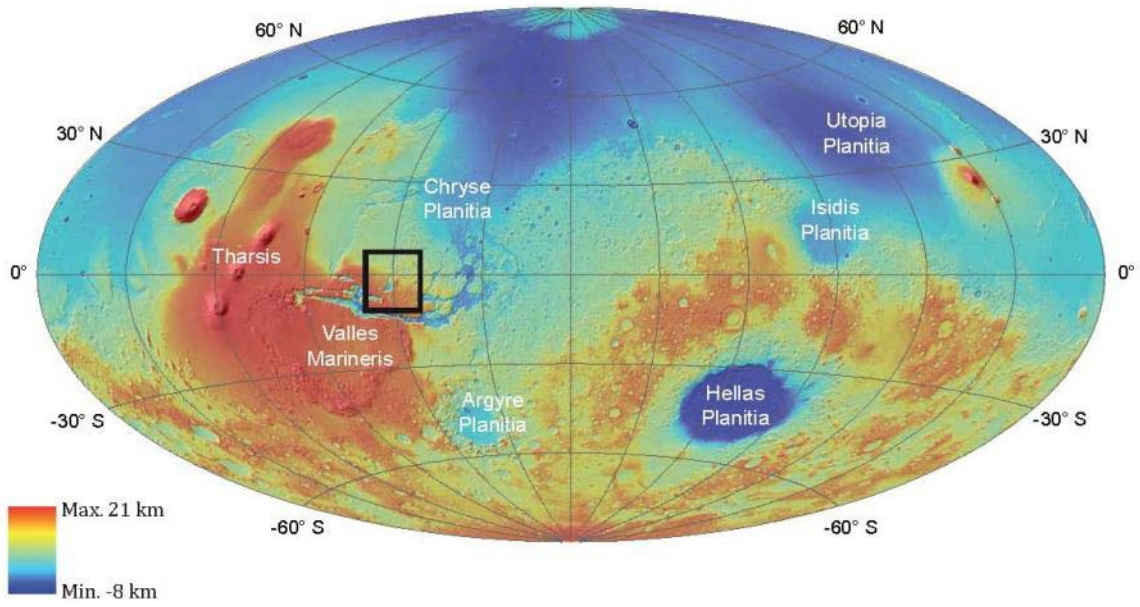

Figure 1: Global topography of Mars. Data derived by the Mars Orbiter Laser Altimeter (MOLA) showing a global shaded relief combined with a transparent MOLA. Juventae Chasma is outlined in black.

1.2.1 Valles Marineris

Although it is still not well understood, the formation of Juventae Chasma with the opening of Valles Marineris appears to be closely related. In 1977, Blasius et al. already described and analyzed the Valles Marineris trough system based on Viking I data. Valles Marineris (Figure 1 and 3) comprises a WNW-ESE parallel extending, partly interconnected, radial canyon system that is 4000 km in length, up to 700 km in width with a maximum depth of 7 km (Carr and Head, 2010). It opens westerly east of Noctis Labyrinthus (101° W, 6.4° S), Syria Planum (104° W, 12.5° S) respectively, on the Tharsis bulge, and the main rift valleys stretch eastward first through Ius Chasma (84° W, 7.1° S), then Melas Chasma (73.5° W, 10.5° S) and Coprates Chasma (62.2° W, 12.5° S) into Capri and Eos Chasma (50° W, 12.5° S; 47.5° W, 16° S). At this point, the direction of the troughs turns toward the NNE and widely opens into Chryse Planitia (part of the northern lowlands on Mars) via Aurorae Chaos and Hydraote Chaos. The northern branch runs parallel to the central troughs through Tithonium Chasma and Candor Chasma which, in turn, is connected to the north seated Ophir Chasma (72° W, 4° S).

When the Valles Marineris trench was formed is still not sufficiently clarified. But assuming the emergence of Valles Marineris goes hand in hand with the rise of the Tharsis bulge then the rift system likely began to open in the early Noachian (Figure 2 and Table 1) (Lucchitta et al., 1992; Chapman et al., 2003; Carr and Head, 2010).

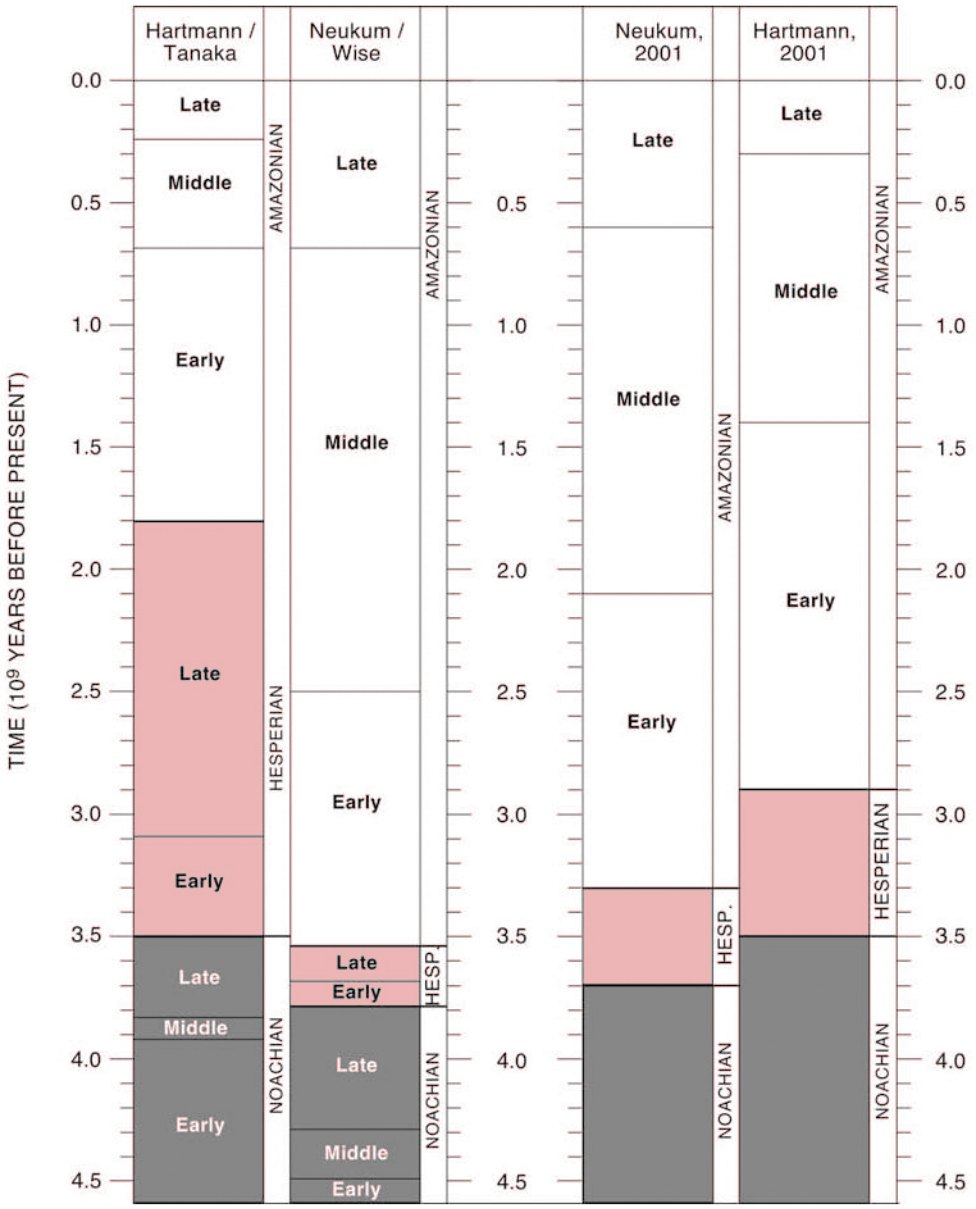

Figure 2: Martian stratigraphies of Hartmann et al. (1981), Neukum and Wise (1976), and the Neukum and Hartmann stratigraphies (both published in a joined paper by Hartmann and Neukum, 2001); modified after Hiesinger and Head (2004).

Carr (1974) delivered a simple but plausible argument: The manner in which this fracture pattern is distributed over such a large area leads inevitably to the assumption that the fractures did not form due to independent regional events but may have proceeded episodically in a stress regime initially caused by the Tharsis rise. According to Carr (1974) and Blasius et al. (1977) the E-W trending depressions were formed due to extensional stress. Anderson et al. (2001) came to the conclusion that five main tectonic-magmatic stages are responsible for the formation of the canyon-system, and that these processes lasted until the Amazonian era. Blasius et al. (1977) supposed that the closed basins, such as Hebes

Chasma (76.2° W, 1° S) north of Valles Marineris, are collapse structures due to N-S trending secondary extensions. But Spencer and Fanale (1990) gave alternative models for the origin of the closed depressions such as Echus Chasma (80° W, 0.5° S), Hebes Chasma, Ganges Chasma (49° W, 6.5° S) and Juventae Chasma, all situated north of the main Valles Marineris canyon-system. They assumed that the basins were formed by dissolution of carbonate deposits due to atmospheric and/or magmatic CO_2 in the presence of water. McCauley et al. (1972), Sharp (1973a), and Schonfeld (1979) argued that the withdrawal of magma in Noctis Labyrinthus led to collapses of the upper crust and that this process extended to Hebes Chasma, Kasei Valles, Juventae Chasma and finally Maja Valles.

Luchitta et al (1992) assumed that a combination of multiple processes including tectonic, erosion and collapse is responsible for the formation of the trough-system.

E-W striking faults or fractures were found during preparation of this study at the eastern base of mound B in Juventae Chasma (discussed in section 6.3) which could be evidence for a secondary extension of the Juventae basin. This then supports the assumption that the origin of the Juventae depression is closely related to tectonic processes as described by Carr (1974), Blasius et al. (1977) and Viviano-Beck et al. (2014).

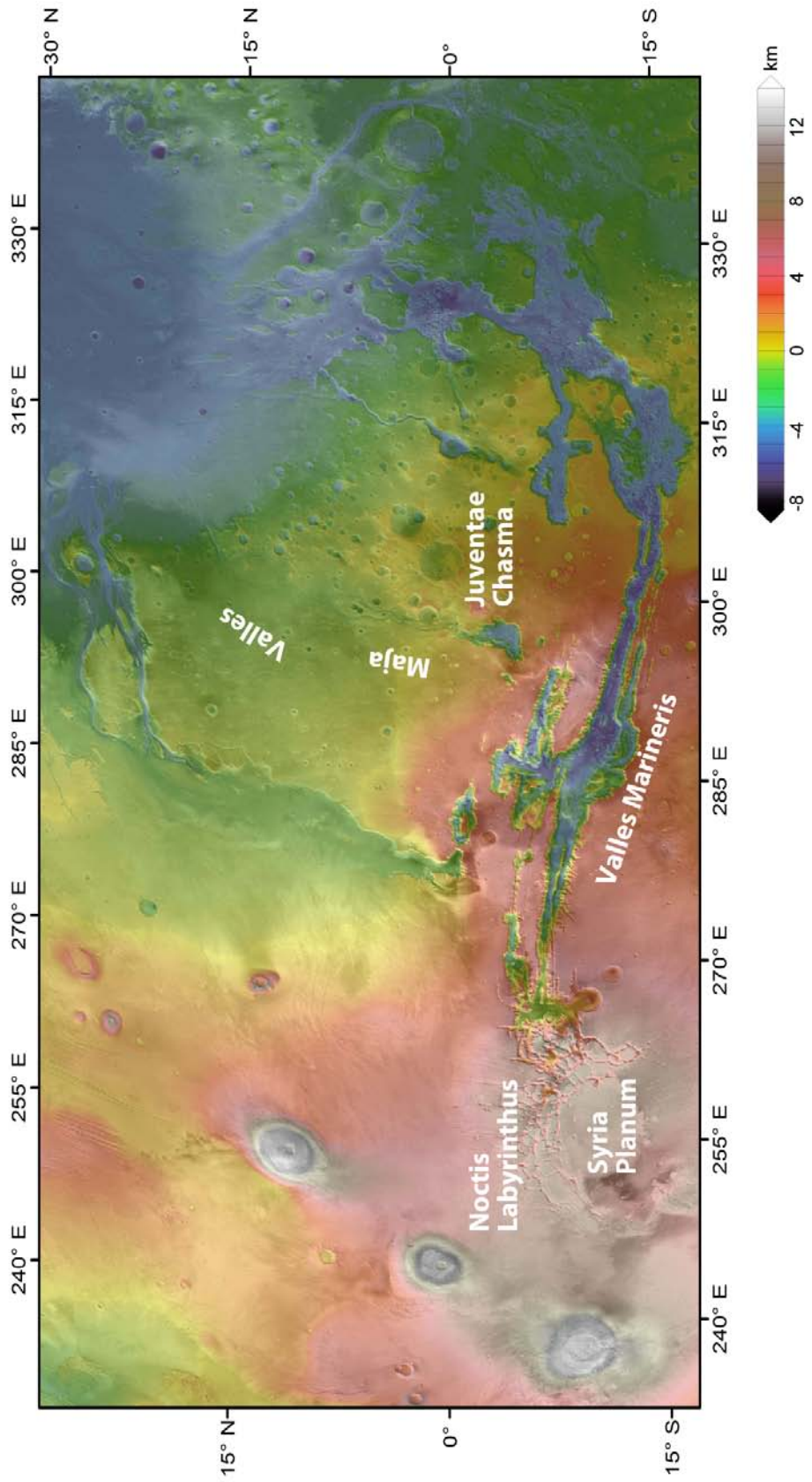

Figure 3: Topographic map created using MOLA data merged with MOC wide angle imagery

Table 1: Major Events in Martian Geological History (modified after Head et al., 2001)

	Volcanism	Tectonism	Fluvial events	Cratering	Exogenous processes
Amazonian	- Late flows in southern Elysium Planitia. - Decreased volcanism in northern plains. - Most recent flows from Olympus Mons. - Emplacement of massive materials at S. edge of Elysium Planitia. - Waning volcanism in Tharsis region. - Waning volcanism in Elysium region. - Widespread flows around Elysium Mons.	- Tharsis tectonism continued through the Amazonian, mostly associated with the large shield volcanoes. - Formation of Elysium Fossae. - Initial formation of Olympus Mons aureoles.	- Channeling in southern Elysium Planitia. - Late period of channel formation - Formation of channels NW of Elysium Mons.		- Emplacement of polar dunes and mantle. - Development of polar deposits? - Formation of ridged lobate deposits on large shield volcanoes. - Emplacement of massive materials at S. edge of Elysium Planitia. - Local degradation and resurfacing of nothern plains. - Erosion in northern plains. - Deep erosion of layered deposits in Valles Marineris. - Development of ridges, grooves, and knobs on northern plains.
Hesperian	- Volcanism at Syrtis Major. - Formation of highland paterae. - Volcanism at Tempe Terra. - Major volcanism in Elysium and Tharsis regions. - Emplacement of ridged plains (Hr).	- Formation of Noctis Labyrinthus. - Formation of Valles Marineris. - Formation of wrinkle ridge systems. - Memnonia and Sirenum Fossae, fractures around Isidis.	- Development of large outflow channels. - Infilling of nothern plains. - Deposition of layered materials in Valles Marineris.		- Degradation of northern plains materials. - Dorsa Argentea formation at South Pole. - Resurfacing of northern plains.
Noachian	- Formation of intercrater plains. -Decreasing highland volcanism. - Beginning of widespread highland volcanism.	- Ceraunius, Tempe, and Noctis Fossae - Tectonism south of Hellas. - Archeron Fossae. - Claritas Fossae.	- Formation of extensive valley networks.	- Waning impact flux. - Intense bombardment. - Argyre impact. - Hellas and Isidis impacts. - Formation of oldest exposed rocks.	- Extensive dessication and etching of highland rocks. - Formation and erosion of heavily cratered plateau surface. - Deep erosion of basement rocks.

1.2.2 Juventae Chasma and Maja Valles

Juventae Chasma located north of Valles Marineris and in the immediate vicinity of Candor- and Ophir Chasma, is an approximately 190 km east-west and ~270 km north-south stretching deep depression (61.5° W, 3.1° S). The site of maximum width and maximum depth (with up to 6.9 km in relation to the surrounding plateau) is located in the southern region (61.5° W, 4.7° S) of the chasma. The shallowest point of the chasma floor is located at the transition to Maja Valles in the northernmost area of Juventae and steeply declines in the southern direction. The surrounding plateau on the other hand dips in a northern direction (Figure 4). The northernmost and narrowest end of the basin forms a strait into the Maja Valles outflow channel via a so called "pour point" (Catling et al., 2006). The basin floor is surrounded by relatively steep chasma walls, that are regarded as an independent geomorphologic unit (Catling et al., 2006). This wall unit shows predominantly a smooth topography with a dune field that covers large parts of the basin floor (Al-Samir et al., 2012; Noel et al., 2015). Close to the pour point at Maja Valles sill hummocky structures and a chaotic terrain structure can be observed. Results of impact crater size-frequency distribution determinations, conducted by Neukum et al. (2009), show an age of 3.33 Ga for Juventae Chasma. This value was later confirmed by investigations of Gross et al. (2009).

De Hon and Pani (1993) and Chapman et al. (2003) investigated the discharge rates and the time span of the Maja Valles outflow channel system via the Lunae Planum basin into Chryse Planitia. Assuming that the water source is located in Juventae Chasma, De Hon and Pani (1993) concluded that an initial catastrophic flooding occurred followed by subsequent progressive, episodic discharge within one to two Earth-years through the 1600 km long Maja Valles. Both studies also assumed a minimum of two flood events across Maja Valles. Age determination results within the Maja Valles channel system show an age of 1.22 Ga (+0.16/-0.16) in the western region and 3.68 Ga (+0.08/-0.17) in the southeastern region (Gross et al., 2009). Gross et al. (2009) concluded that the channel system formed from multiple flooding events, even before the sulfates deposited.

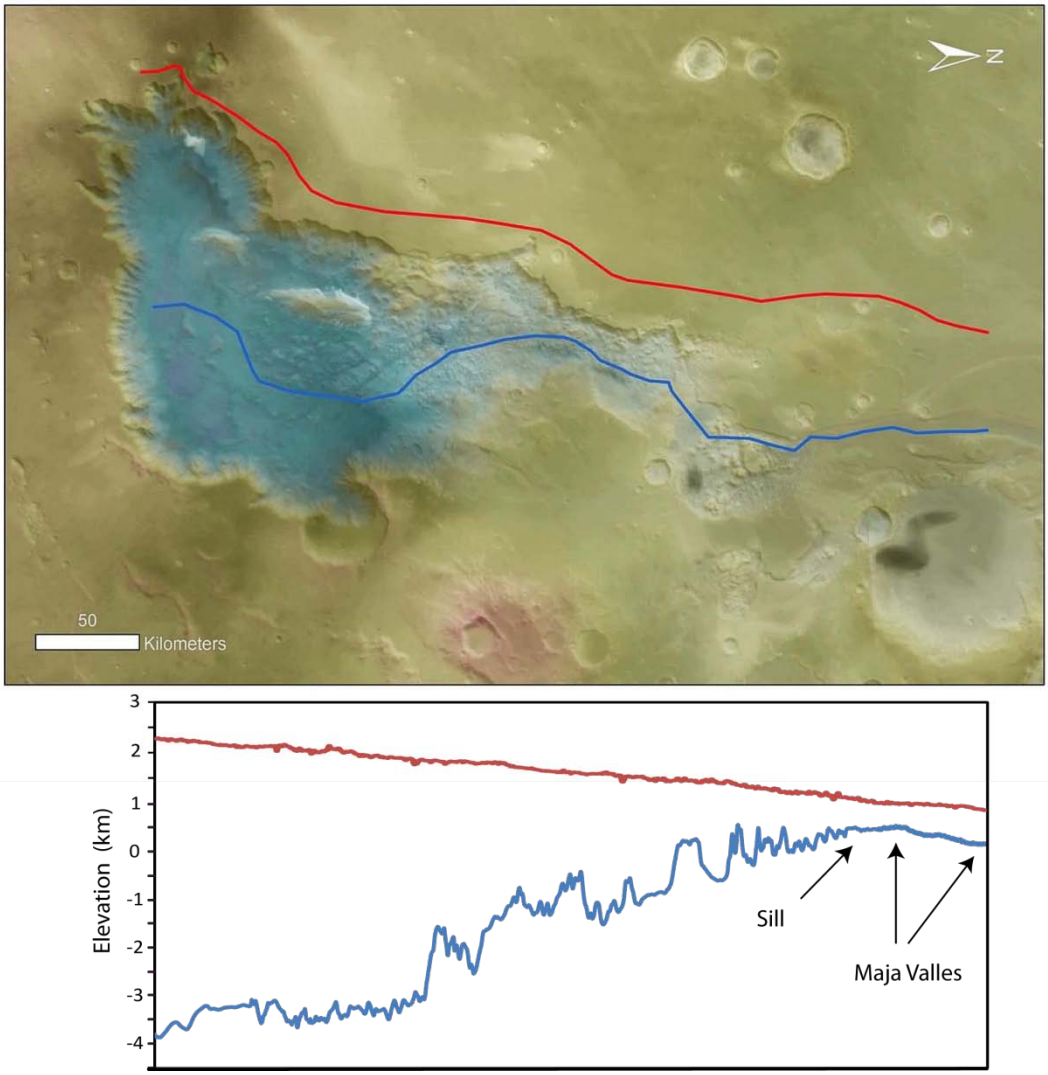

Figure 4: Topographic map created using MOLA data merged with MOC wide angle imagery. The blue line shows the profile of the Juventae basin trending south to north through the sill into the Maja Valles outflow channel. The red line follows the topography of the western plateau from south to north giving information about the relative elevation (adapted from Catling et al., 2006).

The Juventae basin is surrounded by a plateau mostly of early Hesperian age (Tanaka et al., 2014). Only the plateau NNE of Juventae belongs to the middle Noachian unit (Tanaka et al., 2014). According to Tanaka et al. (2014) the early Hesperian volcanic unit is characterized by undifferentiated, plane flood lavas, whereas the middle Noachian unit shows an uneven topography with volcanic and fluvial features on a partly heavily degraded surface.

The plateau regions in close vicinity to the northwestern and southwestern border of Juventae Chasma exhibit several light-toned layered deposits, informally named as LD's (Le Deit et al., 2008). Mangold et al. (2008), Weitz et al. (2008 and 2009), Le Deit et al. (2008 and 2009), Bishop et al. (2009) and others have investigated the deposits in detail.

The study of Bishop et al. (2009) shows that this material consists of opaline silica phases and hydroxylated ferric sulfates. Mangold et al. (2008) discussed morphologic features of the LD's, such as sinuous lineation possibly indicating fluvial-erosional processes.

Juventae Chasma contains several interior light-toned layered deposits (ILD's) (Gendrin et al., 2005; Bishop et al., 2009). These ILD's are generally detached, high albedo units. The shape and composition of the ILD's have led to different possible formation theories on the origin of the ILD's. The formation theories in the Juventae depression were summarized by Bishop et al. (2009) as three main formation models and referred to as the "bathtub-hypothesis", the "bucket-hypothesis" and the "extensive unit-hypothesis":

- The "bathtub-hypothesis": Juventae Chasma formed a so called "bathtub", filled with sulfate-rich sediments. After solidification and partial erosion, four large mounds remain as relics within the chasma.
- The "bucket-hypothesis": Four small basins within the Juventae Chasma depression were additionally infilled with sulfate-rich sediments. After solidification and partial erosion, four large mounds remain as relics within the chasma at the location of the presumed buckets.
- The "extensive unit-hypothesis": Extensive deposition of sulfate-rich sediment over hundreds of kilometers occurred prior to the Juventae Chasma formation. This was originally proposed by Malin and Edgett (2000). They observed "massif unit" deposits on top of light-toned layered material at several similar outcrops in e.g. West Candor Chasma and Melas Chasma in the greater Valles Marineris region. Erosion and the stress, related to the opening of Juventae Chasma, could have exposed the former buried sulfate deposits. In this scenario, the mound-forming, sulfate-rich sediments serve as windows into a time before the formation of the Chasma.

All of the hypotheses mentioned above have one similarity: Water is a prerequisite for the formation of sulfate-rich sediments. Formation of these sediments could be due to subice volcanism (Chapman et al., 2003), glacial, lacustrine or aeolian processes (Malin and Edgett, 2000), results of spring deposit events (Rossi et al. 2008), or products of evaporation (Montgomery and Gillespie, 2005). Published models in the greater Valles Marineris region proposed sulfate formation as a result of ice weathering (Michalski and Niles, 2012) but also as a result of evaporation (Andrews-Hanna et al., 2010). Andrews-Hanna et al. (2007 and

2010) discussed ILD formation by evaporation of upwelling groundwater driven by the Tharsis rise in Meridiani Planum and Valles Marineris.
The number of possible formation models suggests that the origin of ILD's on Mars is still not clarified.

The four most distinctive bright mounds in the Juventae depression (Figure 5) are generally referred to as mounds A, B, C and D, from south to north (Catling et al., 2006). Deposits containing monohydrated sulfates (MHS) and polyhydrated sulfates (PHS) were identified using multiple datasets (CRISM, HRSC, HiRISE and CTX data) at mounds A, B, C, and D within Juventae Chasma (Bishop et al., 2009; Noel et al., 2015). These studies showed that the MHS-rich units were deposited first and were later superimposed by the upper PHS-dominated unit, although the PHS are almost completely eroded in the Juventae basin. Only at mound B are the PHS-bearing materials detected as a unit in significant abundance on top of the mound (Noel et al., 2015). PHS, mixed with MHS at the CRISM scale (18 m per pixel), are also present at mounds A and C. The character and composition of the mounds was summarized recently by Noel et al. (2015).

The chasma additionally contains sedimentary rocks, sand and dust of different thicknesses (Catling et al., 2006) as well as several outcrops of mafic minerals at the vicinity of the mounds and in the chasma walls (Bishop et al., 2009; Flahaut et al., 2012; Noel et al., 2015). A so called chaotic terrain, a mixing of large blocks and cones, is present in the northern and shallowest part of the chasma, around mound C and mound D. Thin light-toned layered deposits (LLD) can be found in some regions at the plateau northwest of Juventae Chasma (Bishop et al., 2009; Bishop and Weitz, 2011). These are composed of opaline silica and hydroxylated ferric sulfates (Bishop et al., 2009).

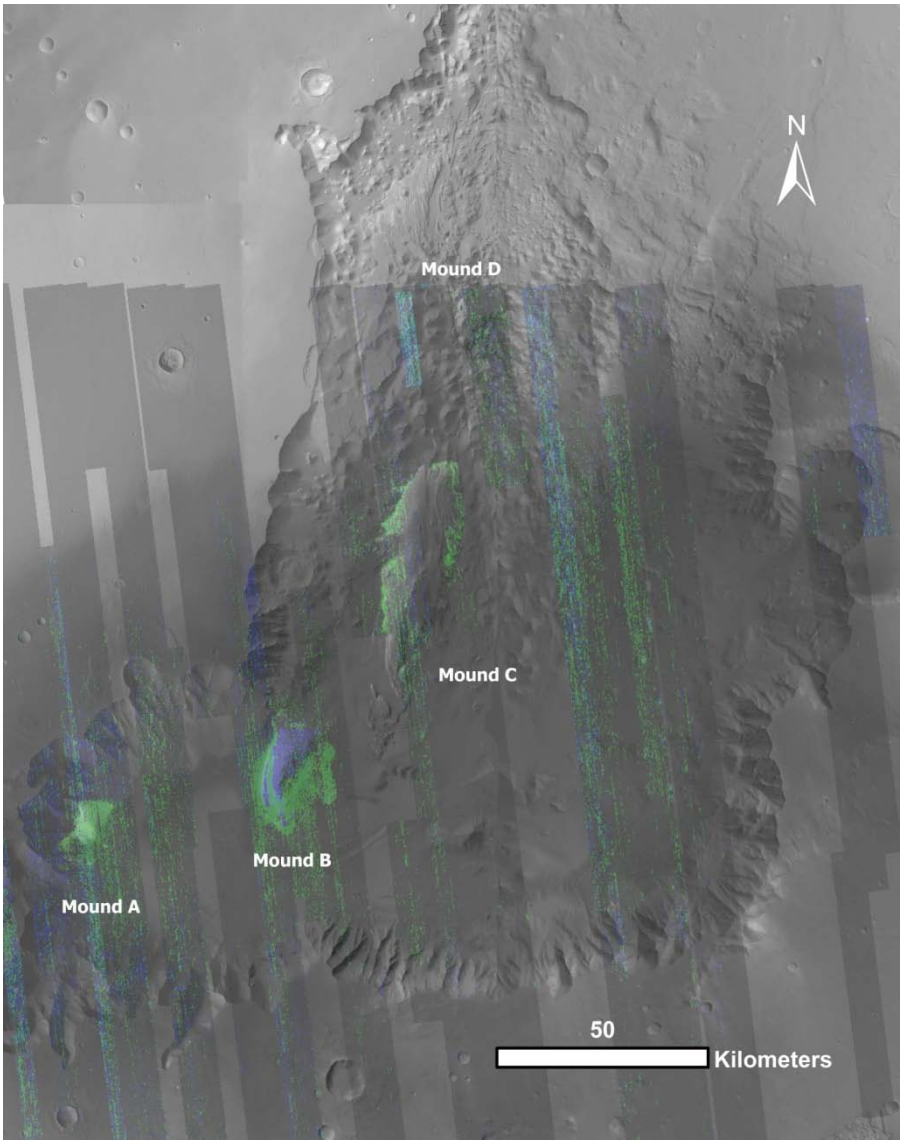

Figure 5: Mosaic of HRSC images superimposed by CRISM multispectral strips from tile T0934 showing sulfate-bearing mounds A-D labeled. Mapped with BD2100, monohydrated sulfates appear in green, polyhydrated sulfates are mapped with BD1900 and appear in blue (modified after Gross et al., 2014).

Mound A:

Mound A, the southwestern-most mound (Figure 5), shows a layered morphology (layer thickness between ~10 m, ~20m and ~30 m), which can only be clearly seen in HIRISE images (Noel et al., 2015). It also seems highly eroded and its volume is difficult to measure with HRSC data.

Spectral data show that mound A mainly consists of MHS. Small areas show PHS patches that are mixed with MHS minerals at the western flank of mound A. Whereas Bishop et al. (2009) and Wendt et al. (2009) interpreted the MHS mineral content mainly as szomolnokite

($FeSO_4 \cdot H_2O$), Noel et al. (2015) identified kieserite ($FeSO_4 \cdot H_2O$) as the predominant MHS mineral, due to the latest CRISM TRR3 images (targeted reduced data, calibration level 3) and the MTRDR (map projected targeted reduced data record) (Seelos et al., 2012) and improved atmospheric separation. Wendt et al. (2009) and Bishop et al. (2009) both additionally identified the two pyroxene endmembers clinopyroxene and orthopyroxene mixed with szomolnokite in the CRISM image data of dark dunes. Determining the MHS composition is complex because of atmospheric features that overlap with the szomolnokite and kieserite bands near 2.1 µm. Recent data with improved atm removal are generally more consistent with the presence of kieserite than szomolnokite (J. Bishop, pers. com. 2014).

Mound B:

Mound B attracted the attention of many scientists due to its strong sulfate signatures and its unique morphology. Mound B shows several terraces, informally named "stairstep-morphology", with low-albedo- and high-albedo units (Figure 6).

Spectral analyses, conducted by Noel et al. (2015), indicate initial MHS deposition, superimposed by subsequent PHS formation. Whereas spectroscopic analysis by Noel et al. (2015) leads to the assumption that the MHS-deposit at the base of mound B is primary composed of kieserite, Bishop et al. (2009) interpreted szomolnokite as the dominating monohydrated sulfate deposit followed by kieserite, superimposed by PHS at higher elevations. They also mentioned the presence of hematite ($FeSO_4 \cdot H_2O$) mixed with the szomolnokite bedrock.

Noel et al. (2015) also suggest monohydrated sulfates on the western flank of mound B, partly mixed with polyhydrated sulfates (e.g. rozenite ($FeSO_4 \cdot 4H_2O$)).

Spectral interpretations by Bishop et al. (2009) and Noel et al. (2015) did not discriminate a specific PHS phase but strongly suggest the presence of the polyhydrated mineral starkeyite ($MgSO_4 \cdot 4H_2O$). However, Wendt et al. (2009) used the Multiple-endmember Linear Spectral Unmixing Model (MELSUM) to subclassify some polyhydrated sulfates in dependence on the underlying data base. According to their investigations, they concluded that the PHS in the upper part of mound B contains romerite ($Fe^{2+}Fe_2^{3+}(SO_4)_4 \cdot 14H_2O$) and rozenite. At the base of mound B they measured szomolnokite in combination with basaltic, pyroxene-containing sand.

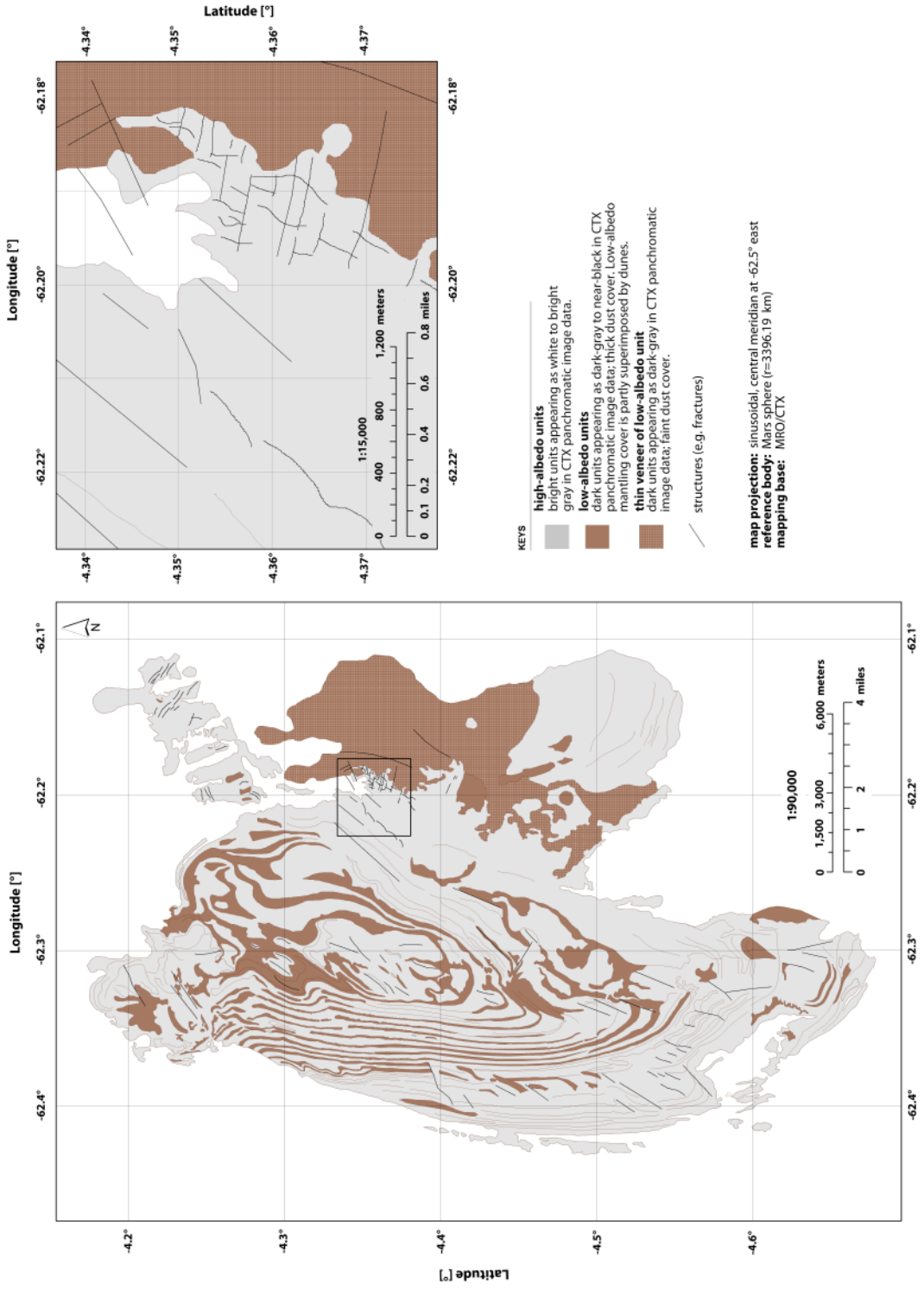

Figure 6: Geologic/geomorphologic map of mound B in Juventae Chasma (1:90,000/1:15,000, MRO/CTX orbit, Al-Samir et al., 2012).

Mound C:

Of all the mounds in Juventae Chasma, mound C is by far the largest and tallest mound in regard to its surface area and the volume. Bishop et al. (2009) discussed the presence of szomolnokite- and kieserite-bearing units partly covered by polyhydrated sulfates. Noel et al. (2015) detected pyroxene and olivine containing outcrops near mound C. They mentioned that two pyroxene endmembers may be present at this location: Low-calcium pyroxene (e.g. enstatite, $(Mg,Fe)_2[Si_2O_6]$) and high-calcium pyroxene minerals, partly mixed. Olivine was carefully interpreted as fayalite. According to Noel et al. (2015) mound C itself mainly contains MHS. Linear unmixing results, carried out by Wendt et al. (2009), show olivine or pyroxene in the dark dune material and sulfate-rich minerals, most likely szomolnokite, in the light-toned material of mound C. Furthermore, unmixing results of the sulfate-rich endmember shows, according to Wendt (2012), a mixture of szomolnokite, pyroxene and hematite.

Mound D:

Mound D is the northern-most and smallest mound in Juventae Chasma. In some areas layering can be observed as at mound A and mound B. The mound D region is largely dust covered within the chaotic terrain.

Spectral analysis, conducted by Noel et al. (2015), showed that the high albedo unit consists of MHS in a mixture with ferric oxides or Fe-bearing sulfates. Unmixing results, performed by Wendt et al. (2009), show the presence of szomolnokite and pyroxenes within the light-toned deposits. They also interpreted the presence of szomolnokite and pyroxenes within the lower albedo units of mound D.

In some areas the MELSUM model favored Na-containing jarosite, mixtures of szomolnokite ($FeSO_4 \cdot H_2O$) and natrojarosite signals and hematite spectra, which could not be confirmed by Wendt et al. (2009).

However, Wendt et al. (2009) did not confirm the presence of kieserite as a result of the linear unmixing at any locations in Juventae Chasma. Spectral interpretation of rocks at mound D, performed by Bishop et al. (2009), exhibit kieserite, szomolnokite and hydrated minerals, most likely PHS.

Mafic minerals:

Most of the Juventae Chasma floor is buried by basaltic sand with outcrops of mafic rich material (Bishop et al., 2009). Bishop et al. (2009) also discovered olivine and pyroxene minerals, predominantly fayalitic olivine and orthopyroxene, in the bedrock and in the southwestern and eastern chasma wall. They also assumed an abundant amount of plagioclase in the wall rock, but they pointed out that this information has to be handled with care.

Noel et al. (2015) is predominantly in agreement with Bishop et al. (2009). They found mafic minerals, olivine and pyroxene, by observations of outcrops in wall rocks, in the catchment area of mound A-D, and spread over the chasma floor. Specifically at the edges of the bright sulfate patches at mound D they observed abundant high calcium pyroxene (HCP) and low calcium pyroxene (LCP) minerals.

Table 2: List of minerals measured with the CheMin instrument (XRD) at the John Klein and Cumberland drilling site, compared with measuring results of APXS instrument at the location Rocknest (taken from Vaniman et al., 2014).

Mineral	Rocknest (wt.%)	John Klein (wt.%)	Cumberland (wt.%)
Plagioclase	29.8	22.4	22.2
Fe-fosterite	16.4	2.8	0.9
Augite	10.7	3.8	4.1
Pigeonite	10.1	5.6	8.0
Orthopyroxene		3.0	4.1
Magnetite	1.5	3.8	4.4
Anhydrite	1.1	2.6	0.8
Bassanite		1.0	0.7
Quartz	1.0	0.4	0.1
Sanidine	0.9	1.2	1.6
Hematite	0.8	0.6	0.7
Ilmenite	0.7		0.5
Akaganeite		1.1	1.7
Halite		0.1	0.1
Pyrite		0.3	
Pyrrhotite		1.0	1.0
Smectite		22	18
Amorphous	27	28	31

wt.%= weight-%

In situ analyses at Mars can help interpret the orbital data. On November 26, 2011, the NASA Mars Science Laboratory (MSL)-mission was launched with an Atlas V rocket from Cape Canaveral Air Force Station.

As part of the mission, the robotic rover Curiosity was onboard the MSL spacecraft. This mission is to investigate Martian climate and geology with the focus of habitability at the landing site in Gale crater. In August 2012, Curiosity began exploring the Martian surface. The first analysis of the Martian soil mineralogy was conducted with the Chemistry and Mineralogy (CheMin) powder x-

ray diffraction (XRD) and fluorescence instrument, and with the Alpha Particle X-ray Spectrometer (APXS) at a location named “Rocknest” (Blake et al., 2013, Bish et al., 2013). Rocknest is the name for an aeolian bedform (Bish et al., 2013) close to Aeolis Mons (“Mount Sharp”). X-ray diffraction results, conducted by CheMin, show the presence of plagioclase, olivine, pigeonite, orthopyroxene, clinopyroxene, augite, and a minor amount of magnetite and anhydrite at this location (Table 2). The second and third sampling sites are John Kline and Cumberland at the sedimentary Yellowknife Bay formation (Vaniman et al., 2014). In contrast to the Rocknest sample method (scoop sampling method of aeolian sediment), John Kline and Cumberland are drilled mudstone samples. The results of Bish et al. (2013) and Vaniman et al. (2014) show that the mineral assemblages in the sand facies and the mud facies are generally similar. Mineral phases of plagioclase, Fe-fosterite, augite, pigeonite and magnetite were detected in all of the three sample sites. XRD interpretations by Vaniman et al. (2014) suggest the presence of ortho- and clinopyroxenes in the mudstone samples.
In addition to the findings from Blake et al. (2013), Bish et al. (2013) and Vaniman et al. (2014), the laser-induced breakdown spectrometer (LIBS) and the Remote Micro Imager (RMI) (referred to as Chemistry and Camera (ChemCam)) and APXS measurements identified Ca-containing sulfates, most likely gypsum ($CaSO_4 \cdot 2H_2O$) (Vaniman et al., 2014), in veins associated with possible late-diagenetic light-toned microfractures (Grotzinger et al., 2014; McLennan et al., 2013). Mafic minerals and sulfates were identified at Gale crater by MSL which are consistent with the orbital observations.

1.3 Comparative studies

In 1997, Banin et al. were the first who conducted leaching experiments with concentrated acids (H_2SO_4, HCl, and HNO_3) of tephras from the Mauna Kea volcano (Big Island, Hawaii, USA). In their research, Banin et al. (1997) focused on the formation of weathering products by tephra leaching experiments with acid volatiles. The major result shows that particularly gypsum and alunogen (iron- and magnesium containing minerals, alunite ($KAl_3(OH)_6(SO_4)_2 + 6\,H^+$) and jarosite respectively, were not observed.

Tosca et al. (2004) reran the “acid fog model” experiments of Banin et al. (1997) on synthesized basalts with different acid strengths of H_2SO_4/HCl mixtures.
In contrast to the results of Banin et al. (1997), they observed the formation of a number of iron- and magnesium sulfates e.g. hexahydrate ($MgSO_4 \cdot 6\,H_2O$), melanterite ($FeSO_4 \cdot 7\,H_2O$), rhomboclase ($HFe(SO_4)_2 \cdot 4\,H_2O$) as well as gypsum and alunogen. The experimentally obtained and measured sample fluids were later used as the basis of geochemical modeling,

published by Tosca et al. (2005) and Tosca et al. (2006). The study of Tosca et al. from 2004 lacks of information concerning the experimental setup to recapitulate their "aqueous batch experiment" results as well as the modeling results published as Tosca et al. (2005) and Tosca et al. (2006).

In 2008, Chevrier et al. studied concentrated aqueous ferric sulfate brines under low temperatures suggested to be present on the surface of Mars related to present-day gully formation. Their model results, conducted with the Geochemist's Workbench^{Tm} software (GWB), show the precipitation of hematite, gypsum and anhydrite as well as K-jarosite and ferricopiapite ($Fe_2^{3+}/Fe_4^{3+}(SO_4)_6(OH)_2 \cdot 20\,H_2O$) to be possible under present day martian conditions.

Altheide et al. (2009) experimentally investigated the evaporation of different brine types ($Mg^{2+}$and Fe^{2+} sulfate brines and Mg^{2+} and Fe^{2+} chloride brines) in order to study e.g. brine evolutions and possible residence time of solutions via the investigation of evaporation rates of different brine types under freezing or almost freezing conditions (between 4.85°C and -15.5°C) at a CO_2 pressure of 0.07 bar, as supposed for Mars. They also observed sulfate mineral precipitation in supersaturated sulfate brines with 25 wt.% $MgSO_4$ and 18 wt.% $FeSO_4$ at the corresponding eutectic while evaporation, and sulfate minerals precipitate simultaneously with the formation of ice in sulfate brines with 20 wt.% $MgSO_4$ and 13 wt.% $FeSO_4$ equal to the eutectic. According to Altheide et al. (2009) mineral precipitation and the formation of ice was not observed for the Mg and Fe chloride brines in the temperature range.

1.4 Atmosphere and Water

Starting from the hypothesis that evaporation is the main process for sulfate deposition in Juventae Chasma the question arises if the early Mars atmosphere was capable of holding such a large amount of H_2O. Groundwater and surface water movements that are suggested during the Noachian and Hesperian era (Grotzinger et al., 2005), require an atmosphere, thick enough to provide conditions for the stability of water on Mars related to a possible warm and wet climate. Since Kliore et al. (1965) it is well known that the surface pressure of Mars is very low with 4-5 mbar up to 7mbar (Squyres and Kasting, 1994), and that therefore liquid water is not stable on the surface according to the triple point of water (Kliore et al., 1965).

Zurek (1992) and Carr (1996) describe the recent martian atmosphere as thin and cold (day-time: ~+ 27°C, night-time: ~ - 140°C; Owen, 1992, see Table 3) and it can only store a minor amount of water, on the order of 1-2 x 10^{15}g (Jakosky and Farmer, 1982; Carr, 1996; Maltagliati et al., 2011). Although low, the water vapor pressure varied with seasons on Mars (e.g. Schorn et al., 1967, Kieffer et al., 1976, Jakosky et al., 1982) dependent on the saturation state of the atmosphere. According to Schorn et al. (1967), Kieffer et al. (1976) and Jakosky et al. (1982), the circulation of water in the atmosphere starts by increasing of the amount of water vapor and water vapor capacity in spring- and summer season at the northern hemisphere due to increasing temperature (~ -123.15°C up to ~ -73.15°C; Kieffer et al., 1976). That leads to complete evaporation and partial sublimation of, first, the CO_2-ice then the subjacent water-ice seasonal polar cap in the northern hemisphere. Haberle (1998) suggests that the polar caps are not the only CO_2 reservoirs but also the regolith and, if present on Mars' subsurface, carbonates. Haberle (1998) pointed out that what is true for atmospheric CO_2 is also true for the water vapor. If the atmosphere cools down again in winter the water will not only condense in the polar region but will also be readsorbed by the regolith especially in the high latitudes (Haberle et al., 1990; Haberle, 1998). Whereas the northern seasonal ice cap completely sublimates, the southern CO_2 dominated ice cap largely resists melting processes due to lower maximum temperatures (Zurek, 1992). If in fact an exchange of water vapor between the two hemispheres on Mars takes place is still under debate. However, spectroscopic observations derived by the SPICAM (Spectroscopy for the Investigation of the Characteristics of the Atmosphere of Mars) instrument onboard of Mars Express, indicate that at least a small amount of atmospheric water vapor globally circulates through the transition of both hemispheres (Maltagliati et al., 2011) preferably from north to south (Jakosky et al., 1990). Maltagliati et al. (2011) showed that the martian atmosphere in the northern hemisphere is not only partly saturated with water vapor but shows an almost permanent supersaturation. One of the major prerequisites for the water vapor in excess of saturation is the absence of dust in the atmosphere (Maltagliati et al., 2011). Without dust, which serves as a nucleus, condensation is inhibited (Maltagliati et al., 2011). Forget et al. (2013) investigated the early martian surface temperature with respect to possible greenhouse effects on early martian climate influenced by atmospheric CO_2, a suggested faint young sun (Forget and Pierrehumbert, 1997), with different obliquity values, and atmospheric water vapor. In contrast to the findings of Forget and Pierrehumbert in 1997, their modeling results in 2013 revealed that the water vapor content was always low irrespective of the saturation state during Mars' history and that the greenhouse effect related to CO_2 ice clouds was not strong enough to provide high surface temperatures.

Lammer et al. (2013) investigated and discussed a more differentiated hypothesis about the loss of a suggested protoatmosphere during the early Noachian era and the subsequent build up of a "secondary outgassed CO_2 atmosphere". Nevertheless, the recent martian atmosphere is not capable of holding a large amount of H_2O and under the present-day atmospheric conditions on Mars the presence of surface water linked to large scale evaporation processes is not possible.

However, the observation of fluvial, glacial and periglacial morphologic features such as valley networks, outflow channels, debris aprons, lineated valley fills, pingos and gullies (see van Gasselt, 2007, Sowe, 2009, and Wendt, 2012) indicate mass transport processes which could only form in the presence of surface water (Carr et al., 1977; Squyres, 1979; Rossbacher et al., 1981; Carr, 1995; Christensen, 2003; Mangold et al., 2004; Head et al., 2005; Mangold et al., 2008a; Dickson, 2008; Hynek et al., 2010; Erkeling et al., 2012; Jaumann et al., 2014, and many more).

Table 3: Atmospheric components and parameters of Mars and Earth.

Atmospheric components and Parameters	Mars	Earth
Carbon dioxide (CO_2) [%]	95.32	0.04
Carbon monoxide(CO) [%]	0.07	90 [ppbv]
Nitrogen (N_2) [%]	2.7	78.08
Argon (Ar) [%]	1.6	0.93
Oxygen (O_2) [%]	0.13	20.95
Water (H_2O) [%]	0.03	(0.04)*
Mean atmospheric pressure [mbar]	6.5	1013
Minimum surface temperature [°C]	-140	-80
Maximum surface temperature [°C]	27	45
Mean surface temperature [°C]	-63	13
Equatorial radius [km]	3396	6378.1
Mass [10^{24} kg]	0.642	5.973
Mean densitiy [kg/m^3]	3.934	5.517
Surface gravity [m/s^2]	3.711	9.807
Moons	2**	1

*water vapor [wt %]; **Phobos and Dimos

The detection of phyllosilicates, sulfates and ferric oxides by the OMEGA (Observatoire pour la Minéralogie, l'Eau, les Glaces et l'Activité) instrument revealed a more differentiated view of the martian paleoclimate (Bibring et al., 2006, Bibring et al., 2007). Based on their analysis, pH-neutral conditions prevailed due to phyllosilicate formation during almost the entire

Noachian epoch, whereas acidic conditions are assumed during the late Noachian-early Hesperian era manifested by predominant sulfate deposits. Anhydrous ferric oxide formation occurred at the end of the Hesperian and during the Amazonian era. The mineralogical investigations enabled Bibring et al. (2006) the subdivision of the eras in mineralogical units and the findings strongly suggest at least one dramatic climate change in the history of Mars' atmosphere. This trend has been observed for much of the planet (e.g. Murchie et al., 2009) although there are a few more recent outcrops of phyllosilicates and sulfates (e.g. Ehlmann et al., 2011; Weitz et al., 2015).

Anders and Owen (1977) were one of the first to develop a model on the basis of data derived by results of the Viking missions combined with data from investigations of metamorphosed (differentiated) and chondritic meteorites. Their model approach is to compare the abundance of outgassing volatiles, such as CO_2, N_2 and H_2O, during accretion on Mars and on Earth, mainly through isotopic investigations of e.g. $^{40}Ar/^{36}Ar$ ratios. They calculated the past atmospheric pressure to be 140 mbar CO_2 plus 2 mbar N_2 that would lead to a global 9 m thick layer of surface water on Mars. Squyres and Kasting (1994) later contradict these findings on the basis of simple volatile mass scaling calculations and postulated higher results up to 10,000 mbar and a global surface water column of ~1200 m. Based on the assumption, that abundant volatile concentrations on early Mars must have been higher than on early Earth due to a cooler solar nebular, they supposed that very early in martian history but after valley network formation a high amount of volatiles not only migrated into the atmosphere but also disappeared to space due to impacts and hydrodynamic escape (steam atmosphere).

Yet another aspect of the martian climate is the so called "greenhouse effect" discussed by Squyres and Kasting (1994) generated due to a thick CO_2 atmosphere. Although it is generally accepted that increasing CO_2 supply to the atmosphere can lead to increasing temperatures, Squyres and Kasting (1994) insisted that this assumption might be true under Earth conditions but does not hold for conditions on Mars, because the present-day Mars receives 57 % less sunlight than the Earth, which would have led to CO_2 ice cloud formation and, therefore, a temperature decrease (Squyres and Kasting, 1994). They mentioned the discrepancy of the residence time of surface water necessary to form valley networks and the publicized climate models, but they give no satisfactory answers. However, they discussed three alternative hypotheses (geothermal heat, additional greenhouse gases such as CH_4 and a hypothesis about a much brighter sun in the past) to explain conditions for at least near-surface aqueous environments. Whether or not methane is present in Mars' atmosphere and its possible origin is currently being evaluated and is still under debate (Krasnopolsky, 2006;

Mumma et al., 2009; Lefèvre & Forget, 2009; Zahnle et al,. 2011; Atreya et al., 2011; Webster et al., 2015; Stevens et al., 2015).

A brighter young sun would have led to dramatic high temperature conditions on early Earth (Carr, 1996). However, at the end, he suggests a wet early Mars with low atmospheric pressure and temperatures below the freezing point but warm enough for liquid surface water related to hydrothermal convection.

Craddock and Howard noted in 2002 that the geology, mineralogy and geochemistry observed on Mars do not fit well into current climatic models assuming a cold and dry early Mars' atmosphere.

Johnson et al. (2008) and most recently Halevy and Head (2014) presented an alternative model about episodic warming due to punctuated volcanic eruption under the release of SO_2 and H_2S, at which SO_2 serves as a greenhouse gas, that might lead to a temperature increase of 25 °C (Johnson et al., 2008) and temperatures up to almost 17°C (Halevy and Head, 2014) on early Mars.

1.5 Sulfuric acid evolution of Mars

The presence of sulfate-bearing mineral deposits on the surface of Mars presumes sulfuric acid formation under oxidative conditions in early Mars's history. Two main hypotheses for sulfuric acid evolution on Mars were proposed: 1. Sulfuric acid evolution by volcanic exhalation (Johnson et al., 2008; Halevy and Head, 2014), and 2. Sulfuric acid evolution by aqueous pyrite oxidation (Burns et al., 1993; and King and McSween, 2005).

1.5.1 Sulfuric acid evolution by volcanic exhalation

As mentioned in section 1.4 Johnson et al. (2008) and Halevy and Head (2014) considered episodic release of sulfur volatiles in Mars' atmosphere to induced greenhouse conditions on early Mars. This hypothesis would explain not only a warmer climate, but would likewise create acidic conditions for the formation of sulfates on Mars (Bibring et al., 2006). This process is similar to the formation of acid rain on Earth.

By exhalative volcanic processes a large amount of sulfur-volatiles such as SO_2 and H_2S emanate into the atmosphere, mainly into the troposphere (Carr and Head, 2010), and gradually form sulfuric acid in the presence of oxygen and water under solar irradiation. For the formation of SO_3 or H_2SO_4 from SO_2, one of several possible reaction paths from Stumm & Morgan (1995) and Holleman and Wiberg (2007) is presented here:

$$O_3 \rightarrow O_2 + O \quad (1)$$

$$O + H_2O \rightarrow 2OH \quad (2)$$

$$H_2S + O_2 \rightarrow SO_2 + 2H^+ \quad (3)$$

$$OH + SO_2 + O_2 \rightarrow HO_2 + SO_3 \quad (4)$$

Sulfur dioxide or the resulting SO_3 reacts with oxygen and water to form sulfuric acid:

$$SO_3 + H_2O \rightarrow H_2SO_4 \quad (5)$$

or

$$SO_2 + H_2O + 0.5O_2 \rightarrow H_2SO_4 \quad (6)$$

The sulfuric acid forming reactions do not only occur immediately in the atmosphere but also upon a wet sediment surface after SO_2 rainout with possible OH, O_3, and H_2O_2 within clouds (Gorham, 1976), that, in turn, could lead to increasing acid input and subsequent washout of ions such as K^+, Mg^{2+} and Ca^{2+}. According to Holleman and Wiberg (2007) gaseous H_2S can easily be liquified, the boiling point is at -60.3°C, and the freezing point is at -85.6°C.
The residence time for atmospheric SO_2 is only a couple of days and its regional distribution is several thousand kilometers, dependent on wind (Gorham, 1976; Holleman and Wiberg, 2007). For this reason an unlimited enrichment of volatiles in the atmosphere is not possible (Stumm and Morgan, 1995).
However, sulfuric acid formation already requires the presence of liquid water and atmospheric dust (Gorham, 1976; Johnson et al., 2008; Halevy and Head, 2014).

1.5.2 Sulfuric acid evolution by aqueous pyrite oxidation

This section describes aqueous pyrite (FeS_2) oxidation and is mainly focused on sulfuric acid production. Hence, it has to be noted, that the process of aqueous pyrite oxidation with regard to formation of ferric hydroxide and other iron minerals is more complex than presented.
As a source for the formation of dissolved sulfate in natural waters, oxidative weathering of divalent Fe incorporated in iron sulfides (e.g. pyrite), has already been proposed and discussed for martian basalt by Burns et al. (1993) and King and McSween (2005). Pyrite is one of the most ubiquitous minerals of Earth's crust and it is expected that pyrite and/or marcasite could be common minerals in magmatic rocks on Mars (Lowson, 1982; King & McSween, 2005).
As an example, aqueous pyrite oxidation (e.g. Nordstrom, 1982) often proceeds via a complex inorganic mechanism but can also occur as a microbial process on Earth. An exclusively abiotic process in an oxidative system runs more slowly than a mechanism with microbial catalysis (Lowson, 1982). According to Nordstrom (1982), Lowson (1982), Stumm & Morgan (1995), and Pfeiffer and Nohlen (2000) this process is commonly described with the simplified overall given reaction:

$$FeS_{2(s)} + (15/4)O_{2(aq)} + (7/2)H_2O_{(l)} \rightarrow Fe(OH)_{3(s)} + 2H_2SO_{4(aq)} \text{ (Nordstrom, 1982)} \quad (7)$$

Sulfuric acid forms out of the reaction of pyrite and water with atmospheric oxygen, that would lead, as presented in reaction 7, to the deposition of ferric hydroxide ($Fe(OH)_3$). Nordstrom (1982) noted that as well from reaction 7 other iron minerals can precipitate.

1. Aqueous pyrite oxidation in the absence of oxygen:
The following reaction steps show the dissolution or breakdown of the pyrite mineral at 25°C and a pH of ≤ 3 based on potentiometric measurements (Nordstrom, 1982; Lowson, 1982; and references therein):

$$FeS_2 + 8H_2O \rightarrow Fe^{3+} + 2S_4^{2-} + 16H^+ + 15e^- \qquad \text{(Nordstrom, 1982)} \qquad (8)$$

and

$$FeS_2 \rightarrow Fe^{3+} + 2S^0 + 16H^+ + 3e^- \qquad \text{(Nordstrom, 1982)} \qquad (9)$$

Reaction 9 does not lead to reaction 8, but is a combination of pyrite dissolution in an aqueous medium without the presence of oxygen (Nordstrom, 1982, and references therein). According to reactions 8 and 9 both neutral and elemental sulfur form. The neutral sulfur, which now covers the surface of the pyrite mineral, is highly unstable and will rapidly transform into elemental sulfur or sulfate (Nordstrom, 1982, and references therein).

2. Aqueous pyrite oxidation by oxygen:
According to Nordstrom (1982) and Lowson (1982) oxygen is often the only oxidizing partner in pH neutral waters. Pyrite oxidation by oxygen in aqueous solution is expressed in the following overall reaction, and leads to the formation of divalent iron sulfate and sulfuric acid (Lowson, 1982):

$$2FeS_2 + 7O_2 + 2H_2O \rightarrow 2FeSO_4 + 2H_2SO_4 \qquad \text{(Lowson, 1982)} \qquad (10)$$

Reaction 10 does not express sulfur as another product due to side reactions. But the sulfur formation rate is according to Lowson (1982) negligible, so that he suggests that sulfides' sulfur almost completely forms sulfate or especially sulfuric acid.

3. Aqueous pyrite oxidation by Fe(III):

This process is faster than the oxidation with oxygen and the reaction takes place at the surface (Nordstrom, 1982; Lowson, 1982; and Stumm and Morgan, 1995) given in the overall equation:

$$FeS_{2(s)} + 14Fe^{3+} + 8H_2O = 15Fe^{2+} + 2SO_4^{2-} + 16H^+ \quad \text{(Stumm and Morgan, 1995)} \quad (11)$$

The slow reoxidation of the resulting Fe(II) to Fe(III), however, is a limiting factor for this reaction process and is therefore a limiting step in pyrite oxidation (Stumm and Morgan, 1995).

Burns and Fisher (1993) pointed out that the observation of sulfate on the martian surface indicates oxidative aqueous iron sulfide weathering of iron-rich komatiitic basalts during Mars' history. They presented a model of oxidative sulfide-bearing basalt weathering in the subsurface of the regolith below the groundwater table.

Initially revealed by volcanic activity and formed under solar irradiation (ultraviolet) in an aqueous medium, in groundwater dissolved oxygen and Fe(III) (given in the reactions 12, 13, and 14) migrates deep through the regolith and initiated weathering (Burns and Fisher, 1993):

$$H_2O \rightarrow H_2 + 1/2\,O \quad \text{(Burns and Fisher, 1993)} \quad (12)$$

$$Fe^{2+} + H_2O \rightarrow FeOH^+ + H^+ \quad \text{(Burns and Fisher, 1993)} \quad (13)$$

$$FeOH^+ + 2H^+ \rightarrow Fe^{3+} + 1/2\,H_2 + H_2O \quad \text{(Burns and Fisher, 1993)} \quad (14)$$

As a next step, the resulting Fe(III) (reaction 14) serves now as the oxidizing agent for pyrrohtite (Fe_7S_8) and leads to the formation of pyrite or marcasite (Burns and Fisher, 1993):

$$Fe_7S_8 + 6Fe^{3+} \rightarrow 4FeS_2 + 9Fe^{2+} \quad \text{(Burns and Fisher, 1993)} \quad (15)$$

Finally, according to Burns and Fisher (1993), sulfate formation can occur on the one hand by aqueous pyrite oxidation by Fe(III):

$$FeS_{2(s)} + 14Fe^{3+} + 8H_2O = 15Fe^{2+} + 2SO_4^{2-} + 16H^+ \quad \text{(Stumm and Morgan, 1995)} \quad (11)$$

or by aqueous pyrite oxidation in the presence of oxygen:

$2FeS_2 + 7O_2 + 2H_2O \rightarrow 2FeSO_4 + 2H_2SO_4$ (Lowson, 1982) (10)

or

$2FeS_2 + 7O_{2(aq)} + 2H_2O \rightarrow 2Fe^{2+} + 4SO_4^{2-} + 4H^+$ (Burns and Fisher, 1993) (16)

All of these processes will lead to acid production during leaching of pyrite, which causes a strong drop in pH. Burns and Fisher (1993) concluded that under these conditions, even in a CO_2 – dominated atmosphere, the formation of carbonate is retarded.

2. Data methods

This section describes data methods based on missions and instruments that provided data relevant for this study. Table 4 gives a chronological overview of past and current successful missions conducted over the past 50 years of Mars exploration:

Table 4: Overview table of successful Mars missions

Mission and Rover	Launch	Agency/Nation	Status
Mariner 4	1964	NASA (USA)	successfully completed
Mariner 6 & 7	1969	NASA (USA)	successfully completed
Mars 2 & 3	1971	(USSR)	successfully completed
Mariner 9	1971	NASA (USA)	successfully completed
Mars 5	1973	(USSR)	successfully completed
Viking 1 & 2	1975	NASA (USA)	successfully completed
Mars Global Surveyor (MGS)	1996	NASA (USA)	successfully completed
Mars Pathfinder (MPF)	1996	NASA (USA)	successfully completed
2001 Mars Odyssey	2001	NASA (USA)	still in duty
Mars Express	2003	ESA (Europe)	still in duty
Mars Exploration Rovers (MER –A-B)	2003	NASA (USA)	MER-B still in duty
Mars Reconnaissance Orbiter (MRO)	2005	NASA (USA)	still in duty
Dawn	2007	NASA (USA)	still in duty
Curiosity (MSL)	2011	NASA (USA)	still in duty
Mars Orbiter Mission	2013	ISRO (India)	still in duty
MAVEN	2013	NASA (USA)	still in duty

2.1 Mars Global Surveyor

After the Viking era and 21 years of several mission failures the spacecraft Mars Global Surveyor (MGS) was launched by the National Aeronautics and Space Administration (NASA) and the Jet Propulsion Laboratory (JPL) of the California Institute of Technology in November 7, 1996. Planned to be primarily a mapping mission, the spacecraft carried five scientific instruments onboard (a Magnetometer and electron reflectometer (MAG/ER), the Mars Orbiter Camera (MOC; Malin and Edgett, 2001), the Mars Orbiter Laser Altimeter (MOLA; Smith et al., 2001), a Mars Relay (MR), and an Ultrastable Oscillator for doppler measurements (USO/RS)) in which one of them is described in the following chapter.

2.2 Mars Orbiter Laser Altimeter

The goal of Mars Orbiter Laser Altimeter (MOLA) was to generate a global digital elevation model of Mars with a full coverage between -87° and +87°. The laser transmitter, designed by the Laser Remote Sensing Branch of the Laboratory for Terrestrial Physics of NASA's Goddard Space Flight Center, transmitted and recorded laser pulses of 10 pulses per second (pps) (Gardner, 1992, Smith et al., 2001). The ranging distance measurements were conducted by the calculation of the laser beams two-way-travel time (TWT) between spacecraft and martian surface in the nadir direction (Smith et al., 2001). The instrument's resolution had a precision as good as 37.5 cm for a smooth topography and up to 10 m for slope angles of 30° (Smith et al., 2001). The laser beam footprint is about 160 m in diameter (Gardner, 1992) with a spacing of ~300 m between the single shots and 4 km spacing between the across-track orbits of each shot (Smith et al., 2001). More than 9500 profiles were interpolated with a resolution of 128 pixels per degree (sub-polar regions) up to 512 pixels per degree (polar regions) (Smith et al., 2003). MOLA operated beginning September 1999 and became silent in June 2001 at the end of its lifetime.

2.3 Mars Orbiter Camera

The Mars Orbiter Camera (MOC) was built by Malin Space Science Systems (MSSS) and consists of a high resolution black-and-white narrow-angle camera (grayscale) with 1.5 to 12 m per pixel, a red and blue pushbroom wide angle context camera with 240 m per pixel and a pushbroom wide angle camera with a resolution between 230 m per pixel up to 7.5 km per pixel (Malin et al., 2010).

2.4 The High Resolution Stereo Camera

The spacecraft Mars Express was launched on June 2nd, 2003 from Baikonur with the Russian Sojus – FG/Fregat rocket after the failure of the Russian-European Mars 96 mission. The MEX mission, conducted by the European Space Agency (ESA), was expected to run only one Mars year. But until now, despite the loss of the British Beagle 2 lander, the MEX mission is not only the first European mission to another planet but also highly successful. Built in record time by European Aeronautic Defence and Space Company (EADS) Astrium with a limited budget the Mars Express spacecraft is armed with seven scientific instruments: Analyser of Space Plasmas and Energetic Neutral Atoms (ASPERA-3), High–Resolution Stereo

Camera (HRSC), Mars Express Radio Science Experiment (MaRS), Mars Advanced Radar for Subsurface and Ionospheric Sounding (MARSIS), Observatoire pour la Minéralogie, l'Eau, les Glaces et l'Activité (OMEGA), Planetary Fourier Spectrometer (PFS), Spectroscopy for the Investigation of the Characteristics of the Atmosphere of Mars (SPICAM). Only the dataset from the High–Resolution Stereo Camera was used in this thesis and will be described in the following chapter.

The High – Resolution Stereo Camera (HRSC) allows photographs of the martian surface in color and in 3D. The HRSC experiment was conceived by Professor Dr. G. Neukum. The camera was constructed at the German Aerospace Center (DLR), under the supervision of Prof. Neukum.
With a weight of 19.5 kg, the HRSC possesses two different photographic systems, which consist of 9 parallel CCD (Charged Coupled Device) line detectors, ordered behind an Apo – Tessar lens (focal length: 175 mm). The Super Resolution Channel (SRC) with a focal length of 975 mm comprises a non-interlaced Kodak CCD array sensor (1.024 x 1.024 pixels) for resolutions up to 2.3 m/pxl (Jaumann et al., 2007). The nine line detectors are laterally installed to the flight direction. Thus, the sensors can record consecutively line by line. The camera is capable of obtaining 5 x stereo images with its additionally combined stereo – and photometry channels (Neukum and Jaumann, 2004).

The observations are performed at a reduced wavelength range to obtain color information. This is performed by applying filters mounted directly in front of the corresponding CCD-lines. For the red (750 +/- 20nm), green (530 +/- 45nm) and blue (440 +/- 45nm) colors. A further channel is installed, sensitive in the near-infrared (970 +/- 45 nm), in order to provide mineralogical composition of the martian surface.

The advantage of the HRSC-system compared to others is the ability to make stereo images. Most attempts to do this during past missions have required the spacecraft to target the same surface feature from two different orbital passes. The HRSC-Camera is the only experiment that can do it in one pass. A successful attempt to obtain topographic information was the Mars Global Surveyor carrying a laser altimeter instrument (MOLA) that provided spot heights across the surface of Mars. But these spots were often separated by many kilometers. HRSC provides altitude data for every data point the camera sees. It is the first time that high-resolution images have been accompanied by high-resolution topography and this makes the Mars Express DTM the most detailed topographic data set for planet Mars.

The principle of stereo observations is obtaining a forward, backward and downward-view images of the object. With the different views one can create 3D information via photogrammetry. To do so, the CCD-lines are installed in such a way, that one line looks forwards (+18.9°), one line looks backwards (-18.9°) and one line looks perpendicular to the surface (Nadir-channel). The photometric- channels are forward-looking and backward-looking in a smaller angle and provide brightness information and in addition to this help to improve the stereo-information of the stereo-channels. Figure 7 shows the HRSC coverage to orbit 14,188 (08 March, 2015):

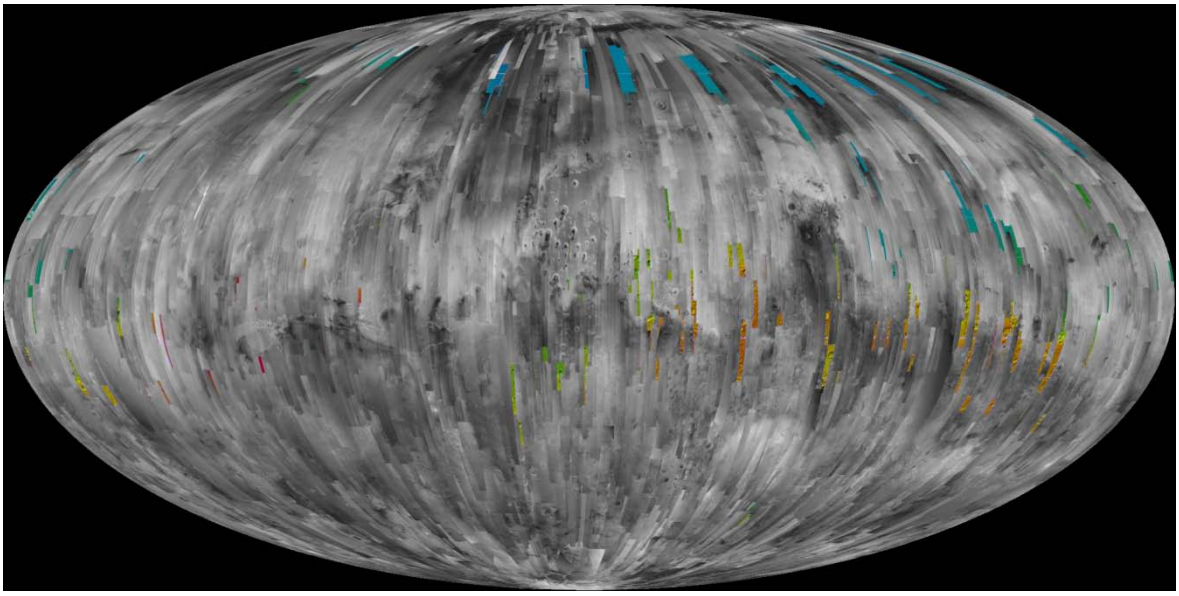

<20m/pixel 70.1% + 0.1%
<40m/pixel 96.1% + 0.3%
<60m/pixel 97.3% + 0.1%
<100m/pixel 97.6% + 0.1%

Figure 7: HRSC coverage up to orbit #14,454 (24 March, 2015) covering a MOLA hillshade (image credit: Deutsches Zentrum für Luft- und Raumfahrt e.V.).

2.5 Mars Reconnaissance Orbiter

The Mars Reconnaissance Orbiter, built by Lockheed Martin on behalf of JPL, was launched onboard an Atlas V-401 rocket from Cape Canaveral Air Force Station in August 2005 and reached Mars in March 2006. The spacecraft is equipped with three cameras (the High Resolution Imaging Science Experiment camera (HIRISE), the Context Camera (CTX), and the Mars Color Imager (MARCI)), two spectrometers (the Compact Reconnaissance Imaging Spectrometer for Mars (CRISM) and the Mars Climate Sounder (MCS)) and one radar (the

Shallow Subsurface Radar (SHARAD)). As only the Context Camera provided data used in this study the CTX instrument will be describe in the following chapter.

2.6 The Context camera

The Context Camera (CTX) instrument was designed and operated by Malin Space Science System (MSSS). This instrument produces data for grayscale image strips of 30 km width and up to 160 km length with a resolution of 5-6.5 m/pixel (Malin, 2007). The instrument is a Cassegrain (Maksutov-type) telescope with a focal length of 350 mm with a 5064 pxl wide line array charge-coupled device (CCD). As of February 2010 (MSSS, 2014) more than 50 % of the martian surface has been covered.

2.7 Software Geographic Information System

The software Geographic Information System (GIS) is a tool, which is able to integrate images, digital terrain and elevation model (DTM, DEM) in vector and raster formats. Additionally, the GIS software processed remote sensing information in several formats and units, collected during planetary missions in the solar system. Thus, within this thesis the commercial ESRI's ArcGIS 9.2 was used.

3 Geochemistry

In order to produce sulfuric acid containing solutions for numerical evaporation modeling ten terrestrial rock and mineral samples as potential Mars analogs and one sample of the martian meteorite Tissint have been reacted with sulfuric acid solutions to transfer ions in significant proportions to the aqueous phase.
The large number of samples analyzed here should cover a range of possible rocks proposed for the regolith on Mars.
Geochemical investigations conducted by the CheMin instrument (XRD) and the APXS instrument onboard the Curiosity rover on Mars were performed after the experiments were completed for this thesis (see chapter 1.2.2). Despite this, investigations conducted by Blake et al. (2013), Bish et al. (2013), and Vaniman et al. (2014) reflect some of the same rock types or minerals characterized in this work.

3.1 Sample selection and description

The mineralogical composition of the massive Mg-, Ca- and Fe-rich sulfate deposits on Mars is controlled by the quantity of aqueous influx and the mineralogical composition of the source rocks that serve as ion donors.

The samples chosen for the leaching experiments used contain Mg, Na, K, Ca, Fe and Al ions. Ten terrestrial samples including two rock standards, the major rock-forming minerals, ortho- and clinopyroxene, olivine and plagioclase and four mafic to ultramafic rocks were examined in this study. Two rock standards were provided by the U.S. Geological Survey (USGS) and include basalt and a dunite which represent analogues for martian rocks. Additionally, the martian meteorite Tissint was investigated.

The samples selected encompass typical expected volcanic rocks, basaltic rocks and minerals such as olivine, pyroxene, plagioclase -and rocks: comprising volcanic glass, basalt and komatiites. These serve as analogues for martian lithologies in accordance with *in situ* measurements of rock soil, performed during the NASA MER-mission and APXS data collected during the most recent MSL-mission (McSween and McLennan., 2014; see section 1.2.2).
The sample ages range between 3.5 Ga (komatiites, Onverwacht group, Barberton Greenstone Belt) up to recent ages (volcanic glass, Kilauea, Hawai, USA). The alteration and weathering state also reflects their different geologic histories and environments.

Pyroxenes are one of the four most prevalent minerals in the Earth's crust and are important rock-forming mafic minerals with the general formula $ABSi_2O_6$ where the A site is commonly occupied by Mg^{2+}, Fe^{2+}, Ca^{2+} or Na^{+}, and B is Mg^{2+}, Fe^{2+}, or Al^{3+} (Füchtbauer, 1988; Matthes, 1993). Pyroxenes crystallize as one of the first minerals under high temperature conditions in a continuously cooling siliceous melt (Füchtbauer, 1988; Matthes, 1993). Results of the Viking lander data and remote sensing data by the Viking orbiters, the Thermal Emission Spectrometer (TES) on board the Mars Global Surveyor spacecraft (MGS) detected pyroxenes in martian surface material (Greeley and Spudis, 1981, Bandfield, 2001).
The clinopyroxene (cpx) used in this study was sampled from the West Eifel volcanic field. The orthopyroxene (opx) originated from Lake Onatchiway, Quebéc (CAN). This unweathered sample contains up to 17 wt.% MgO and about 16 wt.% Al_2O_3 (Hamilton, 2000).

The plagioclase (Pl) comes from Crystal Bay, Minnesota, USA. The specimen is a Ca^{2+}, Na^{+} and Al-rich bytownit (anorthosite) (Emmons and Grout, 1943). According to Emmons and Grout (1943) coarse-grained bytownite occurs at many locations along the north shore of Lake Superior. The bytownite in the presented study was purchased from a dealer and is expected to be similar to the sample analyzed by Emmons and Grout (1943).

The volcanic glass is originated near the volcano house in the volcano park on the big island of Hawaii (USA) close to the Crater Rim Drive at the north - eastern flank of the Kilauea volcano, at the east rift zone. The major element concentration of the selected sample contains a high SiO_2 value around 13 ppm FeO_T concentrations, and with around 5 ppm and up to 3 ppm comparable low MgO and Na_2O concentrations within the samples (12 ppm Al_2O_3, measured with the electron microprobe, analysis of basalt glass, Thornber et al., 2002).

The xenolith sample was taken from a peridotitic xenolith inclusion in Tertiary basalt from the northern Hessian Depression (20-8 Ma). Peridotite is the plutonic equivalent to the volcanic komatiite and is the typical rock from the Earth's Upper Mantle. It consists of minimum 40 wt.% olivine and a mixture of ortho- and clinopyroxene. Based on their mineral composition, Streckeisen (1974) subdivided peridotites into wehrlite, lherzolite, harzburgite and dunite. Xenoliths from the northern Hessian Depression are mainly of lherzolitic to harzburgitic composition (Oehm et al., 1983).

The translucent single crystalline San Carlos olivine (Ol) (Arizona, USA) $(Mg, Fe)_2SiO_4$ sample was also purchased from a dealer, hence the exact location in the San Carlos area cannot be determined. The selected crystals are of high optical and unweathered quality. The specimens are associated with peridotite inclusions in late Tertiary to Quaternary basalt flows (Frey and Prinz, 1978).

Komatiites are ultramafic, volcanic rocks named after the Komati River in South Africa, and occur almost exclusively in the Greenstone Belts of the Archaean shields of Australia, Canada, and southern Africa. They are of high scientific importance, because they prove the extrusion of ultramafic rocks during the Archaean, which was the first step on building continental and oceanic crust. It also shows the higher temperature of the Archaean mantel. Experiments have shown (Green, 1975) that komatiitic magmas develop at temperatures ~1600°C. Unweathered komatiites contain between 18-30 wt.% MgO and consist of olivine, augite, chromite, volcanic glass, and occasionally plagioclase (Matthes, 1993). Because of their age and primary mineralogy, most komatiites found today are highly weathered and mainly consist of secondary minerals such as serpentine, chlorite, amphibole, and plagioclase.

The two komatiite samples studied are from the Onverwacht Group of the Barberton Greenstone Belt and about 3.5 Ga old. The advantage of Barberton Greenstone Belt komatiites is that they only experienced low-grade, greenschist facies metamorphism, which means that their mineralogical and chemical composition did not change much due to metamorphic processes. Sample 1-komatiite is a nearly black komatiite originating from the vicinity of the Umsoli Mine near the Komati River. The sample has experienced little alteration and it still contains some olivine crystals. The altered portions of the sample include serpentine, quartz and iron oxides.

The s-komatiite sample is highly weathered and shows the typical spinifex texture indicating the fast cooling of the ancient olivine crystals. This sample consists almost exclusively of serpentine which is the typical mineral, formed by the alteration of komatiites.

The powdered reference material BIR-1a is a basalt (provided by the USGS) from one of the Reykjavik interglacial lava flows (Iceland) taken by Karl Gronwold in 1974.
According to Flanagan (1984) the sample location is a low hill (~10 m height) 12 km east of Reykjavik.

BIR-1a is an abyssal olivine tholeiite that belongs to the Reykjavik dolerites, presumably from shield volcanos formed during the youngest interglacial periods. Dolerites often consist of pigeonite, rarely hypersthene, with intrusions of olivine (Matthes, 1993).

DTS-2b, the second powdered reference material (provided by the USGS) is a Twin Sister dunite and was sampled in the Twin Sister mass east of Bellingham, Washington (USA). Ragan (1963) described this rock sample as an unaltered, coarse-grained dunite with enstatite in its composition and accessories of chromite and chromium diopside. Mineralogical investigation showed that fosterite (>90 wt.%) is the predominant mineral.

Tissint is the youngest fall of a martian meteorite, observed in the early morning on July 18, 2011 in the region of the Oued Drâa valley, east of Tata, Morocco (29°28.917'N, 7°36.674'W) (Chennaoui Aoudjehane et al., 2012).
Tissint is classified as an anchondrite, a martian olivine-phyric shergottite (SNC meteorite group) with olivine macrocrysts (>1 mm) in a fine grained groundmass of pyroxene, plagioclase, oxides, and smaller olivine microphenocrysts (Chennaoui Aoudjehane et al., 2012; Summerson et al., 2013) in its fresh material. Mineralogical investigations by Summerson et al. (2013) show that the mineral phase plagioclase is completely replaced by maskelynite, generated by a high-pressure shock wave due to impact. The interior olivine-rich matrix is coated with a glassy black fusion crust. The extreme freshness of the material permits determination of the effects of "sulfate acid leaching" on a martian meteorite under laboratory conditions as an analogy to martian processes.

3.2 Analytical methods

In attempt to produce sulfuric acid rich waters for the numerical evaporation experiments the selected powdered Mars analog samples were suspended in pH 1.3 and pH 3 sulfuric acid solutions. Therefore, the experiments must have been carried out under controlled conditions that also required geochemical, petrologic and petrographic investigations of the solid samples. Whereas the focus of the leaching experiments was mainly on the bulk ion uptake of the solutions, alteration of the solid samples due to rock-solution interactions were not discussed in detail within this thesis.

3.2.1 X - ray fluorescence spectrometry

X-ray Fluorescence Spectrometry (XRF) is a method for qualitative and quantitative determination of major and trace elements. For X-ray fluorescence analysis the sample material is irradiated with X-rays, which excite secondary X-ray fluorescence. The characteristic wavelengths of secondary X-rays are produced by the elements of the sample material. The qualitative composition of the sample can be determined by measurement of these characteristic wavelengths. The intensity of the fluorescent radiation allows determination of the element concentrations in the sample. Intensities are compared with standards of known composition. The sample preparation encompasses preparing glass discs for major and some trace elements. The advantage of glass discs is that no matrix and texture effects occur, although they require a relatively large amount of material and effort to prepare. To convert the element concentrations to the sum of 100 vol.%, the loss on ignition was determined. For that purpose, the samples were weighed in a porcelain crucible and calcined at 1000 °C for one hour. The calibration of the analysis was carried out against internal geologic standards whose concentrations were certified in international proficiency tests (Dr. Naumann/GFZ-Potsdam, pers. comm.). To determine the accuracy of the measurements, analyses of the DTS–2b and BIR–1a standards (USGS) were performed. The accuracy of the measurements is around ±5%, the reproducibility of the measurements is ±7% for most of the major and minor elements. A PANalytical Axios wavelength dispersive X-ray spectrometer, equipped with a Cu-tube for the analysis of the geological materials was used at the Helmholtz-Zentrum Potsdam, Deutsches GeoForschungsZentrum (GFZ), Germany.

3.2.2 X-ray diffractometry

The mineralogical compositions of the solid samples were collected with a Bruker AXS Discover diffractometer with CuKα radiation at the GFZ. For that purpose, the dried sample powder was pressed in sample carriers. Diffractograms were recorded 5-90°2θ at a step size of 0.013°2θ and 2 s acquisition times per step. Data processing and one- and two–dimensional phase analysis interpretation were performed using the software Diffrac.EVA (Bruker). Diffractogram processing was performed using the software AutoQuant (Media Cybernetics, Inc.). Minerals with abundances below 5 vol.% were not considered in the calculation.

3.3 Geochemical investigations of major elements

Results of X-ray fluorescence analyses are given in Table 5, classification of the rock samples are given in figure 8. According to the bulk analyses of the samples the major elements are Mg, Ca, Fe, and Al. Trace element concentrations varied between 12 ppm for Nb up to several thousand ppm for Cr and Ni (see appendix 2).

Major element concentrations vary widely. Although the sample selection was mainly focused on Mg and Ca as the major elements, Tissint, the orthopyroxene sample and the volcanic glass sample are dominated by comparatively high Fe (<15.9 wt%) and Mg values (<10.1 wt%). The olivine sample contains 29.1 wt% Mg indicating forsterite as the main mineral phase including a high concentration of Ni (see appendix 2).

Table 5: X-ray fluorescence analyses of the selected mafic to ultramafic rocks, minerals and the martian meteorite Tissint (normalized).

Sample	SiO_2 (wt %)	Al_2O_3 (wt %)	FeO (wt %)	MnO (wt %)	MgO (wt %)	CaO (wt %)	Na_2O (wt %)	K_2O (wt %)	H_2O (wt %)	Σ (%)
Tissint	45.1	5.4	23.1	0.511	17.08	6.96	0.03	< 0.01	bdl	99.37
Olivine	40.5	0.1	10.2	0.131	48.52	0.11	< 0.01	< 0.01	0.04	99.71
Clinopyroxene	48.1	6.1	7.4	0.102	13.42	22.32	0.42	0.14	0.14	99.86
Orthopyroxene	49.2	6.1	19.5	0.265	22.15	1.80	0.04	< 0.01	0.24	99.87
Plagioclase	49.0	31.8	0.5	< 0.01	0.07	15.24	2.42	0.07	0.54	99.94
Volcanic Glass	48.7	11.2	12.9	0.166	12.87	9.36	1.70	0.38	0.18	99.77
1-komatiite	41.1	2.3	12.6	0.180	31.44	1.89	< 0.01	< 0.01	9.38	99.35
S-komatiite	43.5	4.1	12.3	0.171	26.47	5.22	0.08	0.01	7.32	99.59
Xenolith	44.7	1.8	8.0	0.114	41.79	1.37	0.08	< 0.01	1.43	99.49
BIR-1a	47.6	15.2	11.4	0.171	9.48	13.03	1.64	0.01	0.29	99.89
BIR-1a[a]	48.0	15.5	11.3	0.175	9.70	13.3	1.82	0.03	na	--
DTS-2b	39.4	0.4	7.9	0.103	49.16	0.11	0.01	< 0.01	0.87	98.14
DTS-2b[a]	38.4	0.5	7.8	na	49.4	0.12	0.02	na	na	--

[a] These components have been analyzed by the U.S. Geological Survey ; na = not analyzed, wt.% = weight percent; ppm = mg/kg; bdl = below detection limit.

Clinopyroxene has typical compositions with Ca (<15.9 wt.%), Mg (8.0 wt.%) and Fe (< 5.1 wt.%). Plagioclase (bytownite) has low concentration of minor elements but a comparatively high content of Al (up to 16.9 wt.%) and Ca (10.9 wt.%). Based on its mineralogical characteristics determined by X-ray diffraction, the ultramafic komatiite samples 1-komatiite and s-komatiite mainly consist of the mineral phase actinolite ($Ca_2(Mg, Fe^{2+})_5Si_8O_{22}(OH)_2$) with Mg concentrations of up to 18.8 wt.% and heavy element contents of Cr (up to 0.28 wt.%) and Ni (up to 0.19 wt.%). The xenolith sample is dominated by forsterite and enstatite (according to X-ray diffraction) and shows Mg values up to 25.0 wt.%.

The olivine tholeiite BIR-1a mainly consists of pigeonite with intrusions of olivine (compare USGS-material) with low concentrations of most major and minor elements.

The DTS-2b sample has a composition typical for this dunite rock (Ragan, 1963) with Mg as the major element (up to 29.4 wt.%), Fe up to 5.5 wt.% and rather high enrichment of Cr (up to 1.48 wt.%) and Ni (up to 0.37 wt.%).

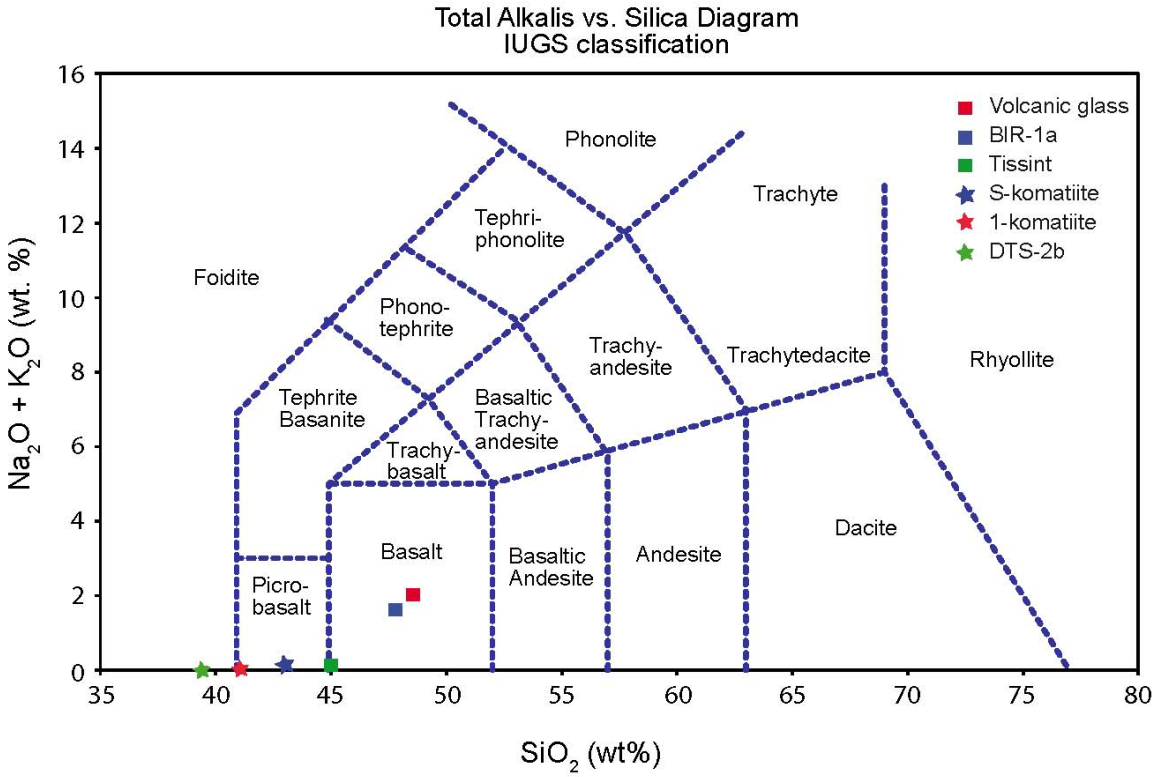

Figure 8: TAS diagram showing the classification of rock samples used in this study based on X-ray fluorescence analyses.

3.4 Mineral content

The diffractogram of the **Tissint** sample (Figure 9) is characterized by prominent peaks at 29.71 and 30.94°2Θ assigned to pigeonite ($Ca_{0.25}(Mg, Fe, Al)[Si, Al)_2O_6]$) and additional peaks at 35.46 and 36.29°2Θ indicative of forsterite ($Mg_2[SiO_4]$). Both mineral phases form in hot basaltic lavas, whereas the presence of pigeonite is an indicator of a rapid cooling melt (Matthes, 1993).

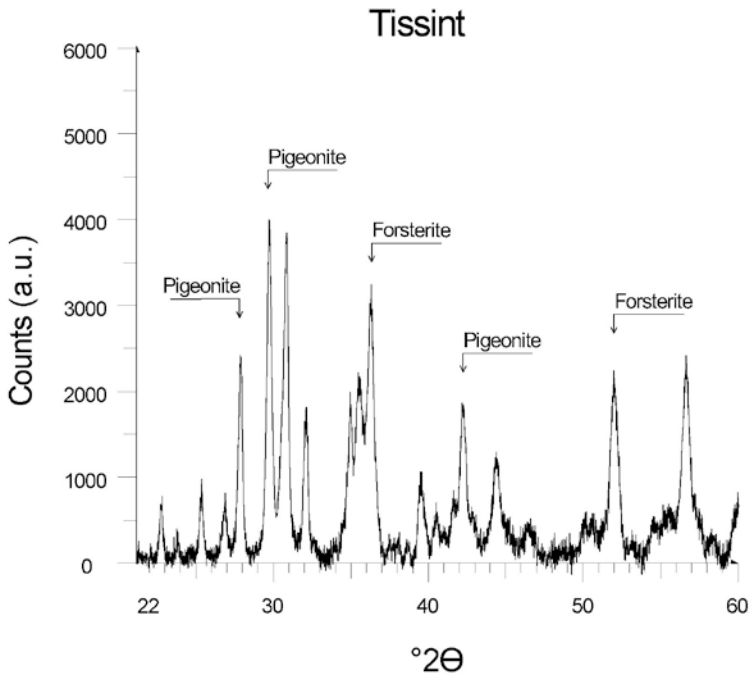

Figure 9: Diffractogram of the martian meteorite Tissint, showing pigeonite and fosterite (background-subtracted).

The **clinopyroxene**-sample contains diopside ($CaMg[Si_2O_6]$) whereas the **orthopyroxene** sample contains enstatite $Mg_2[Si_2O_6]$ with peaks at 28.19 and 35.26°2Θ.

Forsterite and augite ($(Ca, Na)(Mg, Fe, Al)[(Si, Al)_2O_6]$) were identified from XRD peaks in the **volcanic glass** (forsterite: 32.17 and 36.40°2Θ and augite: 29.86 and 35.71°2Θ).

The **olivine** is composed of forsterite (35.77 and 36.57°2Θ) over the entire bandwidth. The same also applies to the **plagioclase** sample with significant peaks at ~22.00, 27.90, and 28.04°2Θ for bytownite.

The **1-komatiite** sample is a mixture of actinolite, antigorite and magnetite. The **s-komatiite** sample is composed of actinolite ($Ca_2(Mg, Fe)_5[(OH)_2/Si_8O_{22}]$) (10.51 and 33.06°2Θ) and

clinochlore ($(Mg_5, Fe^{2+},Al)[(OH)_2(AlSi_3O_{10}) \cdot (Mg,Fe^{2+},Al)_3(OH)_6$) (6.19, 12.41, and 24.96°2θ). And finally, the **xenolith** sample contains forsterite (35.77 and 36.57°2θ) and entstatite (28.19 and 35.26°2θ).

4 Experimental solution production and analytical methods

Rock-solution interaction on Earth occurs at various temperatures, between low temperatures to hydrothermal conditions. Due to the absence of suitable Mars samples the temperature conditions cannot be doubtless determined, in which only one sample of an altered rock may not represent an entire system. Thus, for comparisons, the leaching experiments described in this section were performed at ~21°C.
In order to observe any differences in mineral precipitation during evaporation, sulfuric acid solutions with two different acid strengths (pH 1.3 and pH 3) were used for the leaching experiment.

The leaching experiment for the production of sulfuric acid solutions with ion contents as proposed for evaporation processes in Juventae Chasma is based primarily on standardized procedures that are common in aqueous geochemistry and hydrogeology. The samples were ground with an agate disc mill to fine powder (<63µm) and were subsequently homogenized. The total amount of the solid samples was dried at around 106°C for 24 h. Three grams of each of the samples were sub sampled into three parts. For each experiment 1 gram of rock powder together with 100 ml H_2SO_4 (pH 1.3 and pH 3) was placed into a 100 ml PET-test tube (batch cup). The batch cups and two blanks were placed in an overhead shaker, in an attempt to avoid layering and concentration gradients as well as to simulate time and fluid flow while leaching. The samples were retained in the cups for about 30 days (Figure 10). The fluids were analyzed and the undigested solids were stored for later use. As a next step, the solutions were filtered through 11 µm standard Schleicher & Schuell cellulose filters. The pH values of the resulting leachate were measured at each batch cup with a standard pH - electrode (pH-meter WTW pH 196). A fifteen-ml aliquot of each of the untreated, filtered solution was analyzed using ICP OES Optima 2100 from PerkinElmar in order to measure the bulk-ion-concentration (Fe^{3+}, Mg^{2+}, Ca^{2+}, K^{+}, Na^{+}, Mn^{2+}, Al^{3+}, and Cl^{-}). Experiments and wet-chemical analyses were conducted in the laboratories of the Freie Universität Berlin, Germany.

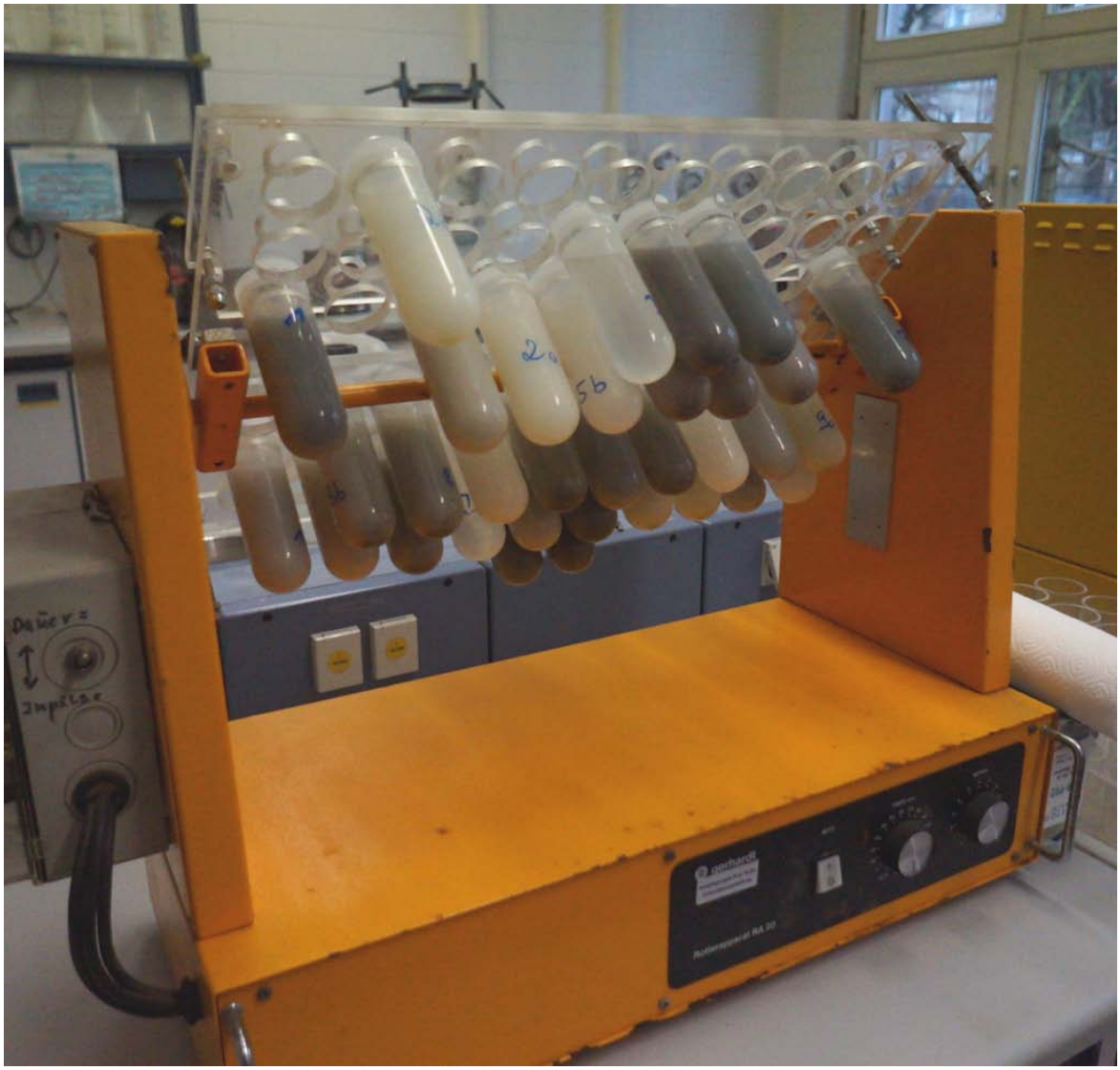

Figure 10: Experimental acid-sulfate leaching process of various source rocks, minerals and the martian meteorite Tissint in an overhead shaker in the laboratories at the Freie Universität Berlin, Germany. Three grams of each of the grinded and homogenized samples were sub sampled into three parts. For each experiment 1 gram of rock powder together with 100 ml H_2SO_4 (pH 1.3 and pH 3) was placed into a 100 ml PET-test tube (batch cup). The batch cups and two blanks were placed in an overhead shaker. The samples were retained in the cups for about 30 days.

4.1 Leaching experiment results

Results of the leaching experiments were presented in this section to investigate the ion uptake into the leachates, as a prerequisite for evaporation modeling.
Experimentally derived Fe values in the leachates must be interpreted with care, because of possible loss of dissolved iron by precipitation of iron hydroxides, iron complexes, or iron sulfides in contact with atmospheric oxygen during shaking. Only the total iron content was measured, due to the strong acidic starting pH of pH 1.3 and pH 3. According to the Eh – pH diagram (Figure 17), the occurrence of Fe^{2+} ions below a pH value of 4 and under high Eh conditions in the solution was not expected. Therefore, the iron content in fluid samples with pH values below 4 will be interpreted as Fe^{3+}. Fe^{2+} and Fe^{3+}-ions in samples with pH results above 4 were coupled for the modeling and referred to as Fe_{tot}.
Possible precipitations in the batch cups were macroscopically not observed. Hydrogen carbonate was not expected to form in the solutions resulting at pH values below 4. Hence, HCO_3^- was not measured.

As a result of the leaching experiment with pH 3 sulfuric acid, nitrate was measured in four of the leachates (**plagioclase$_{(pH\ 3)}$**, **s-komatiite$_{(pH\ 3)}$**, **xenolith$_{(pH\ 3)}$**, and **Bir-1a$_{(pH\ 3)}$**) although all samples were treated the same and the batch cups (including the caps) were cleaned consciently. Therefor, it can be assumed that the sample fluid contamination happened after the leaching experiment of the pH 3 sulfuric acid fluid samples was completed. Nonethless, the measurement results of the polluted samples were standardized and the ionic potentials were calculated with respect to the impurities. Hence, the results of the four affected pH 3 fluid samples have to be taken with care.

The leachates with the highest ion concentrations come from the samples of the martian meteorite Tissint, both from the pH 1.3 leachate as well as from the pH 3 leachate. The complete datasets are given in Table 6 and 7.
Using a piper diagram (Piper, 1944; Figure 11) for a more differentiated classification of waters is a common technique to provide a brief overview of the measured data. The piper diagram is structured into two triangles and a rhombus, whereas the concentrations are expressed as % meq/L. Cations (Na^+, K^+, Ca^{2+} and Mg^{2+}) are plotted on the left in the cation triangle. Anions (HCO_3^-, Cl^- and SO_4^{2-}) are plotted on the right in the anion triangle. Both, the cation and anion triangle are combined into the adjacent rhomboidal or quadrilateral field that shows the overall chemical species distribution of the fluid samples. The piper plots

show graphically the nature of the leachates derived by weathering. A more detailed water-type classification is not possible due to a lack of data in the hydrogen carbonate or CO_2 abundance. It is assumed that at pH >4 equilibrium with the partial pressure of the atmosphere prevails.

The fluid chemistries resulting from dissolution of the samples at pH 1.3 produce similar classifications in the rhomboidal fluid diagram, which more variance is observed in the pH 3 fluids. The pH 3 samples are characterized by high SO_4^{2-} values. The content of dissolved Ca, Mg, Na, N, K, Cl, Al, Fe and Mn is generally low, but shows comparably significant variations.

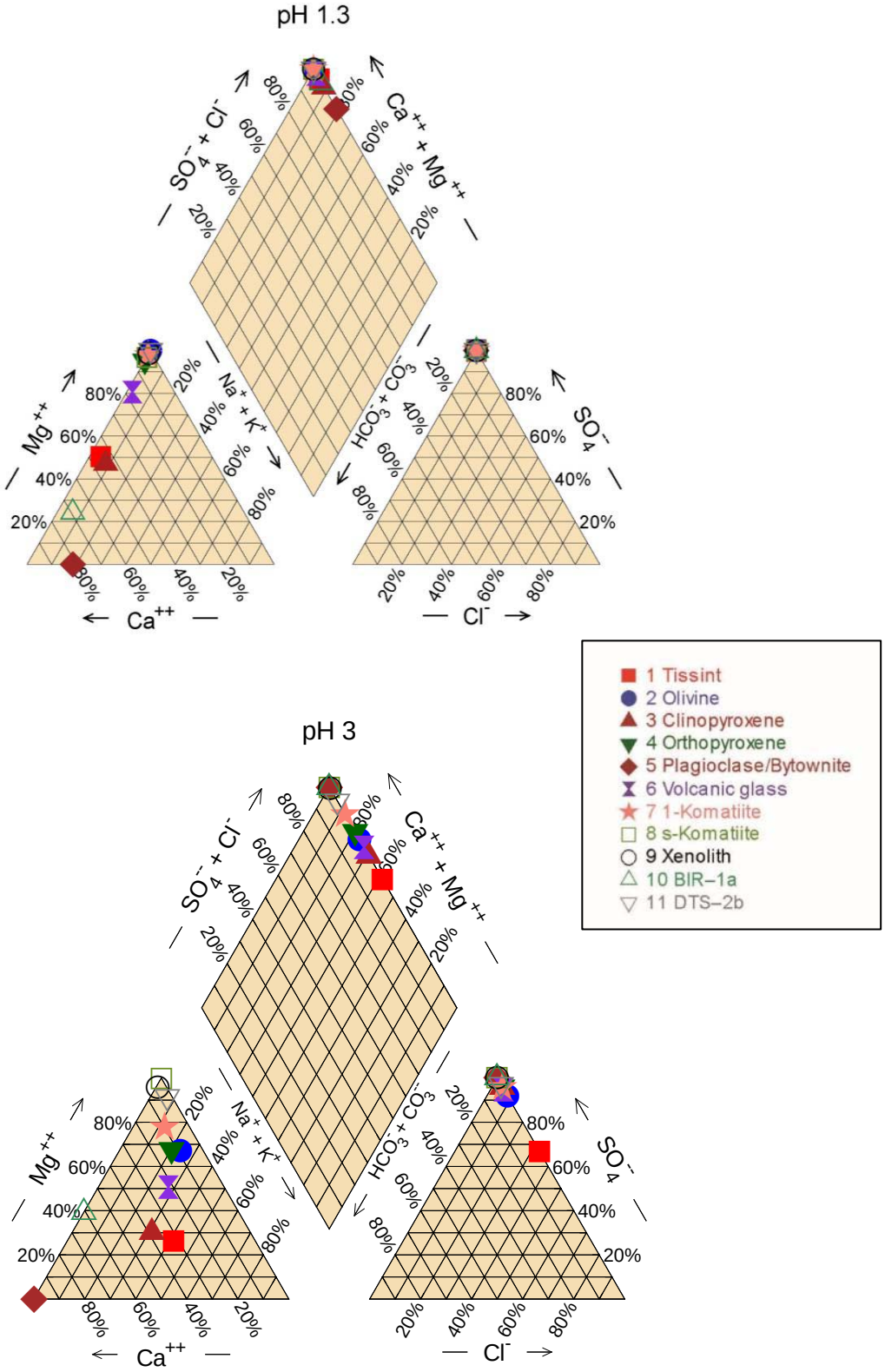

Figure 11: Piper plot (in meq %) of major ions showing the species distribution in the (a) pH 1.3 fluid samples and in the (b) pH 3 fluid samples.

4.1.1 Dissolved species distribution in the pH 1.3 samples

The major elements of the dissolved solid samples are substantially determined by the relative proportions of the calcium and magnesium species. The results are given in Table 6 and 7.
The content of dissolved magnesium is comparably high in almost all of the samples. Only two samples show higher calcium than magnesium concentrations (**plagioclase$_{(pH\ 1.3)}$** and **BIR – 1a$_{(pH\ 1.3)}$**) and two samples, **Tissint$_{(pH\ 1.3)}$** and **cpx$_{(pH\ 1.3)}$**, show a Ca/Mg ratio close to 1 with respective Ca concentrations of 1395 µmol l^{-1} and 803 µmol l^{-1} and respective Mg concentrations of 1569 µmol l^{-1} and 850 µmol l^{-1}. The SO_4^{2-} values range between 3592 µmol l^{-1} (**cpx$_{(pH\ 1.3)}$**) and 4820 µmol l^{-1} (**Tissint$_{(pH\ 1.3)}$**).

The **Tissint$_{(pH\ 1.3)}$** sample fluid contains 749.2 µmol l^{-1} Fe^{3+}, Al^{3+} with a concentration of 495.9 µmol l^{-1}, sodium with a concentration of 170.9 µmol l^{-1}, potassium with a value up to 120.2 µmol l^{-1} and a minor amount of Mn^{2+} with a concentration of 20.57 µmol l^{-1}. The sulfate – anion SO_4^{2-} and Cl^- species occure with a concentration of 4820 µmol l^{-1} and 6.49 µmol l^{-1}. The measured pH value is 3.55.

The **olivine$_{(pH\ 1.3)}$** sample fluid does not contain calcium. It is mainly enriched in magnesium up to 3917 µmol l^{-1} and SO_4^{2-} with a concentration of 4060 µmol l^{-1}. Furthermore, Fe^{3+} and Mn^{2+} can be found in the solution with comparibly low concentrations of 181 µmol l^{-1} and 6 µmol l^{-1} at a pH value of 4.1.

As mentioned above, the **cpx$_{(pH\ 1.3)}$** sample fluid shows a Ca/Mg ratio of almost 1. Other solute species within this fluid are sodium with a concentration of 118.7 µmol l^{-1}, potassium with a concentration of 185.9 µmol l^{-1}, aluminium with a value up to 693.4 µmol l^{-1}, a ferric iron content of 181.6 µmol l^{-1}, manganese with a concentration of 5.1 µmol l^{-1} and a SO_4^{2-} content of 3592 µmol l^{-1}. The measured pH value is 2.75.

The **opx$_{(pH\ 1.3)}$** sample fluid shows a higher magnesium species concentration (806 µmol l^{-1}) than calcium (39.17 µmol l^{-1}) in the solution. The Fe^{3+} content is around 427 µmol l^{-1}, followed by Al^{3+} with 308 µmol l^{-1} and Mn^{2+} with 4.19 µmol l^{-1} at a pH value of 2.17.

The **plagioclase$_{(pH\ 1.3)}$** fluid is enriched in calcium with a concentration of 818.4 µmol l^{-1}. This sample contains the highest Al^{3+} and Na^+ concentrations of all ph 1.3 fluid samples with

1608 µmol l^{-1} and 378.4 µmol l^{-1}, respectively. Calcium has only a concentration of 818.4 µmol l^{-1}. Ferric iron and manganese occur with a minor mineral concentration of 11.46 µmol l^{-1} and 1.09 µmol l^{-1} at a pH – value of 3.75.

Table 6: Measured ion concentration and pH values of the pH 1.3 solutions

	Ca^{2+} mg/l	Mg^{2+} mg/l	Na^{+} mg/l	K^{+} mg/l	SO_4^{2-} mg/l	Cl^{-} mg/l	Al^{3+} mg/l	Fe^{3+}/Fe^{2+} mg/l	Mn^{2+} mg/l	pH
Tissint	55.93	38.13	3.93	4.7	463	0.23	13.38	41.84	1.13	3.55
Olivine	0	95.2	0	0	390	0	0	10.11	0.33	4.1
Clinopyroxene	32.2	20.67	2.73	7.27	345	0	18.71	10.14	0.28	2.75
Orthopyroxene	1.57	19.6	0	0	356.3	0	8.31	23.84	0.23	2.17
Plagioclase	32.8	0	8.7	0	362.3	0	43.38	0.64	0.06	3.75
Volcanic glass	17.2	49.53	2.5	0.7	386.7	0	11.14	28.24	0.5	3.6
1-komatiite	2.5	72.17	0	0	362	0	5.24	6.41	0.8	2.81
S-komatiite	3.17	61.87	0	0.17	363.3	0	10.68	9.84	0.5	2.95
Xenolith	1.65	84.2	0	0.15	347	0	0	1.04	0.3	4.56
BIR-1a	30.37	6.53	3.17	0	360	0	38.41	6.41	0.1	3.79
DTS-2b	0	92.8	0	0	360.3	0	0	0	0.07	5.81

The measurement results of the **volcanic glass$_{(pH\ 1.3)}$** fluid sample show concentrations of about 428 µmol l^{-1} for Ca and 2038 µmol l^{-1} for Mg, followed by a Na^{+} concentration of 108.7 µmol l^{-1}, Fe^{3+} concentration of 505.7 µmol l^{-1}, Al^{3+} concentration of 413 µmol l^{-1}, K^{+} concentration of 17.9 µmol l^{-1} and Mn^{2+} concentration of 9.1 µmol l^{-1} at a pH value of 3.6.

The **1-komatiite$_{(pH\ 1.3)}$** results show a calcium concentration of 62.38 µmol l^{-1} and a magnesium value of 2969 µmol l^{-1}. The aluminium concentration is up to 194 µmol l^{-1}, the Mn^{2+}concentration is up to 15 µmol l^{-1} and $Fe^{3+}$is about 115 µmol l^{-1}. The measured pH value is 2.81.

The **s-komatiite$_{(pH\ 1.3)}$** fluid sample contains Ca^{2+} with 79.09 µmol l^{-1}, Mg^{2+} with 2546 µmol l^{-1}, K^{+} with 4.35 µmol l^{-1}, Al^{3+} with 395.8 µmol l^{-1}, Fe^{3+} with 176.2 µmol l^{-1} and a minor amount of Mn^{2+} with a concentration of 9.1 µmol l^{-1} at a pH value of 2.95.

The **xenolith$_{(pH\ 1.3)}$** fluid sample is characterized by a Ca^{2+} concentration of 41.17 µmol l^{-1} and a magnesium content of 3464 µmol l^{-1}. The fluid is enriched with a minor amount of 3.84 µmol l^{-1} K^{+}, 18.62 µmol l^{-1} Fe^{3+} and 5.46 µmol l^{-1} Mn^{2+}. The resulting pH is 4.56.

The **BIR – 1a$_{(pH\ 1.3)}$** leaching results show calcium and magnesium concentrations of 757.7 µmol l^{-1} and 268.7 µmol l^{-1}. Sodium has a concentration of 137.9 µmol l^{-1}. With a concentration of 1424 µmol l^{-1} aluminium shows the second highest mesured concentration of all $pH_{(1.3)}$ fluid samples. The iron conten is up to 114.8 µmol l^{-1}. The measured pH value is 3.79.

The highest solute magnesium load is acquired in the **DTS – 2b$_{(pH\ 1.3)}$** fluid sample with a concentration of 3818 µmol l^{-1}. In addition to the magnesium content only manganese occurs in the solution with a minor amount of 1.3 µmol l^{-1}. The fluid results also show the highest pH value up to 5.81.

4.1.2 Dissolved species distribution in the pH 3 samples

The pH 3 results show a broader variation of the species distribution within the fluids compared to the pH 1.3 experimental results (Table 6 and 7).
In more than half of the samples, magnesium is the dominant solute species. The results of two out of eleven samples (**cpx$_{(pH\ 3)}$** and **volcanic glass$_{(pH\ 3)}$**) identify sodium as the dominant cation with the highest concentrations. The SO_4^{2-} values range between 596.8 µmol l^{-1} (**plagioclase$_{(pH\ 3)}$**) and 648.9 µmol l^{-1} (**1-komatiite$_{(pH\ 3)}$**).

Table 7: Measured ion concentration and pH values of the pH 3 solutions

	Ca^{2+} mg/l	Mg^{2+} mg/l	Na^{+} mg/l	K^{+} mg/l	SO_4^{2-} mg/l	Cl^{-} mg/l	Al^{3+} mg/l	Fe^{3+}/Fe^{2+} mg/l	Mn^{2+} mg/l	pH
Tissint	12	6	5.15	21.95	62	22.9	0	0.01	0.1	6.54
Olivine	25	11.67	7.55	0.55	60.67	4.067	0	0.218	0.01	7.51
Clinopyroxene	7.23	3.47	5.55	2.08	60	1.9	0.24	0.4	0.06	4.18
Orthopyroxene	2.03	6.83	3.75	0.32	60	1.9	0.08	2.43	0.1	4.13
Plagioclase	4	0	0	0.02	57.33	0	5	0.1	0	4.21
Volcanic glass	4.63	6.53	6.52	0.35	60	2.4	0.01	0.27	0.06	4.66
1-komatiite	2.53	12.27	3.65	0.18	62.33	2.07	0	0	0.01	6.28
S-komatiite	0	14.4	0	0.15	59	0	0	0	0	6.83
Xenolith	0.87	14.93	0	0.38	58.33	0	0	0	0	7.88
BIR-1a	3.57	1.4	0	0.02	57.67	0	4.14	1	0.06	4.43
DTS-2b	0.53	15.77	2.08	0.22	60	1.43	0	0	0	8.88

The **Tissint$_{(pH\ 3)}$** sample fluid contains 299.4 µmol l^{-1} calcium and 248.9 µmol l^{-1} magnesium. Fe_{tot} occurs with only 0.791 µmol l^{-1}, sodium with a concentration of 224 µmol l^{-1}, potassium with a value up to 561.4 µmol l^{-1} and a minor amount of Mn^{2+} with a concentration of 1.82 µmol l^{-1}. The Cl^{-} species occurs with a concentration of 645.9 µmol l^{-1}. The solution's final pH is 6.54.

The **olivine$_{(pH\ 3)}$** sample fluid contains calcium up to 62 µmol l^{-1}. This fluid is mainly enriched in magnesium up to 480 µmol l^{-1} and Na^{+}- with a concentration of 328.4 µmol l^{-1}. Other ions occure in the fluid such as K^{+} with 14.07 µmol l^{-1}, Fe_{tot} with 3.9 µmol l^{-1} and Mn^{2+} with 0.18 µmol l^{-1}. Chloride can be found in the solution with a comparibly high concentration of 114.7 µmol l^{-1}. The pH value is up to 7.51.

The **cpx$_{(pH\ 3)}$** sample fluid shows a Ca^{2+} value of 180.4 µmol l^{-1} and a Mg^{2+} concentration of 142.8 µmol l^{-1}. Other solute species within this fluid are sodium with a concentration of 241.4 µmol l^{-1}, potassium with a concentration of 53.2 µmol l^{-1}, chloride with a value up to 54 µmol l^{-1}, a total iron content of 7.16 µmol l^{-1} and manganese with a concentration of 1.092 µmol l^{-1}. The pH value is about 4.18.

The **opx$_{(pH\ 3)}$** sample shows a high magnesium species concentration (281 µmol l^{-1}) followed by sodium with a content of 163.1 µmol l^{-1} in the solution. The Fe^{3+} content is around 43 µmol l^{-1}, Al^{3+} occurs with 2.97 µmol l^{-1} and Mn^{2+} with 1.82 µmol l^{-1}. The chloride concentration is up to 53.59 µmol l^{-1} at a pH of 4.13.

As mentioned above, the **plagioclase$_{(pH\ 3)}$** fluid is enriched in aluminium with a concentration of 185.3 µmol l^{-1}. This sample also contains calcium with 99.8 µmol l^{-1}. The potassium and the total iron concentration is very low with 0.512 µmol l^{-1} and 1.79 µmol l^{-1}. The fluid shows a pH of 4.21. Magnesium, sodium and manganese do not occur in the solution.

The measurment results of the **volcanic glass$_{(pH\ 3)}$** fluid sample show a calcium concentration of about 116 µmol l^{-1} and magnesium with 268.7 µmol l^{-1} at a pH of 4.66. The major ion in this fluid sample is Na^{+} with a concentration of 283.6 µmol l^{-1}. The total iron concentration is at around 4.84 µmol l^{-1}, followed by Al^{3+} with a value of 0.37 µmol l^{-1}. The potassium value is about 8.95 µmol l^{-1}, Cl^{-} has a concentration of 67.7 µmol l^{-1} and Mn^{2+} has a concentration of 1.46 µmol l^{-1}.

The **1-komatiite$_{(pH\ 3)}$** results show a calcium concentration of 63.12 µmol l^{-1} and a magnesium value of 504.8 µmol l^{-1}. The Na^{+} concentration is up to 158.8 µmol l^{-1}, Cl^{-} occurs up to 58 µmol l^{-1} and the K^{+} concentration is up to 5 µmol l^{-1} at a pH of 6.28.

The **s-komatiite$_{(pH\ 3)}$** – fluid sample contains Mg^{2+} with 592.5 µmol l^{-1}, K^{+} occurs with 3.84 µmol l^{-1}. The solution shows a pH value of 6.83.

The **xenolith$_{(pH\ 3)}$** – fluid sample is characterized by a Ca^{2+} concentration of 21.71 µmol l^{-1} and a magnesium content of 614.3 µmol l^{-1}. The fluid is enriched with a minor amount of 9.72 µmol l^{-1} K^{+}. The pH value increased up to 7.88 during shaking and has therefore the second highest pH value of all of the "pH 3" fluid samples.

The **BIR – 1a$_{(pH\ 3)}$** leaching results show calcium and magnesium concentrations of 89.07 µmol l^{-1} and 57.6 µmol l^{-1}. Potassium has only a concentration of 0.51 µmol l^{-1}. With a concentration of 153 µmol l^{-1} aluminium shows the second highest mesured concentration of all pH 3 sample fluids. The total iron content is up to 18 µmol l^{-1} and manganese has a concentration of 1.09 µmol l^{-1} at a resulting pH of 4.43.

Again, the highest solute magnesium load is acquired in the **DTS – 2b$_{(pH\ 3)}$** sample fluid with a concentration of 648.8 µmol l^{-1}. The calcium species occurs with a concentration of 13.22 µmol l^{-1}. Potassium, sodium and aluminium can be found in the solution with concentration of 90.47 µmol l^{-1}, 5.63 µmol l^{-1} and 40.34 µmol l^{-1}. The fluid also shows the highest measured pH value with a pH of 8.88.

4.2 Comparisons of solution samples and solid samples

In order to describe and illustrate the results of the modeling, in this section the data from the solid sample investigations are compared with the results of the solution experiment.

Tissint

The XRD mearsurments of martian meteorite sample Tissint indicate the presence of pigeonite and forsterite which are consistent with previous analyses of the meteorite (see section 3.1). The XRF results reproduce very well this observation.

The measured values of Fe, Ca and Mg correlate well with the composition expected for pigeonite and forsterite containing ions. In addition to the detection of the trace element Ti, Ba was observed in the sample. This aspect could be interesting for further studies, since the measurement results of barium are generally difficult to predict in meteorites. Due to the sometimes long periods of time between impact of the meteorite and its discovery barium can be assembled in the crystal lattice of the meteorite by terrestrial weathering processes (pers. com. Dr. Jana Berlin). In the case of the Martian meteorite Tissint extensive weathering can be excluded as it was a fall rather than a find. It is assumable that the determined values of all elements represent the element constituents of the meteorite rather than weathered components. The fluid data essentially reflect the mineral content of the sample Tissint. The measured magnesium content wihtin the fluid can be derived both from the crystal lattice of the forsterite and from the pigenoite. Both the relatively high calcium values and the calculated aluminum and iron originate mainly from the mineral composition of pigeonite.

Olivine

The olivine, which exclusively exists of forsterite, shows matching results that correlate largely with the results of the dissolution experiment.

The results show relatively high magnesium values that were expected according to the XRD measurements. Furthermore, according to the results of the XRF measurements, iron was detected with an amount of 7.2 wt.% in the crystal lattices of the olivine. The fluid sample results reflects this observation if only in low concentrations.

Unusually high sodium and chloride concentrations were found as a result of the pH 3 fluid sample measurements. Apparently this resulted because some of the olivine crystals are more weathered than indicated by observations.

Clinopyroxene

The XRD and XRF measurements of the clinopyroxene sample are consistent. The clinopyroxene was measured as a diopside and contains, as expected, substantial calcium and magnesium, with traces of aluminum, iron, sodium and barium.

The results of the two fluid samples coincide clearly with the contents in the measured solid samples.

Plagioclase

The XRD results indicate this sample is an anorthite-rich bytownite. This is consistent with the high aluminum values, relatively high calcium values, no magnesium, a little bit of sodium and a low iron content. Both fluid samples resulting from the digestions at pH 1.3 and pH 3, show similar proportions and therefore supports well the XRD and XRF measurements of the solid samples.

Orthopyroxene

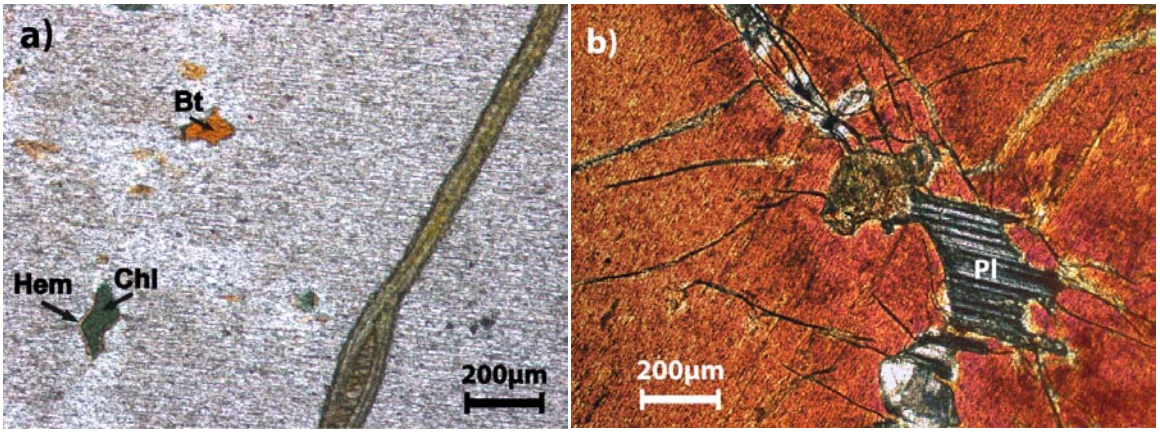

Figure 12: Thin section of the orthopyroxene sample; (a) plane polarized light (ppl). Biotite (Bt) and chlorite (Chl) grains with characteristic microcrystalline alteration seam of hematite (Hem) in microcystalline orthopyroxene. (b) crossed polarized (xpl). Plagioclase (Pl) crystal with polysynthetic lamellar twins filling open spaces in orthopyroxene.

The XRD measurements show that the orthopyroxene sample is an enstatite. However, the XRF data also show high concentrations of iron, suggesting that the ferroan enstatite in this sample is part of a solid solution series with ferrosilite ($Fe_2^{2+}[Si_2O_6]$). However, it is closer to the enstatite endmember than to ferrosilite. A decomposition of the mineral surface as a cause of high iron values cannot be excluded. The thin section shows fine hematite coatings within the cracks (Figure 12).

Furthermore, low proportions of calcium, aluminium, manganese und titanium can be found within the sample (appendix 2). Again, the results of the ph 1.3 fluid sample reflect the results of the solid sample. The fluid sample with the pH 3 sulfuric acid digestion shows repeated high sodium and relatively high chloride values, similar to that observed for the clinopyroxene sample.

Microscopic investigations show the presence of accessory plagioclase and probably biotite in the mineral fractures that could be supplying the Na.

Chlorite is also found in the thin section and Al^{3+} and K^{+} can be relatively easily dissolved from the chlorite and biotite.

Volcanic glass

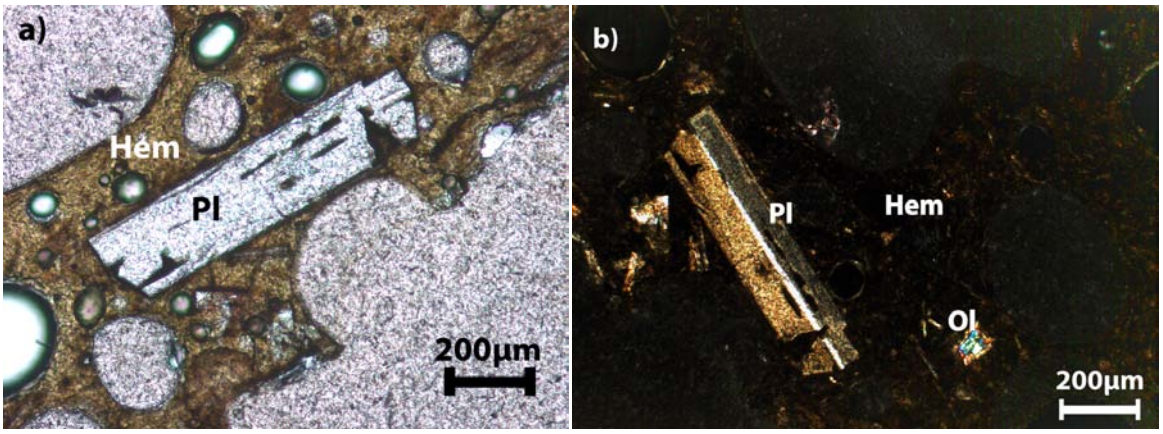

Figure 13: Thin section of the volcanic glass sample from the Kilauea volcano, Hawaii (USA); (a) ppl. Plagioclase (Pl) surrounded by microcrystalline hematite (Hem). (b) xpl. Plagioclase (Pl) grain with characteristic polysynthetic twins and an olivine (Ol) grain both, in microcrystalline hematite (Hem) matrix embedded in amourphous volcanic glass.

The constituents in the volcanic glass sample were identified as forsterite and augite from XRD, which were also observed in thin section analyses. However, the XRF results also show high weight percentages of iron.

While the fluid data of the pH 1.3 solution confirms these results, the solution with the initial pH 3 sulfuric acid shows sodium as the dominant species, whose major supplier is the mineral augite. Examination of the thin section confirms the presence of plagioclase that can be recognized by characteristic polysynthetic twins. Hence, it can be assumed that the plagioclase is likely the major supplier of Na^{+}. The red matrix of the rock suggests that the iron within the sample is already oxidized, which points to an advanced weathering state. Overall, the matrix contains many small, needle-like minerals (Figure 13(a)).

An increased chloride value occurs in this solution which could not be detected in the solid volcanic glass sample.

The high porosity together with the fine crystalline structure offers solutions a large surface area, so that ions originating in the mineral surface go more readily into solution.

It must be noted that the plagioclase is much more weathering resistant than the pyroxene.

1-komatiite

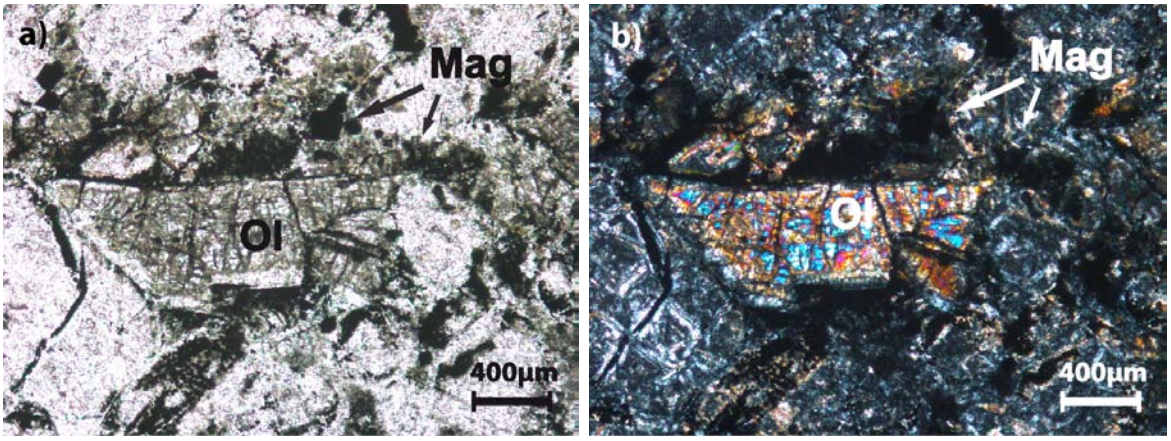

Figure 14: Thin section of the 1-komatiite sample from the Onverwacht Group of the Barberton Greenstone Belt; (a) ppl. Irregular cracks in an olivine (Ol) crystal. Open fractures are filled with dark magnetite (Mag) grains. (b) xpl. Irregular cracks in an olivine (Ol) crystal surrounded by dark magnetite (Mag) grains.

The pH 1.3 and pH 3 acid leaching results underline very clearly the results of the XRF and XRD analyzes. Magnesium is the most abundant ion that originates from both the actinolite and antigorite. Thin section analyses (Figure 14) also shows sporadically altered olivine crystals that may also be suppliers of Mg and Fe. The presence of olivine minerals in the 1-komatiite rock sample show that this sample is less altered than the s-komatiite rock sample analyzed in this study.

As a result of the thin section interpretation, one can assume that the comparatively holocrystalline structure prevented the rock sample from complete alteration.

The iron content comes from both the actinolite and the magnetite present in the sample. The Ca content is most likely derived from the actinolite.

Both komatiite samples used in this work have a relatively high H_2O content of 9.38 wt % in the 1-komatiites and 7.32 wt % in the s-komatiite. This is due to the high degree of OH-groups whitin the actinolite, antigorite and clinochlore (see Table 5).

s-komatiite

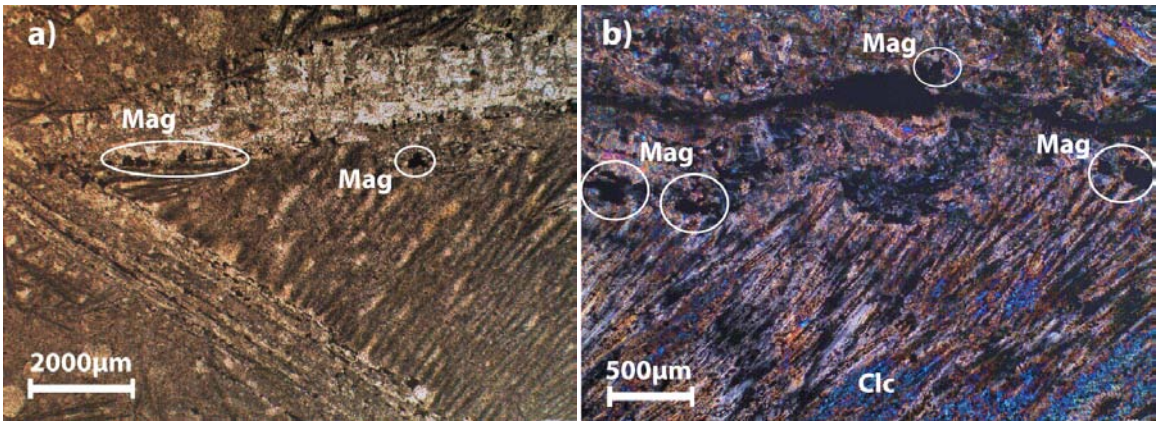

Figure 15: Thin section of the s-komatiite sample from the Onverwacht Group of the Barberton Greenstone Belt; (a) ppl. Microcrystalline magnetite (Mag) grains assembled alongside the edge of the spinnifex-texture. (b) xpl. Microcrystalline magnetite (Mag) grains in a spinnifex-texture of clinochlore (Clc).

The second komatiite sample was unexpectedly highly serpentinized. The XRD analyses show actinolite and clinochlore as the main mineral constituents of the sample. Mainly Mg ions were dissolved out of the crystal lattices of actinolite and clinochlore by the pH 3 solution. That explains the relatively high magnesium values in the fluid samples.

The stronger sulfuric acid solution at pH 1.3 was required to disolve aluminum and iron from the crystal lattice of the clinochlore, in addition to magnesium.

Thin section analyses (Figure 15) confirmed XRD results and also determined a high proportion of magnetite. Therefore, it is assumed that magnetite would be reflected as high Fe concentrations in the solutions. However, this was not the case. It can only be supposed that any dissolved Fe was removed from the solution and precipitated as iron oxides or iron bearing sulfates while shaking. Another explanation could be that the sulfuric acid was not strong enough to dissolve the iron from the magnetite mineral surface.

Xenolith

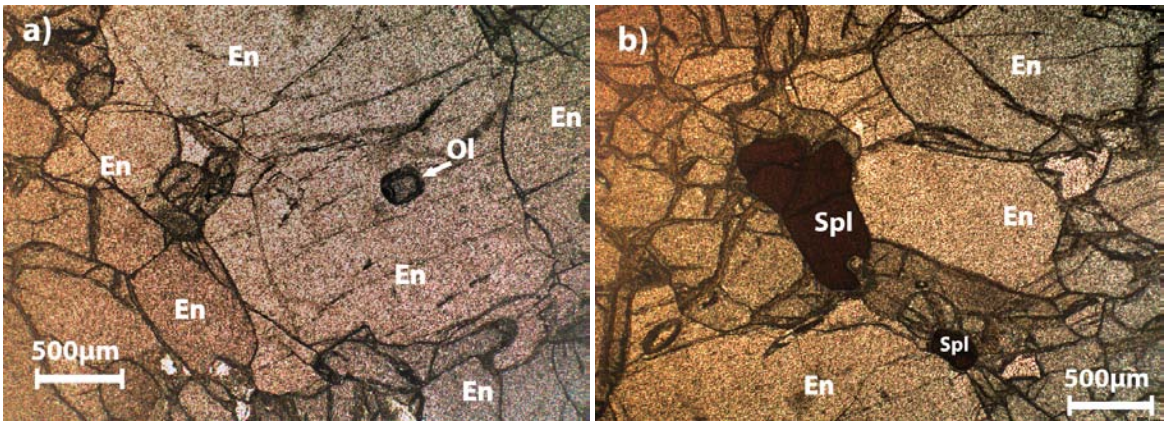

Figure 16: Thin section of the xenolith sample from the northern Hessian Depression; (a) ppl. Olivine (Ol) crystal in enstatite (En). (b) ppl. Spinel (Spl) grains embedded in enstatite (En).

The xenolith sample, taken as a plutonic equivalent to the volcanic komatiites, contains, according to the XRD analysis, forsterite and enstatite, which are both well reflected in the fluid analysis. Comparing the relatively high Mg values determined in the fluid analysis with those of the XRF results, achieves a consistent impression. The Mg concentrations measured in the fluids may originate from enstatite or forsterite (Figure 16). The Ca^{2+} values measured in the pH 1.3 fluid sample can be explained by the low absorption rate of enstatite minerals (until max. 5 mol % $Ca_2[Si_2O_6]$-components; Matthes, 1993).

5 Numerical modeling of evaporation

Numerical modeling was conducted to compare the conceptual model of evaporation under martian conditions with the results of investigations carried out in the Valles Marineris region by Gendrin (2005), Bishop et al. (2009), Sowe (2009) and Wendt (2012) and at Gale Crater by the ongoing MSL mission (McLennan et al., 2013; McSween and McLennan, 2014). The concept was refined using the interpreted aqueous species concentration derived from experimental results and geochemical analyses (see chapter 4). The saturation states and precipitation of mineral assemblages were estimated by the calculation of thermodynamic equilibria using the commercial computer software Geochemist's Workbench™ (GWB).

The aim of the modeling was to reproduce some or all of the observed sulfate precipitates on Mars in order to develop a better understanding of sulfate formation processes and sulfate–formation sequence deposition within the studied area. The objective was to develop a reasonable scenario for sulfate formation while accounting for the fact that the input data volume is very limited concerning the initial solution chemistry and possible local source rock petrography.

Evaporation occurred over a wide temperature range and most likely in an open system with atmospheric exchange. Compared to Earth, the martian CO_2-dominated atmosphere is quite thinner than Earth's atmosphere -- the mean surface pressure is only 0.7 % of that of the Earth (Owen, 1992).
However, using Earth-based, thermodynamic datasets is currently the only possibility to investigate and reproduce the occurrence of possible sedimentary stratification on Mars.

Some iron species under Earth-like and Mars-like conditions are given in the Eh-pH diagrams in Figure 17(a) and (b) with hematite as an example in order to compare mineral precipitation under Earth and Mars conditions. The figures show the phase relations in a simple system, Fe-C-O-H, assuming hematite is the stable phase for the Fe(III) precipitate. The figures are characterized by a large field of hematite, a large field of Fe^{2+}, and under reducing conditions, a smaller field of $FeCO_3$.
The stability fields under terrestrial and martian conditions show only subtle differences. The most significant difference appears in the pH range of 9 to 14 in the $FeCO_3$ field in Figure 17(a) and the pH 8.3 to 14 $FeCO_3$ field in Figure 17(b). The $FeCO_3$ field extends deeper into the hematite field under martian conditions than on Earth. These differences are most likely

caused by the higher martian CO_2 partial pressure rather than by lower martian atmospheric pressure. According to Braitsch (1962), pressure only slightly affects the equilibrium phases. Therefore, and because the program GWB is designed for Earth-like conditions, an atmospheric pressure of 1.013 bar was set for the model. In the following sections it is considered that the total external atmospheric pressure P_{atm} is equal to one bar (P = 1 bar).

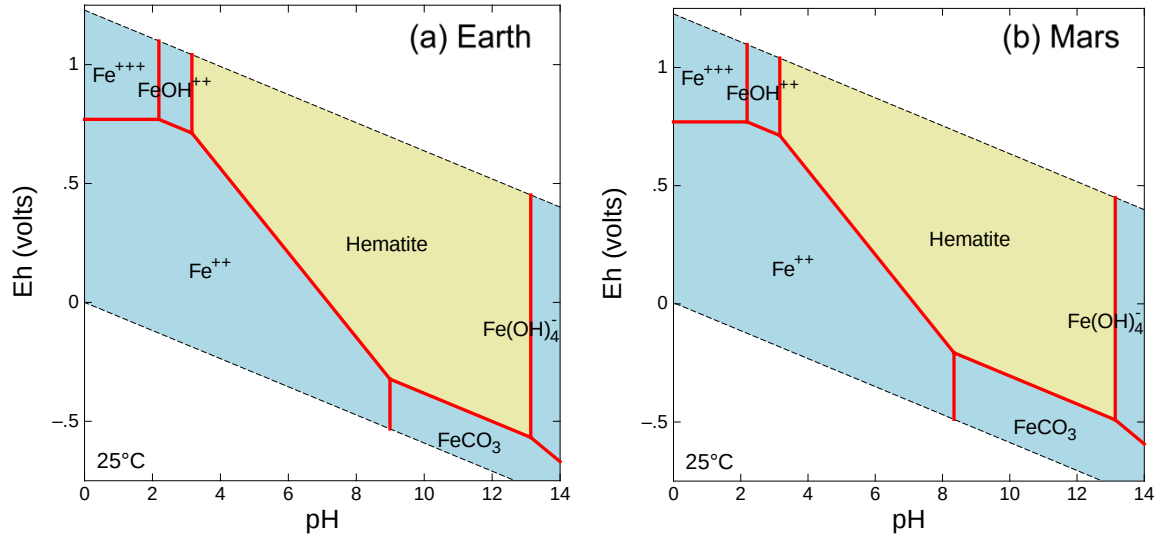

Figure 17: Illustrates the divergent Eh-pH stability fields at 25°C for part of the system Fe-C-O-H under Earth's conditions (a) compared to those of Mars's (b) using the database "thermo.dat". Under martian conditions (0.07 bar; CO_2 log fug. -2.2), the stability field of hematite (solid) is smaller in favor of a larger $FeCO_3$ (dissolved) stability field than in an Earth's conditions.

5.1 Modeling software

Modeling was conducted using the program REACT (implemented in the software package Geochemist's Workbench™ (GWB) Professional Release 8.0.12 from RockWare Inc.) to calculate evaporites from different initial solutions. The corresponding reaction equations were developed with the help of the implemented software RXN. Phase diagrams were produced with the program Act2 (also part of GWB).

The thermodynamic data base "thermo.dat", which is provided in the GWB-suite, is a compilation by Thomas Wolery, Ken Jackson and numerous co-workers at Lawrence Livermore National Laboratory (LLNL dataset; Delany and Lundee, 1989; Bethke, 2008, and references theirin). Selected equilibrium constants taken from the data base are presented in Table 8.

Table 8: List of minerals, chemical formulas and equilibrium constants used in this study (Wolery, 1983 & 1992; Delany & Lundeen, 1989, and references therein; Blanc et al., 2009).

Phase	Formula	log *K* 25°C	log *K* 60°C	log *K* 200°C	Mineral class
Alunite	$KAl_3(OH)_6(SO_4)_2$	0.6615	-3.3300	-15.3162	Sulfate
Anhydrite	$CaSO_4$	-4.2652	-4.7225	-7.2132	Sulfate
Calcite	$CaCO_3$	1.7130	1.2133	-0.5349	Carbonate
Epsomite	$MgSO_4 \cdot 7H_2O$	-1.8126	-1.5447	0.2330	Sulfate
Gibbsite	$Al(OH)_3$	7.9603	6.2491	2.3913	Hydroxide
Gypsum	$CaSO_4 \cdot 2H_2O$	-4.4433	-4.5746	-6.0580	Sulfate
Hematite	Fe_2O_3	0.0433	-2.2916	-7.8548	Iron(III) oxide
Hexahydrite	$MgSO_4 \cdot 6H_2O$	-1.5759	-1.7171	-2.6391	Sulfate
K-Jarosite	$KFe_3(SO_4)_2(OH)_6$	-8.8889	-12.4748	-21.8913	Hydroxy-sulfate
Na-Jarosite	$NaFe_3(SO_4)_2(OH)_6$	-4.8714	-	-	Hydroxy-sulfate
Kieserite	$MgSO_4 \cdot H_2O$	-0.1099	-1.1171	-4.3205	Sulfate
Melanterite	$FeSO_4 \cdot 7H_2O$	-2.3726	-2.1997	-2.1606	Sulfate
Mercallite	$KHSO_4$	-1.3751	-0.6468	0.2822	Sulfate
MHSH($Mg_{1.5}$)	$Mg_{1.5}OHSO_4$	9.1660	6.7623	-0.4548	Hydroxy-sulfate
Mirabilite	$Na_2SO_4 \cdot 10H_2O$	-1.0914	0.5443	6.9322	Sulfate
Misenite	$K_8H_6(SO_4)_7$	-10.5807	-4.8207	3.4563	Sulfate
Szomolnokite	$FeSO_4 \cdot H_2O$	-1.6569	-2.4749	-5.2496	Sulfate
Thenardite	Na_2SO_4	-0.2360	-0.3771	-1.7990	Sulfate

The GWB software package was initially developed at the University of Illinois and is distributed today by Aqueous Solutions LLC. The chemical modeling techniques applied in GWB are described by Bethke (2008, and references therein) and Stumm & Morgan (1981, and references therein) and are summarized here.

The modeling procedure is referred to as the "B-dot model". The so called "B-dot equation" (equ. 20) is an extension of the Debye-Hückel equation (Bethke, 2008) to calculate the activity coefficient γ_i:

Debye-Hückel equation: $$\log \gamma_i = -\frac{Az_i^2 \sqrt{I}}{1+\mathring{a}_i B\sqrt{I}} \quad (17)$$

where z_i^2 is the charge number of the ion, the variable $\mathring{a}_i$ is the ion size parameter, A and B are temperature-dependent constants (with A = 0.5092 and B = 0.3282 at 25°C) and I is the solution ionic strength with the equation:

Ionic strength: $$I = \frac{1}{2}\sum_i m_i z_i^2 \quad (18)$$

Bethke (2008) noted that the ionic strength *I* (used in molal) is the solutions' representative in equation 17 and 20, where m_i is the molality of each individual species. Stumm & Morgan (1981) and Bethke (2008) mentioned that according to the Debye-Hückel equation (equ. 19) the activity coefficient γi declines monotonically with ionic strength *I*. To avoid this inaccuracy, Davies (1962) set the product of $å_i \cdot B$ to be one at 25°C, and added the empirical term 0.3 *I*:

Davies equation: $$\log\ \gamma_i = -Az_i^2\ (\frac{\sqrt{I}}{1+\sqrt{I}}) - 0.3\ I \qquad (19)$$

According to Bethke (2008) the Davies equation is valid for solutions with an ionic strength of 0.3 or 0.5 molal whereas, finally, the B-dot equation, mentioned above, is accurate to an ionic strength of up to 3 molal:

B-dot equation: $$\log\ \gamma i = -\frac{Az_i^2\ \sqrt{I}}{1+å_i B\sqrt{I}} + \dot{B}I \qquad (20)$$

In contrast to equation 17 the former variable $å_i$ is now a constant for the individual species, whereas $\dot{B}$, which depends on the ion size, z_i^2, varies with temperature along with the coefficients *A* and *B*, and is therefore designed to operate between 0°C and 300°C (Bethke, 2008).

The CO_2-fugacity, comparable to the martian CO_2 partial pressure, which was used to model the mineral assemblages in this study, was calculated at CO_2(g)= 2.2, based on the data taken from Owen (1992).
The amount of 999 grams of the reactant H_2O was evaporated in order to simulate the extreme conditions on Mars and to produce significant amounts of sulfate to simulate comparable precipitation products.
Minerals formed initially are allowed to back-react with the solution in the calculations under equilibrium conditions, as evaporation proceeds.

5.2 Limitations

Geochemical modeling of processes under martian conditions is still difficult to validate. Therefore, a simplified and workable geochemical model was developed to illustrate the evaporation processes based on the leaching experiments of martian analog rocks, minerals and a martian meteorite.
The experimental setup, analysis and interpretation are based primarily on common procedures in geochemistry and hydrogeology.
The chemical process of evaporation was calculated by the program REACT using the "B-dot equation" to calculate activity coefficients. Errors can occur due to the limited number of minerals and aqueous species in the data base. Furthermore, the thermodynamic datasets do not differentiate the substitution and enclosure of ions within the mineral's crystal lattice or the sorption onto mineral surfaces (Bethke, 2008). Thus, the modeling results should be considered with respect to these requirements.

Although dolomite, magnesite, siderite and rhodochrosite occurred in first test runs in some of the model results, these carbonate minerals normally do not form directly from aqueous solutions (Braitsch, 1962; Sonnenfeld, 1984; Stumm & Morgan, 1996; Railsback, 1999; Warren, 2006).
The reason for this is that, according to Lippmann (1973) and Mackenzie (2013), carbonate cannot bond with the magnesium ion because it is not able to "overcome the hydration shell", although modern sea water is supersaturated with respect to dolomite.
Using the example of calcite precipitation from seawater, the calcium carbonate nucleation is inhibited or blocked by the presence of precipitation inhibitors such as SO_4^{2-}, Mg^{2+} or species with similar ionic strength (Chave & Suess, 1970; Zhong & Mucci, 1993; Zuddas & Mucci, 1994; Zuddas & Mucci, 1998). According to Chave & Suess (1970) and Zuddas & Mucci (1998), calcite precipitation requires the presence of a nucleus or a distinct supersaturation to initiate carbonate precipitation.
However, primary precipitation of dolomite from aqueos solutions requires generally the following reactions:

$$Ca^{2+} + Mg^{2+} + 2\,CO_3^{2-} \rightarrow CaMg(CO_3)_2 \qquad \text{(Warren, 2000)} \qquad (21)$$

$$Ca^{2+} + Mg^{2+} + 2\,HCO_3^{-} \rightarrow CaMg(CO_3)_2 + 2\,H^{+} \qquad (22)$$

The equilibrium balance reactions mentioned above with the ions: Ca^{2+}, Mg^{2+}, CO_3^{2-} and H^+ take place in the presence of CO_2.

A high CO_2 content and therefore a high atmospheric partial pressure of CO_2 (pCO_2) in an aqueous solution could lead to a dissolution of $CaCO_3$, whereas a low pCO_2 can support the mineralization of calcium carbonate. In addition to this, low pH values also normally lead to a dissolution of calcium carbonate in favour of an increasing amount of hydrogen carbonate (HCO_3^-) (Stumm & Morgan, 1981; Schulz & Zabel, 2000). At around a pH of 7.8, dolomite is a more stable carbonate form than calcite (Sonnenfeld, 1984).

Open questions include the formation setting of dolomite and when the solution equilibrium is reached (Stumm & Morgan, 1981). Countless studies have been carried out over more than 150 years about the so called “dolomite-problem” (Warren, 2000) or “dolomite-question” (Sonnenfeld, 1984; Lippmann, 1973). Nonethless, it appears that solely undersaturation can cause a solubility equilibrium and the presence of certain carbonate minerals, such as dolomite, magnesite, siderite and rhodochrosite is generally associated with evaporitic conditions (Sonnenfeld 1984;Morse & Mackenzie,1990; Warren, 2000). Thus, the carbonate species mentioned above were surpressed in the model.

5.3 Modeling results

5.3.1 Tissint

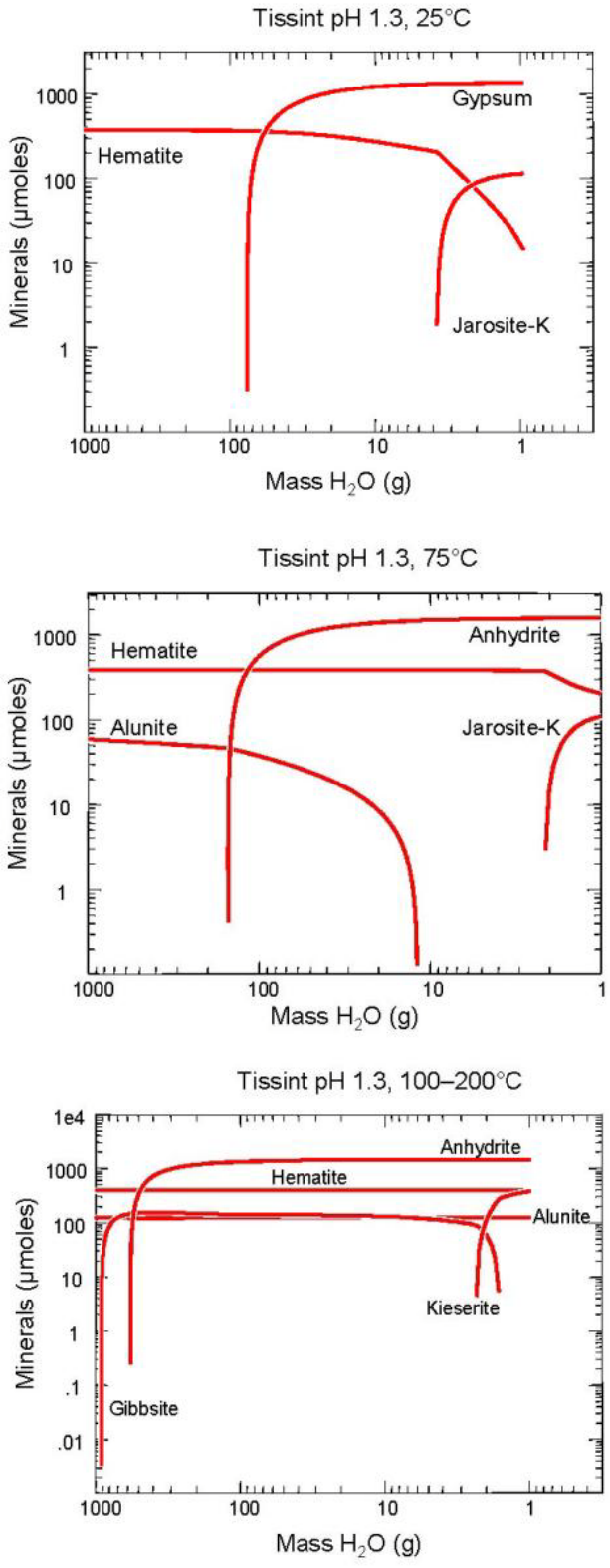

Figure 18: Concentration of minerals precipitated during numerical evaporation of the Tissint$_{(pH\ 1.3)}$ leachate at 25°C, 75°C and between 100-200°C.

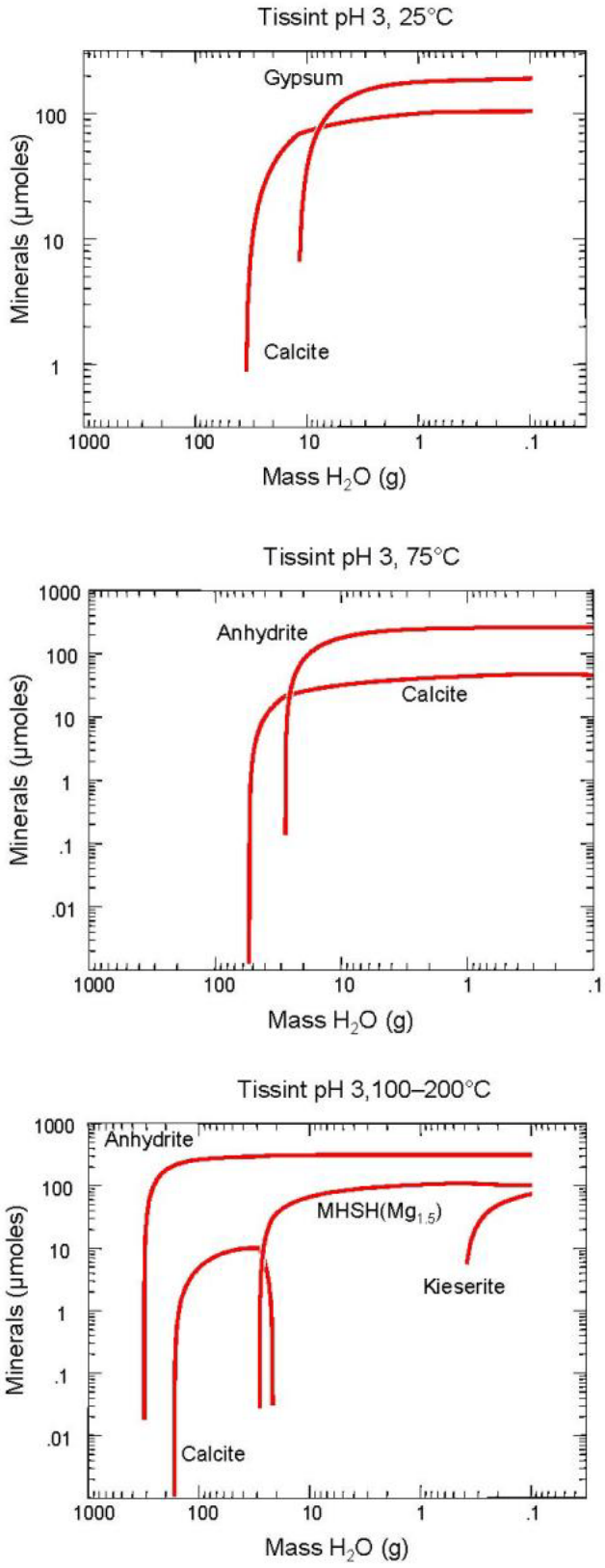

Figure 19: Concentration of minerals precipitated during numerical evaporation of the Tissint$_{(pH\ 3)}$ leachate at 25°C, 75°C and between 100-200°C.

The mineral saturation state for the **Tissint$_{(pH\ 1.3)}$** fluid was calculated as a function of modeled evaporation of 1 kg H_2O and as a function of pH and temperature.
The main precipitates at 25°C (Figure 18) are hematite (Fe_2O_3), gypsum ($CaSO_4{:}2H_2O$) and K-jarosite ($KFe_3(SO_4)_2(OH)_6$). Hematite is oversaturated:

$$2\ Fe^{2+} + 2\ H_2O + 0.5\ O_{2(aq)} \rightarrow \underset{hematite}{Fe_2O_3} + 4\ H^+ \quad (23)$$

up to 369.9 µmol l^{-1}. At lower pH values Fe_2O_3 becomes undersaturated.
When the fluid pH falls below 1.3, the decreasing water activity prevents further formation of hematite. Hematite dissolves in favor of the formation of K-jarosite:

$$3\ Fe^{2+} + K^+ + 2\ SO_4^{2-} + 4.5\ H_2O + 0.75\ O_{2(aq)} \rightarrow \underset{K\text{-}jarosite}{KFe_3(SO_4)_2(OH)_6} + 3\ H^+ \quad (24)$$

$$Hematite + 2\ H_2O + 1.333\ SO_4^{2-} + 0.6667\ K^+ \rightarrow 0.6667\ K\text{-}Jarosite \quad (25)$$

The mineral phase K-jarosite forms with a maximum concentration of 113.9 µmol l^{-1} at a pH of 1.2.

Gypsum is supersaturated at a pH value 1.99 and starts to precipitate from the fluid at a remaining water mass of around 7.7 %:

$$Ca^{2+} + SO_4^{2-} + 2\ H_2O \rightarrow \underset{gypsum}{CaSO_4 \cdot 2\ H_2O} \quad (26)$$

with a concentration of 0.31 µmol l^{-1} and rapidly increases to a maximum concentration of 1360 µmol l^{-1} under the consumption of nearly all of the calcium and SO_4^{2-} species originally in solution. When nearly 98 % of H_2O is evaporated, no mineral precipitates from the solution. The remaining 2 % water is consumed by the precipitation of the hydrated mineral gypsum.
The fluid's pH decreases down to 1.2 with increasing evaporation.

Modeling results calculated at a temperature of 75°C show the precipitation of anhydrite with a maximum concentration of 1566 µmol l^{-1} instead of gypsum:

$$Ca^{2+} + SO_4^{2-} \rightarrow \underset{anhydrite}{CaSO_4} \quad (27)$$

compared to the calculation at 25°C. The precipitation of alunite:

$$K^+ + 3\,Al^{3+} + 2\,SO_4^{2-} + 6\,H_2O \rightarrow \underset{alunite}{KAl_3(OH)_6(SO_4)_2} + 6\,H^+ \quad (28)$$

occurs additionally to the precipitation of hematite up to a maximum concentration of 203.1 µmol l^{-1} and K-jarosite. The calculated final pH is about 1.185.

At temperatures between 100 and 200°C K-jarosite does not occur while hematite still precipitates as an ubiquitous mineral in the presence of gibbsite:

$$Al^{3+} + 3\,H_2O \rightarrow \underset{gibbsite}{Al(OH)_3} + 3\,H^+ \quad (29)$$

which dissolves with respect to alunite and in the presence of kieserite. At the end of the reaction path the highest concentration of alunite is 126 µmol l^{-1}, of kieserite 381.8 µmol l^{-1}, of hematite 392.7 µmol $l^{-1}$and of anhydrite 1452 µmol l^{-1}. At this point the final pH is 1.62.

The calculation of the **Tissint$_{(pH\ 3)}$** (Figure 19) fluid sample at 25°C determines that calcite:

$$Ca^{2+} + HCO^{3-} \rightarrow \underset{calcite}{CaCO_3} + H^+ \quad (30)$$

starts to precipitate at a remaining water mass of 2.4 % with a concentration of 0.758 µmol l^{-1}, up to a maximum of 103.9 µmol l^{-1} after nearly all of the water is evaporated.
Gypsum occurs when 98.8 % of water is removed out of the reaction path and has a maximum precipitation of 189.3 µmol l^{-1}. From the starting pH of 6.54, the pH decreases to 5.439.

Calculation at a temperature of 75°C shows the precipitation of anhydrite as the primary mineral with 260.2 µmol l^{-1}. Calcite forms with a maximum concentration of 45.86 µmol l^{-1} giving a final pH of 5.43 at the end of evaporation.

Between 100 and 200°C anhydrite is the first mineral that precipitates with a maximum concentration of 313.8 µmol l^{-1}, followed by calcite which dissolves with increasing temperature and decreasing pH. At 197°C the magnesium hydroxy sulfate MHSH($Mg_{1.5}$):

$$1.5\ Mg^{2+} + SO_4^{2-} + H_2O \rightarrow \underset{\textit{magnesium hydroxy sulfate}}{MG_{1.5}OHSO_4} + H^+ \qquad (31)$$

forms out of the solution with a concentration of 100.7 µmol l^{-1}, followed by kieserite:

$$Mg^{2+} + SO_4^{2-} + H_2O \rightarrow \underset{\textit{kieserite}}{MgSO_4 \cdot H_2O} \qquad (32)$$

with 73.52 µmol l^{-1} just below 200°C.

5.3.2 Olivine

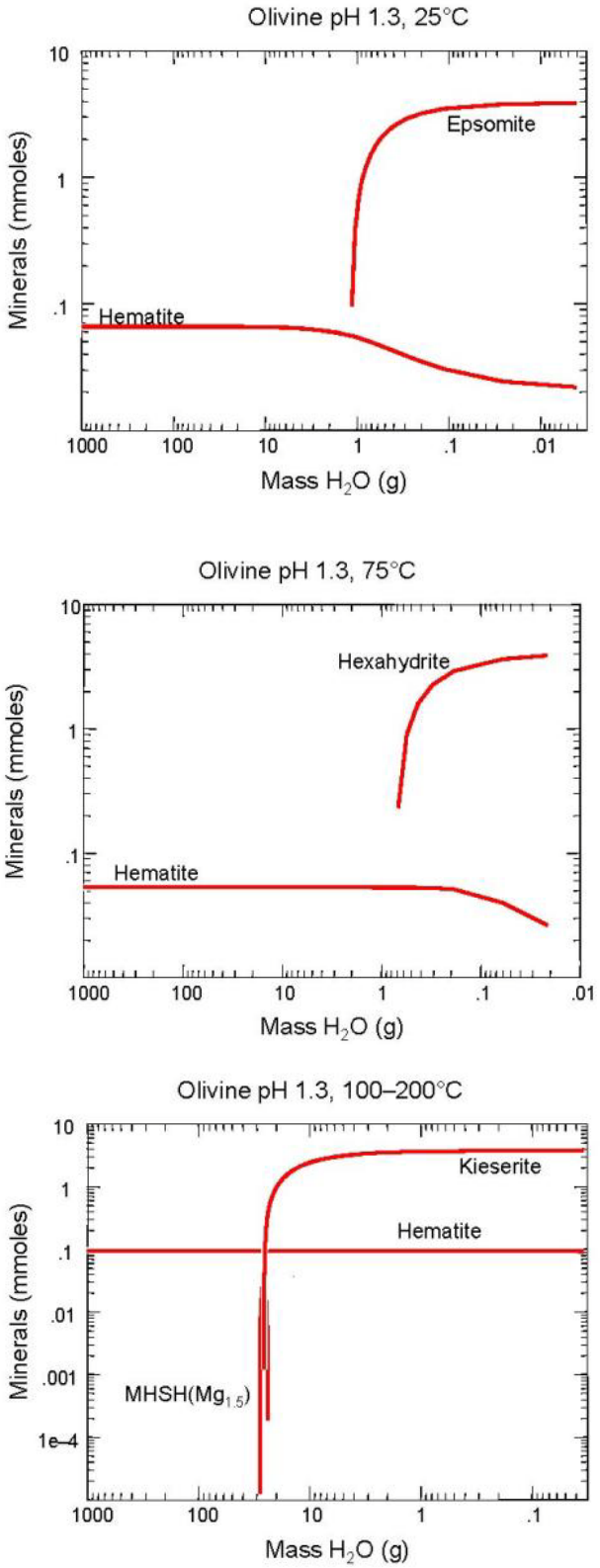

Figure 20: Concentration of minerals precipitated during numerical evaporation of the olivine$_{(pH\ 1.3)}$ leachate at 25°C, 75°C and between 100-200°C.

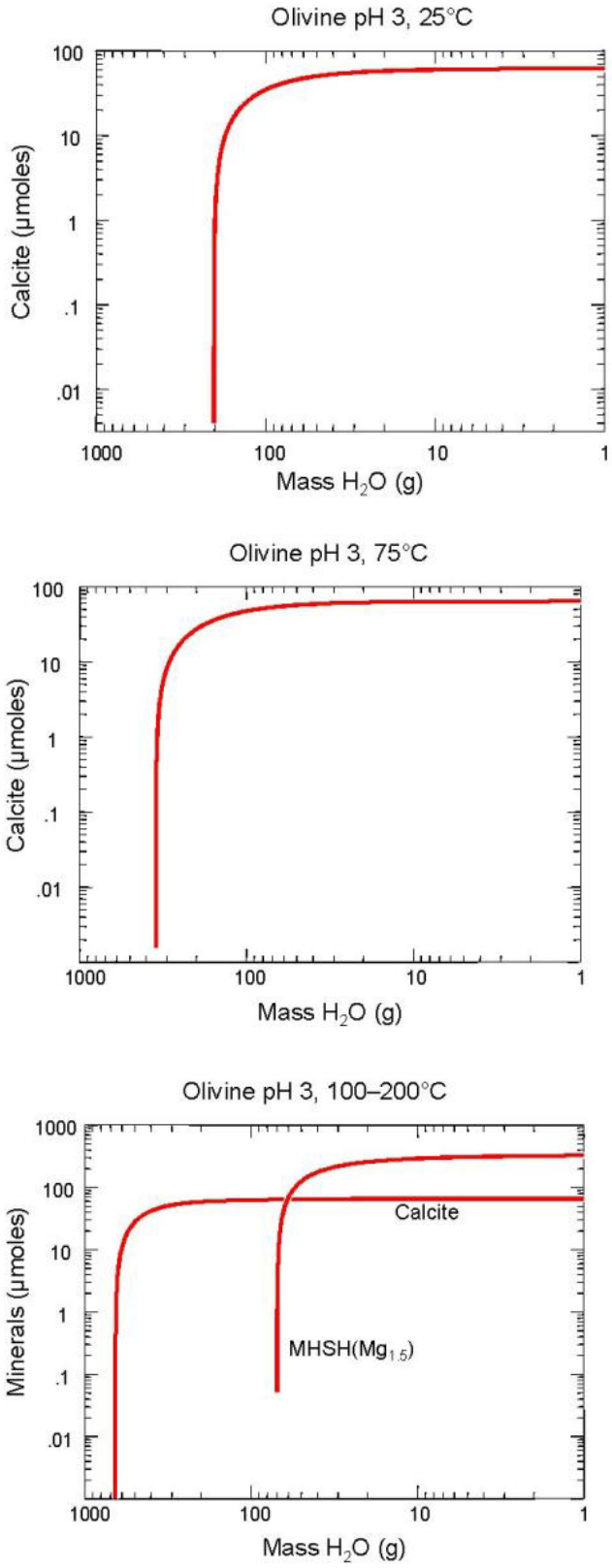

Figure 21: Concentration of minerals precipitated during numerical evaporation of the olivine$_{(pH\ 3)}$ leachate at 25°C, 75°C and between 100-200°C.

Numerical evaporation of the **olivine$_{(pH\ 1.3)}$** solution sample at 25°C show the consumption of Mg^{2+} during the formation of epsomite:

$$Mg^{2+} + SO_4^{2-} + 7\ H_2O \rightarrow \underset{epsomite}{MgSO_4 \cdot 7\ H_2O} \quad (33)$$

starting at a calculated pH of 1.75. Until about 99 % of the water has disappeared, epsomite increasingly saturates to a concentration of 95.9 µmol l^{-1}.
Fe^{3+} is consumed throughout almost the entire evaporation process and precipitates as hematite with a concentration of 65.92 µmol l^{-1} down to the final concentration of 55.67 µmol l^{-1}.
The pH decreases from 4.1 down to 1.75 during this process.

Modeling results at 75°C show the precipitation of hexahydrate:

$$Mg^{2+} + SO_4^{2-} + 6\ H_2O \rightarrow \underset{hexahydrate}{MgSO_4 \cdot 6\ H_2O} \quad (34)$$

with a concentration of 4017 µmol l^{-1} instead of epsomite, which occurs in the modeling results at 25°C. Hematite precipitates with a maximum concentration of 8.2 µmol l^{-1} at the end of the reaction path. The experimentally measured pH decreases down to the calculated pH of 0.101.

Between 100 and 200°C the ubiquitous hematite precipitates over the entire reaction path and gradually decreases from 94.89 µmol l^{-1} down to 9.2 µmol l^{-1}.
At 197°C MHSH($Mg_{1.5}$) occurs shortly bevore kieserite starts to precipitate. MHSH($Mg_{1.5}$) dissolves with respect to kieserite, which forms with a concentration of 3791 µmol l^{-1}. The calculated pH decreases down to 0.236.

The initial o**livine$_{(pH\ 3)}$** solution is a Na-HCO_3 brine and it does not evolve during the calculated evaporation at 25°C, 75°C and between 100 and 200°C. By removing nearly 80 % of the H_2O, calcium carbonate is oversaturated**.** With further evaporation, the precipitation of calcite increases to a maximum of 61.38 µmol l^{-1} at a pH of 6.89 at 25°C and a maximum concentration of 63.87 µmol l^{-1} at a pH of 6.9 at 75°C.

Between 100 and 200°C in additionall to the precipitation of calcite with a concentration of 65.37 µmol l^{-1}, MHSH($Mg_{1.5}$) is supersaturated with 324.5 µmol l^{-1} at the end of the reaction path. The pH decreases during this process from 7.51 down to 6.969.

5.3.3 Clinopyroxene

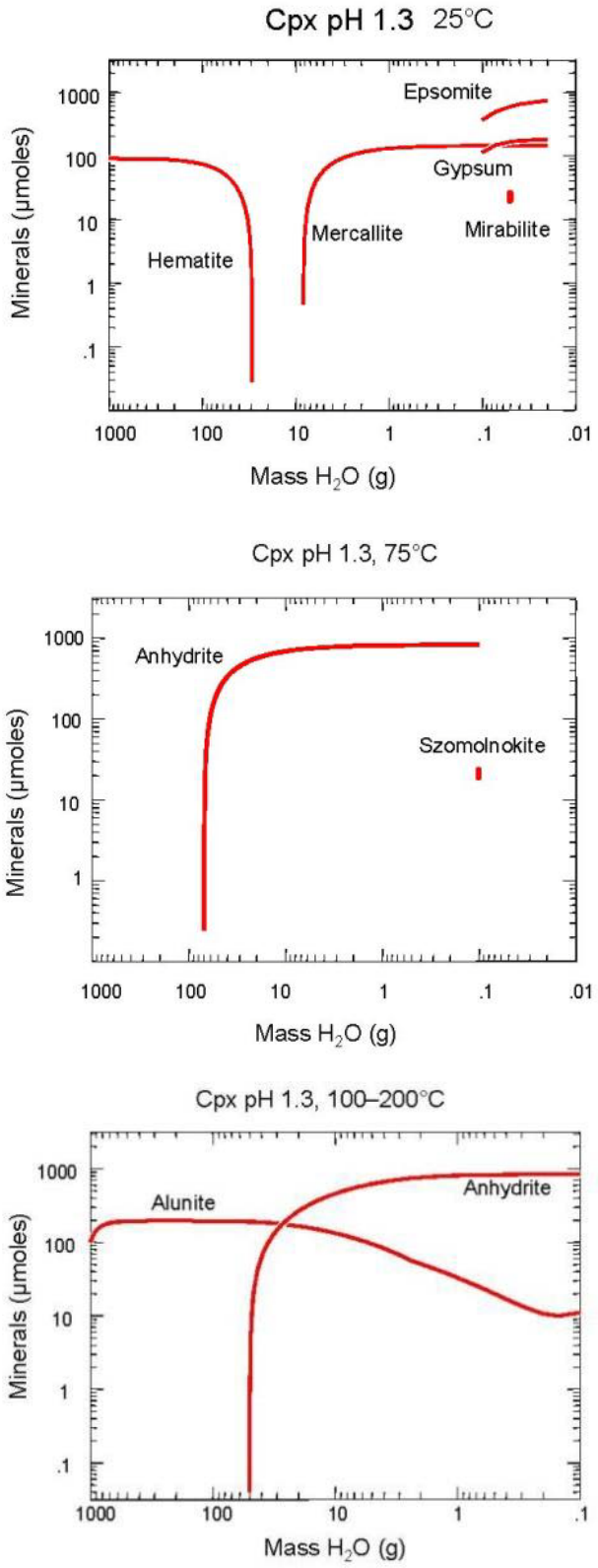

Figure 22: Concentration of minerals precipitated during numerical evaporation of the $cpx_{(pH\ 1.3)}$ leachate at 25°C, 75°C and between 100-200°C (results were included in Noel et al., 2015).

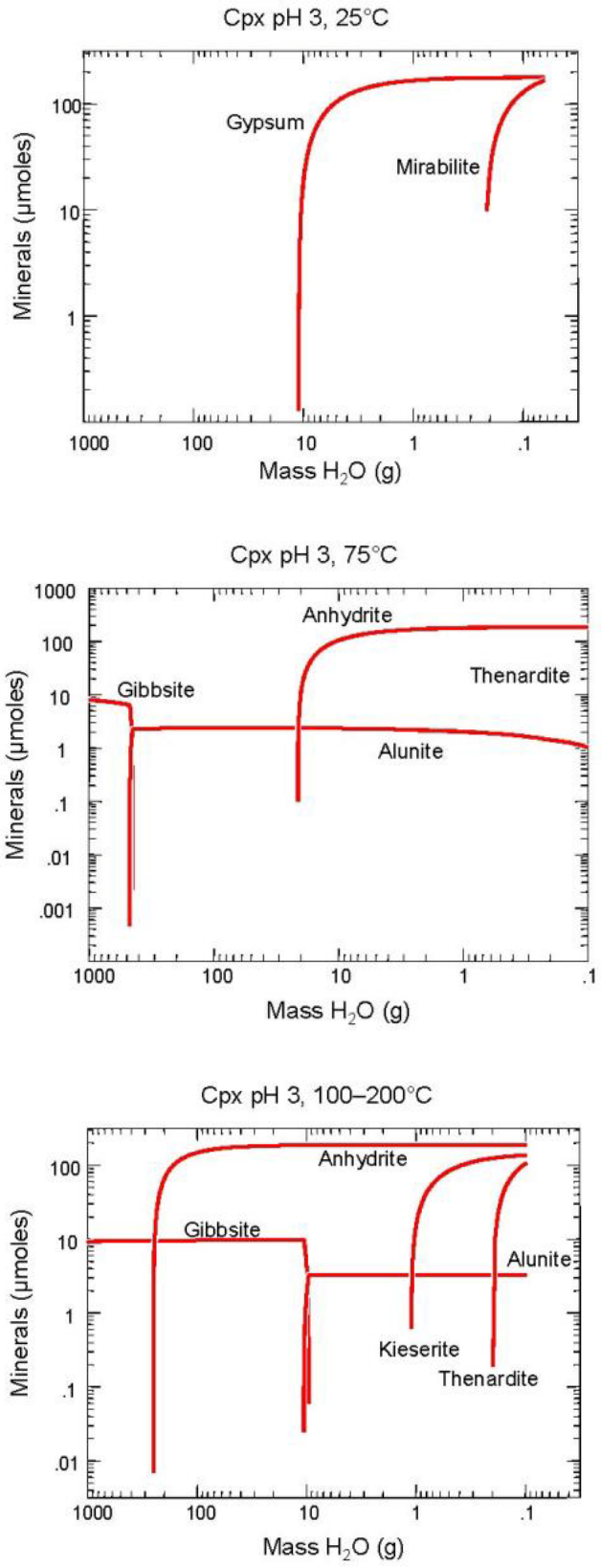

Figure 23: Concentration of minerals precipitated during numerical evaporation of the $cpx_{(pH\ 3)}$ leachate at 25°C, 75°C and between 100-200°C.

At 25°C, the **cpx$_{(pH\ 1.3)}$** shows, that hematite forms with a concentration of 89 µmol l^{-1} but completely dissolves along a decreasing pH down to a minimum of -3.5.

Between pH 1.5 and pH 1.09, no mineral is formed in this system. The solution is oversaturated with respect to gypsum at around pH 1.09, with a maximum concentration of 145 µmol l^{-1} after 99.9 % of the water is removed.
When nearly all of the solution is evaporated, epsomite, with a concentration of 839 µmol l^{-1}, and mercallite:

$$K^+ + SO_4^{2-} + H^+ \rightarrow \underset{mercallite}{KHSO_4} \quad (35)$$

with a concentration of 183 µmol l^{-1} form.
Mirabilite occurs at pH -1.7 with a concentration of 1.5 µmol l^{-1}:

$$2\ Na^+ + SO_4^{2-} + 10\ H_2O \rightarrow \underset{mirabilite}{Na_2SO_4 \cdot 10\ H_2O} \quad (36)$$

At a temperature of 75°C anhydrite precipitates instead of gypsum with a concentration of 822.6 µmol l^{-1}. Almost at the end of the evaporation process a small amount of szomolnokite:

$$SO_4^{2-} + H_2O + Fe^{2+} \rightarrow \underset{szomolnokite}{FeSO_4 \cdot H_2O} \quad (37)$$

occurs with a concentration of 35.48 µmol l^{-1}. The pH value decreases down to -0.7.

According to the modeling results between 100 and 200°C the water free Al-sulfate alunite is supersaturated along the reaction path with a final concentration of 10.97 µmol l^{-1}. Anhydrite precipitates with a concentration of 840.2 µmol l^{-1}, while the calculated pH decreases down to -0.476.

After 95.1 % of the H_2O is removed from the **cpx$_{(pH\ 3)}$** solution system**,** gypsum starts to precipitate at pH 2.6. The maximum concentration of 177 µmol l^{-1} is reached at around pH of 0.9 when nearly all of the H_2O is removed. Mirabilite occurs at pH 1.4 and the concentration ranges between 35 µmol l^{-1} and 166 µmol l^{-1}.

Calculations at 75°C lead to the precipitation of gibbsite at the beginning of the reaction path, but also to a dissolution with respect to the precipitation of alunite with an amount of 1.017 µmol l^{-1}. The sodium containing sulfate thenardite:

$$SO_4^{2-} + 2\,Na^+ \rightarrow \underset{thenardite}{Na_2SO_4} \qquad (38)$$

occurs with a minor concentration of 11.75 µmol l^{-1}. The dominant precipitate is anhydrite with a maximum concentration of 184.4 µmol l^{-1} at a final pH of around 1.8.

The calculated results at temperatures between 100 and 200°C show gibbsite as the first supersaturated mineral and anhydrite as the major precipitate with 189.1 µmol l^{-1}. When almost all of the water is removed from the system, a minor amount of alunite occurs with 3.24 µmol l^{-1} while gibbsite dissolves. At a temperature shortly below 200°C kieserite and thenardite are supersaturated with 135.7 µmol l^{-1} and 106.4 µmol l^{-1}, respectively, at around a minimum pH of 3.58.

5.3.4 Orthopyroxene

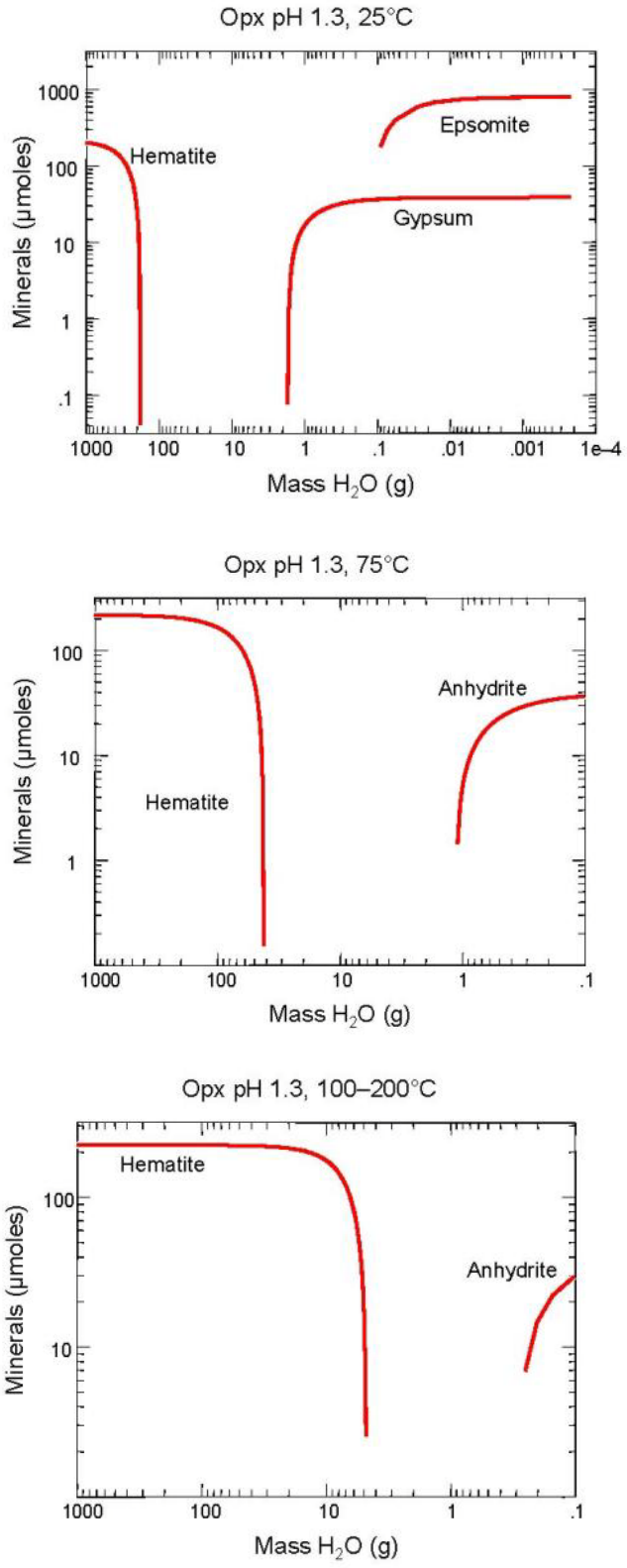

Figure 24: Concentration of minerals precipitated during numerical evaporation of the opx$_{(pH\ 1.3)}$ leachate at 25°C, 75°C and between 100-200°C.

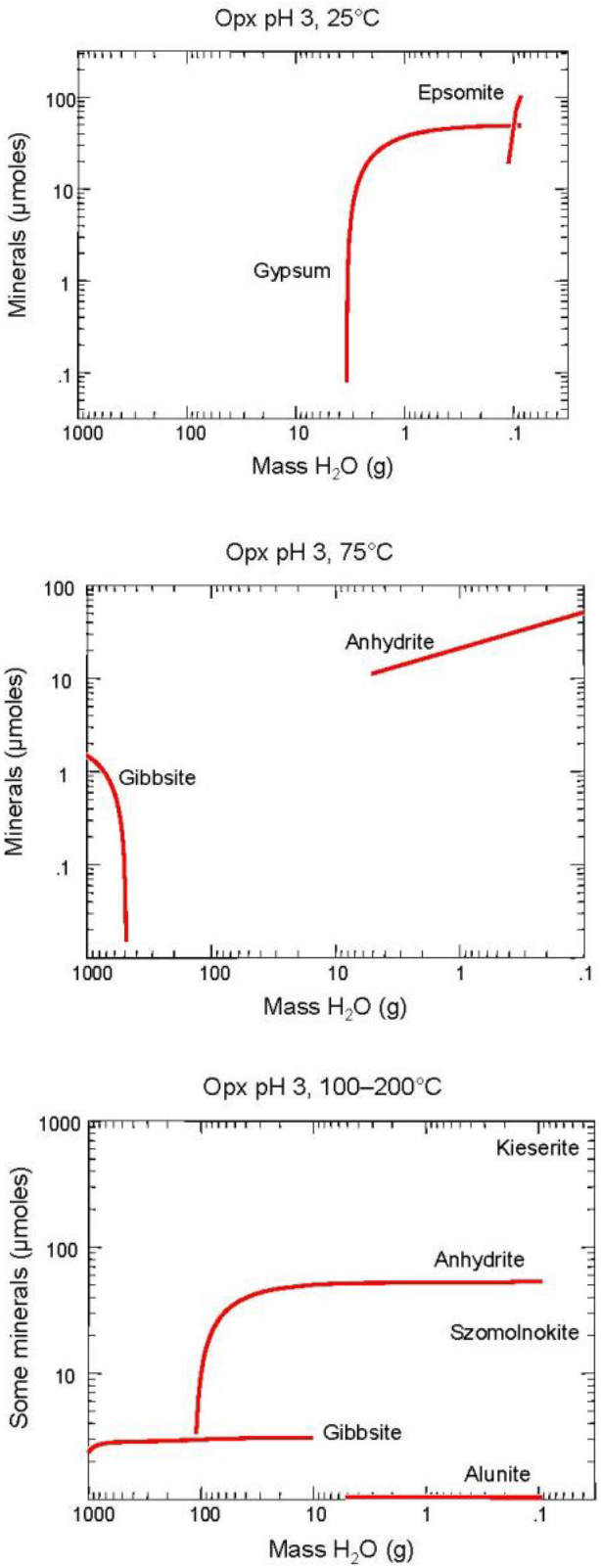

Figure 25: Concentration of minerals precipitated during numerical evaporation of the $opx_{(pH\ 3)}$ leachate at 25°C, 75°C and between 100-200°C.

The **opx$_{(pH\ 1.3)}$** evaporation modeling shows that hematite is oversaturated and precipitates with a maximum concentration of 2015 µmol l^{-1} but dissolves completely at around pH 1.57. Between pH 1.54 and pH -0.34 the solution is undersaturated with respect to the minerals hematite, goethite and gypsum. The calcium-sulfate gypsum starts to precipitate out of the solution after 99 % of the fluid is evaporated, with concentrations from 1.0 µmol l^{-1} up to 36.3 µmol l^{-1}. As evaporation proceed, the fluid becomes oversaturated with respect to epsomite with a maximum concentration up to 66.8 µmol l^{-1}.

Calculations at a temperature of 75°C and between 100 to 200°C show the precipitation and solution of hematite and the supersaturated phase anhydrite with a concentraion of 36.82 µmol l^{-1} at 75°C and 29.38 µmol l^{-1} between 100 to 200°C. The final calculated pH value at 75°C is -1.59 and between 100 to 200°C is around -1.3.

At pH 2.2 and a temperature of 25°C the **opx $_{(pH\ 3)}$** fluid calculation shows that gypsum is isolated from the system with a concentration of 0.078 µmol l^{-1}. Epsomite precipitates with a higher concentration of 1029 µmol l^{-1} at pH 1.1.

Numerical evaporation at 75°C leads to the precipitation and, subsequent, dissolution of gibbsite and the formation of anhydrite with 51.36 µmol l^{-1} at a final pH of around 1.8.

Between 100 and 200°C modeling shows the precipitation of alunite, anhydrite, szmolnokite and kieserite at the very end of the temperature scale. Kieserite forms with a concentration of 407.2 µmol l^{-1} followed by anhydrite with 53.06 µmol l^{-1}, szomolnokite with 14.68 µmol l^{-1} and alunite with 1.036 µmol l^{-1}. The final pH is at 3.58.

5.3.5 Plagioclase

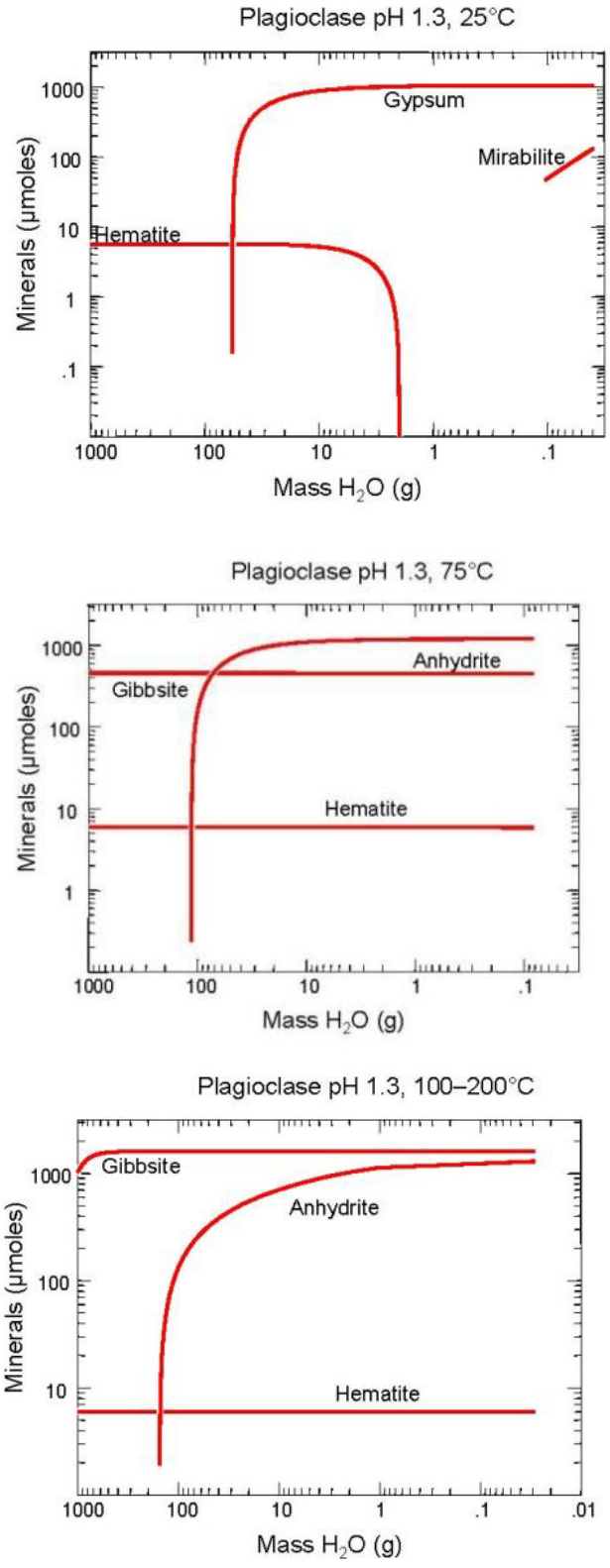

Figure 26: Concentration of minerals precipitated during numerical evaporation of the plagioclase$_{(pH\ 1.3)}$ leachate at 25°C, 75°C and between 100-200°C.

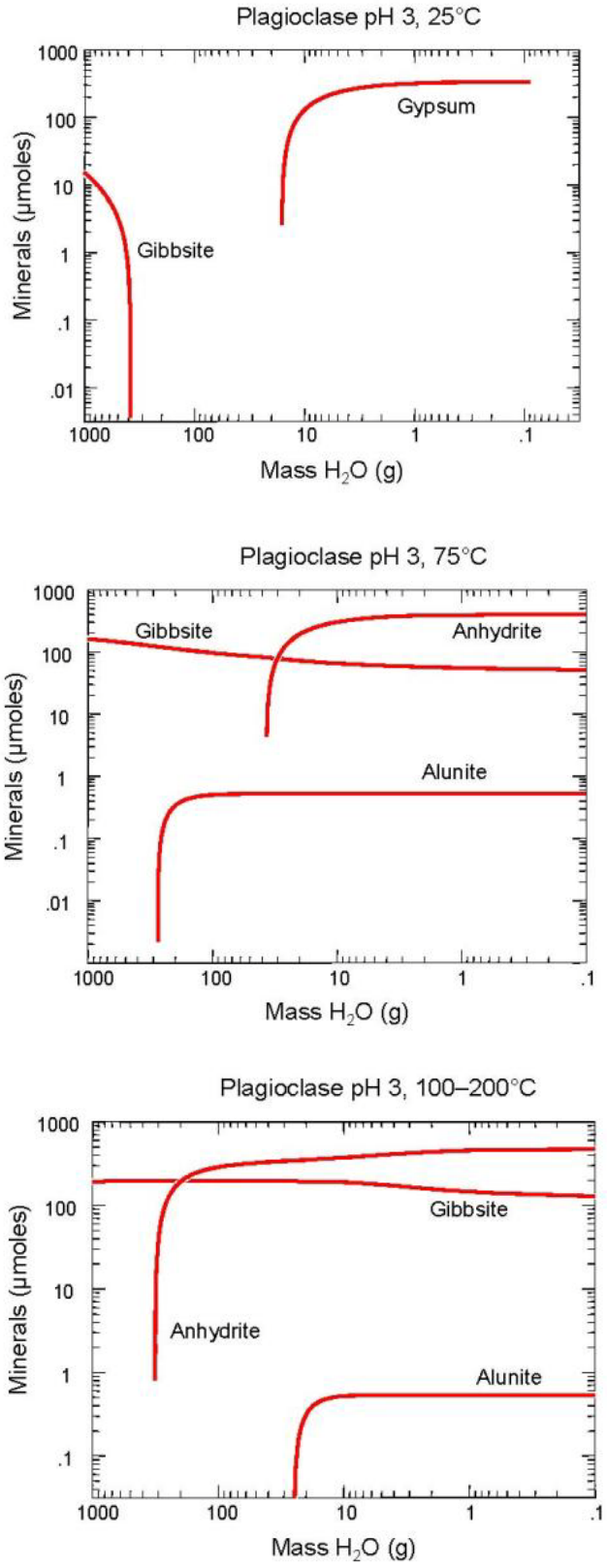

Figure 27: Concentration of minerals precipitated during numerical evaporation of the plagioclase$_{(pH\ 3)}$ leachate at 25°C, 75°C and between 100-200°C.

The modeling result of the **plagioclase$_{(pH\ 1.3)}$** sample at 25°C, shows the formation of Fe_2O_3. At pH 2.79, gypsum is oversaturated and reaches its maximum concentration of 1049 µmol l^{-1} at the end of the reaction path. Mirabilite occurs at pH 0.48 with an increasing concentration up to 133 µmol l^{-1}. The pH value decreases overall down to -0.061.

Numerical evaporation at 75°C leads to the precipitation of gibbsite with 455.5 µmol l^{-1}, anhydrite with 1199 µmol l^{-1} and the ubiquitous mineral hematite with 5.837 µmol l^{-1}. The resulting pH is at -0.114.

Even at temperatures between 100 and 200°C the mineral assemblage does not change, only gibbsite is now the dominant component with a concentration of 1593 µmol l^{-1} followed by anhydrite with 1296 µmol l^{-1} and hematite with 6 µmol l^{-1} along the temperature scale. The calculated final pH is considerably below -1.

The **plagioclase$_{(pH\ 3)}$** sample shows gibbsite precipitation at pH 4.02 down to pH 3.92 with a decreasing concentration of maximum 15.2 µmol l^{-1} at 25°C.
At pH 3.92 gibbsite is entirely dissolved and no mineral is in the system. At pH 2.83, the solution is oversaturated with respect to $CaSO_4{:}2H_2O$ with 289.6 µmol l^{-1}. At this stage, the calculated pH value decreases down to 0.911.

Modeling at 75°C and temperatures between 100 to 200°C shows similar mineral precipitations. Gibbsite is the first supersaturated mineral phase with a maximum concentration of 51.45 µmol l^{-1} at 75°C and 127.5 µmol l^{-1} at 200°C, followed by alunite with a maximum concentration of 0.5245 µmol l^{-1} at 75°C and a concentration of 0.5362 µmol l^{-1} at 200°C. Anhydrite is again the dominant mineral with a concentration of 400.5 µmol l^{-1} at 75°C and 465.4 µmol l^{-1} between 100 and 200°C. At the end of the reaction path the calculated pH decreases down to 1.603.

5.3.6 1-komatiite

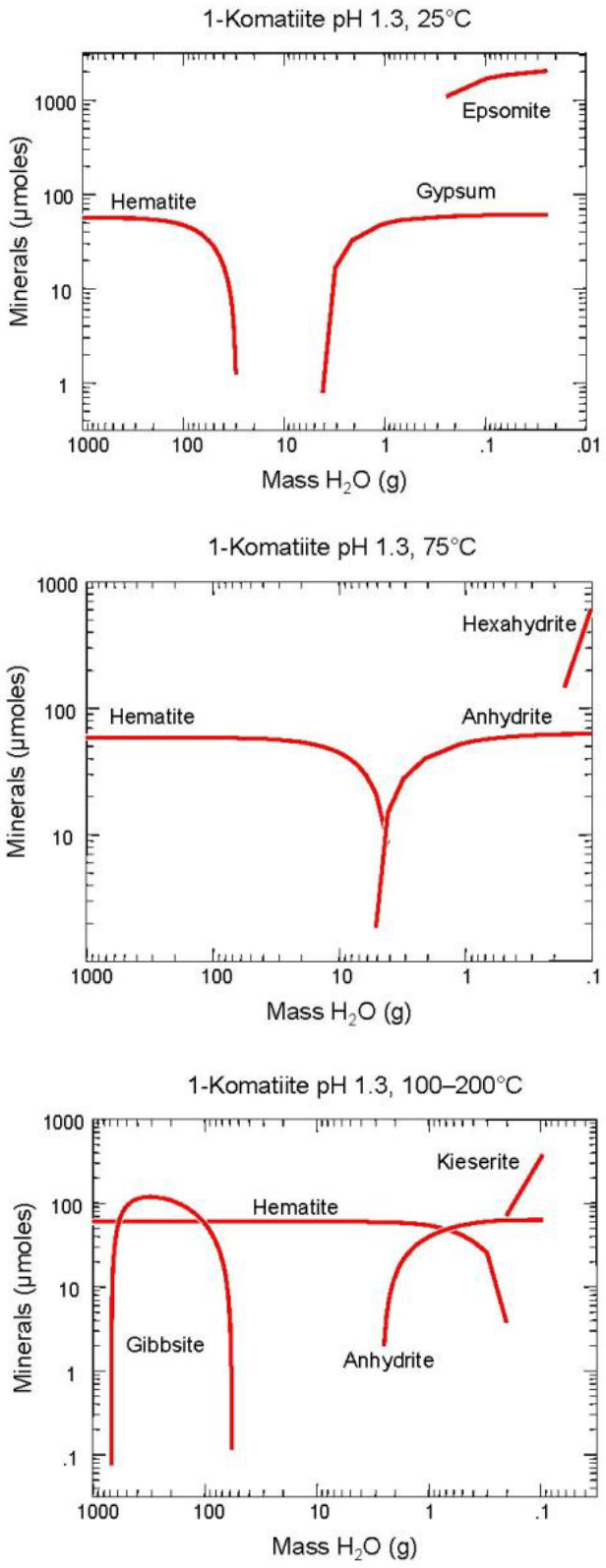

Figure 28: Concentration of minerals precipitated during numerical evaporation of the 1-komatiite$_{(pH\ 1.3)}$ leachate at 25°C, 75°C and between 100-200°C.

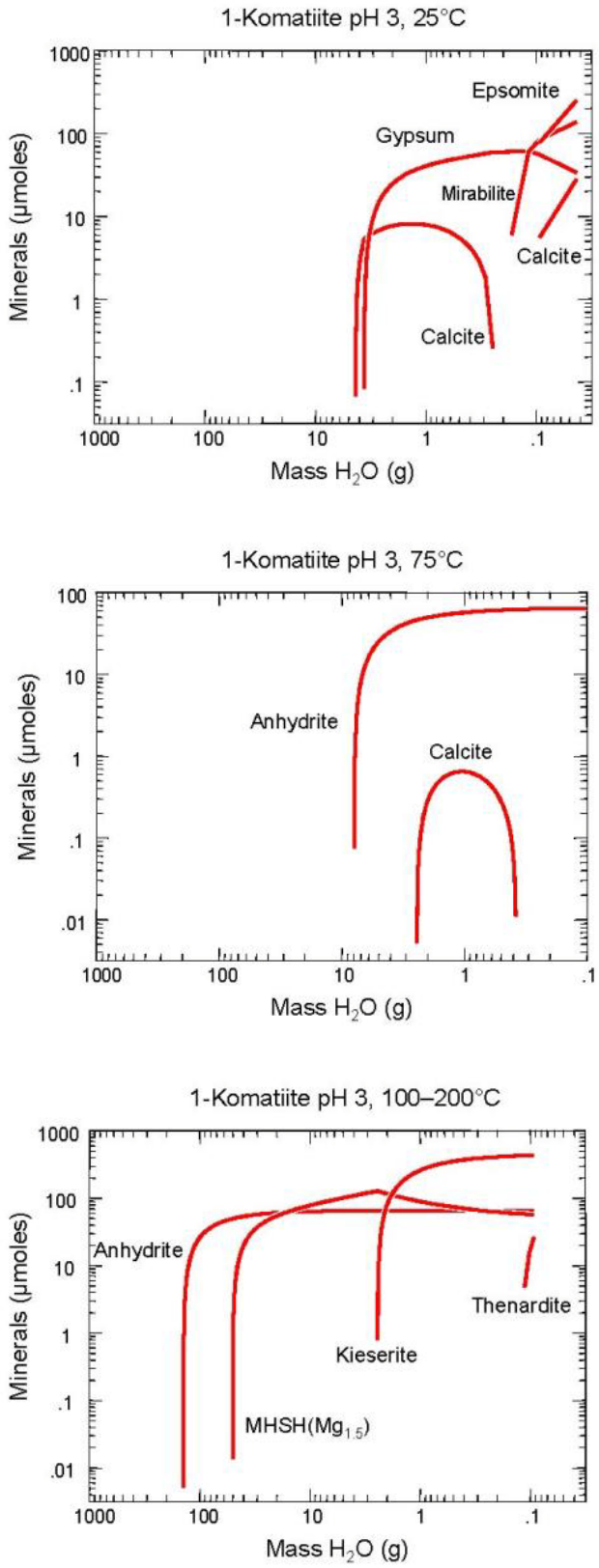

Figure 29: Concentration of minerals precipitated during numerical evaporation of the 1-komatiite$_{(pH\ 3)}$ leachate at 25°C, 75°C and between 100-200°C.

According to the calculation results of sample **1-komatiite$_{(pH\ 1.3)}$** hematite appears with a concentration of 56.6 µmol l^{-1} and dissolves at a pH >1.6. Between pH 1.6 and about pH >0.97 the solution is undersaturated with respect to the minerals hematite, goethite and gypsum. Gypsum occurs at pH >0.97 and has its highest concentration of 61.6 µmol l^{-1} followed by epsomite with a concentration of 2196 µmol l^{-1} at pH -3.503.

At 75°C hematite occurs at the beginning of the reaction, but dissolves when anhydrite precipitates with a concentration of 62.25 µmol l^{-1} followed by hexahydrate with a concentration of 146.4 µmol l^{-1} approximately at the very end of the numerical evaporation and at pH -0.805.

Between 100 and 200°C (Figure 28) hematite appears to precipitate along the entire reaction path but dissolves at a pH of 0.071 shortly before the water is evaporated gibbsite occurs but also disappears at a pH of >2.3 and a temperature of 190°C. Only kieserite and anhydrite precipitate almost at the end of the reaction with a concentration of 62.97 µmol l^{-1} (anhydrite) and 372.8 µmol l^{-1} (kieserite).

After nearly 99 % of the H_2O is removed from the system, calcite occurs with an increasing concentration up to 5.226 µmol l^{-1} followed by gypsum with a maximum concentration of 59.3 µmol l^{-1} in the **1-komatiite$_{(pH\ 3)}$**-sample, calculated at 25°C. Mirabilite starts to precipitate at pH 5.64 at the expense of gypsum, caused by the depletion of SO_4^{2-} in the solution with a rising concentration up to 136.8 µmol l^{-1}. The calcite precipitation is interrupted and the mineral is entirely dissolved when mirabilite occurs. Calcite precipitates again close to the end of the reaction path with a maximum concentration of 28.1 µmol l^{-1} at the same time when epsomite precipitates with a maximum concentration of 250 µmol l^{-1}.

At 75°C, anhydrite precipitates with a maximum concentration of 64.12 µmol l^{-1} at a pH of > 5.5 followed by calcite which immediately re-dissolves at a pH of 5.57 when almost all of the water is evaporated.

Between 100 and 200°C (Figure 29) anhydrite is supersaturated from the solution with a concentration of 66.14 µmol l^{-1} followed by MHSH($Mg_{1.5}$) with a maximum concentration of 126.9 µmol l^{-1}. MHSH($Mg_{1.5}$) partly dissolves when kieserite occurs with a concentration of 431.7 µmol l^{-1}. At the very end of the reaction path and temperature scale thenardite precipitates with a concentration of 26.39 µmol l^{-1} at a pH of 5.143.

5.3.7 s-komatiite

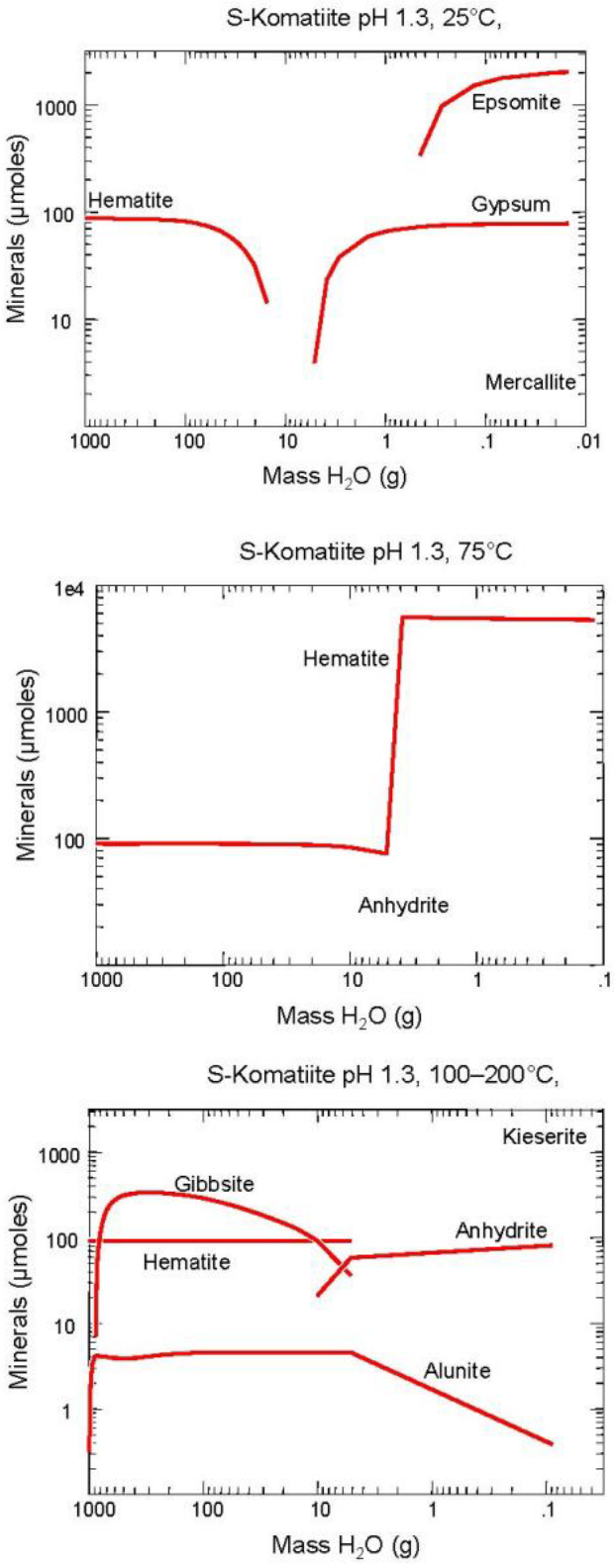

Figure 30: Concentration of minerals precipitated during numerical evaporation of the s-komatiite$_{(pH\ 1.3)}$ leachate at 25°C, 75°C and between 100-200°C.

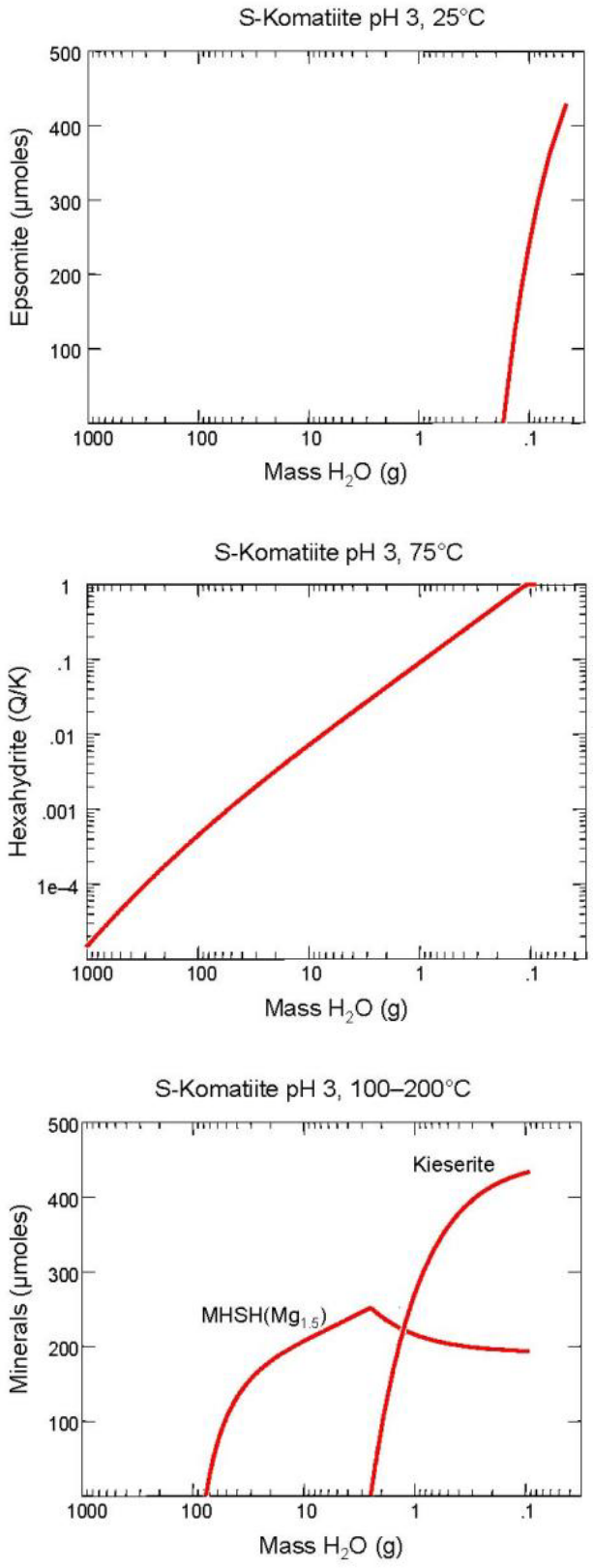

Figure 31: Concentration and saturation indices of minerals precipitated during numerical evaporation of the s-komatiite$_{(pH\ 3)}$ leachate at 25°C, 75°C and between 100-200°C.

The **s-komatiite$_{(pH\ 1.3)}$** results at 25°C show the formation of hematite with a decreasing value from 86.94 µmol l^{-1} down to a concentration of 81.45 µmol l^{-1} before dissolution. Between pH 2 and pH 1.4, no mineral saturates. Gypsum is the next mineral which forms at a pH of 1.4 up to a concetration of 77.9 µmol l^{-1} almost at the end of the reaction path. The magnesium sulfate epsomite is oversaturated after nearly all of the water is removed from the system and has its maximum at the end of the reaction with a concentration of 2024 µmol l^{-1}. At the very end, a small amount (1.69 µmol l^{-1}) of mercallite precipitates.

Figure 30 shows the numerical evaporation at 75°C with hematite as the only mineral phase which precipitates with a final concentration of 5324 µmol l^{-1} at a calculated pH of -0.327. Anhydrite briefly occurs but redissolves while reaction.

At temperatures above 100 up to 200°C the sulphate phases kieserite, anhydrite and alunite are the only minerals in the system. Kieserite occurs with a maximum concentration of 905.9 µmol l^{-1}, anhydrite with 81.55 µmol l^{-1} and a minor amount of alunite with 0.3831 µmol l^{-1} at a pH of -0.142.

The **s-komatiite$_{(pH\ 3)}$** sample only shows the precipitation of epsomite with an increasing concentration from 0.99 µmol l^{-1} up to 429 µmol l^{-1} between an initial pH of 6.83 down to a final pH of 6.36.

Figure 31 shows the mineral saturation state of hexahydrate at 75°C. The mineral phase hexahydrate precipitates with 104.8 µmol l^{-1} at a pH of 6.21 at the very end of evaporation when almost all of the water is removed from the system. Because hexahydrate precipitates in several orders of magnitude, Figure 31 shows the mineral saturation state instead of the concentration.

While epsomite precipitates at 25°C and hexahydrite at 75°C, kieserite is the dominat sulfate mineral phase which is supersaturated at a temperature near 200C° with a concentration of 433.8 µmol l^{-1}. Also MHSH($Mg_{1.5}$) starts to precipitate at 192.4°C up to 200°C with a maximum concentration of 193,7 µmol l^{-1}, according to the modeling results.

5.3.8 Volcanic glass

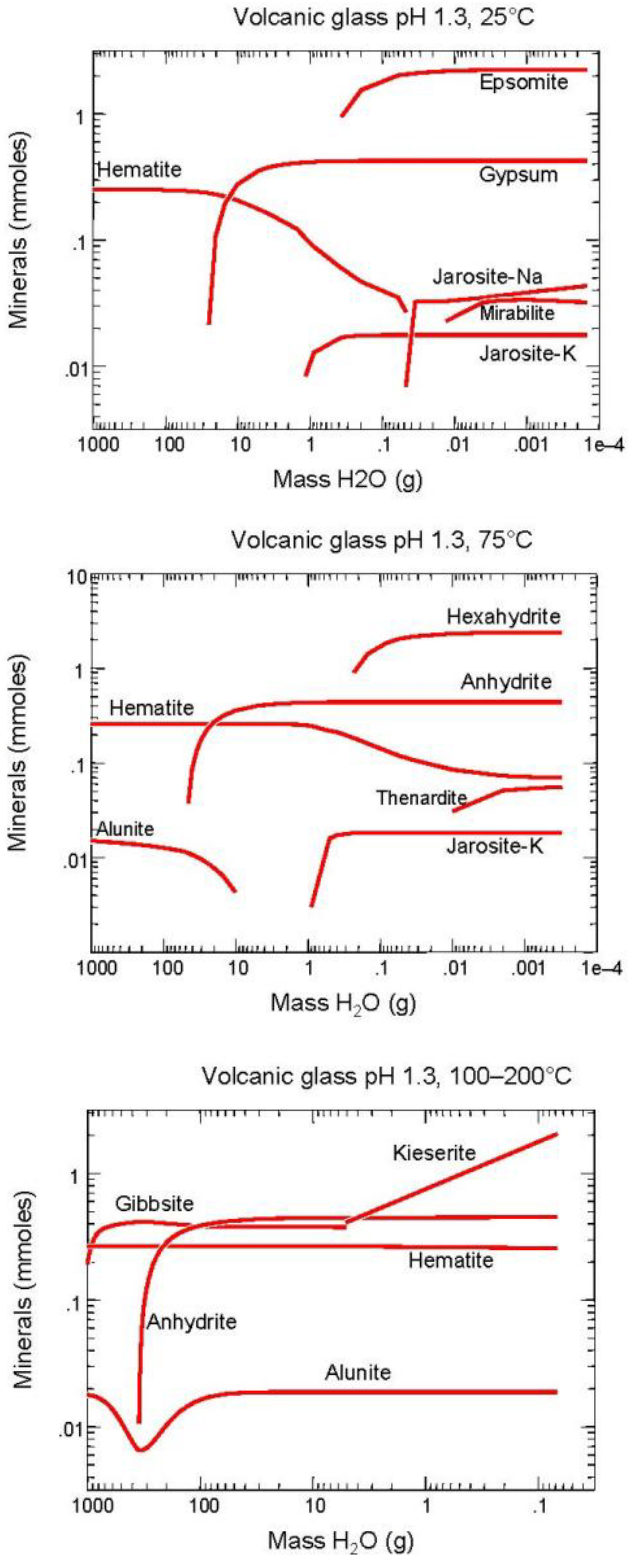

Figure 32: Concentration of minerals precipitated during numerical evaporation of the volcanic glass$_{(pH\ 1.3)}$ leachate at 25°C, 75°C and between 100-200°C (results were included in Noel et al., 2015).

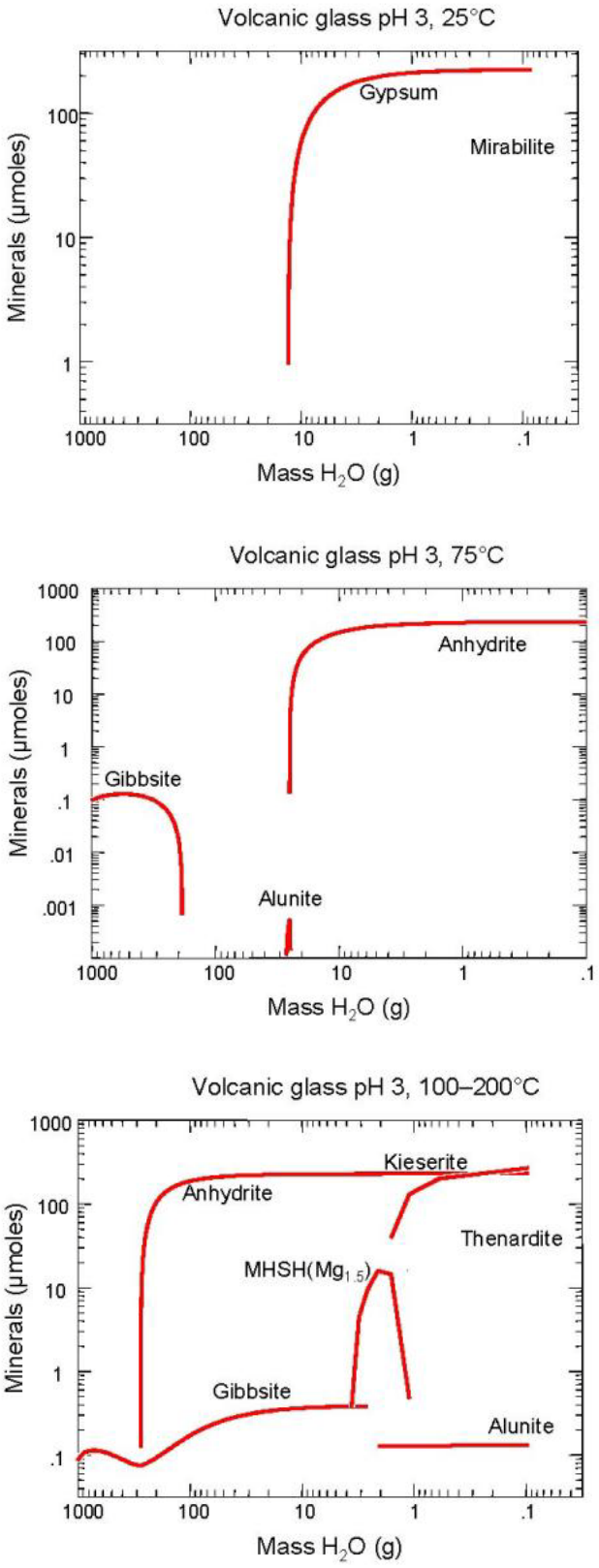

Figure 33: Concentration of minerals precipitated during numerical evaporation of the volcanic glass$_{(pH\ 3)}$ leachate at 25°C, 75°C and between 100-200°C.

The numerical calculation of the **volcanic glass$_{(pH\ 1.3)}$** fluid sample shows that hematite is the first mineral which forms with a decreasing concentration of 249.7 µmol l^{-1} down to a concentration of 59.3 µmol l^{-1} before it goes back into solution. When nearly 26 % H_2O is removed from the system and pH achieved a value of 1.8, gypsum starts to precipitate and reaches a maximum concentration of 423 µmol l^{-1}. At a pH of 1.29, K-jarosite is oversaturated with an increasing value up to 17.7 µmol l^{-1}, while hematite is depleted in the solution:

$$\text{Hematite} + 2\ H_2O + 1.333\ SO_4^{2-} + 0.6667\ K^+ \rightarrow 0.6667\ \text{K-Jarosite}. \quad (39)$$

Epsomite occurs at a pH of 1.13 and reaches a maximum concentration of 2222 µmol l^{-1}. When the pH value is below 0.9, Na-jarosite appears:

$$3\ Fe^{2+} + Na^+ + 2\ SO_4^{2-} + 4.5\ H_2O + 0.75\ O_{2(aq)} \rightarrow \underset{\textit{Na-jarosite}}{NaFe_3(SO_4)_2(OH)_6} + 3\ H^+ . \quad (40)$$

followed by mirabilite. Na-jarosite and mirabilite reach their maximum concentration of 43.9 µmol l^{-1} and 31.7 µmol l^{-1}, respectively, at pH -0.22.

At 75°C the Mg-sulfate phase hexahydrate with 2331 µmol l^{-1}, anhydrite with 440.1 µmol l^{-1} and the Na-sulfate mineral thenardite with 30.77 µmol l^{-1} precipitate at a pH of 0.378, instead of epsomite, gypsum, Na-jarosite and mirabilite, compared to the calculations at 25°C, due to the higher temperature. Hematite occurs along the entire reaction path with a final concentration of 84.90 µmol l^{-1} and K-jarosite was calculated with a concentration of 18.36 µmol l^{-1} at the end of the reaction. Alunite starts to precipitate but redessolves shortly after the beginning of evaporation.

Numerical modeling at temperatures between 100 and 200°C leads to the formation of alunite with a concentration of 18.76 µmol l^{-1} and hematite with 255.4 µmol l^{-1} along the entire reaction path. The Al-containing oxide gibbsite is supersaturated along almost the whole calculation process but is interrupted when kieserite begins to form with a concentration of 2040 µmol l^{-1} at 199.5°C.
At 165°C anhydrite begins to precipitate and influences temporarily the precipitation of alunite. The pH value decreases from the measured starting pH of 3.6 down to the calculated pH of 0.378.

Only two sulfate minerals precipitates occur after numerical modeling of the **volcanic glass$_{(pH\ 3)}$** fluid sample when 13 g of H_2O is left. Gypsum precipitates with 223 µmol l^{-1}, followed to a smaller amount of mirabilite with a concentration of 49 µmol l^{-1} at pH 1.72.

Already in the beginning of the calculations at 75°C gibbsite precipitates but goes back into solution. Alunite is the next mineral that occurs but also redessolves apparently with respect to anhydrite. Under these conditions, anhydrite is the only mineral that remains in the system with a maximum concentration of 228.9 µmol l^{-1} at a final pH of 2.3.

As a result of the calculations under hydrothermal conditions at temperatures between 100 and 200°C (Figure 33), the formation of kieserite with a concentration of 268.6 µmol l^{-1}, anhydrite with a concentration of 228.7 µmol l^{-1}, thenardite with 26.31 µmol l^{-1} and a small amount of alunite with a concentration of about 0.3 µmol l^{-1} can be observed. Precipitation takes place at almost 200°C and pH values down to a minimum of 4.2. The mineral phases gibbsite and MHSH($Mg_{1.5}$) occur but could not precipitate in the end.

5.3.9 DTS-2b

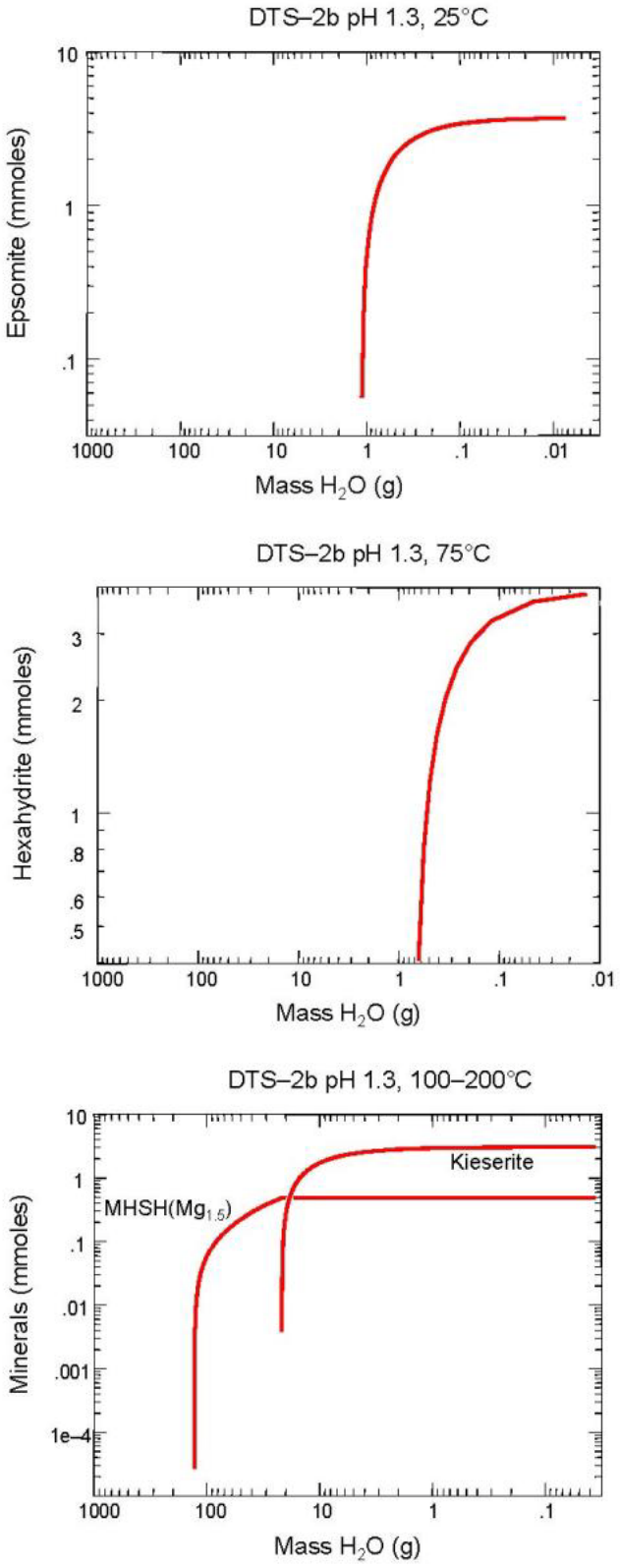

Figure 34: Concentration of minerals precipitated during numerical evaporation of the DTS-2b$_{(pH\ 1.3)}$ leachate at 25°C, 75°C and between 100-200°C.

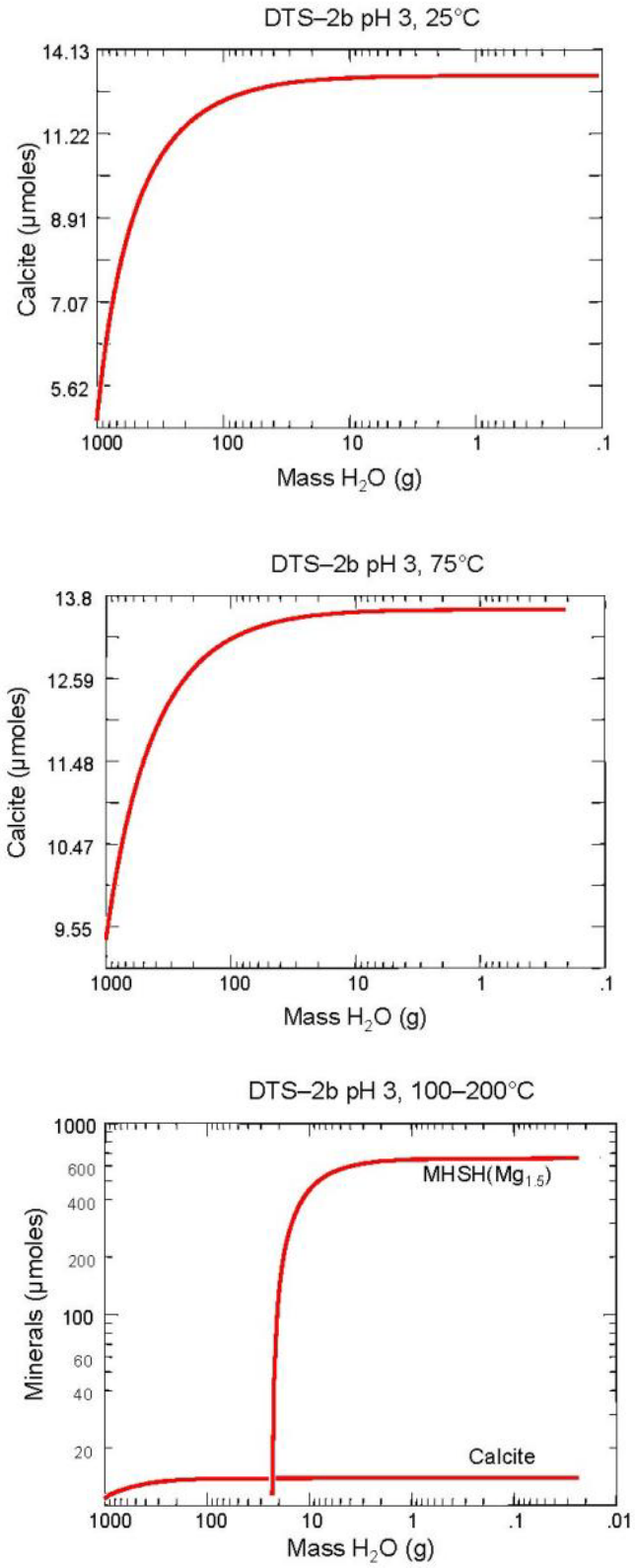

Figure 35: Concentration of minerals precipitated during numerical evaporation of the DTS-2b$_{(pH\ 3)}$ leachate at 25°C, 75°C and between 100-200°C.

Figure 34 shows the calculated mineral precipitation of the **DTS-2b$_{(pH\ 1.3)}$** sample at a temperature of 25°C. Only epsomite occurs at pH 5.21 when more than 99 % of H_2O is evaporated. The maximum concentration for $MgSO_4$:$7H_2O$ is about 3738 µmol l^{-1} at a pH of 5.42 at the end of the reaction path.

Calculation at 75°C leads to the formation of hexahydrite with a maximum concentration of 3903 µmol l^{-1} at a calculated pH of 5.38.

Modeling conducted at temperatures between 100 and 200°C leads to the formation of MHSH($Mg_{1.5}$) with a concentration of 479.9 µmol l^{-1} above 187°C and kieserite with 3073 µmol l^{-1} above 197°C at a final pH of 4.9.

Numerical modeling of the **DTS-2b$_{(pH\ 3)}$** sample at 25°C and 75°C leads to the supersaturation of calcite. The calculation at 25°C leads to the precipitation of calcite over the entire reaction process with a concentration of 5.11 µmol l^{-1} up to a maximum of 13.14 µmol l^{-1}. The pH value evolves from 8.88 down to pH 8.35.

At 75°C only calcite occurs and reaches a maximum concentration of 13.59 µmol l^{-1} at a final pH of 8.43.

Modeling conducted at temperatures between 100 and 200°C leads to the formation of calcite with a concentration of 13.88 µmol l^{-1} and the precipitation of MHSH($Mg_{1.5}$) above 197°C at a pH of 8.22 with a maximum concentration of 655.4 µmol l^{-1}.

5.3.10 Bir-1a

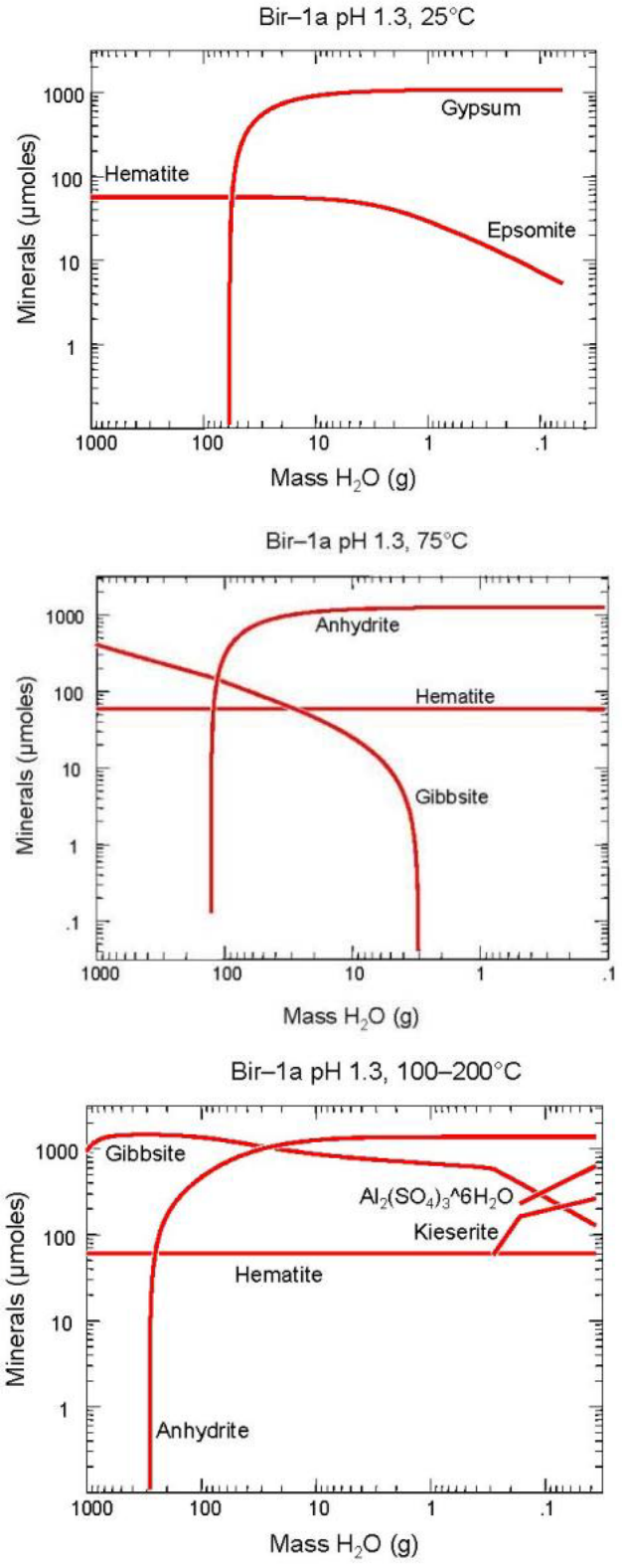

Figure 36: Concentration of minerals precipitated during numerical evaporation of the Bir-1a$_{(pH\ 1.3)}$ leachate at 25°C, 75°C and between 100-200°C.

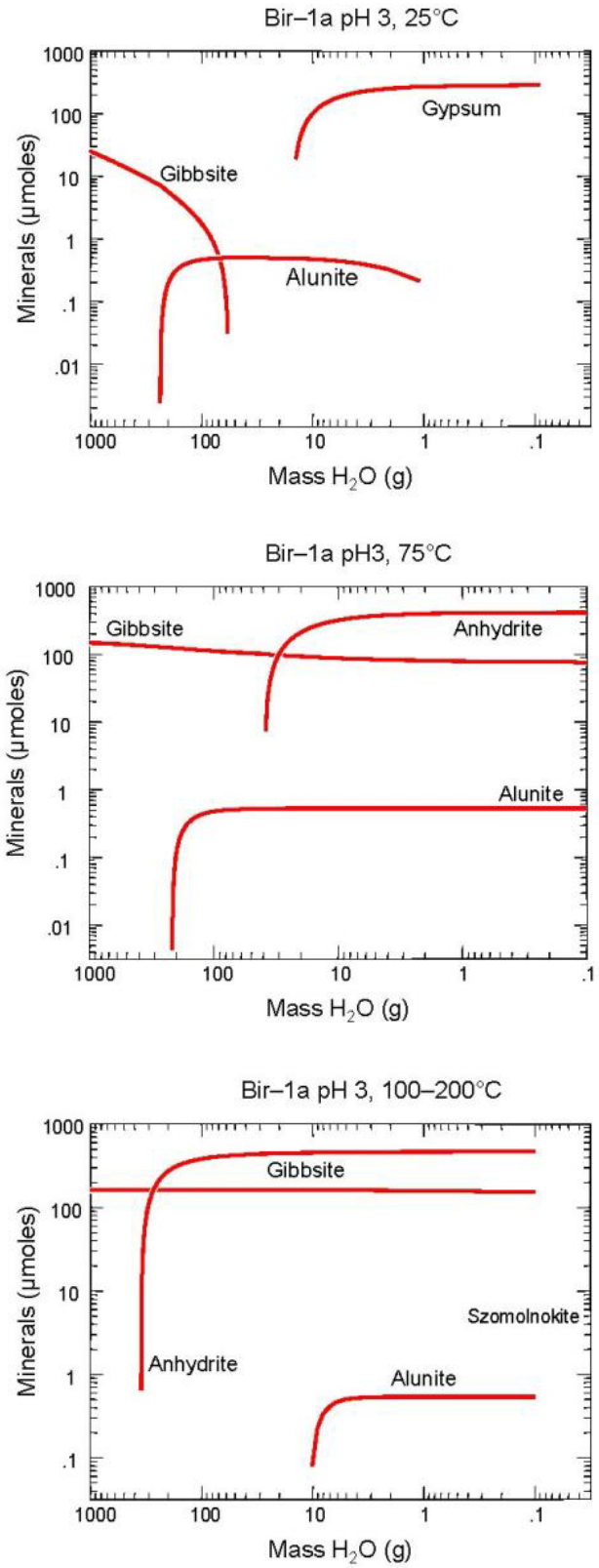

Figure 37: Concentration of minerals precipitated during numerical evaporation of the Bir-1a$_{(pH\ 3)}$ leachate at 25°C, 75°C and between 100-200°C.

In the beginning of the evaporation process of the **Bir-1a$_{(pH\ 1.3)}$** fluid sample at 25°C, hematite is oversaturated up to 56.7 µmol l^{-1} and decreases over the entire range of the reaction path down to a concentration of 5.28 µmol l^{-1}. Gypsum is oversaturated at a pH value of 2.57 and at a remaining water mass of around 5.8 % with a concentration of 0.31 µmol l^{-1} and rapidly increase to a concentration of 1077 µmol l^{-1}. At a pH of 0.96 the solution is oversaturated with respect to a small amount of epsomite with a concentration of 7.3 µmol l^{-1}.

Calculations at 75°C show the precipitation of hematite, which is supersaturated up to 58.56 µmol l^{-1} and anhydrite with a maximum concentration of 1256 µmol l^{-1} at a pH of 1.53. The mineral phase gibbsite occurs but redissolves during reaction.

Only calculations at temperatures near 200°C, under hydrothermal conditions, show a higher diversity of precipitating minerals. At the end of the reaction path anhydrite is the dominant mineral phase with a concentration of 1377 µmol l^{-1}, followed by the Al-phase $Al_2(SO_4)_3 \cdot 6\,H_2O$ with an amount of 628 µmol l^{-1}, kieserite with a concentration of 263.1 µmol l^{-1}, gibbsite with 127.4 µmol l^{-1} and the ubiquitous mineral hematite with a concentration of 60.16 µmol l^{-1}. The pH value evolves from 3.79 down to pH 1.61.

Sample **Bir-1a$_{(pH\ 3)}$** (Figure 37) shows that gibbsite ($Al(OH)_3$) is the first mineral that precipitates out of the fluid at 25°C, with a concentration of 24.97 µmol l^{-1}. The mineral completely dissolves below a pH of 3.82. While the gibbsite concentration decreases down to 1.7 µmol l^{-1}, the solution is oversaturated with respect to alunite with a maximum concentration of 0.495 µmol l^{-1} before it also entirely dissolves.
At pH 3.45 gypsum starts to precipitate at a remaining water mass of up to 2 % with a concentration of 8.7 µmol l^{-1} up to a maximum of 338 µmol l^{-1} after nearly all of the water is evaporated. The starting pH of 4.43 decreases down to finally pH 1.85.

If the pH value decreases below a specific range, in a strong sulfur acidic solution, gibbsite is no longer stable and an Al - hydroxy sulfate forms, such as alunite:

$$\text{Gibbsite} + H^+ + 0.3333\ K^+ + 0.6667\ SO_4^{2-} \rightarrow H_2O + 0.3333\ \text{Alunite} \qquad (40)$$

But calculations at 75°C show the mineral precipitation of both gibbsite with a concentration of 75.72 µmol l^{-1} and alunite with a concentration of 0.53 µmol l^{-1}, together with anhydrite with a concentration of 412.9 µmol l^{-1}. The pH decreases down to 2.74.

Calculations at temperatures between 100 to 200°C show similar results besides that szomolnokite additionally form close to 200°C. The dominant mineral anhydrite precipitates with a concentration of 464.9 µmol l^{-1}, gibbsite with 153 µmol l^{-1}, szomolnokite with 2.74 µmol l^{-1} and alunite with a concentration of 0.536 µmol l^{-1} at the end of evaporation. The final pH at the last modeling step is 2.1.

5.3.11 Xenolith

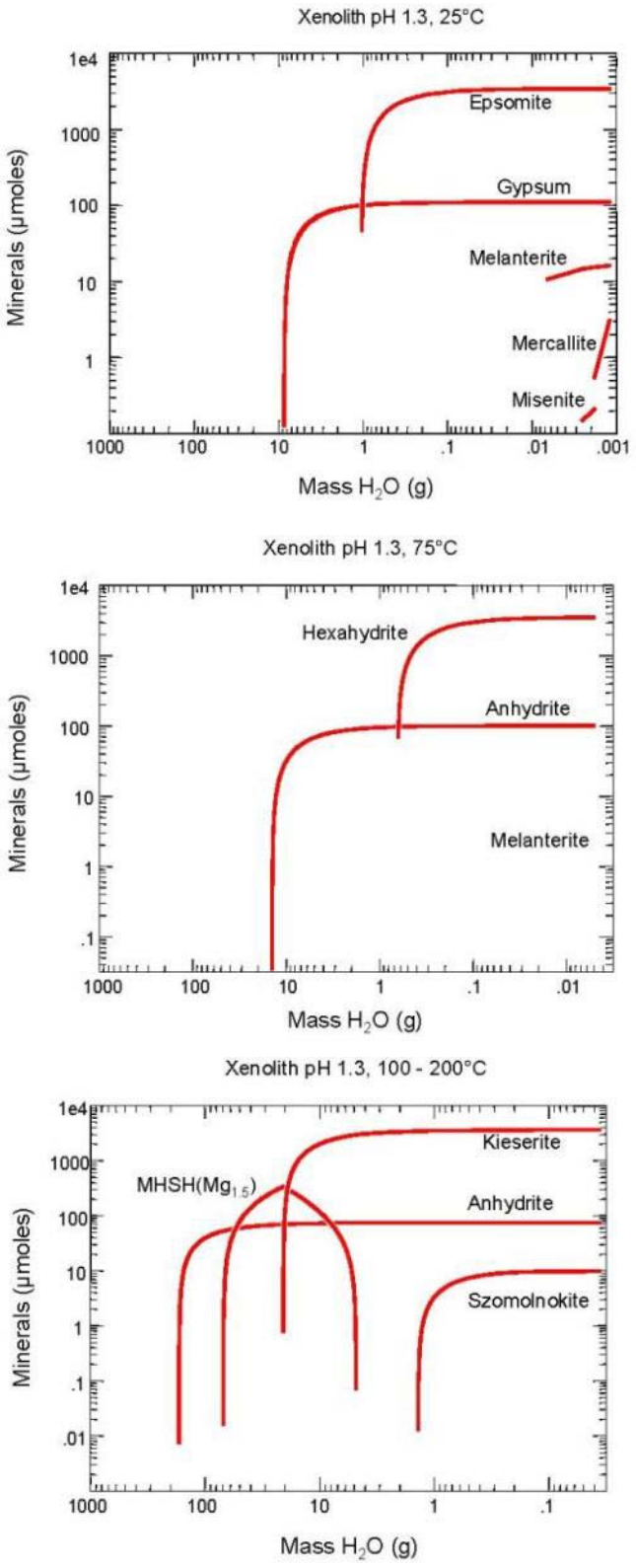

Figure 38: Concentration of minerals precipitated during numerical evaporation of the xenolith$_{(pH\ 1.3)}$ leachate at 25°C, 75°C and between 100-200°C.

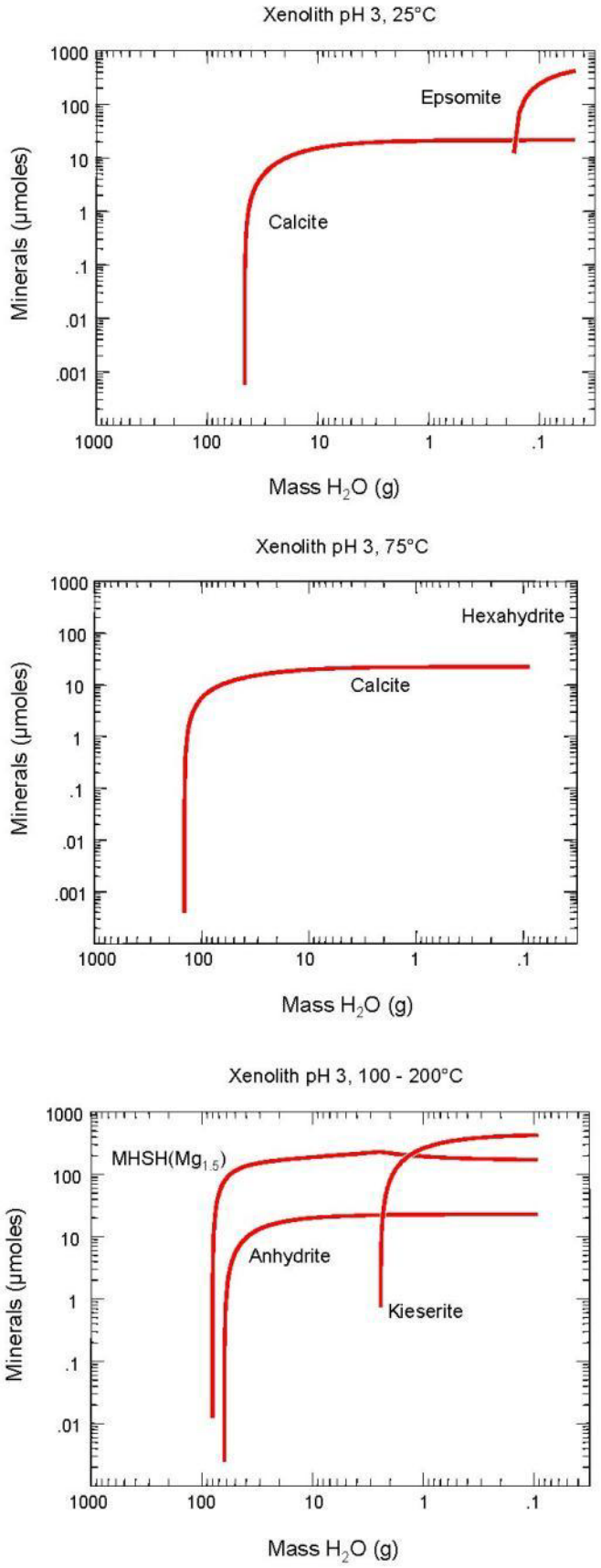

Figure 39: Concentration of minerals precipitated during numerical evaporation of the xenolith$_{(pH\ 3)}$ leachate at 25°C, 75°C and between 100-200°C.

The calculated results of the sample fluid **xenolith$_{(pH\ 1.3)}$** at 25°C are oversaturated with respect to gypsum, epsomite, melanterite, mercallite and misenite between pH 4.5 and pH -1.4. Gypsum is the first mineral that precipitates with a maximum concentration of 110 µmol l^{-1}, followed by epsomite with the highest concentration of 3418 µmol l^{-1} when more than 97 % of H_2O is evaporated. Nearly at the end of the reaction path, when almost all of the water is removed, melanterite, mercallite and misenite occur:

$$Fe^{2+} + SO_4^{2-} + 7\ H_2O \rightarrow \underset{melanterite}{FeSO_4 \cdot 7\ H_2O} \quad (42)$$

$$8\ K^+ + 7\ SO_4^{2-} + 6\ H^+ \rightarrow \underset{misenite}{K_8H_6(SO_4)_7} \quad (43)$$

with concentrations of 17.3 µmol l^{-1} ($FeSO_4$:$7H_2O$), 2 µmol l^{-1} ($KHSO_4$) and 0.2 µmol l^{-1} ($K_8H_6(SO_4)_7$), respectively.

The xenoliths$_{(pH\ 1.3)}$ modeling experiment at 75°C differs from the 25°C experiment primarily in the diversity and hydration state of the minerals. In contrast to the modeling results of the xenoliths$_{(pH\ 1.3)}$ experiment at 25°C, the experiment at 75°C shows no saturation of K-minerals. The less hydrated minerals hexahydrate and anhydrate form with concentrations up to 3530 µmol l^{-1} for $MgSO_4 \cdot 6H_2O$ and 100.6 µmol l^{-1} for $CaSO_4$ instead of epsomite and gypsum. A small amount of the hydrated iron sulfate melanterite is saturated with a concentration of 7.40 µmol l^{-1} almost at the end of the reaction path at a final calculated pH of -0.486.

The concentration ratios of the precipitating Mg, Ca and Fe containing minerals in the **xenoliths$_{(pH\ 1.3)}$** modeling experiment at temperatures between 100 and 200°C are almost the same as the calculation results at 75°C. Differences can be determined in the hydration state of both the Mg-sulfate and Fe-sulfate. Kieserite, the dominant mineral, is saturated with 3583 µmol l^{-1} and anhydrate, the most stable phase during reaction, is saturated with 75.31 µmol l^{-1}.

The less hydrated mineral szomolnokite replaces melanterite with a similar concentration of 9.88 µmol l^{-1}. MHSH(Mg 1.5) occurs during reaction but is not stable at increasing temperatures up to 200°C and decreasing pH.

According to the calculated results of the evaporation of the **xenolith$_{(pH\ 3)}$** sample fluid, the calcium carbonate calcite and the polyhydrated magnesium sulfate epsomite precipitates with maximum concentrations of 21.42 µmol l^{-1} (calcite) and 418.6 µmol l^{-1} (epsomite) after more than 84 % of water is removed from the system. The pH value decreases from pH 7.88 down to pH 6.77 along the reaction path.

The xenolith$_{(pH\ 3)}$ modeling results coducted at 75°C show similar results compared to the modeling results performed at 25°C. The less hydrated Mg-sulfate hexahydrate replaces epsomite with a concentration of 117.9 µmol l^{-1}. The calcite concentration of 22.23 µmol l^{-1} at 75°C is similar to the calcite concentratio calculated at 25°C at a final pH of 6.82.

The xenolith$_{(pH\ 3)}$ calculated results between 100 to 200°C differ in the Mg and Ca saturation. Additionally to kieserite with a concentration of 423.8 µmol l^{-1}, the Mg-hydroxy sulfate MHSH(Mg 1.5) precipitates with a concentration of 170.6 µmol l^{-1}. Anhydrate forms with a maximum concentration of 22.73 µmol l^{-1} in contrast to calcite, which does not occur between 100 and 200°C at a final pH of 4.91.

6. Interpretation and discussion

6.1 Fluid geochemistry

The major focus of this chapter is on the fluid-geochemical aspect of the occurring metal and alkaline earth metal sulfate minerals as well as on the sulfate mineral assemblages that are indicative of an extremely acidic environment as a consequence of the numerical evapo-concentration of the experimentally generated fluids. In the previous chapters, the petrologic and geochemical characteristics of the investigated samples were described in detail. Geochemical modeling using the software GWB as described in chapter 5.1 resulted in precipitation of several different sulfate and oxide minerals for pH 1.3 and pH 3 for temperatures up to 200°C. These are summarized in tables 9-14.

As a first result, all occurring mineral assemblages correspond, more or less as predicted, to non-marine evaporites. The minerals produced include e.g. epsomite, mirabilite, mercallite and thenardite. Marine and non-marine evaporites form in order of increasing solubility. Initially the most insoluble compound Ca-carbonate forms followed by gypsum and anhydrite respectively. The next stage of precipitation would be characterized by the formation of chlorides. Finally, the last mineral phases to form are the K, Al, Na and Mg sulfate minerals.

Table 9: List of minerals precipitated from pH 1.3 sample solutions at 25°C.

	Sample ID (pH 1.3) at 25°C										
	Tissint	Ol	Cpx	Opx	Pl	1-komatiite	s-komatiite	Volcanic Glas	Xenolith	DTS-2b	Bir-1a
						Sulfates					
epsomite		+	+	+		+	+	+	+	+	+
gypsum	+		+	+	+	+	+	+	+		+
K-jarosite	+							+			
Na-jarosite								+			
melanterite									+		
mercallite			+				+		+		
mirabilite			+		+			+			
misenite									+		
						Iron(III) oxide					
hematite	+	+	+	+	+	+	+	+			+

Table 9 shows the minerals precipitated at pH 1.3 and 25°C from solutions resulting from dissolution of the eleven samples studied. Epsomite, gypsum and hematite were observed in many cases.

Table 10: List of minerals precipitated from pH 1.3 sample solutions at 75°C.

	Sample ID (pH 1.3) at 75°C										
	Tissint	Ol	Cpx	Opx	Pl	1-komatiite	s-komatiite	Volcanic Glas	Xenolith	DTS-2b	Bir-1a
						Sulfates					
alunite	+										
anhydrite	+		+	+	+	+	+	+	+		+
gibbsite					+						
hexahydrite						+		+	+	+	
K-jarosite	+	+							+		
melanterite									+		
szomolnokite			+								
thenardite								+			
						Iron(III) oxide					
hematite	+			+	+		+	+			+

Table 11: List of minerals precipitated from pH 1.3 sample solutions between 100-200°C.

	Sample ID (pH 1.3) at 100-200°C										
	Tissint	Ol	Cpx	Opx	Pl	1-komatiite	s-komatiite	Volcanic Glas	Xenolith	DTS-2b	Bir-1a
						Sulfates					
$Al_2(SO_4)_3 \cdot 6\,H_2O$											+
alunite	+		+				+	+			
anhydrite	+		+	+	+	+	+	+	+		+
gibbsite	+				+						+
K-jarosite											
kieserite	+	+				+	+	+	+	+	+
MHSH(Mg1.5)										+	
szomolnokite									+		
						Iron(III) oxide					
hematite	+	+		+	+	+		+			+

Given in Table 10 are the mineral expected to precipitate from the eleven sample solutions at pH 1.3 and 75°C. Increasing the temperature from 25°C to 75°C produces anhydrite instead of gypsum. This is consistent with previous observations of Ca sulfates (e.g. Bishop et al. 2014). Epsomite is also no longer observed at 75°C, but instead hexahydrite is produced, the monohydrated sulfate szomolnokite is observed for one sample at 75°C and another sample

at 100-200°C (Table 11). The monohydrated sulfate kieserite is observed at 100-200°C at pH 1.3 (Table 11) but not below this temperature range.

Gypsum is again observed at 25°C (Table 12) but not at higher temperatures. The results at pH 3 also show epsomite formation at 25°C, but hexahydrite formation at higher temperatures. Gibbsite formation occurs in more cases at pH 3 than at pH 1.3 and is more prevalent at 75°C and 100-200°C than at 25°C.

Table 12: List of minerals precipitated from pH 3 sample solutions at 25°C.

	Sample ID (pH 3) at 25°C										
	Tissint	Ol	Cpx	Opx	Pl	1-komatiite	s-komatiite	Volcanic Glas	Xenolith	DTS-2b	Bir-1a
		Sulfates									
alunite											
epsomite				+		+	+		+		
gibbsite					+						
gypsum	+		+	+	+	+		+			+
mirabilite			+			+		+			
		Carbonates									
calcite	+	+				+			+	+	

Table 13: List of minerals precipitated from pH 3 sample solutions at 75°C.

	Sample ID (pH 3) at 75°C										
	Tissint	Ol	Cpx	Opx	Pl	1-komatiite	s-komatiite	Volcanic Glas	Xenolith	DTS-2b	Bir-1a
		Sulfates									
alunite			+		+						+
anhydrite	+		+	+	+	+		+			+
gibbsite			+	+	+						+
hexahydrite							+		+		
thenardite			+								
		Carbonates									
calcite	+	+							+	+	

Table 14: List of minerals precipitated from pH 3 sample solutions between 100-200°C.

	Sample ID (pH 3) at 100-200°C										
	Tissint	Ol	Cpx	Opx	Pl	1-komatiite	s-komatiite	Volcanic Glas	Xenolith	DTS-2b	Bir-1a
						Sulfates					
alunite			+	+	+			+			+
anhydrite	+		+	+	+	+			+		+
gibbsite			+	+	+						+
kieserite	+		+	+		+	+	+	+		
MHSH(Mg1.5)	+	+				+	+		+	+	
szomolnokite											+
thenardite			+			+		+			
						Carbonates					
calcite		+								+	

The monohydrated kieserite, MHSH($Mg_{1.5}$), and szomolnokite occur in the 100-200°C range at pH 3 with kieserite being the most common monohydrated sulfate product.

pH:

The measured pH-values at the beginning of the modeled evaporation are listed in table 6 and 7 and the calculated pH values were described in sections 5.3.1 to 5.3.11. As expected, the pH-values generally decrease along the reaction path. The parameter pH shows significant changes during calculation of the fluid chemistry from almost neutral down to extremely acidic values.

However, the results also show that the sample fluids which can be situated from the outset in the extremely acidic milieu (pH 1.3) exhibit at the end of the evaporation process extremely low pH values, all the way down to -3.989 (**$opx_{(pH\ 1.3)}$**).

These, at first, surprising results are supported by the discussion of Nordstrom et al. (2000). They measured negative pH values down to -3.6 in fluids sampled in the Richmond Mine at Iron Mountain, CA (USA). The reason for the extreme decrease in the pH parameters within this study is a consequence of the increasing H^+ concentration by evaporation (see Figure 41). This results from hydrolysis of e.g. Fe(III) and the consumption of acid by mineral precipitation which leads to an ongoing increase of acidity. At these low pH-values, Fe(III) will not be completely oxidized and forms instead of Fe(III)-oxides, Fe(III) – hydroxy sulfates such as jarosite under the release of H^+:

$$3\,Fe^{2+} + K^{+} + 2\,SO_4^{2-} + 4.5\,H_2O + 0.75\,O_{2(aq)} \rightarrow KFe_3(SO_4)_2(OH)_6 + 3\,H^{+} \quad (44)$$

K-jarosite

This process is enhanced by the precipitation of minerals such as hematite, magnesium hydroxy-sulfate and even calcite.

It is noteworthy, that the higher the calculated temperature is the lower are the resulting pH parameters (Figure 41).

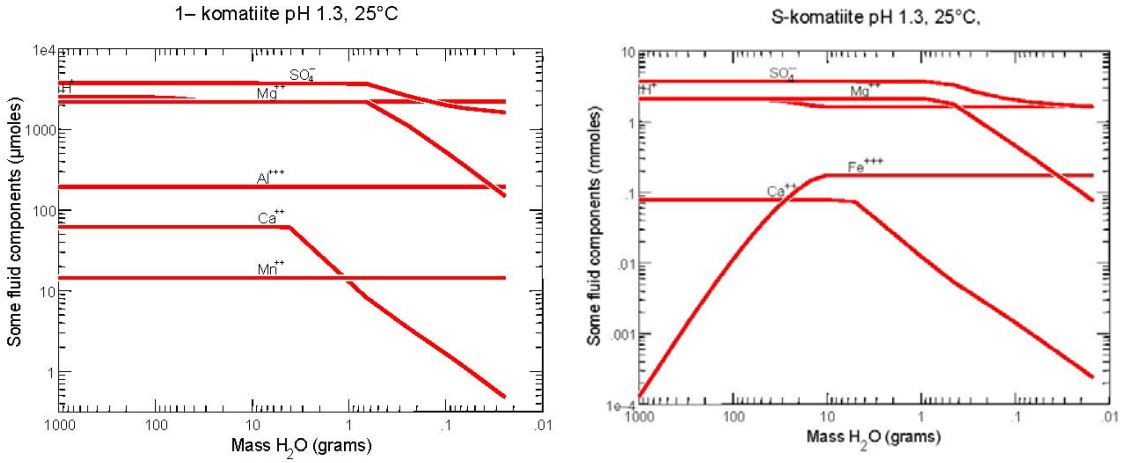

Figure 40: Calculated concentrations of components in the 1-komatiite$_{(pH1.3)}$ and s-komatiite$_{(pH1.3)}$ sample fluid, at 25°C.

The experiments described in the study about hydrothermal basalt alteration from Bischoff and Dickson (1975) show that fluid-cooling leads to a drop of pH, mainly due to precipitation of sulfide minerals under the generation of H^+ (Ding and Seyfried-Jr., 1992, Seyfried and Mottl, 1982).

SO_4^{2-}:

The concentration of dissolved sulfate at all temperatures is reduced by the consumption of reactants towards sulfate mineral precipitation. The SO_4^{2-} depletion in the fluid is accompanied with decreasing dissolved metal and alkaline earth metal ion contents (Figure 40). Sulfuric acid is a strong, dibasic acid. The dissociation reactions of sulfuric acid can be expressed as follows:

1. $$H_2SO_4 \leftrightarrow H^{+} + HSO_4^{-} \quad (45)$$

2. $$HSO_{4(aq)}^{-} \leftrightarrow SO_{4(aq)}^{2-} + H_{(aq)}^{+} \quad (46)$$

The largest amount of SO_4^{2-} is consumed by the formation of Ca^{2+} and Mg^{2+}-bearing sulfate minerals, most notably the formation of anhydrite or gypsum respectively.

As shown in the example of the **Tissint$_{(pH\ 3)}$** modeling results (section 5.3.1) at 100° to 200°C, the SO_4^{2-} gradient steeply decreases from 0.677 mmol l^{-1} down to 0.383 mmol l^{-1} until MHSH occurs, similar to the Ca^{2+} gradient between 160° and 180°C. A second steep drop in SO_4^{2-} concentration from 0.383 mmol l^{-1} down to 0.189 mmol l^{-1} almost at 200°C can be observed similar to the trend of the Mg^{2+} gradient. However, simultaneously to the magnesium hydroxide sulfate hydrate (MHSH) precipitation hydrogen ion concentration rises in one order of magnitude up to 0.169 mmol l^{-1}.

$$3\ Fe^{2+} + K^+ + 2\ SO_4^{2-} + 4.5\ H_2O + 0.75\ O_{2(aq)} \rightarrow \underset{\textit{K-jarosite}}{KFe_3(SO_4)_2(OH)_6} + 3\ H^+ \quad (47)$$

$$K^+ + 3\ Al^{3+} + 2\ SO_4^{2-} + 6\ H_2O \rightarrow \underset{\textit{alunite}}{KAl_3(OH)_6(SO_4)_2} + 6\ H^+ \quad (48)$$

$$1.5\ Mg^{2+} + SO_4^{2-} + H_2O \rightarrow \underset{\textit{magnesium hydroxy sulfate}}{Mg_{1.5}OHSO_4} + H^+ \quad (49)$$

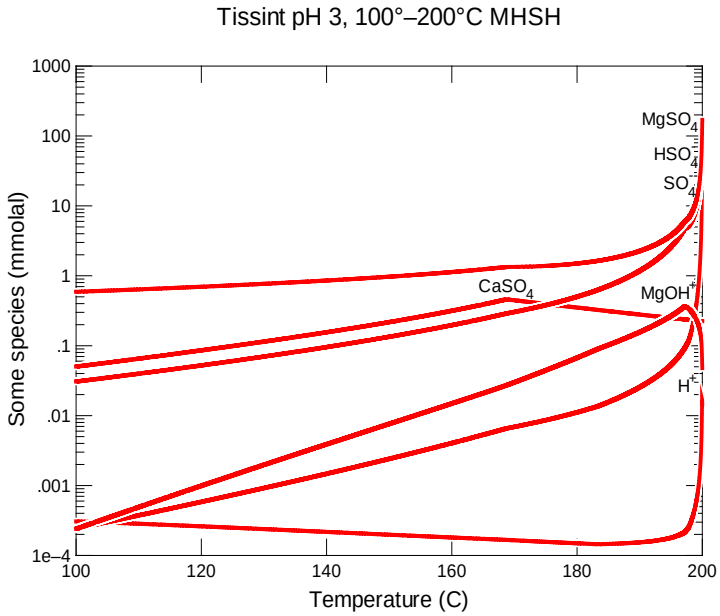

Figure 41: Species concentration in the calculated Tissint$_{(pH\ 3)}$ sample fluid between 100 to 200°C.

Figure 41 shows the species concentration in the fluid of **Tissint$_{(pH\ 3)}$**. The formation of sulfate minerals such as MHSH($Mg_{1.5}$) lead to the release of a large amount of H^+ ions near 200°C. Due to a significant increase in sulfate mineral formation SO_4^{2-} is increasingly consumed in favor of lower pH – values. This process contributes further to the acidity of the fluids.

These trends are similar to the sulfate-forming species such as, Al and Fe. The modeling results also show that increasing temperature leads to increasing activity of SO_4^{2-} in the solutions.

Fe:

The formation of ferruginous minerals is highly dependent on the hydrogen concentration and the redox potential. It also depends on whether there will be a reduction of SO_4^{2-} to SO_2 in the solution. Hematite precipitates due to highly oxidative solutions. But precipitation of Fe_2O_3 can only be observed as a result of the numerical evaporation of the initial pH 1.3 fluid samples within this study. None of the calculations of the former pH 3 sulfuric acid solutions initialized the saturation and precipitation of hematite. The results of the fluid measurements show that dissolved iron is less concentrated in the “pH 3” solutions than in the “pH 1.3” fluids. This is due to the different acid strengths of the initial sulfate acid solutions and the different solubility of the leached minerals and rocks. On the other hand, it cannot be

excluded that an unknown amount of the dissolved iron was already released from the solution and deposited as pyrite at corresponding pH values and redox potentials. Exceptions are the two DTS-2b samples (pH 1.3 and pH 3). In none of the two measured solutions iron was detected. The results show the precipitation of hematite as an ubiquitous mineral in the **Tissint**-, **olivine**- and the basalt sample **BIR-1a** at all temperature ranges. The **volcanic glass$_{(pH\ 1.3)}$**- and **plagioclase$_{(pH\ 1.3)}$** calculation results show hematite solidification only at temperatures of 75 °C and 100° to 200 °C. In all other samples that were leached with pH 1.3 in a sulfuric acid solution hematite is not stable nor does it precipitate.

According to Schwertmann (1969) and Schwertmann and Fischer (1973), hematite forms in sea water at pH values below 6. If the pH declines to values of about 3 to 2, KFe-hydroxy sulfates can precipitate (Scheffel and Schachtschabel, 2010; Sonnenfeld, 1984). At these low pH-values, the trivalent iron will not be completely oxidized and form instead of Fe(III)-oxides Fe(III)-hydroxy sulfates such as jarosite due to the hydrolysis of iron oxide in a sulfate and iron-rich environment (Scheffel and Schachtschabel, 2010). Madden et al. (2012) and Pritchett et al. (2012) basically confirm the modeling results of hematite and jarosite deposition by dissolution rate experiments on synthesized potassium- and sodium-bearing jarosites. Their experiments were run at pH 1 to 10 and at temperatures between 3.85 up to 49.85°C (277 to 323 K). They endorsed the pH-dependency on mineralization of K,NaFe-hydroxy sulfates by the observation of increasing dissolution rates with increasing pH beyond pH 3.5.
Nordstrom et al. (2000) and later Druschel et al. (2004) discovered melanterite deposition by sampling of pH -0.7 acid mine waters with a temperature of 38°C. They also discovered massive melanterite mineralization by cooling of the untreated fluid. These observations partly confirm the modeling results of the **xenolith$_{(pH\ 1.3)}$** sample conducted at 25°C and 75°C within this study. Melanterite precipitates with an amount of 7.4 µmol l^{-1} (pH -0.48) at 75°C and with a concentration of 17.3 µmol l^{-1} (pH -1.41) at 25°C which leads to the conclusion that decreasing temperature generates increasing melanterite saturation. Nordstrom et al. (2000) also reason that the formation of melanterite has minor influences on the pH gradient in contrast to the formation of jarosite precipitation due to the release of H^+.

The **xenoltih$_{(pH\ 1.3)}$** (100-200°C), **BIR-1a$_{(pH\ 3)}$** (100-200°C) and **cpx$_{(pH\ 1.3)}$** (75C°C) sample calculations show amongst other mineralization the formation of the Fe(II)-sulfate-hydrate szomolnokite ($FeSO_4 \cdot H_2O$). Szomolnokite is one of the most important Fe(II)-sulfate-hydrates, together with melanterite ($FeSO_4 \cdot 7\ H_2O$) and rozenite ($FeSO_4 \cdot 4\ H_2O$) (Koebel et al., 1989), but is rarely found in nature.

The deposition of szomolnokite is dependent on the temperature but also on the water vapor pressure (Kobylin et al., 2011; Koebel et al., 1989; Bruhn et al., 1965; Bullough et al., 1952 and Fraenckel, 1907). Experimental observations and thermodynamic models with respect to investigations of the solubility of ferrous sulfates described above show that the solubility of $FeSO_4 \cdot H_2O$ is above 60°C. Experiments conducted by Fraenckel (1907) show that the "transformation point" or point of solubility starts even at 56.6°C due to the unusual slow transformation rate of ferrous sulfates. The studies mentioned above are largely in agreement that $FeSO_4 \cdot H_2O$ and $FeSO_4 \cdot 7\,H_2O$ are the most stable phases within the $Fe_2O_3 - H_2SO_4 - H_2O$ system.

The study of Koebel at al. (1989) gives the most reasonable explanation why szomolnokite, according to the modeling results of the **xenoltih$_{(pH\ 1.3)}$** (100-200°C), **BIR-1a$_{(pH\ 3)}$** (100-200°C) and **cpx$_{(pH\ 1.3)}$** (75°C) samples, still precipitates even in extremely acidic conditions at pH values down to pH -0.7. Szomolnokite has an extremely strong association to its OH^- water, which is why Koebel et al. (1989) prefer the notation "$HO - Fe - SO_4H$" instead of $FeSO_4 \cdot H_2O$, to represent this mineral an extremely high resistance against oxidation over a broad temperature range and, according to this study, water activity range.

Investigations conducted by Opportunity during the Mars Exploration Rover mission (MER-B) detected jarosite associated with hematite in outcrops in Meridiani Planum on the surface of Mars (Christensen et al., 2004; Klingelhofer et al., 2004; McLennan et al., 2005; Squyres et al, 2006). Jarosite and hematite were found to form at pH 1.3 and 25°C in the solution resulting from dissolution of volcanic glass (Table 9). Both of these minerals were also produced from the Tissint solution at pH 1.3 and 75°C (Table 10).

Mg:

The presence of Mg^{2+} in a sulfuric acid solution can lead to the precipitation of a number of possible magnesium salts with similar solubilities. Only four of all known magnesium sulfates do precipitate during evapo-concentration as a result of the numerical calculations within this study. At low temperatures, the 7-hydrated magnesium sulfate epsomite precipitates whereas at a temperature of 75°C the 6-hydrated magnesium mineral hexahydrite forms out of the solutions. Between 100° to 200°C kieserite and the magnesium hydroxide sulfate MHSH($Mg_{1.5}$) ($Mg1.5OHSO_4$) forms.

Several investigations about primary salt deposition by evaporation at elevated temperatures were performed during the last 165 years (beginning with evaporation experiments of Usiglio, 1849). Countless thermodynamic models were developed and they predicted by solubility diagram approaches the formation of kieserite, anhydrite and dolomite due to

evaporation. Although expected, it was never observed in nature that these minerals precipitate at low temperatures.

Hardie (1984) called the lack of precipitation of the predicted minerals as primary evaporites in the early stages of seawater evaporation the “nucleation problem”. Until Hardie published his study in 1984, there was a general agreement that anhydrite and the mineral phase polyhalite ($K_2Ca_2Mg(SO_4)_4 \cdot H_2O$) were formed as secondary replacements after gypsum. But he provided an alternative hypothesis of anhydrite and polyhalite precipitation by introducing the term *syndepositional reaction minerals*. Experiments conducted by Autenrieth (1958) and Hardie (1967) indicated the synthesis of these two minerals. The origin of both minerals is, therefore, not necessarily diagenetic. Hence, Hardie (1984) assumed, that both mineral phases anhydrite and polyhalite form as equilibrium products due to back-reactions of early precipitates with the evolving, evaporitic brine. He also noticed that this assumption is also valid for kieserite (for detailed information read Hardie, 1984).

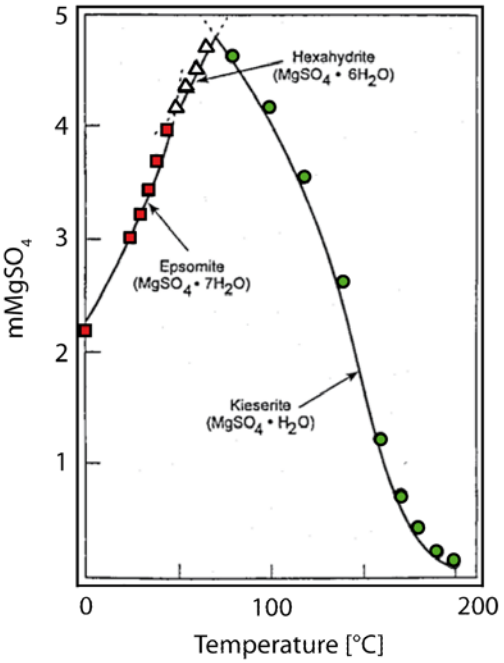

Figure 42: Solubility diagram of epsomite, hexahydrite and kieserite as a function of temperature (modified after Pabalan & Pitzer, 1987; Ptacek & Blowes, 2000; and Warren, 2006)

Kieserite, a magnesium sulfate monohydrate with a molality of 5.619 (Spencer, 2000) only occurs at temperatures between 100° and 200°C according to the thermodynamic models (see chapter 5) and is unstable at 25°C. Similar to anhydrite, kieserite has a retrograde solubility due to the negative temperature coefficient of solubility (Nishri et al., 1988). As discussed by Braitsch (1962) due to a negative temperature coefficient of kieserite, kieserite precipitates with increasing temperatures. Epsomite and hexahydrite in contrast precipitate while cooling (Braitsch, 1962).

At around 195°C the magnesium hydroxide sulfate hydrate MHSH($Mg_{1.5}$) precipitates in addition to the main mineral phases anhydrite and kieserite. The hydroxide sulfate hydrate MHSH was first described by Braitsch (1962). Based on the work of Bischoff and Seyfried (1978) the drop of pH and increasing acidity can be explained by the formation of MHSH.

According to their experiments, with progressive heating of the fluid Ca, Mg and SO_4 were more and more depleted due to precipitation of, at first, anhydrite at 200°C. This process already led to an increase of acidity. At around 250°C up to 350°C Mg compounds additionally started to form. Ca-bearing mineral precipitation was more and more inhibited due to the co-consumption of SO_4 by a specific amount of the Mg content. The remaining Mg-fraction was bound to OH^- and formed $Mg(OH)_2$ which corresponds quantitatively with the ionizable hydrogen gain.
Bischoff et al. (1983) noted that MHSH occurs in different stoichiometries. Kieserite partly precipitates in composition with $Mg(OH)^*$ to the mineral phase MHSH($Mg_{1.5}$) while heating the solution to temperatures up to 200°C (Bischoff and Seyfried, 1978; Keefer et al., 1981; Janecky and Seyfried, 1983; Seyfried and Ding, 1995). Progessive heating to temperatures of 200° and above 400°C can lead to the formation of the water free Mg anhydrite.

In this study, Ca anhydrite only co-precipitated in 3 of 6 calculation results (**Tissint$_{(pH\ 3)}$**, **1-komatiite$_{(pH\ 3)}$** and **xenolith$_{(pH\ 3)}$**) probably due to the great Mg and SO_4 excess. The formation temperatures are also not consistent with previous studies. The MHSH initial precipitation temperature observed by Bischoff and Seyfried (1978) was 300°C. Within this study MHSH($Mg_{1.5}$) starts to form at a calculated temperature of 195°C, 105°C less than that of Bischoff and Seyfried (1978).

While kieserite precipitation as a primary mineral in aqueous solutions is not clarified, it is generally known that hexahydrite and epsomite can form due to evaporation at low temperatures.
The magnesium sulfate mineral hexahydrite consists of (SO_4) tetrahedral acceptor ligands and $\{M^{2+}(H_2O)_6\}$ octahedral donor ligands according to the following equation (Hawthorne et al., 2000):

$$\{Mg(H_2O)_6\}(SO_4)$$

and its molality is 3.565 (Spencer, 2000). Only the octahedral structures are able to bind hydrogen molecules. But the hydrogen bonding is weak and applies to all other hydrated magnesium sulfates (Spencer, 2000). The percentage water content of hexahydrite is about 90 % related to $MgSO_4$ = 100, that of the heptahydrate structure epsomite is about 104.76 % and kieserite has up to 15 % H_2O content (Ide, 1938). Data for kieserite, hexahydrite and epsomite solubility between 0° and 200°C are presented in Figure 42. Epsomite, the

heptahydrated magnesium sulfate mineral occurs below 27°C (Fulda. 1928) or 28°C (Braitsch. 1962) and is well known for its deposition even below the freezing point. In addition to the M^{2+}-coordination of hexahydrite one H_2O molecule is bonded to the structure (Hawthorne et al., 2000):

$$\{Mg(H_2O)_6\}(SO_4)(H_2O)$$

Of all the magnesium sulfate hydrates presented here, hexahydrite is the most stable phase at room temperature. Epsomite is only stable under humid conditions. Exposed to dry air, the magnesium heptahydrate will slowly be altered over hexahydrite to the final stage kieserite. The reverse process, the rehydration of the monohydrate always leads to the immediate formation of epsomite. But by rehydration of empsomite the mineral phase will decay to fine powder (Ide, 1938).

Ca:

Anhydrite forms at temperatures above 75°C and consumes significant amounts of calcium and sulfate in the solution due to precipitation. At increasing temperatures anhydrite becomes less soluble and therefore has a retrograde solubility whereas gypsum is insoluble in cold sulfuric acid. This behavior of anhydrite is well known in marine hydrothermal systems (Halbach et al., 2001).

The modeling results show anhydrite precipitation beginning at 75°C. In marine environments, anhydrite is stable at temperatures above ~150°C and has a major role in the buildup of black smoker chimneys (Halbach et al., 2001). Small amounts of anhydrite were also detected in white smoker chimneys at temperatures between 100° and 300°C (Halbach et al., 2001). But at temperatures around 100°C anhydrite is an extremely metastable mineral phase. The absence of Cl^- and the presence of increasing SO_4^{2-} leads to the decrease of anhydrite solubility which supports the formation of anhydrite at 75°C (see Braitsch, 1962). Anhydrite precipitation above 75°C and gypsum mineralization at 25°C can be observed in almost all of the modeling results as the major mineral phase except in the **olivine**- and **DTS-2b** sample results due to the small amount or absence of Ca^{2+} in the initial solution. In all other sample results anhydrite and gypsum consume a significant amount of Ca^{2+} and SO_4^{2-} in the solution.

According to the modeling results the most commonly occurring low temperature mineral was gypsum followed by epsomite in both of the different pH water types (pH 1.3 and pH 3). Gypsum occurs in almost all samples except for the **olivine** samples and the **s-komatiite**$_{(pH\ 3)}$

sample at 25°C. Once formed, the solubility of gypsum is nearly temperature independent (Stumm and Morgan, 1996).

Carbonate minerals belong to the most common minerals on Earth, and they are likely to be present on Mars as well (Gooding et al., 1988; McKay et al., 1996; Romanek et al., 1994; Ehlman et al., 2008). In an evaporitic environment carbonate minerals form in the earliest stages of evaporation. The first calculation results within this study led to the precipitation of dolomite. As discussed before, dolomite as a primary mineral phase has a nucleation problem and was therefore suppressed in the model with respect to calcite and anhydrite precipitation. Calcite is supersaturated at 25°C, 75°C and between 100° to 200°C only in the pH 3 solutions. $CaCO_3$ is present in the pH 3 mineral assemblages of **Tissint$_{(pH\ 3)}$** at temperatures of 25° - 200°C, **olivine$_{(pH\ 3)}$** 100°-200°C, **1-komatiite$_{(pH\ 3)}$** 25°-75°C and **DTS-2b$_{(pH\ 3)}$** at temperatures between 25° and 75°C calcite is the only mineral phase that precipitates. For the formation of $CaCO_3$ four environmental criteria are most important in aqueous solution: pressure, temperature, pH and CO_2 partial pressure ($p(CO_2)$). Low pH values and increasing $p(CO_2)$ support the dissolution of $CaCO_3$, whereas high pH values and low $p(CO_2)$ support precipitation as described by the following reactions (Stumm and Morgan, 1996; Appelo and Postma, 1996; Schulz and Zabel, 2006):

$$Ca^{2+} + CO_3^{2-} \leftrightarrow CaCO_3 \quad (50)$$

$$Ca^{2+} + 2(HCO_3)^- \leftrightarrow CaCO_3 + CO_2 \uparrow + H_2O \quad (51)$$

$$Ca^{2+} + HCO_3^- + OH^- \leftrightarrow CaCO_3 + H_2O \quad (52)$$

Equation (50) is valid for pH > 8, equation (51) describes $CaCO_3$ formation at pH < 8, and the reaction (52) shows $CaCO_3$ formation at pH ~ 7.5.

Comparisons with the modeling results show that in the case of calcite precipitation particularly reaction (50) and (52) may apply since the calculated pH range of the relevant samples largely match with the environmental criteria.

However, it should be noted that carbonate minerals contains transition metals and noncarbonated anions in their crystal lattice, which could have a major impact on the subsequent water evolution even though calcite makes only up a small amount of the total mineralogy of the solution system, especially those samples that show exclusively calcite precipitation.

Al:

The measurment results of the **Tissint$_{(pH\ 3)}$-**, **1-komatiite$_{(pH\ 3)}$-** and **S-komatiite$_{(pH\ 3)}$-** solutions show that they don not contain Al^{3+}. With few exceptions, the hydroxide gibbsite precipitates always associated with the mineral phase alunite. Frequently, alunite occurs also in addition to jarosite and deposits similar to jarosite under low pH and high Eh environments (Long et al., 1992, Nordstrom, 1982, Dill, 2001). Alunite and gibbsite are common minerals (Scheffel and Schachtschabel, 2010), often associated with acid mine drainage environments, but they are also well known in metamorphic, igneous and in sedimentary rocks as APS minerals (alunite supergroup; Dill, 2001) which are part of the "alunite-jarosite family" (Dill, 2001).

The modeling result of the sample solution **plagioclase$_{(pH3)}$** shows gibbsite precipitation already at 25°C. Modeling results of the sample solution **BIR-1a$_{(pH\ 3)}$** show alunite and gibbsite deposition together at all temperatures. In all other samples where gibbsite and alunite occur, these minerals are supersaturated at least at temperatures above 75°C. The measured and calculated pH values of the samples where gibbsite and alunite occur at 25°C do not differ significantly from those of the other samples where these mineral phases deposit above 75°C. Hence, the high concentration of Al^{3+} in the solution must be responsible for alunite and gibbsite deposition even at low temperatures because gibbsite and especially alunite precipitation is temperature dependent. Alunite also usually forms in hydrothermal environments (Halbach, 2001).

As mentioned by Long et al. (1992), the formation conditions of alunite and jarosite are similar because they belong to the same mineral class according to the general formula:

$$AB_3(XO_4)_2(OH)_6$$

where *AB* is a combination of two corresponding cations (such as e.g. K^+, Na^+ and Ca^+ for *A* and Al^{3+} or Fe^{3+} for *B*). The term XO_4^{n-} can be substituted by an anion (e.g. SO_4^{2-}) (Long et al., 1992). Thus, the classification into the so called alunite or jarosite supergroup (Scott, 1987; Long et al., 1992; Dutrizac & Jambor, 2000) is dependent on the dominant, large cation. Long et al. (1992) and Nordstrom (1982) investigated alunite and jarosite precipitation associated with hypersaline, evaporitic environments at pH <5.5. However, Hemley et al. (1980) indicate that alunite is stable down to pH 3.

Gibbsite forms due to hydrolysis by weathering of Al-rich aluminosilicates and pyrite. The presence of SiO_2 in the solution would result in the re-formation of Al-rich clay minerals and would prevent gibbsite formation. However, the measurement results of the initial solutions showed no dissolved SiO_2. This is also reflected in the increased Al-values of both plagioclase solutions (see chapter 5).

Gibbsite and hematite can occur together, depending on the concentrations of Al^{3+} and Fe^{3+}, as they both belong to the Fe_2O_3-Al_2O_3-H_2O system. Thereby, Fe^{3+} will be partly replaced by the smaller Al^{3+} which leads to the formation of gibbsite and hematite as shown by the **plagioclase$_{(pH\ 1.3)}$** modeling results above 25°C and between 100° to 200°C.

The numerical evaporation of the **BIR-1a$_{(pH\ 1.3)}$** sample solution also results in the formation of the mineral $Al_2(SO_4)_2 \cdot H_2O$:

$$2Al(OH)_3 + 3H_2SO_4^2 \rightarrow Al_2(SO_4)_3 + 6H_2O \qquad (53)$$

This mineral phase is supersaturated in the Al_2O_3-SO_3-H_2O system, if, according reaction 53 the ratio of $Al(OH)_3$ and H_2SO_4 is 2:3. Sulfuric acid must be present in a sufficient quantity and is therefore the limiting reactant.

Na:

While large amounts of dissolved potassium cations are consumed for the formation of K-jarosite, Na is numerically removed from the solution. Na-jarosite (natrojarosite) only can be found in the **volcanic glass$_{(pH\ 1.3)}$** sample as a result of the calculation at 25 °C. This suggests that K-jarosite preferably forms in the K-Na-Fe-S-H2O system.

All other samples that have significant Na contents between 90 to 328.4 µmol l^{-1} in the pH 1.3 solutions and 108 to 378 µmol l^{-1} in the pH 3 solutions form as a result of numerical evapo-concentration, preferably the sodium sulfates mirabilite and thenardite. As a result of the numerical calculations thenardite occurs in the samples **cpx$_{(pH\ 3)}$**, **1-komatiite$_{(pH\ 3)}$**, **volcanic glass$_{(pH\ 1.3)}$** and **volcanic glass$_{(pH\ 3)}$** between 75 °C and 200 °C. At temperatures around 25 °C the polyhydrated form mirabilite formed instead of anhydrous thenardite in both sample **cpx$_{(pH\ 1.3)}$** and **cpx$_{(pH\ 3)}$**, **volcanic glass$_{(pH\ 1.3)}$** and **volcanic glass$_{(pH\ 3)}$**, **1-komatiite$_{(pH\ 3)}$** and **plagioclase$_{(pH\ 1.3)}$**. Supported by the investigations of Spencer et al. (1985) and Stoiber and Rose (1974) it is most likely that thenardite and mirabilite crystallization is temperature dependent. According to Spencer et al. (1985) the 10-hydrate mineral mirabilite is the stable phase up to 20°C. Møller (1988) noted that according to her calculations $Na_2SO_4 \cdot 10\ H_2O$ becomes less stable at temperatures above 32°C and that

thenardite reaches highest solubility at 50°C. Nevertheless, Sonnenfeld (1984) noted that thenardite and mirabilite can co-exist in nature.

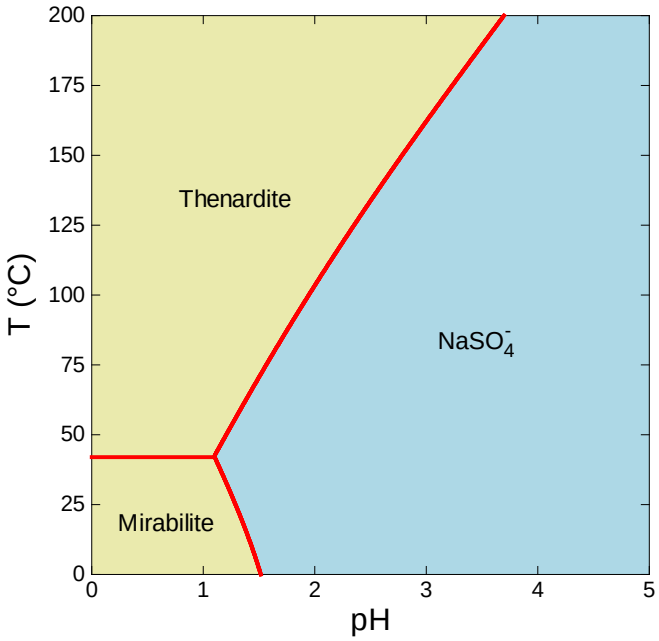

Figure 43: Solubility diagram for $\mathbf{NaSO_4^-}$- species in a $\mathbf{H_2SO_4}$-solution as a function of temperature and pH. The solid $\mathbf{NaSO_4^-}$-phase mirabilite is stable below 41°C and under acidic conditions. Increasing temperatures and increasing pH generate a large stability field of thenardite.

The calculations and observations on mirabilite and thenardite solubility in solution by Møller (1988) were performed in the presence of Cl^- containing brines. Thenardite solubility and the transition to the stable phase mirabilite in the presence of H_2SO_4 based on simple calculations with the "thermodat" database are given in Figure 43.

According to these simplified calculations the transition from thenardite to mirabilite is at around 41°C under strongly acidic conditions. According to Fulda (1928) thenardite is exclusively stable at temperatures above 13.5°C, and is often a product of mirabilite dehydration (Sonnenfeld, 1984). In nature, mirabilite often precipitates during cold winter periods (Spencer et al., 1985; Møller, 1988).

K:

The numerical calculations of the solution samples **xenolith$_{(pH\ 1.3)}$**, **s-komatiite$_{(pH1.3)}$** and **cpx$_{(pH1.3)}$** at 25°C, results in the formation of K-hydrogen sulfate mercallite and in the case of the **xenolith$_{(pH\ 1.3)}$** sample additionally to mercallite to the deposition of the potassium sulfate misenite. But the formation of primary potassium containing sulfates is limited. The absence of sufficient chloride anions in the solution inhibited the deposition of the well known evaporite minerals carnallite ($KMgCl_3 \cdot 6H_2O$) and sylvite (KCl) (Scheffer and Schachtschabel, 2010). The measurement results, however, show that the fluid sample **xenolith$_{(pH\ 1.3)}$** do not contain Al^{3+}, and only a relatively small amount of Fe. Hence, potassium cannot be removed early by the formation of K-jarosite from the solution.

Under these geochemical conditions, particularly with a SO_4^{2-} content of 3.57 mmol l^{-1} in the solution, the formation of misenite and mercallite are favored at 25°C. The formation of misenite and mercallite under these conditions on Earth is rare. Especially mercallite is a common mineral component in fumaroles and stalactites at Vesuvius at temperatures <650°C (Obenholzner et al., 2003). But potassium containing evaporites belong to the minerals of the final stages of evaporation that are rarely reached by episodic flooding. Additionally, K^+ is usually removed early in the evolution of hypersaline fluids due to e.g. jarosite formation.

As mentioned by Christov and Møller (2004) the data set for the ternary K_2SO_4 – H_2SO_4 – H_2O system is lean. They tested the solid-liquid equilibration in this system, with respect to the solubility of mercallite and misenite at 25°C. Their work shows, in principle, a good agreement with the model results within this study. Both minerals misenite and mercallite are two of the stable phases in the K_2SO_4 – H_2SO_4 – H_2O system at 25°C.

6.2 Volume calculations of Juventae Chasma, the mounds A to D, and water contents

This section describes the volume of Juventae Chasma and mound A to D (measured with Esri ArcGIS) in order to reconstruct the amount of water needed to form the mounds in Juventae Chasma in its composition as modeled (see chapter 5).
With a measured volume of 25.15 km^3, mound A is the smallest mound in Juventae Chasma. Mound B is 213.28 km^3 in size. Mound C is the largest mound with a size of 1028.23 km^3. Finally, mound D only reaches 104.01 km^3 in size. The net volume of the Juventae basin is up to 55,349 km^3. The following results of the water quantity were calculated from the total amount of the precipitated evaporites out of one liter water, extrapolated to the volume of each mound (see appendix 6). Porosities were not considered in the simple calculations because the values are most likely within the error, which is not determinable anyway. Possible erosion was also not considered. Tables 15-17 show the calculated amount of water based on the modeling results the volume calculations for mound A, B, C, D, and the Juventae basin from 25 to 200°C.

With 2.296 $cm^3\ l^{-1}$, the sample **DTS-2b$_{(pH\ 1.3)}$** shows modeled evaporite precipitation at 25 ° C, the highest deposition amount of all samples (see appendix 6, p. 184). In general, the results, summarized and presented in table 6 to 7, show that the pH 1.3 sulfuric acid has a higher ion uptake than the pH 3 sulfuric acid, as expected. Major exceptions are both **opx$_{(pH\ 1.3)}$** and **opx$_{(pH\ 3)}$** samples and **1-komatiite$_{(pH\ 1.3)}$** and **1-komatiite$_{(pH\ 3)}$**, evaporated at 75°C and 100°-200°C. The numerical evaporation of the **opx$_{(pH\ 3)}$** sample shows that the amount of deposition at 75°C and 100°-200°C is higher than that of the **opx$_{(pH\ 1.3)}$** calculations at 75°C and 100-200°C. This observation is also true for the **1-komatiite$_{(pH\ 1.3)}$** and **1-komatiite$_{(pH\ 3)}$** calculation results between 100-200°C.
Furthermore, the calculations reveal that the evaporation at 25°C tend to need less water to form the mounds than evaporation at 75°C and 100-200°C. Hence, the higher the temperature the more water is needed to generate the volume of mound A-D by evaporation. Almost the entire sample results show that the samples that were treated with sulfuric acid at pH 1.3 generate less water than those that were treated with sulfuric acid at pH 3. Each precipitated mineral phase suggests that the incorporation of water into the crystal lattice is the key mechanism, with temperature and pH as the limiting factors.

Under the assumption that the mounds consist of 100% evaporites, the calculated total water amount of the **1-komatiite$_{(pH\ 1.3)}$**, **s-komatiite$_{(pH\ 1.3)}$**, **xenolith$_{(pH\ 1.3)}$** and **DTS-2b$_{(pH\ 1.3)}$** at 25°C

would not be enough to fill the Juventae basin and subsequently form Maja Valles. Assuming that the ILD's consist of 50 % conglomerates or background sedimentation, the calculated water amount also has to be reduced, in this example, by half.

Table 15: Calculated water amount at 25°C

Sample	Mound A (km^3)	Mound B (km^3)	Mound C (km^3)	Mound D (km^3)	Total water amount (km^3)
Tissint pH 1.3	$2.11 \cdot 10^5$	$1.79 \cdot 10^6$	$8.61 \cdot 10^6$	$8.71 \cdot 10^5$	$1.15 \cdot 10^7$
Tissint pH 3	$1.40 \cdot 10^5$	$1.18 \cdot 10^7$	$5.71 \cdot 10^7$	$5.77 \cdot 10^6$	$7.48 \cdot 10^7$
Olivine pH 1.3	$4.15 \cdot 10^5$	$3.52 \cdot 10^6$	$1.70 \cdot 10^7$	$1.72 \cdot 10^6$	$2.27 \cdot 10^7$
Olivine pH 3	$1.11 \cdot 10^7$	$9.41 \cdot 10^7$	$4.54 \cdot 10^8$	$4.59 \cdot 10^7$	$6.05 \cdot 10^8$
Clinopyroxene pH 1.3	$4.57 \cdot 10^4$	$3.88 \cdot 10^5$	$1.87 \cdot 10^6$	$1.89 \cdot 10^5$	$2.49 \cdot 10^6$
Clinopyroxene pH 3	$5.05 \cdot 10^5$	$4.28 \cdot 10^6$	$2.06 \cdot 10^7$	$2.09 \cdot 10^6$	$2.75 \cdot 10^7$
Orthopyroxene pH 1.3	$5.11 \cdot 10^4$	$4.33 \cdot 10^5$	$2.09 \cdot 10^6$	$2.11 \cdot 10^5$	$2.79 \cdot 10^6$
Orthopyroxene pH 3	$3.76 \cdot 10^5$	$3.19 \cdot 10^6$	$1.54 \cdot 10^7$	$1.56 \cdot 10^6$	$2.05 \cdot 10^7$
Plagioclase pH 1.3	$2.33 \cdot 10^5$	$1.98 \cdot 10^6$	$9.54 \cdot 10^6$	$9.65 \cdot 10^5$	$1.27 \cdot 10^7$
Plagioclase pH 3	$1.16 \cdot 10^6$	$9.86 \cdot 10^6$	$4.75 \cdot 10^7$	$4.81 \cdot 10^6$	$6.33 \cdot 10^7$
1-komatiite pH 1.3	$1.86 \cdot 10^1$	$1.58 \cdot 10^2$	$7.59 \cdot 10^2$	$7.68 \cdot 10^1$	$1.01 \cdot 10^3$
1-komatiite pH 3	$1.34 \cdot 10^5$	$1.14 \cdot 10^6$	$5.49 \cdot 10^6$	$5.56 \cdot 10^5$	$7.32 \cdot 10^6$
S-komatiite pH 1.3	$2.01 \cdot 10^1$	$1.71 \cdot 10^2$	$8.23 \cdot 10^2$	$8.32 \cdot 10^1$	$1.10 \cdot 10^3$
S-komatiite pH 3	$9.55 \cdot 10^4$	$8.10 \cdot 10^5$	$3.91 \cdot 10^6$	$3.95 \cdot 10^5$	$5.21 \cdot 10^6$
Volcanic glass pH 1.3	$1.76 \cdot 10^1$	$1.49 \cdot 10^2$	$7.21 \cdot 10^2$	$7.29 \cdot 10^1$	$9.61 \cdot 10^2$
Volcanic glass pH 3	$9.17 \cdot 10^5$	$7.78 \cdot 10^6$	$3.75 \cdot 10^7$	$3.79 \cdot 10^6$	$5.00 \cdot 10^7$
Xenolith pH 1.3	$1.19 \cdot 10^1$	$1.01 \cdot 10^2$	$4.85 \cdot 10^2$	$4.91 \cdot 10^1$	$6.47 \cdot 10^2$
Xenolith pH 3	$9.75 \cdot 10^4$	$8.27 \cdot 10^5$	$3.99 \cdot 10^6$	$4.03 \cdot 10^5$	$5.32 \cdot 10^6$
DTS-2b pH 1.3	$1.10 \cdot 10^1$	$9.29 \cdot 10^1$	$4.48 \cdot 10^2$	$4.53 \cdot 10^1$	$5.97 \cdot 10^2$
DTS-2b pH 3	$5.18 \cdot 10^7$	$4.39 \cdot 10^8$	$2.12 \cdot 10^9$	$2.14 \cdot 10^8$	$2.82 \cdot 10^9$
Bir-1a pH 1.3	$2.96 \cdot 10^5$	$2.51 \cdot 10^6$	$1.2 \cdot 10^7$	$1.22 \cdot 10^6$	$1.60 \cdot 10^7$
Bir-1a pH 3	$1.18 \cdot 10^6$	$1.00 \cdot 10^7$	$4.83 \cdot 10^7$	$4.88 \cdot 10^6$	$6.44 \cdot 10^7$

Table 16: Calculated water amount at 75°C

Sample	Mound A (km^3)	Mound B (km^3)	Mound C (km^3)	Mound D (km^3)	Total water amount (km^3)
Tissint pH 1.3	$2.65 \cdot 10^5$	$2.25 \cdot 10^6$	$1.08 \cdot 10^7$	$1.10 \cdot 10^6$	$1.44 \cdot 10^7$
Tissint pH 3	$1.84 \cdot 10^6$	$1.56 \cdot 10^7$	$7.53 \cdot 10^7$	$7.62 \cdot 10^6$	$1.00 \cdot 10^8$
Olivine pH 1.3	$4.72 \cdot 10^4$	$4.00 \cdot 10^5$	$1.93 \cdot 10^6$	$1.95 \cdot 10^5$	$2.57 \cdot 10^6$
Olivine pH 3	$1.07 \cdot 10^7$	$9.04 \cdot 10^7$	$4.54 \cdot 10^8$	$4.41 \cdot 10^7$	$5.99 \cdot 10^8$
Clinopyroxene pH 1.3	$6.32 \cdot 10^5$	$5.36 \cdot 10^6$	$2.58 \cdot 10^7$	$2.61 \cdot 10^6$	$3.44 \cdot 10^7$
Clinopyroxene pH 3	$2.68 \cdot 10^6$	$2.27 \cdot 10^7$	$1.09 \cdot 10^8$	$1.11 \cdot 10^7$	$1.45 \cdot 10^8$
Orthopyroxene pH 1.3	$1.49 \cdot 10^7$	$1.26 \cdot 10^8$	$6.08 \cdot 10^8$	$6.15 \cdot 10^7$	$8.10 \cdot 10^8$
Orthopyroxene pH 3	$1.07 \cdot 10^7$	$9.04 \cdot 10^7$	$4.36 \cdot 10^8$	$4.41 \cdot 10^7$	$5.81 \cdot 10^8$
Plagioclase pH 1.3	$3.60 \cdot 10^5$	$3.06 \cdot 10^6$	$1.47 \cdot 10^6$	$1.49 \cdot 10^6$	$6.38 \cdot 10^6$
Plagioclase pH 3	$1.25 \cdot 10^6$	$1.06 \cdot 10^7$	$5.09 \cdot 10^7$	$5.15 \cdot 10^6$	$6.79 \cdot 10^7$
1-komatiite pH 1.3	$2.12 \cdot 10^5$	$1.80 \cdot 10^6$	$8.68 \cdot 10^6$	$8.78 \cdot 10^5$	$1.16 \cdot 10^7$
1-komatiite pH 3	$8.54 \cdot 10^6$	$7.24 \cdot 10^7$	$3.49 \cdot 10^8$	$3.53 \cdot 10^7$	$4.65 \cdot 10^8$
S-komatiite pH 1.3	$1.56 \cdot 10^5$	$1.32 \cdot 10^6$	$6.38 \cdot 10^6$	$6.46 \cdot 10^5$	$8.50 \cdot 10^6$
S-komatiite pH 3	$1.81 \cdot 10^6$	$1.54 \cdot 10^7$	$7.40 \cdot 10^7$	$7.49 \cdot 10^6$	$9.87 \cdot 10^7$
Volcanic glass pH 1.3	$7.48 \cdot 10^4$	$6.34 \cdot 10^5$	$3.06 \cdot 10^6$	$3.09 \cdot 10^5$	$4.08 \cdot 10^6$
Volcanic glass pH 3	$2.39 \cdot 10^6$	$2.03 \cdot 10^7$	$9.78 \cdot 10^7$	$9.90 \cdot 10^6$	$1.30 \cdot 10^8$
Xenolith pH 1.3	$5.27 \cdot 10^4$	$4.47 \cdot 10^5$	$2.15 \cdot 10^6$	$2.18 \cdot 10^5$	$2.87 \cdot 10^6$
Xenolith pH 3	$1.53 \cdot 10^6$	$1.30 \cdot 10^7$	$6.25 \cdot 10^7$	$6.32 \cdot 10^6$	$8.34 \cdot 10^7$
DTS-2b pH 1.3	$4.86 \cdot 10^4$	$4.12 \cdot 10^5$	$1.99 \cdot 10^6$	$2.01 \cdot 10^5$	$2.65 \cdot 10^6$
DTS-2b pH 3	$5.01 \cdot 10^7$	$4.25 \cdot 10^8$	$2.05 \cdot 10^9$	$2.07 \cdot 10^8$	$2.73 \cdot 10^9$
Bir-1a pH 1.3	$4.23 \cdot 10^5$	$3.59 \cdot 10^6$	$1.73 \cdot 10^7$	$1.75 \cdot 10^6$	$2.31 \cdot 10^7$
Bir-1a pH 3	$1.17 \cdot 10^6$	$9.90 \cdot 10^6$	$4.77 \cdot 10^7$	$4.83 \cdot 10^6$	$6.36 \cdot 10^7$

Table 17: Calculated water amount at 100° to 200°C

Sample	Mound A (km^3)	Mound B (km^3)	Mound C (km^3)	Mound D (km^3)	Total water amount (km^3)
Tissint pH 1.3	$1.83 \cdot 10^5$	$1.55 \cdot 10^6$	$7.49 \cdot 10^6$	$7.58 \cdot 10^5$	$9.98 \cdot 10^6$
Tissint pH 3	$1.05 \cdot 10^6$	$8.89 \cdot 10^6$	$4.28 \cdot 10^7$	$4.33 \cdot 10^6$	$5.71 \cdot 10^7$
Olivine pH 1.3	$1.16 \cdot 10^5$	$9.81 \cdot 10^5$	$4.73 \cdot 10^6$	$4.78 \cdot 10^5$	$6.31 \cdot 10^6$
Olivine pH 3	$1.26 \cdot 10^6$	$1.07 \cdot 10^7$	$5.17 \cdot 10^7$	$5.23 \cdot 10^6$	$6.89 \cdot 10^7$
Clinopyroxene pH 1.3	$6.02 \cdot 10^5$	$5.10 \cdot 10^6$	$2.46 \cdot 10^7$	$2.49 \cdot 10^6$	$3.28 \cdot 10^7$
Clinopyroxene pH 3	$1.09 \cdot 10^6$	$9.28 \cdot 10^6$	$4.47 \cdot 10^7$	$4.52 \cdot 10^6$	$5.96 \cdot 10^7$
Orthopyroxene pH 1.3	$1.86 \cdot 10^7$	$1.58 \cdot 10^8$	$7.62 \cdot 10^8$	$7.70 \cdot 10^7$	$1.02 \cdot 10^9$
Orthopyroxene pH 3	$9.45 \cdot 10^5$	$8.02 \cdot 10^6$	$3.86 \cdot 10^7$	$3.91 \cdot 10^6$	$5.15 \cdot 10^7$
Plagioclase pH 1.3	$2.27 \cdot 10^5$	$1.93 \cdot 10^6$	$9.30 \cdot 10^6$	$9.40 \cdot 10^5$	$1.24 \cdot 10^7$
Plagioclase pH 3	$9.82 \cdot 10^5$	$8.33 \cdot 10^6$	$4.01 \cdot 10^7$	$4.06 \cdot 10^6$	$5.35 \cdot 10^7$
1-komatiite pH 1.3	$1.05 \cdot 10^6$	$8.89 \cdot 10^6$	$4.29 \cdot 10^7$	$4.34 \cdot 10^6$	$5.72 \cdot 10^7$
1-komatiite pH 3	$7.88 \cdot 10^5$	$6.68 \cdot 10^6$	$3.22 \cdot 10^7$	$3.26 \cdot 10^6$	$4.29 \cdot 10^7$
S-komatiite pH 1.3	$4.56 \cdot 10^5$	$3.87 \cdot 10^6$	$1.87 \cdot 10^7$	$1.89 \cdot 10^6$	$2.49 \cdot 10^7$
S-komatiite pH 3	$7.19 \cdot 10^5$	$6.10 \cdot 10^6$	$2.94 \cdot 10^7$	$2.97 \cdot 10^6$	$3.92 \cdot 10^7$
Volcanic glass pH 1.3	$1.68 \cdot 10^5$	$1.43 \cdot 10^6$	$6.89 \cdot 10^6$	$6.97 \cdot 10^5$	$9.19 \cdot 10^6$
Volcanic glass pH 3	$9.27 \cdot 10^5$	$7.86 \cdot 10^6$	$3.79 \cdot 10^7$	$3.83 \cdot 10^6$	$5.05 \cdot 10^7$
Xenolith pH 1.3	$1.22 \cdot 10^5$	$1.03 \cdot 10^6$	$4.97 \cdot 10^6$	$5.03 \cdot 10^5$	$6.63 \cdot 10^6$
Xenolith pH 3	$7.35 \cdot 10^5$	$6.23 \cdot 10^6$	$3.00 \cdot 10^7$	$3.04 \cdot 10^6$	$4.00 \cdot 10^7$
DTS-2b pH 1.3	$1.26 \cdot 10^5$	$1.07 \cdot 10^6$	$5.15 \cdot 10^6$	$5.21 \cdot 10^5$	$6.87 \cdot 10^6$
DTS-2b pH 3	$7.02 \cdot 10^5$	$5.95 \cdot 10^6$	$2.87 \cdot 10^7$	$2.90 \cdot 10^6$	$3.83 \cdot 10^7$
Bir-1a pH 1.3	$2.99 \cdot 10^5$	$2.54 \cdot 10^6$	$1.22 \cdot 10^7$	$1.24 \cdot 10^6$	$1.63 \cdot 10^7$
Bir-1a pH 3	$9.47 \cdot 10^5$	$8.03 \cdot 10^6$	$3.87 \cdot 10^7$	$3.92 \cdot 10^6$	$5.16 \cdot 10^7$

As mentioned in section 1.2.2) investigations conducted by De Hon and Pani (1993), Chapman et al. (2003) and Gross et al. (2009) exhibit several episodic flood events in Juventae Chasma and Maja Valles.

For this reason, a more detailed morphological investigation of mound B was carried out and was already presented as preliminary results by Al-Samir et al. (2012). It has to be noted that the question, if the so called “stairstep”-morphology shows sediment layers or strata formed by episodic evaporation processes, cannot be answered based on current image data. It is also possible that the unique morphology shows terraces formed by multiple water lines. Erosional terraces formed by subsequent water ingressions would have change the chemism of the mineral deposits and would have led to undefined lithostratigraphies. Nevertheless, for all of the processes mentioned above, episodic flooding is a premise.

Thickness determination of the terraces was conducted by using an HRSC digital elevation model (DEM) with a grid size of 50 m coupled with the corresponding HRSC image data (Al-Samir et al., 2012). Dip and dip-direction measurements for each individual terrace were conducted, in order to minimize possible appearances of thickness errors, which can occur by simple height measurements between individual terrace boundaries (Al-Samir et al., 2012). These calculations were performed with the LayerTools extention for ESRI's ArcGIS described in detail by Kneissl et al. (2010). The software is based on the concept to combine measurement points of xy- and z-coordinates (elevation values) determined from an underlain digital terrain model (DTM). According to Kneissl et al. (2010), the LayerTools software generates an interpolated plane by performing a one-degree polynomial fit to receive strike and dip values of e.g. geological layers. Subsequent individual layer thickness measurements in strike direction were conducted to minimize elevation distortions due to dipping of layers (Figure 44; Al-Samir et al., 2012).

The measurement results of the layer thicknesses do not show distinct horizontal tendencies (Table 18). A steady increase or decrease of the layer heights between the bottom layer and the uppermost layer cannot be determined. Comparisons of the layer thicknesses between the western and eastern flank of mound B show that the layers at the eastern flank are thicker, almost by half.

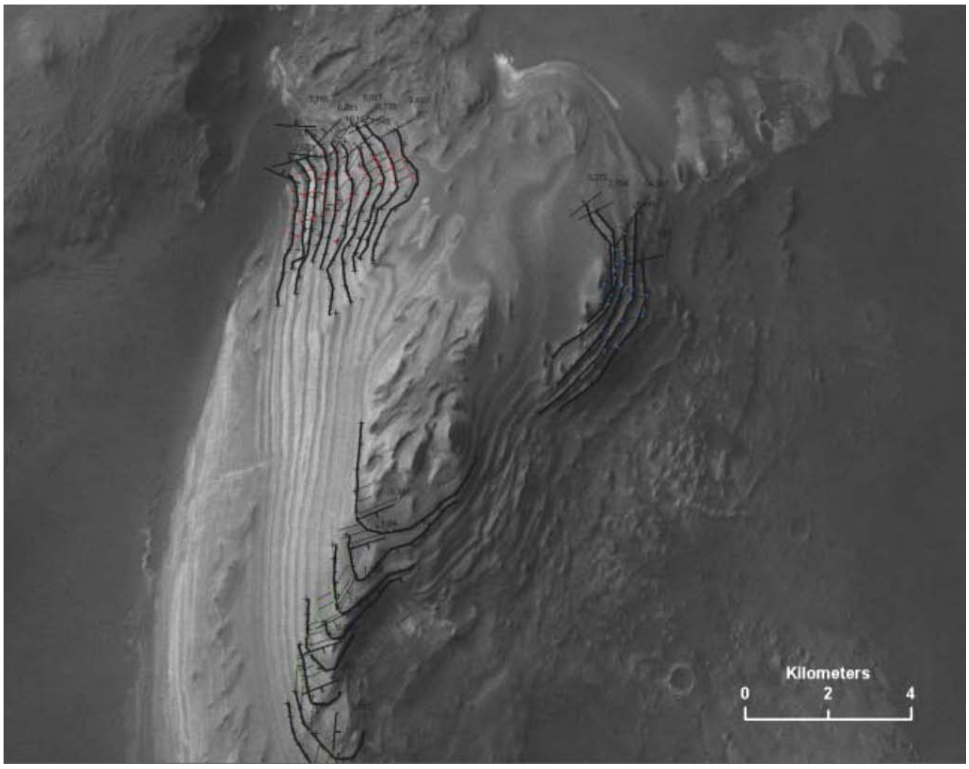

Figure 44: Measurment points of strike and dip carried out by using the LayerTools extensionin ArcGis (Al-Samir et al., 2012).

Determination of dip and dip-direction revealed dipping of average 2° in southern direction. Hence, circular strike and dip do not occur, which could have been an important evidence for a spring deposit origin of mound B, and therefore of all ILD's in Juventae Chasma.

Table 18: List of the measurement points of the thickness determinations at mound B (Al-Samir et al., 2012).

South			West			East		
Layer Point ID	Thickness individual measurements [m]	Mean thickness of layers [m]	Layer Point ID	Thickness individual measurements [m]	Mean thickness of layers [m]	Layer Point ID	Thickness individual measurements [m]	Mean thickness of layers [m]
1a	96.80		1a	65.48		1a	161.64	
1b	92.50		1b	48.62		1b	164.60	
1c	115.10	101.47	1c	58.95	57.68	1c	115.10	147.11
2a	75.52		2a	53.51		2a	109.30	
2b	141.92		2b	59.27		2b	89.69	
2c	118.98	112.14	2c	66.08	59.62	2c	131.49	110.16
3a	77.28		3a	61.03		3a	135.26	
3b	65.96		3b	68.31		3b	95.92	
3c	79.69	74.31	3c	55.16	61.50	3c	94.04	108.41
4a	111.40		4a	81.93		4a	115.66	
4b	127.07		4b	72.74		4b	122.34	
4c	131.08	123.18	4c	114.47	89.71	4c	85.19	107.73
5a	86.05		5a	102.42				
5b	115.10		5b	117.54				
5c	150.42	117.19	5c	116.08	112.01			
6a	144.27		6a	91.09				
6b	162.66		6b	104.18				
6c	199.82	168.92	6c	119.56	104.94			
7a	140.55		7a	89.91				
7b	118.91		7b	107.06				
7c	83.62	114.36	7c	129.09	108.69			
8a	131.22		8a	76.20				
8b	150.45		8b	90.78				
8c	134.18	138.62	8c	100.92	89.30			
9a	88.68		9a	82.18				
9b	80.74		9b	82.58				
9c	100.28	89.90	9c	75.17	79.98			

6.3 Brittle fractures at mound B

In context of this study, brittle lineaments were found at 62.1° W/4.2° S located just off the eastern flank of mound B (Figure 45). Assuming, that the formation of these structures is associated to the formation of Valles Marineris, then the features, seen on the CTX image, can be interpreted as brittle fractures.

The identifiable major NW-SE-trending fractures (see rose diagram Figure 46) follow the main orientation of the Valles Marineris graben system. Tentatively, the fracture pattern may thus belong to the same extensional fracture zone of the Valles Marineris trough-system.

Fractures are preferably filled with minerals due to perculating fluids. Depending on the fluid temperature, composition and pressure the resulting veins may consist of different mineral assemblages, eg. calcite, quartz or chlorite.

According to the CTX image (Figure 45) the high albedo units east of mound B may be caused by mineral precipitation out of migrating thermal fluids.

The presence of these veins could indicate a possible major pathway in which thermal water migrated within the chasma floor and entered into the Juventae basin. The individual fracture appear to be filled with rock material of similar mineralogical composition as mound B, however a confirmation of this observation depends on the availability of high-resolution images and spectra, but this area is yet not been imaged by CRISM.

Nevertheless, this could support the assumption of a hydrothermal cell below mound B and therefore a hydrothermal system as the source of ion- and metal-enriched fluids. Hence, these fractures may be the preferred major pathway for fluid flow from the subsurface to the bottom of the Juventae basin. Head and Mustard (2006) and Saper and Mustard (2013) e.g. discussed similar fracture systems in which these, however, were related to impact cratering.

The current image data base cannot confirm the assumptions presented here, open questions can only be answered in future studies.

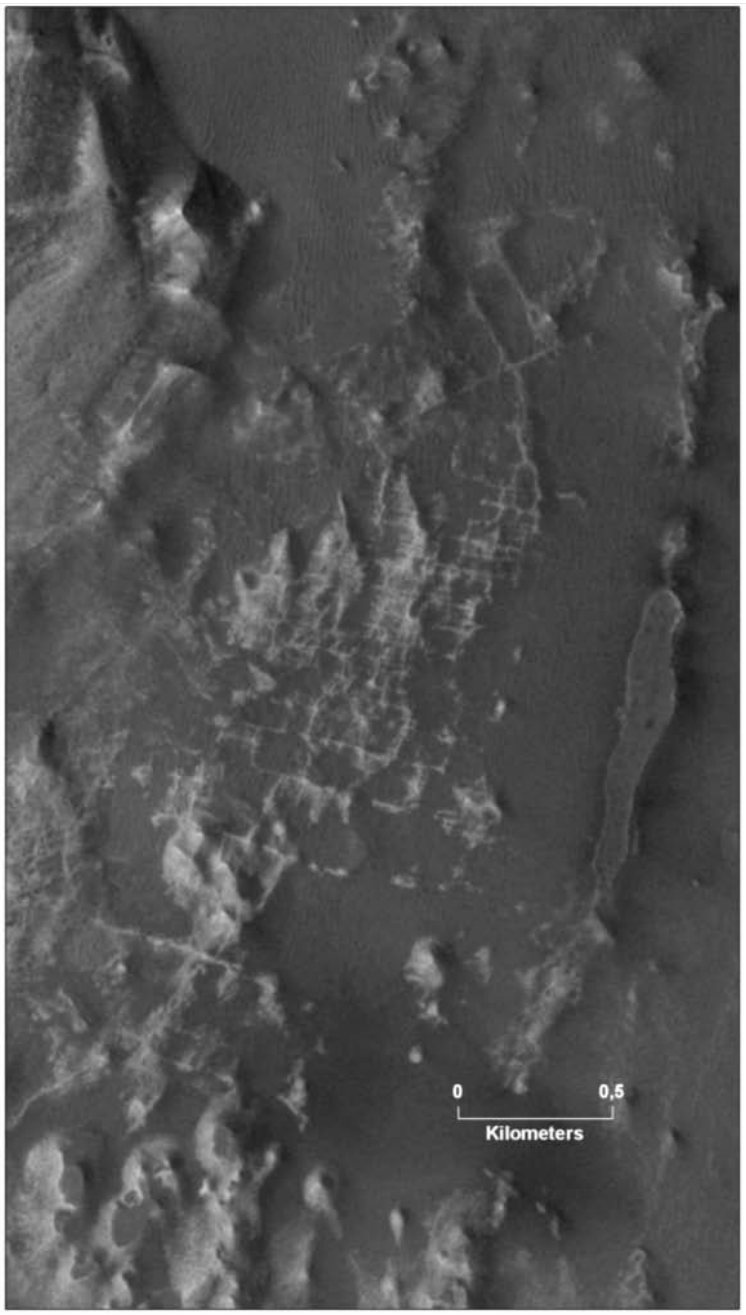

Figure 45: CTX image B10_013600 showing putative fractures at the eastern foot of mound B (north is up). These structures support the assumption of a hydrothermal cell below mound B.

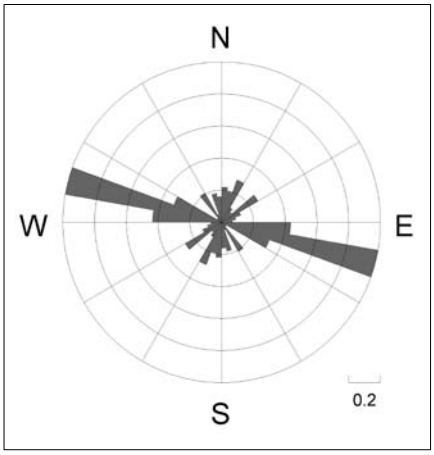

Figure 46:
Rose diagram, showing orientations of the joint system observed east of mound B. Directions have been measured in an appropriate local conformal map projection using 2 points (start and end point) of each fault, respectively. Results have been weighted linearly by length of the faults. A total of 151 fractures were measured.

6.4 Dependency of mineral formation on fluid temperature

The purpose of this study is to test the conceptual model of evaporation as much as possible under martian conditions with respect to possible martian rock types, the temperature, and pH of the sulfuric acid solution in context of the ILD formation in Juventae Chasma.

The sample selection was one of the first major decisions that had to be made. The samples should cover a broad spectrum of Mars' analog rocks and used to contain Mg, Na, K, Ca, Fe and Al - ions. Therefore, ten terrestrial samples including two basalt standards, the major rock forming minerals, ortho- and clinopyroxene, as well as olivine and plagioclase and 4 mafic to ultra mafic rocks were selected as martian rock analogs (described in section 3.1). By a fortunate coincident, short before the beginning of the experimental phase, it was possible to receive a sample from the martian meteorite Tissint, that was then added to the sample list.

As a next step, the eleven solid samples were qualitatively and quantitatively investigated by XRD and XRF to determination, primarily, major elements and major element concentrations (described in section 3.3).

One gram of each solid sample was subsequently placed into a 100 ml PET-batch cup together with 100 ml pH 1.3 H_2SO_4, a second gram of each sample was also placed into a 100 ml PET-batch cup together with 100 ml pH 3 H_2SO_4 solution. Thereafter, the batch-cups were placed in an overhead shaker for about 30 days, as described in chapter 4, to produce possible Mars analog solutions.

Afterwards, the pH parameters and the ion uptake of the resulting solutions were measured and classified (chapter 4.1 and 4.2) in order to receive the individual ion concentration.

Finally, based on the wet-chemical leaching experiments, numerical evaporation was conducted at 25°C, 75°C and between 100-200°C by using the software program GWB, described in chapter 5, and interpreted in chapter 6.

The modeling results from section 5 can now be compared with the CRISM-results and mineralogical measurements derived by the curiosity-mission to test the plausibility of the model setup.

Table 8 lists the minerals, which were formed while evaporation, table 9-14 list the precipitated minerals in context to each sample. The program REACT also provides the modeled mineral formation in unit cm^3 (Figure 47; the complete list is given in appendix 6)

which allows volume calculations of the mineral deposits and the water quantity (presented in section 6.2).

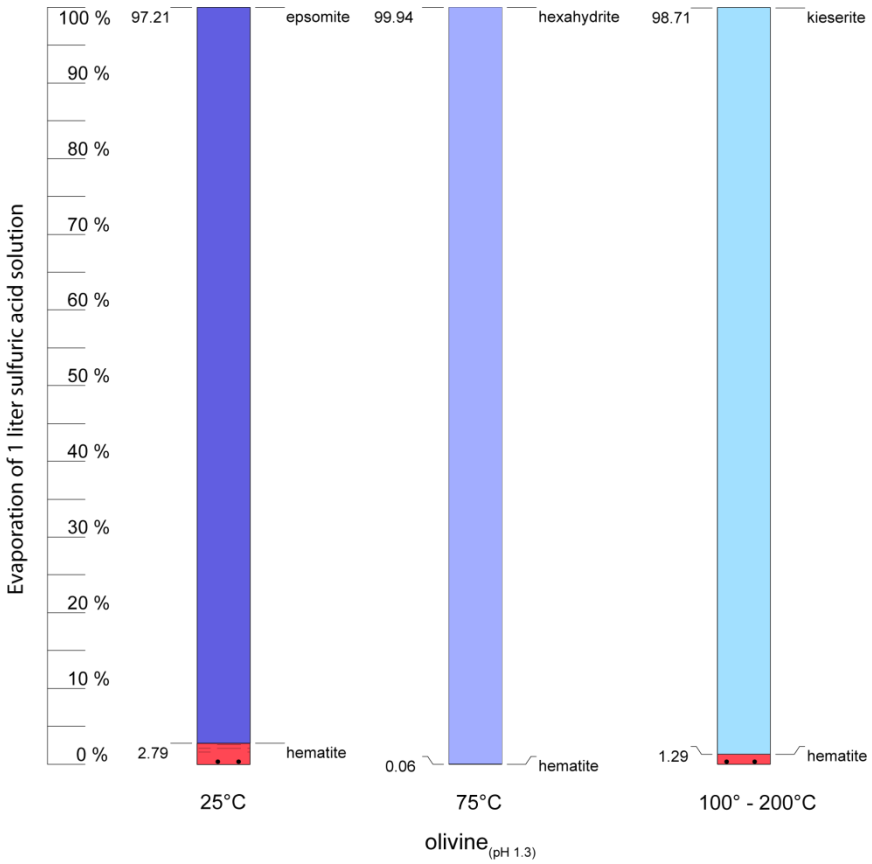

Figure 47: Results of modeled mineral precipitation out of one liter of the **olivine$_{(pH\ 1.3)}$** fluid sample at 25°C, 75°C, and 100-200°C (expressed in percentage).

The modeling results show that the **xenolith$_{(pH\ 1.3)}$**-sample moderately match with the CRISM interpretations by Bishop et al. (2009), Wendt (2012), and Noel et al. (2015). At 25°C and 75°C the PHS precipitate, such as epsomite, hexahydrite, melanterite and gypsum.
At a temperature of 75°C to 100-200°C the MHS precipitate, such as kieserite as the dominant MHS as well as szomolnokite.

Curiosity measuring results, detected at drilling sites in the Yellow Knife bay, Mars (samples John Kline and Cumberland, see chapter 1.2.2) revealed the mineral phases plagioclase, olivine, augit, and magnetite as well as ortho- and clinopyroxenes (Vaniman et al. 2014).
Not only the results of the **xenolith$_{(pH\ 1.3)}$** modeling show, that in the frame of this study temperatures up to 200°C are required to deposit the corresponding MHS and PHS mineral species.

As interpreted in section 6.1 the monohydrated Mg-sulfates preferably precipitate at temperatures beween 100-200°C, while the PHS form at 25°C and 75°C. These results point out that, compared with the CRISM data and interpretation lithostratigraphy of mound A-D the PHS and MHS possibly formed from a cooling solution.

The modeling results of the samples **olivine$_{(pH\ 3)}$**, **plagioclase$_{(pH\ 1.3)}$**, **plagioclase$_{(pH\ 3)}$** and **DTS-2b$_{(pH\ 1.3)}$** do not show any mineral phases that match with the literature data of Bishop et al. (2009), Wendt et al. (2012) and Noel et al. (2015). Hence, these results were not considered in the ILD formation model.

Of all 22 fluid samples investigated in this study, only the modeling results of **olivine$_{(pH\ 1.3)}$**, **s-komatiite$_{(pH\ 3)}$** and the **DTS-2b$_{(pH\ 1.3)}$** come close to the CRISM interpretation although szomolnokite do not precipitate. All other investigated samples show mineral depositions which do not match with the spectral data. None of the remote sensing data derived by CRISM show the presence of gypsum, anhydrite or calcite in the Juventae basin, keeping in mind that they, on the other hand, simply do not crop out.
Across all temperature ranges the pH parameters of the **DTS-2b$_{(pH\ 1.3)}$** (pH 5.81 – pH 4.9) and **s-komatiite$_{(pH\ 3)}$** (pH 6.83 – pH 6.21) are moderate. Only the **olivine$_{(pH\ 1.3)}$** sample shows strong acidic pH values of pH 4.1 down to pH 0.1. (see section 5.3.2). All three samples have in common that epsomite (PHS) forms at 25°C, hexahydrate (PHS) precipitates at 75°C, and kieserite (MHS) is oversaturated at 100-200°C. As mentioned in chapter 6, according to Braitsch (1962) kieserite generally precipitates with increasing temperatures while epsomite and hexahydrite form when the solution cools down. These results support the hypothesis that MHS and PHS precipitation might took place by down cooling waters in the Juventae basin. Figure 47 shows the results of the sample **olivine$_{(pH\ 1.3)}$** as an example for modeled mineral precipitation out of 1 liter water at 25, 75, and 100-200°C in percentage (image was created by using the software GeODin developed from Fugro Consult GmbH). At 25°C the hematite content of 2.79% is low compared to 97.21% epsomite (PHS). At 75°C, hexahydrite (PHS) precipitates with 99.94%. With 98.71%, kieserite (MHS) is the dominant mineral deposit between 100-200°C.
The results of each temperature range do not completely coincide with the observations of Bishop et al. (2009), Wendt (2012), and Noel et al. (2015).
Assuming decreasing water temperature from 200°C down to 25°C while the solution completely evaporates lithostratigraphic similarities of the precipitates compared to those in Juventae Chasma interpreted by Bishop et al. (2009), Wendt (2012), und Noel et al. (2015)

can be observed. As discussed in section 1.2.2, according to the studies of the authors mentioned above PHS on top of MHS deposits were identified. According to Noel et al. (2015), the monohydrated minerals at mound A, B and C mainly consist of kieserite (section 1.2.2) which only occur between 100-200°C in the modeling results. Bishop et al. (2009) interpreted szomolnokite as the dominant monohydrated mineral phase at mound B followed by kieserite. The discrimination of polyhydrated sulfates by spectral interpretations at the mounds in Juventae Chasma is not feasible. Noel et al. (2015) assumed the polyhydrated mineral starkeyite to be present at mound B. However, none of the modeled fluid sample results show starkeyite as part of the mineral assemblages. Bishop et al. (2009) also mentioned the presence of hematite at mound B. Similar conclusions can be drawn for the samples **s-komatiite**$_{(pH\ 3)}$ and **DTS-2b**$_{(pH\ 1.3)}$**.**

Those high fluid-temperatures occur in hydrothermal systems (>400°C) or hot springs with temperatures >200°C (Halbach et al., 2003; Nordstrom, 2009). But the following aspect does not support the origin of hot fluids in a hydrothermal environment on Mars as it can be found in oceans on Earth:

The oceanic crust is well known to be a sink of Mg due to the formation of Mg-smectite veins underneath the vent field, on-axis, and is usually not part in endmember hydrothermal vent fluids (Snow and Dick, 1995; Halbach et al. 2003; Humphris et al., 2003)(Figure 48). Thus, such high-temperature fluids do not provide Mg in a sufficient quantity to form Mg-rich sulfates on the surface. This seems to exclude hydrothermal activity as a possible origin of the initial solution evaporated in Juventae Chasma. But according to Snow & Dick (1995), Kelley et al. (2001) and Humphris et al. (2003), the estimated maximum Mg uptake to the oceans from ultramafic rocks can be equivalent up to 85% of the yearly Mg flux from rivers. Nearly 20% along slow- and ultraslow-spreading ridges are ultramafic rocks, peridotites respectively (Humphris et al., 2003). Abyssal peridotites crop out in close vicinity of ridge discontinuities, associated with walls of rift valleys, they are present in transform faults and in fracture zones as well as in corners of ridge-offset intersections (Humphris et al., 2003). These ultramafic rocks are serpentinizied and weathered in a low-temperature hydrothermal environment (Humphris et al., 2003).

Kelley et al. (2001) discovered active mounds in the Lost City vent field, off-axis, at a location nearly 15 km away from spreading centers with 40°C to 75°C venting fluids with an alkalinity of pH 9-9.8 and Mg content of 9-19 mmol kg^{-1}. Hence, relatively cold vent fluids, driven by water-ultramafic rock interactions in the lower crust along slow- to ultraslow spreading centers is possibly a source for Mg-rich solutions. However, as for strong acidic sulfate

solutions, a better definition of the low- to high-temperature serpentinizied rock-solution interaction under martian conditions is required. Furthermore, Halbach et al. (2003) and Koschinsky et al. (2014) noted that sulfate precipitation is a common process in mixing zones.

Thermal acid-sulfate waters are common in hot spring systems in areas in the western United States, e.g. in the Yellowstone National Park (Nordstrom et al., 2009) and spread all over the Earth's crust, often associated with volcanic activity. Several of these solutions with pH values of 1-5 were collected and classified by Nordstrom et al. (2009): e.g. (1) meteoric water, (2) meteoric water, heated by high-temperature gases, (3) deep hydrothermal water, (4) boiled, deep hydrothermal water that has been subsequently heated with H_2S-enriched gases, and mixtures of all of these types. But they do have in common that their Mg concentration (between <0.007 and 21.9 mg/L, Nordstrom et al. (2009)) is lower than the Mg uptake into the solution assumed and measured in this study.

The results of the water amount calculations of **olivine$_{(pH\ 1.3)}$**, **s-komatiite$_{(pH\ 3)}$** and **DTS-2b$_{(pH\ 1.3)}$** (chapter 6.2) show that already one flooding event is sufficient to completely fill the Juventae basin as well as to provide enough water to flood the northern plateau. Thus, a new and less complex hypothesis of decreasing surface water temperatures during evaporation as a geologic process for ILD formation in Juventae Chasma on planet Mars can be postulated (presented in chapter 7).

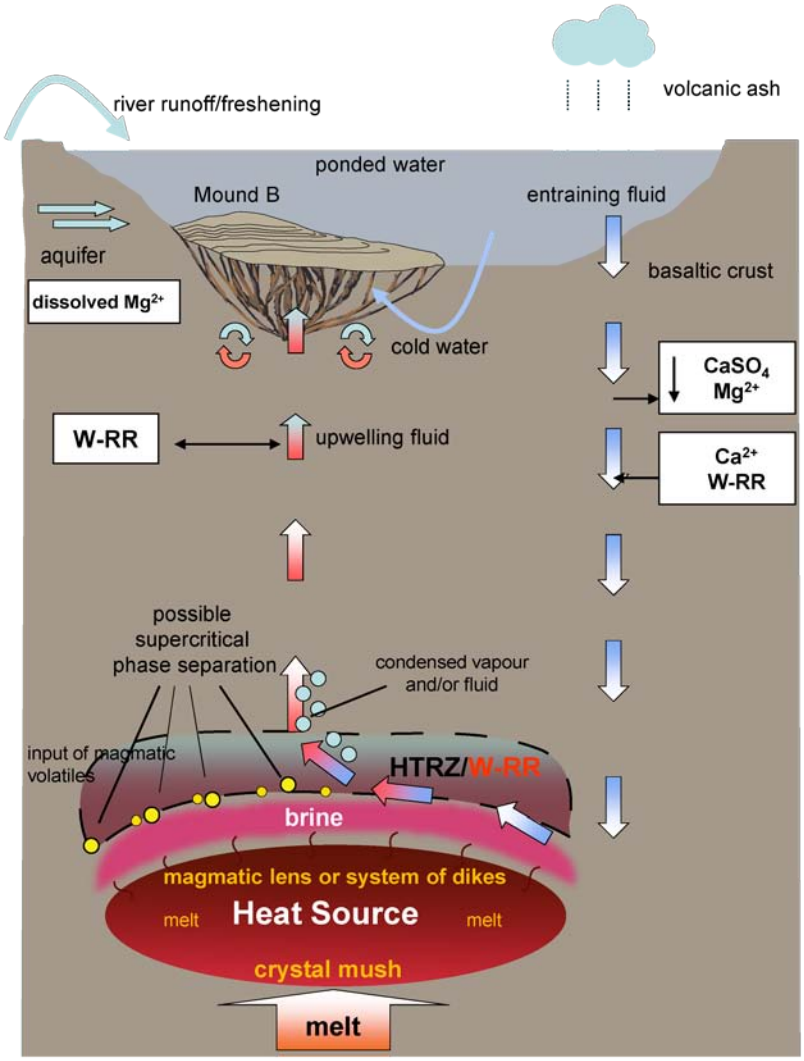

Figure 48: Simplified schematic of a hydrothermal circulation cell showing the depletion of Mg^{2+} and enrichment of Ca^{2+} in the solution caused by the precipitation of $Mg(OH)_2$ and alteration of the rock (W-RR = water-rock reactions). Hence, the altered rock in the subsurface is the major sink for Mg-species in the system. Between the heat source and the high-temperature reaction zone (HTRZ), the fluid may be enriched with degassed magmatic volatiles. Subsequently, the hot fluid will rise fast into the upwelling zone and reaches the basin floor, where it will be mixed with cold water. Thus, remarkable input of Mg^{2+} into Juventae Chasma only occur via meteoric water or groundwater inflow (image modified after Halbach et al., 2003; and references therein).

7 Paleolacustrine evolution of Juventae Chasma

Results of the experiments and numerical modeling were applied in this section to understand the evolution of the paleolacustrine environment at Juventae Chasma.

A simple model investigating several dilute solutions and based on evaporation in equilibrium with the atmosphere and precipitation of sulfate minerals were discussed earlier in this study (chapter 5). In spite of its simplicity, the results provide insights into the development of the paleolacustrine evolution of ILD's in Juventae Chasma. Using the geochemical formation conditions of the observed sulfates, it is now possible to create a new model about the origin of the lithostratigraphy or the deposition sequences for formation of monohydrated and polyhydrated sulfates. Previously published models for Juventae Chasma and the greater Valles Marineris region (Malin and Edged, 2000; Chapman et al., 2003; Montgomery and Gillespie, 2005; Rossi et al., 2008) may need to be reversed in part to take into account the relationships determined here, for sulfates formed in evaporative conditions from dissolution of martian rocks.

Due to the work of Catling et al. (2006) it is assumed that the Juventae Chasma was filled with water at least once and Maja Valles was formed by water outflow from the Juventae basin. Investigations conducted by De Hon and Pani (1993) and Chapman et al. (2003) confirmed this assumption. However, the origin of the water cannot be answered satisfactorily. The geochemical and numerical studies performed here cannot provide complete information about the duration and extent of the water ingression into the Juventae depression. But direct inflow into the lake is most likely provided by coupled processes such as river runoff, meteoric water and ground water recharge.

Gross et al. (2009) indicated an age of 3.68 (+0.08 / -0.17) as the earliest limit for the formation of Maja Valles. According to De Hon and Pani (1993), the episodic discharge lasted for one to two years with a minimum of two flood events, most likely after the opening of the Juventae basin was almost completed.

At this time, the pH values of the ponded solutions must have been in a moderate to acidified range, likely from pH 4 to pH 7 (section 6.1.1). The inflow of water must have sustained a standing body of water and exceeded evaporation, while the outflow of water into Maja Valles was restricted by the sill. Outwash of ash and volatiles by rain led to increasing sulfuric acid concentrations in the lake water as described in section 1.5.1.

After a subsequent extensional tectonic phase, associated with the opening of Valles Marineris (Carr, 1974; Blasius et al., 1977; Luchitta et al., 1992; Anderson et al., 2001), emplacement of magmatic dikes or lenses in the subsurface of the basin took place. Brittle fractures were formed which are present on CTX images at mound B (section 6.3).

This process could have caused heating of the surrounding rocks and the rise of percolating hydrothermal fluids through pathways (brittle fractures). The lake bottom water temperature would have then increased by admixture of upwelling hydrothermal fluids.

Meanwhile, the extreme atmospheric conditions (e.g. temperature and pressure) were intensified by increasing volcanic eruptions (Johnson et al., 2008; Halevy and Head, 2014) from Tharsis but also from volcanoes in close vicinity of the Chasma. At the same time the atmospheric temperature possibly rose beyond 25°C (Johnson et al., 2008). The entry of ash and aerosols by volcanic activity, and the fact that the evaporation at that point exceeded the water inflow into the Chasma led to a further increase in sulfate concentration of the lake water. At this stage, the water level no longer reached the sill, which is confirmed by the absence of sulfates in Maja Vallis.

Several diagrams were created to aide in illustrating the likely scenario of sulfate formation at Juventae Chasma (Figures 49-52).

Crystallization of monohydrated sulfates began due to warming of the water. They precipitated on the basin floor, where they successively formed massive layers of salt. The presence of massive monomineralic magnesium sulfate deposits indicate hot, acidic conditions prevailed during the evaporation phase of non stratificated water (section 6.1). The supersaturation and subsequent precipitation of sulfates as well as the continuous reduction of the lake water resulted in the drastic decrease in pH (Figure 50) and the formation of kieserite at the lower H_2O mass environment.

Possibly, for an unknown but most likely short period the basin dried up between two flooding events. However, there is no indication for this assumption (e.g. mineral alteration).

As the last tectonic phase then slowly subsided, and after the final flooding episode was completed, no fresh magma was replenished, the underground heat source slowly cooled down as did the temperature of the lake water while again intense evaporation progressively continued.

At this stage, due to low water temperatures below 75°C, only polyhydrated sulfates precipitated (section 5.3 and chapter 6). Freshwater river runoff or groundwater recharge

into Juventae Chasma is now negligible. Ongoing evaporation led to a further decline of the water level. So that now only polyhydrated sulfates deposited in deeper basin areas, above the monohydrated sulfates, which is confirmed by the absence of PHS in shallower locations (Bishop et al, 2009; Noel et al, 2015) (Figure 51).

During the early Hesperian, the water globally withdrew almost completely from the surface of Mars due to catastrophic atmospheric changes (section 1.4). Incipient erosion formed and changed the external appearance of the mounds in Juventae Chasma, and the layered structures became visible. Sulfate deposits, which may fully extend across the surface of the basin floor, are not recognizable in orbital images due to aeolian sediments and dunes covering much of the floor and walls of the chasma.

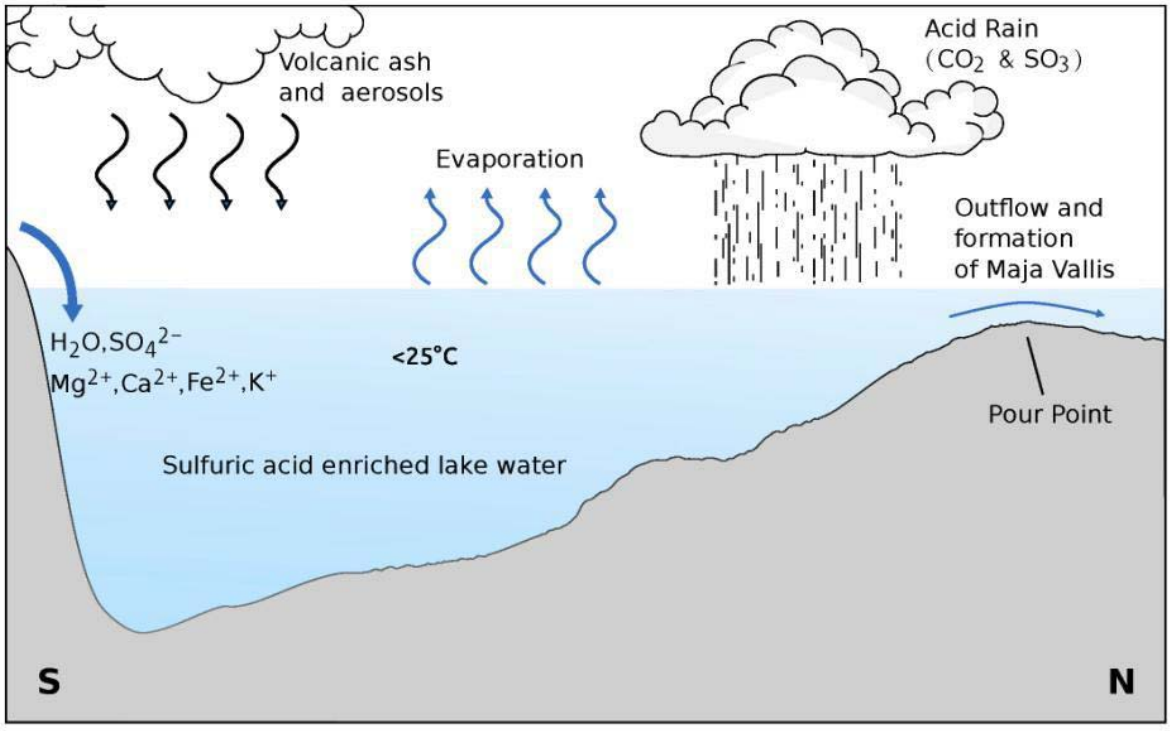

Figure 49: Schematic of the paleolacustrine situation of Juventae Chasma approximately 3.68 Ga ago. Sulfuric acid enriched lake water flooded episodically the northern plains and formed the Maja Valles outflow channel system. Due to climatic changes to warm and wet conditions, the entry of Mg, Ca, Fe and K enriched water and rock material increased. Acidification occurred by processes such as aqueous pyrite oxidation and inflow of acidified meteoric water. Inflow, e.g rain or groundwater recharge, was sufficient to sustain a standing body of water and exceeded evaporation.

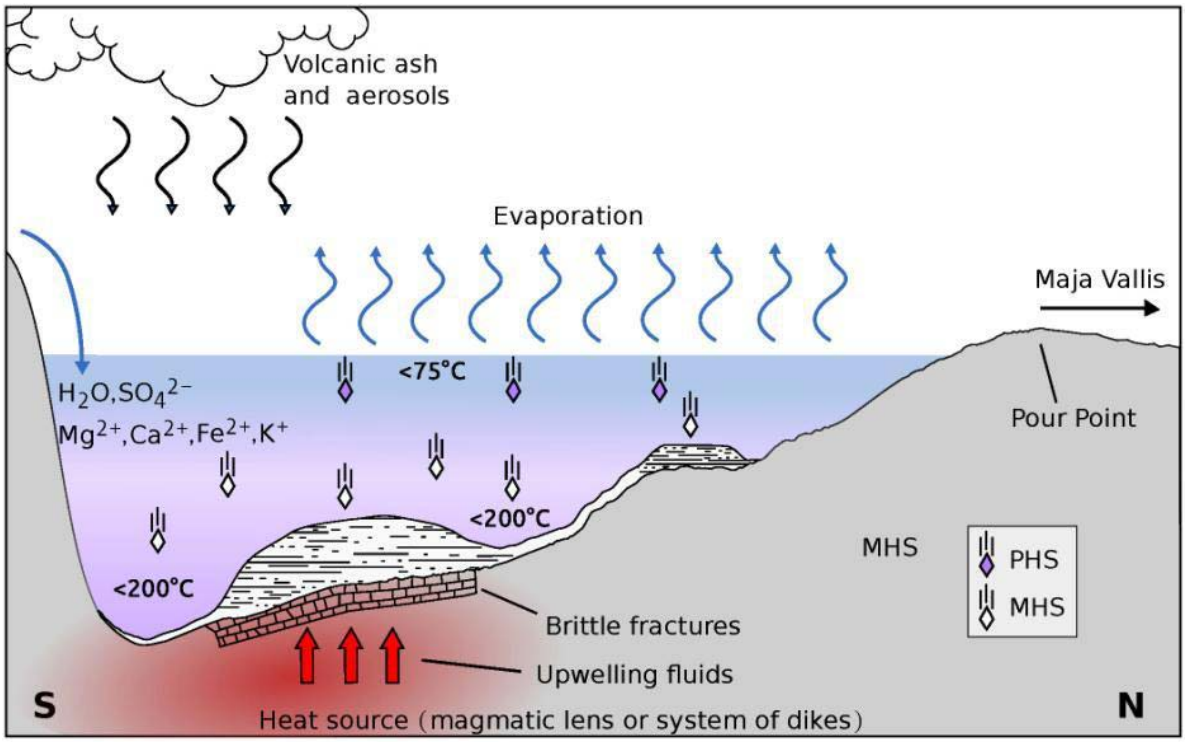

Figure 50: Schematic of the paleolacustrine situation of Juventae Chasma during the early Hesperian period. A tectonic phase associated with the opening of Valles Marineris led to emplacements of magmatic dikes or lenses in the subsurface. Fluid pathways (brittle fractures) opened and admixtures of upwelling hydrothermal fluids infiltrated the hypersaline water column and led to increasing temperatures of the water body. Outflow of water was restricted and evaporation exeeded inflow. The lake water became supersaturated with monohydrated sulfates (MHS), which formed, partly mixed with polyhydrated sulfates (PHS), interior layered deposts (ILD's) on the basin floor.

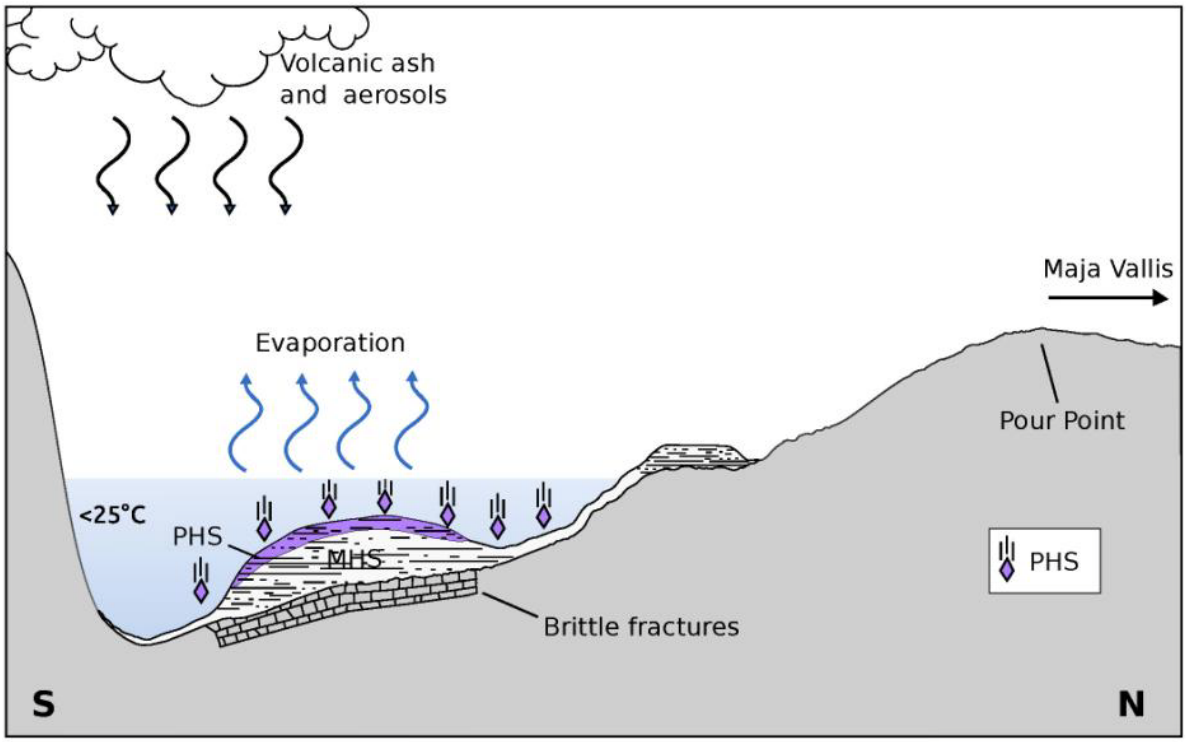

Figure 51: Schematic of the paleolacustrine situation of Juventae Chasma during the early Hesperian period. After the final tectonic phase slowly subsided, the entire system cooled down coupled with brine drawdown due to ongoing evaporation that exceeded inflow. The brine depth decreased. Basinward, autochthonous massive monohydrated sulfates (MHS) were now capped by polyhydrated sulfates (PHS), that formed as acidification continued (pH ~7 down to pH 0.1).

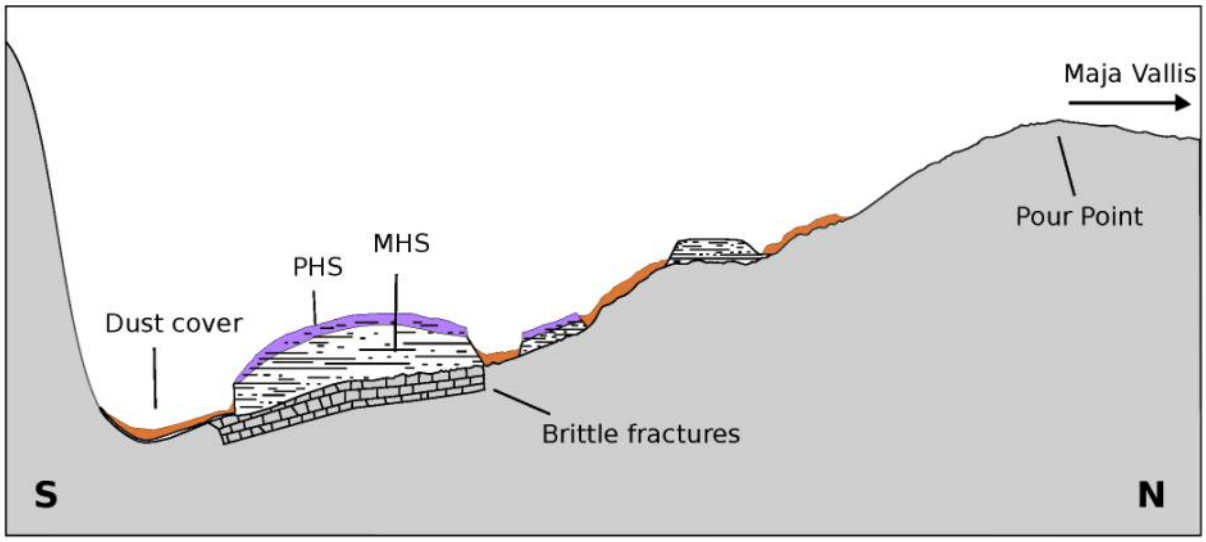

Figure 52: Schematic of the paleolacustrine situation of Juventae Chasma during the early Hesperian period. In response to global catastrophic atmospheric changes large areas of desert soils and dune sands covered the Juventae basin floor and postdated the regolith. Water disappeared to space or receded into the rock, sulfate deposits were exposed to erosional cool and dry continental-like winds, which produced outcrops of thick-bedded monohydrated sulfates (MHS) such as kieserite partly capped by layers of polyhydrated sulfates (PHS), e.g. epsomite and/or hexahydrate.

8 Summary of results

This study incorporated acid dissolution treatment of Mars analogs in the laboratory, geochemical modeling of evaporation scenarios on Mars based on these experiments, and applications of the resulting data to understand the mineralogy of evaporite settings on Mars.

Ten suitable terrestrial rock and mineral samples and the martian meteorite Tissint were examined. All samples were mineralogically and geochemically processed. Numerical evaporation based on a simple model in a closed-basin setting provided input for potential sedimentation mechanisms.

First, it was essential to select the samples according to their mineralogical and geochemical composition. The samples used contain primarily Mg, Na, K, Ca, Fe and Al in order to produce sulfate precipitates similar to those observed in Juventae Chasma. For this purpose each sample was leached with a pH 1.3 and a pH 3 sulfuric acid solution. In the next phase of the project, the resulting brines were analyzed according to their individual chemical composition. Subsequently, the brine solutions were numerically evaporated under plausible martian conditions in order to reproduce the observed sulfate precipitation and to test the conceptual model of evaporation as a reasonable process of sulfate formation. Finally, the geochemical modeling results were applied toward understanding the sulfate formation deposition sequence within the study area.

The summary of the results shows that sulfates and sulfate assemblages are comparable to those observed in Juventae Chasma and form under this depositional framework due to evaporation, from sulfuric acid solutions that were in contact with olivine minerals or olivine containing rocks such as komatiites and dunites. The presence of the olivine-bearing rocks and soils on Mars has been confirmed through orbital and rover analysis.

By simulating hydrothermal activity, as it occurs in many variations on Earth, the characteristic lithostratigraphy, namely the deposition of PHS above MHS was explained.

In addition to these findings the modeling also allows, in context with volume measurements of the ILD's (mound A-D), the calculation of the minimum water amount needed to form the mounds. It turned out that the water mass is sufficient to fill the Juventae basin and subsequently to form Maja Valles. The presence of brittle fractures on the basin floor that were found during this study lead to conclusions about the origin of at least parts of the

influent water. The summary of all results that were conceded in this study enables the development of a paleolacustrine model for Juventae Chasma.

For the first time, this study represents the comprehensive numerical analyses with a large number of samples developed by experimental geochemical and wet-chemical standardized methods. Although this work is focuses on the Juventae basin, the experimental and numerical modeling results could be applied to other regions of Mars in future studies.

References

Al-Samir, M., van Berk, W., Kneissl, T., van Gasselt, S., Gross, C., Wendt, L., Jaumann, R., 2012, A model scenario for kieserite dominated evaporites in Juventae Chasma. 43nd Lunar Planet. Sci., Vol. 43, The Woodlands, Tx, abs.#2453.

Al-Samir, M., Nabhan, S., Winkler, A., Fritz, J., Greshake, A., Jaumann, R., 2013, Experimental leaching processes and the formation of sulfates with sulfuric acid on terrestrial rocks, martian – like rocks and the martian meteorite Tissint related to the formation of ILD`s on Mars. 44nd Lunar Planet. Sci., Vol. 44, The Woodlands, Tx, abs.#2014.

Altheide, T., Chevrier, V., Nicholson, C., Denson, J., 2009, Experimental investigation of the stability and evaporation of sulfate and chloride brines on Mars. Earth Planet. Sci. Lett., 282, 69-78, doi:10.1016/j.epsl.2009.03.002.

Anders E. and Owen, T., 1977, Mars and Earth: Origin and abundance of volatiles. Science, 198, 453-465

Anderson, R.C., Dohm, J.M., Golombek, M.P., Haldemann, A.F.C., Franklin, B.J., Tanaka, K.L., Lias, J., Peer, B., 2001, Primary centers and secondary concentrations of tectonic activity through time in the western hemisphere of Mars. J. Geophys. Res., 106, 20,563-20,585.

Andrews – Hanna, J.C., Philips, R.J., Zuber, M.T., 2007, Meridiani Planum and the global hydrology of Mars. Letters to Nature, 446, 163-166, doi:10.1038/nature05594.

Andrews – Hanna, J.C., Zuber, M.T., Arvidson, R.E., Wiseman, S.M., 2010, Early Mars hydrology: Meridiani playa deposits and the sedimentary record of Arabia Terra. J. Geophys. Res. Planets, 115, 1-22, doi:10.1029/2009JE003485.

Appelo, C.A.J., Postma, D., 1993, Geochemistry, groundwater and pollution. 3rd Edition: A.A. Balkema Publishers, Leiden, The Netherlands, pp. 649.

Atreya, S.K., Witasse, O., Chevrier, V.F., Forget, F., Mahaffy, P.R., Price, P.B., Webster, C.R., Zurek, R.W., 2011, Methane on Mars: Current observations, interpretation, and future plans. Planet. Sci., 59, 133-136

Autenrieth H, 1958, Untersuchungen am Sechs-Komponenten-System K^{*}, Na^{*}, Mg^{**}, Ca^{**}, SO_4, (CI‘), H_20 mit Schlußfolgerungen für die Verarbeitung der Kalisalze. Kali u. Steinsalz, 2, 181-200.

Bandfield, J.L., 2001, Global mineral distributions on Mars. J. Geophys. Res., 107, 1-21.

Banin, A., Han, F.X., Kan, I., Cicelsky, A., 1997, Acidic volatiles and the Mars soil. J. Geophys. Res.. 102 (E6)**,** 13,341-13,356.

Bethke, C.M., 2008, Geochemical Reaction Modeling. Oxford University Press, Inc, New York, pp. 543.

Bibring, J.-P., Langevin, Y., Gendrin, A., Gondet, B., Poulet, F., Berthé, M., Soufflot, A., Arvidson, R., Mangold, N., Mustard, J., Drossart, P., 2005, Mars surface diversity as revealed by the OMEGA/Mars Express observations. Science 307, 1576-1581.

Bibring, J.-P., Langevin, Y., Mustard, J.F., Poulet, F., Arvidson, R., Gendrin, A., Gondet, B., Mangold, N., Pinet, P., Forget, F., 2006, Global mineralogical and aqueous Mars history derived from OMEGA/Mars Express data. Science, 312, 400-404.

Bibring, J.-P., Arvidson, R.E., Gendrin, A., Gondet, B., Langevin, Y., Le Mouelic, S., Mangold, N., Morris, R.V., Mustard, J.F., Poulet, F., Quantin, C., Sotin, C., 2007, Coupled ferric oxides and sulfates on the martian surface. Science, 317, 1206-1210.

Bigham, J.M. & Nordstrom, D.K., 2000: Iron and aluminium hydroxysulfates from acid sulfate waters. In: Alpers, C. N., Jambor, J. L. & Nordstrom, D. K. (eds.): Sulfate Minerals, Crystallography, Geochemistry, and Environmental Significance. Rev. Mineral. Geochem., Mineralogical Society of America, Chantilly, Virginia, 40, 351 – 403

Bischoff, J.L. and F.W. Dickson, 1975, Seawater-Basalt interaction at 200°C and 500 bars: Implications for origin of sea-floor heavy metal deposits and regulation of seawater chemistry. Earth Planet. Sci. Lett., 25, pp. 385-397.

Bischoff, J.L. and Seyfried, W.E, 1978, Hydrothermal chemistry of seawater from 25° to 350°C. Am. J. Sci., 278, 838-860.

Bischoff, J.L. and Rosenbauer, R.J, 1983, A note on the chemistry of seawater in the range 350°-500°C. Geochim. Cosmochim. Acta, 47, 139-144.

Bish, D.L., Blake, D.F., Vaniman, D.T., Chipera, S.J., Morris, R.V., Ming, D.W., Treiman, A.H., Sarrazin, P., Morrison, S.M., Downs, R.T., Achilles, C.N., Yen, A.S., Bristow, T.F., Crisp, J.A., Morookian, J.M., Farmer, J.D., Rampe, E.B., Stolper, E.M., Spanovich, N., and the MSL Science Team, 2013, X-ray diffraction results from Mars Science Laboratory: Mineralogy of Rocknest at Gale crater. Science, 341, 1238932-1, doi: 10.1126/science.1238932

Bishop, J. L., Parente, M., Weitz, C.M., Noe Dobrea, E.Z., Roach, L.H., Murchie, S.L., McGuire, P.C., McKeown, N.K., Rossi, C.M., Brown, A.J., Calvin, W.M., Miliken, R., and John Mustard, 2009. Mineralogy of Juventae Chasma: Sulfates in the Light-toned Mounds, Mafic Minerals in the Bedrock, and Hydrated Silica and Hydroxylated Ferric Sulfate on the Plateau. J. Geophys. Res.. 114**,** doi:10.1029/2009JE003352.

Blake, D.F., Morris, R.V., Kocurek, G., M., Morrison, S., Downs, R.T., Bish, D., Ming, D. W., Edgett, K. S., Rubin, D., Goetz, W., Madsen, M. B., Sullivan, R., Gellert, R., Campbell, I., Treiman, A.H., McLennan, S.M., Yen, A.S., Grotzinger, J., Vaniman, D.T., Chipera, S.J., Achilles, C.N., Rampe, E.B., Sumner, D., Meslin, P.-Y., Maurice, S., Forni, O., Gasnault, O., Fisk, M., Schmidt, M., Mahaffy, P., Leshin, L.A., Glavin, D., Steele, A., Freissinet, C., Navarro-González, R., Yingst, R.A., Kah, L.C., Bridges, N., Lewis, K.W., Bristow, T.F., Farmer, J.D., Crisp, J.A., Stolper, E.M., Des Marais, D.J., Sarrazin, P., and the MSL Science Team, 2013, Curiosity at Gale crater,

Mars: Characterization and analysis of the Rocknest sand shadow. Science, 341, 1239505-1, doi: 10.1126/science.1239505

Blanc, P., Lassin, A., Piantone, P., 2009, Thermoddem, a thermodynamic database for modelling the alteration of waste minerals. URL: http://thermoddem.brgm.fr/ 2014.

Blasius, K.R., Cutts, J.A., Guest, J.E., Masursky, H., 1977, Geology of the Valles Marineris: first analysis of imaging from the Viking I Orbiter primary mission. J. Geophys. Res., 82, 4067–4091, doi:10.1029/JS082i028p04067.

Braitsch, O. 1962, Entstehung und Stoffbestand der Salzlagerstätten. Mineralogie und Petrographie in Einzeldarstellungen, Springer Vlg., Berlin-Göttingen-Heidelberg, 3, pp. 297.

Bruhn, G., Gerlach, J., Pawlek, F., 1965, Untersuchungen über die Löslichkeiten von Salzen und Gasen in Wasser und wäßrigen Lösungen bei Temperaturen oberhalb von 100°C. Zeitschrift für Anorganische und Allgemeine Chemie, 337, p. 68–79.

Bullough, W., Canning, T.A., Strawbridge, M.I., 1952, The solubility of ferrous sulphate in aqueous solutions of sulphuric acid. J. Appl. Chem., 2, 703–707.

Burns, R., Fisher, D.S., 1993. Rates of oxidative weathering on the surface of Mars. J. Geophys. Res.(Planets), v. 98, E2, 3365-3372.

Carr, M.H.,1974, Tectonism and volcanism of the Tharsis region of Mars. J. Geophys. Res., 79, 3943-3949.

Carr, M.H., Schaber, G.G., 1977, Martian permafrost features. J. Geophys. Res. 82, 4039-4054.

Carr, M.H., 1989, Recharge of the early atmosphere of Mars by impact-induced release of CO2. Icarus, 79, 311-327.

Carr, M. H., 1995, The Martain drainage system and the origin of valley networks and fretted channels. J. Geophys. Res., 100, E4, 7497-7507.

Carr, M.H., 1996, Water on Mars. Oxford Univ. Press, New York, p. 229.

Carr, M., Head, J.W., 2010, Acquisition and history of water on Mars. In: Lakes on Mars, edited by N. A. Cabrol and E. A. Grin, pp. 31-67.

Catling, D.C., Wood, S.E., Leovy, C., Montgomery, D.R., Greenberg, H.M., Lein, C.R., Moore, J.M., 2006, Light-toned layered deposits in Juventae Chasma, Mars. Icarus. 181, 1, 26-51.

Chapman, M.G., and Tanaka, K.L., 2001, Interior trough deposits on Mars: Subice volcanoes? J. Geophys. Res., 106, pp. 10,087-10,100.

Chapman, M.G., Gudmundsson, M.T., Russell, A.J. and T.M. Hare, 2003, Possible Juventae Chasma subice volcanic eruptions and Maja Valles ice outburst floods on Mars: Implications of Mars Global Surveyor crater densities, geomorpholoy, and topography, J. Geophys. Res., 108(E10), 5113, doi:10.1029/2002JE002009.

Chennaoui Aoudjehane, H., Avice, G., Barrat, J.A., Boudouma, O., Chen, G., Duke, M.J.M., Franchi, I.A., Gattacceca, J. Grady, M.M., Greenwood, R.C., Herd, C.D.K., Jambon, A., Marty, B., Rochette, P., Smith, C.L., Sautter, V., Verchovsky, A., Weber, P., Zanda, B., 2012, Tissint martian meteorite: A fresh look at the interior, surface and atmosphere. Science, 338, 785-788, doi: 10.1126/science.1224514.

Chevrier, V.F., Altheide, T.S., 2008, Low temperature aqueous ferric sulfate solutions of the surface of Mars. Geophysical Res. Lett., 35, 1-5, doi: 10.1029/2008GL035489.

Christensen, P.R., 2003, Formation of recent Martian gullies through melting of extensive water-rich snow deposits. Nature, 422, 45-48, doi:10.1038/nature01436.

Christensen, P.R., Wyatt, M.B., Glotch, T.D., Rogers, A.D., Anwar, S., Arvidson, R.E., Bandfield, J.L., Blaney, D.L., Budney, C., Calvin, W.M., Faracaro, A., Fergason, R.L., Gorelick, N., Graff, T.G., Hamilton, V.E., Hayes , A.G., Johnson, J.R., Knudson, A.T., McSween, H.Y., Mehall, G.L., Mehall, L.K., Moersch, J.E., Morris, R.V., Smith, M.D., Squyres, S.W., Ruff, S.W. and Wolff ,M.J., 2004, Mineralogy at Meridiani Planum from the Mini-TES experiment on the Opportunity Rover. Science 306,pp. 1733–1739.

Christov, C., Møller, N., 2004, Chemical equilibrium model of solution behavior and solubility in the H-Na-K-OH-Cl-HSO_4-SO_4-H_2O system to high concentration and temperature. Geochim. Cosmochim. Acta, 68, pp. 1309-1331.

Clark, B.C., and D.C. van Hart, 1981, The salts of Mars. Icarus, 45, 2, 370 – 378, doi:10.1016/0019-1035(81)90041-5.

Craddock, R.A., Howard, A.D., 2002, The case for rainfall on a warm, wet early Mars. J. Geophys. Res., 107, 1-36, doi:10.1029/2001JE001505.

Davies, C.W., 1962, Ion Association. Butterworths, Washington DC (USA), pp. 190.

De Hon, R.A., Pani, E.A., 1993, Duration and Rates of Discharge: Maja Valles, Mars. J. Geophys. Res., 98, 9129-9138.

Delany, J.M. and S.R. Lundeen, 1989, The LLNL thermochemical database. Lawrence Livermore National Laboratory Report UCRL-21658.

Dickson, J.L., Head, J.W., Marchant, D.R., 2008, Late Amazonian glaciations at the dichotomy boundary on Mars: Evidence for glacial thickness maxima and multiple glacial phases. Geology, 36, 411-414.

Dill, H.G., 2001, The geology of aluminium phosphates and sulphates of the alunite group minerals: a review. Earth-Sci. Rev., 53, 35-93.

Ding, K. and W.E., Seyfried, 1992, Determination of Fe-Cl complexing in the low pressure supercritical region (NaCl fluid): Iron solubility constraints on pH of subseafloor hydrothermal fluids. Geochim. Cosmochim. Acta, 56, pp. 3681-3692.

Druschel, G.K., Baker, B.J., Gihring, T.M., Banfield, J.F., 2004, Acid mine drainage biogeochemistry at Iron Mountain, California. American Institute of Physics, 5 (2), 13-32, doi:10.1063/1.1769131.

Dutrizac, J.E., Jambor, J.L., 2000, Jarosites and their application in hydrometallurgy. In: Sulfate Minerals: Crystallography, Geochemistry, and Environmental Significance, Rev. Mineral. Geochem., Vol. 40, edited by C. N. Alpers, J. L. Jambor, and D. K. Nordstrom, pp. 405 – 454, Mineral. Soc. of Am., Washington, D. C.

Ehlmann, B.L., Mustard, J.F., Murchie, S.L., Poulet, F., Bishop, J.L., Brown, A.J., Calvin, W.M., Clark, R.N., Des Marais, D.J., Miliken, R.E., Roach, L.H., Roush, T.L., Swayze, G.A., and Wray, J.J., 2008, Orbital Identification of Carbonate – Bearing Rocks on Mars. Science 322, pp. 1828.

Ehlmann, B.L., Mustard, J.F., Murchie, S.L., Bibring, J.-P., Meunier, A., Fraeman, A.A., 2011, Subsurface water and clay mineral formation during the early history of Mars. Nature, 479, 53-60.

Eisbacher, G.H., 1996, Einführung in die Tektonic. Ferdinand Enke Vlg., Stuttgart, 2nd edition, pp. 374.

Elwood Madden, M.E., Madden, A.S., Rimstidt, J.D., Zahrai, S., Kendall, M.R., Miller, M.A., 2012. Jarosite dissolution rates and nanoscale mineralogy. Geochim. Cosmochim. Acta, 91, pp. 306-321.

Emmons, W.H., Grout, F.F., 1943, Mineral resources of Minnesota. Minneapolis: The University of Minnesota Press, pp. 149.

Erkeling, G., Reiss, D., Hiesinger, H., Poulet, F., Carter, J., Ivanov, M., Hauber, E., Jaumann, R., 2014, Valleys, paleolakes and possible shorelines at the Libya Montes/Isidis boundary: Implications for the hydrologic evolution of Mars. Icarus, 219, 393-413.

Eugster, H.P., Hardie, L.A., 1978, Saline Lakes. Springer, New York, Heidelberg, Berlin, pp. 237 – 293.

Flahaut, J., Quantin, C., Clenet, H., Allemand, P., Mustard, J.F., Thomas, P., 2012, Pristine Noachian crust and key geologic transitions in the lower walls of Valles Marineris: Insights into early igneous processes on Mars. Icarus, 221, 420-435.

Flanagan, F.J., 1984, Three USGS mafic rock reference samples, W-2, DNC-1, and BIR-1. U.S. Geological Survey Bulletin 1623, 1-54.

Forget, F., Pierrehumbert, R.T., 1997, Warming early Mars with carbon dioxide clouds that scatter infrared radiation. Science, 278, 1273-1276.

Forget, F., Wordsworth, R., Millour, E., Madeleine, J.-B., Kerber, L., Leconte, J., Marcq, E., Haberle, R.M., 2013, 3D modeling of the early martian climate under a denser CO_2 atmosphere: Temperatures and CO_2 ice clouds. Icarus, 222, 81-99.

Fraenckel, F., 1907, Über die Existenzgebiete der Ferrosulfat-Hydrate. Z. anorg. Chem., 55, 223–232.

Frey, F.A., Prinz, M., 1978, Ultramafic inclusions from San Carlos, Arizona: Petrologic and geochemical data bearing on their petrogenesis. Earth Planet. Sci. Lett., 38, 129-176.

Füchtbauer, H.,1988, Sedimente und Sedimentgesteine. Schweizbart, Stuttgart, pp. 1141.

Fueten, F., Stesky, R., MacKinnon, P., Hauber, E., Zegers, T., Gwinner, K., Scholten, F., Neukum, G., 2008, Stratigraphy and structure of interior layered deposits in west Candor Chasma, Mars, from High Resolution Stereo Camera (HRSC) stereo imagery and derived elevations. J. Geophys. Res., 113, 1-19, doi:10.1029/2007JE003053.

Fulda, E., 1928, Das Kali. Die Gewinnung, Verarbeitung und Verwertung der Kalisalze; ihre Geschichte und wirtschaftliche Bedeutung. II. Teil: Die Chemie und Mineralogie der Kalisalze; die Geologie der Kalisalzlagerstatten; die Gewinnung, Verarbeitung und Verwertung der Kalisalze. Enke Verlag, Stuttgart, Bd. 8, 1-400.

Gardner, C.S., 1992, Ranging performance of satellite laser altimeters. IEEE Trans. Geosci. Remote Sens., 30, 1061-1072.

Gendrin, A., Mangold, N., Bibring, J.-P., Langevin, Y., Gondet, B., Poulet, F., Bonello, G., Quantin, C., Mustard, J., Arvidson, R., LeMouélic, S., 2005, Sulfates in Martian layered terrains: The OMEGA/Mars Express view. Science. 307**,** 1587-1591.

Gooding, J.L., Wentworth, S.J., Zolensky, M.E., 1988, Calcium carbonate and sulfate of possible extraterrestrial origin in the EETA 79001 meteorite. Geochim. Cosmochim. Acta, 52, p. 909-915.

Gorham, E., 1976, Acid precipitation and its influence upon aquatic ecosystems-an overview. Water, Air, Soil Pollut., 6, 457-481.

Greeley, R., Spudis, P.D., 1981, Volcanism on Mars. Rev. Geophys. Space Phys., 19, 13-41.

Green D. H., 1975, Genesis of Archean peridotitic magmas and constraints on Archean geothermal gradients and tectonics. Geology (Boulder), 3, 15-18.

Gross, C., Wendt, L., Dumke, A., Neukum, G., 2009, Further evidence of multiple flooding events at Juventae Chasma and Maja Valles, Mars. 40th Lunar Planet. Sci., The Woodlands, Tx, abs. #1890.

Gross, C., Noel, A., Bishop, J.L., Al-Samir, M., Flahaut, J., McGuire, P., Weitz, C., Seelos, F., Murchie, S.,2009, Investigating the mineralogy, morphology and stratigraphy of mound B in Juventae Chasma, Mars using multiple datasets. 45th Lunar Planet. Sci., The Woodlands, Tx, abs. #1918.

Grotzinger, J.P., Sumner, D.Y., Kah, L.C., Stack, K., Gupta, S., Edgar, L., Rubin, D., Lewis, K., Schieber, J., Mangold, N., Milliken, R., Conrad, P.G., DesMarais, D., Farmer, J., Siebach, K., Calef III, F., Hurowitz, J., McLennan, S.M., Ming, D., Vaniman, D., Crisp, J., Vasavada, A., Edgett, K.S., Malin, M., Blake, D., Gellert, R., Mahaffy, P., Wiens, R.C., Maurice, S., Grant, J.A., Wilson, S., Anderson, R.C., Beegle, L., Arvidson, R., Hallet, B., Sletten, R.S., Rice, M., Bell III, J., Griffes, J., Ehlmann, B., Anderson, R.B., Bristow, T.F., Dietrich, W.E., Dromart, G., Eigenbrode, J., Fraeman, A., Hardgrove, C., Herkenhoff, K., Jandura, L., Kocurek, G., Lee, S., Leshin, L.A., Leveille, R., Limonadi, D., Maki, J., McCloskey, S., Meyer, M., Minitti, M., Newsom, H., Oehler, D., Okon, A., Palucis, M., Parker, T., Rowland, S., Schmidt, M., Squyres, S., Steele, A., Stolper, E., Summons, R., Treiman, A., Williams, R., Yingst, A., and the MSL Science Team, 2014, A habitable fluvio-lacustrine environment at Yellowknife Bay, Gale crater, Mars. Science, 343, 1242777-1, doi: 10.1126/science.1242777.

Grotzinger, J.P., Arvidson, R.E., Bell III, J.F., Calvin, W., Clark, B.C., Fike, D.A., Golombek, M., Greeley, R., Haldemann, A., Herkenhoff, K.E., Jolliff, B.L., Knoll, A.H., Malin, M., McLennan, S.M., Parker, T., Soderblom, L., Sohl-Dickstein, J.N., Squyres, S.W., Tosca, N.J., Watters, W.A., 2005, Stratigraphy and sedimentology of a dry to wet eolian depositional system, Burns formation, Meridiani Planum, Mars. Earth Planet. Sci. Lett. 240, 1, 11-72.

Haberle, R.M., Jakosky, B.M., 1990, Sublimation and transport of water from the north residual polar cap on Mars. J. Geophys. Res., 95, 1423–1437.

Haberle, R.M., 1998, Early Mars climate models. J. Geophys. Res., 103, 28,467–28,479.

Halbach, P.E., Fouquet, Y., Herzig, P., 2003, Mineralization and Compositional Patterns in deep-sea hydrothermal systems. In Energy and Mass Transfer in Marine Hydrothermal Systems (eds. P. Halbach, V. Tunnicliffe, and J. Hein). DUP, Berlin, pp. 85-122.

Halevy, I., Head, J.W., 2014, Episodic warming of early Mars by punctuated volcanism. Nat. Geosci., doi:10.1038/ngeo2293.

Hamilton, V.E., 2000, Thermal infrared emission spectroscopy of the pyroxene mineral series. J. Geophys. Res., 105, No. E4, pp.S 9701–9716.

Hardie, L.A., 1967, The gypsum-anhydrite equilibrium at one atmosphere pressure. The American Mineralogist, 52, p. 171-200.

Hardie, L.A., 1984, Evaporites: Marine or non-marine? Am. J. Sci., 284, p. 193-240.

Hartmann, W.K., Neukum, G., 2001, Cratering chronology and the evolution of Mars. Space Sci. Rev., 96, 165-194.

Hartmann, W.K., Strom, R.G., Grieve, R.A.F., Weidenschilling, S.J., Diaz, J., Blasius, K.R., Chapman, C.R., Woronow, A., Shoemaker, E.M., Dence, M.R., Jones, K.L., 1981, Chronology of planetary volcanism by comparative studies of planetary cratering. In Basaltic volcanism on the terrestrial planets, Pergamon Press, New York, USA, pp. 1050-1125.

Hawthorne, F.C., Krivovichev, S.V., and Burns, P.C., 2000, The crystal chemistry of sulfate minerals. In C.N. Alpers, J.L. Jambor, and D.K. Nordstrom, Eds., Sulfate Minerals: Crystallography, Geochemistry and Environmental Significance, 40, 1–101. Rev. Mineral. Geochem., Mineralogical Society of America, Chantilly, Virginia.

Head, J.W., Greeley, R., Golombek, M.P., Hartmann, W.K., Hauber, E., Jaumann, R., Masson, P., Neukum, G., Nyquist, L.E., Carr, M.H., 2001, Geological processes and evolution. Space Sci. Rev., 96, 263-292.

Head, J.W., Nahm, A.L., Marchant, D.R., Neukum, G., 2005, Modification of the dichotomy boundary on Mars by Amazonian mid-latitude regional glaciation. Geophys. Res. Lett., 33, LO8S03.

Head, J.W., Mustard, J.F., 2006, Breccia dikes and crater-related faults in impact craters on Mars: Erosion and exposure on the floor of a crater 75 km in diameter at the dichotomy boundary. Meteorit. Planet. Sci., 41 (10), 1675-1690.

Helgeson, H.C., 1969, Thermodynamics of hydrothermal systems at elevated temperatures and pressures. Am. J. Sci., 267, 729-804.

Hemley, J.J., Montoya, J.W., Marinenko, J.W., Luce, R.W., 1980, Equilibria in the system Al_2O_3–SiO_2–H_2O and some general implications for alteration/mineralization processes. Economic Geology, 75, 210-228.

Herrmann, A.G., 1981, Grundkenntnisse über die Entstehung mariner Salzlagerstätten. Heidelberg, Der Aufschluss, 32, p. 45 – 72.

Hiesinger, H., Head, J.W., 2004, The Syrtis Major volcanic province, Mars: Synthesis from Mars Global Surveyor data. J. Geophys. Res., 109, E01,004, doi:10.1029/2003JE002143.

Holleman, A. F., Wiberg, E., 2007, Lehrbuch der Anorganischen Chemie. 102. Edition, Walter de Gruyter, Berlin-New York, pp. 1-2149.

Humphris, S.E., Halbach, P.E., Juniper, K.., 2003, Low-temperature alteration: Fluxes and mineralization. In Energy and Mass Transfer in Marine Hydrothermal Systems (eds. P. Halbach, V. Tunnicliffe, and J. Hein). DUP, Berlin, pp. 163-182.

Hynek, B. M., Beach, M., Hoke, M. R. T., 2010, Updated global map of Martian valley networks and implications for climate and hydrologic processes. J. Geophys. Res. 115, E9, E09008.

Ide, K.H., 1938, Zur hydratation und dehydratation des Magnesiumsulfats und seiner Hydrate. Z. anorg. u. allg. Chem., 235, 305-323.

Jakosky, B.M., Farmer, C.B., 1982, The seasonal and global behavior of water vapor in the Mars atmosphere: Complete global results of the Viking atmospheric water detector experiment. J. Geophys. Res., 87, 2999-3019.

Jakosky, B.M., Haberle, R.M., 1990, Year-to-year instability of the Mars south polar cap. J. Geophys. Res., 95, 1359-1365.

Janecky, D.R., Seyfried, W.E. Jr., 1983, The solubility of magnesium-hydroxide-sulfate-hydrate in seawater at elevated temperatures and pressurs. Am. J. .Sci., 283, 831-860.

Jaumann, R., Neukum, G., Behnke, T., Duxbury, T.C., Eichentopf, K., Flohrer, J., van Gasselt, S., Giese, B., Gwinner, K., Hauber, E., Hoffmann, H., Hoffmeister, A., Köhler, U., Matz, K. D., McCord, T. B., Mertens, V., Oberst, J., Pischel, R., Reiss, D., Ress, E., Roatsch, T., Saiger, P., Scholten, F., Schwarz, G., Stephan, K., Wählisch, M., the HRSC Co-Investigator Team, 2007, The high-resolution stereo camera (HRSC) experiment on Mars Express: Instrument aspects and experiment conduct from interplanetary cruise through the nominal mission. Planet. Space Sci. 55, 928-952.

Jaumann, R., Tirsch, D., Hauber, E., Erkeling, G., Hiesinger, H., Le Deit, L., Sowe, M., Adeli, S., Petau, A., Reiss, D.,2014, Water and Martian Habitability: Results of an integrative study of water related processes on Mars in context with an interdisciplinary Helmholtz research alliance "Planetary Evolution and Life". Planet. Space Sci., 98, 128-145.

Johnson, S.S., Mischna, M.A., Grove, T.L., Zuber, M.T., 2008, Sulfur-induced greenhouse warming on early Mars. J. Geophys. Res. (Planets), 113, 1-15, E08005.

Keefer, K.D., Hochella, F. Jr., De Jong, B.H.W.S., 1981, The structure of the magnesium hydroxide sulfate hydrate $MgSO_4$ – $Mg(OH)_2$ H_2O. Acta Cryst, B37, 1003-1006.

Kelley, D.S., Karson, J.A., Blackman, D.K., Früh-Green, G.L., Butterfield, D.A., Lilley, M.D., Olson, E.J., Schrenk, M.O., Roe, K.K., Lebon, G.T., Rivizzigno, P., and the AT3-60 Shipboard Party, 2001, An off-axis hydrothermal vent field near the Mid-Atlantic ridge at 30°N. Nature, 412, 145-149.

Kieffer, H.H., Chase, S.C. Jr., Martin, T.Z., Miner, E.D., Palluconi, F.D., 1976, Martian north pole summer temperatures: Dirty water ice. Science, 194(4271), 1341-1344.

King, P.L., McSween, H.Y., 2005, Effects of H_2O, pH, and oxidation state on the stability of Fe minerals on Mars. J. Geophys. Res., 110, 1-15.

Klingelhofer, G., Morris, R. V., Bernhardt, B., Schroder, C.,Rodionov, D.S., de Souza, P.A., Yen, A., Gellert, R., Evlanov, E.N., Zubkov, B., Foh, J., Bonnes, U., Kankeleit, E., Gutlich, P., Ming, D.W., Renz, F., Wdowiak, T., Squyres, S.W. and Arvidson, R.E. 2004, Jarosite and hematite at Meridiani Planum from Opportunity's Mossbauer spectrometer. Science 306, pp. 1740–1745.

Kliore, A.J., Cain, D.L., Levy, G.S., Eshleman, V.R., Fjeldbo, G., Drake, F.D., 1965, Occultation experiment: Results of the first direct measurement of Mars' atmosphere and ionosphere. Science, 149, 1243-1248.

Kneissl, T., van Gasselt, S., Neukum, G., 2011. Measurement of Strike and Dip of Geologic Layers from Remote Sensing Data - New Software Tool for ArcGIS. 41st Lunar Planet. Sci., The Woodlands, Tx, abs.# 1533.

Kobylin, P.M., Sippola, H., Taskinen, P.A., 2011, Thermodynamic modelling of aqueous Fe(II) sulfate solutions. CALPHAD: Computer Coupling of Phase Diagrams and Thermochemistry, 35, p. 499-511.

Koebel, M., Elsener, M., Zimmermann, U., 1989, Der Oxidationsmechanismus von Szomolnokit im intermittierend befeuerten Warmwasserkessel. Werkstoffe und Korrosion, 40, p. 382-392.

Koschinsky, A., Kausch, M., Borowski, C., 2014, Metal concentrations in the tissues of hydrothermal vent mussel Bathymodiolus: Reflection of different metal sources. Mar. Environ. Res., 95, 62-73, doi: 10.1016/j.merenvres.2013.12.012.

Krasnopolsky, V.A., 2006, Some problems related to the origin of methane on Mars. Icarus, 180 (2), 359-367.

Lammer, H., Chassefière, E., Karatekin, Ö., Morschhauser, A., Niles, P.B., Mousis, O., Odert, P., Möstl, U.V., Breuer, D., Dehant, V., Grott, M., Gröller, H., Hauber, E., Pham, L.B.S, 2013, Outgassing history and escape of the martian atmosphere and water inventory. Space Sci. Rev., 174, 113-154, doi: 10.1007/s11214-012-9943-8.

Langford, R.P., 2003, The Holocene history of the White Sands dune field and influences on eolian deflation and playa lakes. Quaternary International, 104, pp. 31-39.

Le Deit, L., Bourgeois, O., Le Mouélic, S., Mége, D., Combe, J. P., Sotin, C., Massé, M., 2008, Light-toned layers on plateaus above Valles Marineris (Mars). 39th Lunar Planet. Sci., The Woodlands, Tx.,Vol. 39, abs.#1740.

Le Deit, L., Bourgeois, O., Mége, D., Le Mouélic, S., Massé, M., Hauber, E., Jaumann, R., Bibring, J.-P., 2009, Geological history of a light-toned formation draping the plateaus in the region of Valles Marineris, Mars. 40th Lunar Planet. Sci., The Woodlands, Tx, Vol. 40, abs. #1856.

Lefèvre, F., Forget, F., 2009, Observed variations of methane on Mars unexplained by known atmospheric chemistry and physics. Nature, 460, 720-723, doi:10.1038/nature08228.

Lippman, F., 1973, Sedimentary carbonate minerals. New York, Springer Verlag, pp. 228.

Long, D.T., Fegan, N.E., Lyons, W.B, Hines, M.E., Mabumber, P.G., Giblin, A.M., 1992**(a)**, Geochemistry of acid brines: Lake Tyrrell, Victoria, Australia. Chem. Geol., 96, pp. 33-52.

Long, D.T., Fegan, N.E., McKee, J.D., Lyons, W.B, Hines, M.E., Mabumber, P.G., 1992**(b)**, Formation of alunite, jarosite and hydrous iron oxides in a hypersaline system: Lake Tyrrell, Victoria, Australia. Chem. Geol., 96, pp. 33-52.

Lowson, R.T, 1982, Aqueous oxidation of pyrite by molecular oxygen. Chem. Rev., American Chemical Society, 82 (5), 461-497.

Lucchitta, B.K., McEwen, A.S., Clow, G.D., Geissler, P.E., Singer, R.B., Schultz, R.A., Squyres, S.W., 1992, The Canyon System of Mars. In: Kieffer HH, Jakosky BM, Snyder CW, Matthews MS (eds) Mars. University of Arizona Press, Tucson, pp. 453-492.

Madden, M.E.E., Madden, A.S., Rimstidt, J.D., Zahrai, S., Kendall, M.R., Miller, M.A., 2012, Jarosite dissolution rates and nanoscale mineralogy. Geochim. Cosmochim. Acta, 91, pp. 306-321.

Malin, M.C., Edgett, K.S., 2000, Sedimentary rocks of early Mars. Science, 290, 1927–1937, doi:10.1126/science.290.5498.1927.

Malin, M.C., Edgett, K.S., 2001, Mars Global Surveyor Mars Orbiter Camera: Interplanetary cruise through primary mission. J. Geophys. Res., 106, 23429-23570.

Malin, M.C., Bell, J.F., Cantor, B.A., Caplinger, M.A., Calvin, W.M., Clancy, R.T., Edgett, K.S., Edwards, L., Haberle, R.M., James, P.B., Lee, S.W., Ravine, M.A., Thomas, P.C., Wolff, M.J., 2007, Context Camera Investigation on board the Mars Reconnaissance Orbiter. J. Geophys. Res. (Planets) 112, E510.1029/2006JE002808.

Malin, M.C., Edgett, K.S., Cantor, B.A., Caplinger, M.A., Danielson, G.E., Jensen, E.H., Ravine, M.A., Sandoval, J.L., Supulver, K.D., 2010, An overview of the 1985-2006 Mars Orbiter Camera science investigation. Mars, 5, 1-60, doi:10.1555/mars.2010.0001.

Maltagliati, L., Montmessin, F., Fedorova, A., Korablev, O., Forget, F., Bertaux, J.-L., 2011, Evidence of water vapor in excess of saturation in the atmosphere of Mars. Science, 333, 1868-1871, doi:10.1126/science.1207957.

Mangold, N., Quantin, C., Ansan, V., Delacourt, C., Allemand, P., 2004, Evidence for Precipitation on Mars from Dendritic Valleys in the Valles Marineris Area. Science, 305,78-81, doi: 10.1126/science.1097549.

Mangold, N., Ansan, V., Masson, M.P., Quantin, C., Neukum, G., 2008, Geomorphic study of fluvial landforms on the northern Valles Marineris plateau. J. Geophys. Res., 113, E08009, doi: 10.1029/2007JE002985.

Matthes S., 1993, Mineralogie. Springer-Lehrbuch, 4.Auflage, Berlin-Heidelberg. pp. 461.

McCauley, J.F., 1978, Geologic map of the Coprates quadrangle of Mars. US Geological Survey Miscellaneous Investigations Series Map I-897.

McKay D.S., Gibson E.K.Jr., Thomas-Keprta K.L., Vali H., Romanek C.S., Clemett S.J., Chillier X.D.F., Maechling C.R., Zare R.N., 1996, Search for past life on Mars: Possible relic biogenic activity in martian meteorite ALH 84001. Science, 273, 924-930.

McLennan, S.M., Bell, J.F., Calvin, W.M., Christensen, P.R., Clark, B.C., de Souza, P.A., Farmer, J., Farrand, W.H., Fike, D.A., Gellert, R., Ghosh, A., Glotch, T.D., Grotzinger, J.P., Hahn, B., Herkenhoff, K.E., Hurowitz, J.A., Johnson, J.R., Johnson, S.S., Jolliff, B., Klingelhofer, G., Knoll, A.H., Learner, Z., Malin, M.C., McSween, H.Y., Pocock, J., Ruff, S.W., Soderblom, L.A., Squyres, S.W., Tosca, N.J., Watters, W.A., Wyatt, M.B. and Yen, A., 2005, Provenance and diagenesis of the evaporite-bearing Burns formation, Meridiani Planum, Mars. Earth Planet. Sci. Lett., 240, pp. 95–121.

McLennan, S.M., Anderson, R.B., Bell III, J.F., Bridges, J.C., Calef III, F., Campbell, J.L., Clark, B.C., Clegg, S., Conrad, P., Cousin, A., Des Marais, D.J., Dromart, G., Dyar, M.D., Edgar, L.A., Ehlmann, B.L., Fabre, C., Forni, O., Gasnault, O., Gellert, R., Gordon, S., Grant, J.A., Grotzinger, J.P., Gupta, S., Herkenhoff, K.E., Hurowitz, J.A., King, P.L., Le Mouélic, S., Leshin, L.A., Léveillé, R., Lewis, K.W., Mangold, N., Maurice, S., Ming, D.W., Morris, R.V., Nachon, M., Newsom, H.E., Ollila, A.M., Perrett, G.M., Rice, M.S., Schmidt, M.E., Schwenzer, S.P., Stack, K., Stolper, E.M., Sumner, D.Y., Treiman, A.H., VanBommel, S., Vaniman, D.T., Vasavada, A., Wiens, R.C., Yingst, R.A., and the MSL Science Team, 2013, Elemental geochemistry of sedimentary rocks at Yellowknife Bay, Gale crater, Mars. Science, 343, 1244734-1, doi: 10.1126/science. 1244734.

McSween, H.Y., McLennan, S.M., 2014, In: Treatise on geochemistry; Chapter 2.10. 2nd Ed., volume 2, Planets, Asteroids, Comets and The Solar System, (eds. H. Holland, and K. Turekian). Elsivier, 251-300, doi.org/10.1016/B978-0-08-095975-7.00125-X.

Metz, Joannah M (2010), A study of the record of ancient sedimentary rocks on Mars using MER, HiRISE and CRISM images. Dissertation (Ph.D.), California Institute of Technology.

Møller, N., 1988, The prediction of mineral solubilities in natural waters: A chemical equilibrium model for the Na-Ca-CI-$S0_4$-H_20 system, to high temperature and concentration. Geochim. Cosmochim. Acta, 52, pp. 821-837.

Montgomery, D.R., and A. Gillespie 2005, Formation of Martian outflow channels by catastrophic dewatering of evaporite deposits, Geology, 33, 625– 628, doi:10.1130/G21270.1.

Morse, J.W., Mackenzie, F.T., 1990, Geochemistry of sedimentary Carbonates. New York, Elsevier, pp. 696.

Mumma, M.J., Villanueva, G.L., Novak, R.E., Hewagama, T., Bonev, B.P., DiSanti, M.A., Mandell, A.M., Smith, M.D., 2009, Strong release of methane on Mars in northern summer 2003. Science, 323, 1041-1045.

Murchie, S.L., Mustard, J.F., Ehlmann, B.L., Miliken, R.E., Bishop, J.L., McKeown, N.K., Noe Dobrea, E.Z., Seelos, F.P., Buczkowski, D.L., Wiseman, S.M., Arvidson, R.E., Wray, J.J., Swayze, G., Clark, R.N., Des Marais, D.J., McEwen, A.S., Bibring, J.-P., 2009, A synthesis of Martian aqueous mineralogy after 1 Mars year of observations from the Mars Reconnaissance Orbiter. J. Geophys. Res., 114, 1-30, E00D06, doi: 10.1029/2009JE003342.

Neukum, G., Wise, D.U., 1976, Mars-A standart crater curve and possible new time scale. Science, 194, 1381-1387, doi:10.1126/science.194.4272.1381.

Neukum, G., Jaumann, R., 2004, HRSC: the High Resolution Stereo Camera of Mars Express. Mars Express: the Scientific Payload, 17-35.

Neukum, G., Jaumann, R., Basilevsky, A.T. Dumke, A., Van Gasselt, S., Giese, B., Hauber, E., Head III, J.W., Heipke, C., Hoekzema, N., Hoffmann, H., Greeley, R., Gwinner, K., Kirk, R., Markiewicz, W., McCord, T.B., Michael, G., Muller, J.-P., Murray, J.B., Oberst, J., Pinet, P., Pischel, R., Roatsch, T., Scholten, F., Willner, K., the HRSC Co-Investigator Team and HRSC Associates, 2009, HRSC: High resolution stereo camera. In: Mars Express: The scientific investigations. ESA, SP-1291, 15-73.

Nishri, A., Herbert, H., Jockwer N., Stichler, W., 1988, The geochemistry of brines and minerals from the Asse salt mine, Germany. Appl. Geochem., 3 (3), pp. 317-332. http://dx.doi.org/10.1016/0883-2927(88)90109-6

Noel, A., Bishop, J., Al-Samir, M., Gross, C., Flahaut, J., McGuire, P.C., Weitz, C.M., Seelos, F., Murchie, S., 2015, Mineralogy, morphology and stratigraphy of the light-toned interior layered deposits at Juventae Chasma. Icarus, 251, 315-331.

Nordstrom, D.K., 1982, The effect of sulfate on aluminum concentrations in natural waters: some stability relations in the system Al_2O_3-SO_3-H_2O at 298 K. Geochim. Cosmochim. Acta, 46, pp. 681-692.

Nordstrom, D.K., 1982, Aqueous pyrite oxidation and the consequent formation of secondary iron minerals. In: Acid Sulfate Weathering, Soil Sci. Soc. Am. J. (SSSA) Special Publication, Fort Collins, Colorado, pp.1-234.

Nordstrom, D.K., Alpers, C.N., Ptacek, C., Blowes, D.W., 2000, Negative pH and extremely acidic mine waters from Iron Mountain, California. Environ. Sci. Technol., 34, 254 – 258.

Nordstrom, D.K., McCleskey, R.B, Ball, J.W., 2009, Sulfur geochemistry of hydrothermal waters in Yellowstone National Park: IV Acid-sulfate waters. Appl. Geochem., 24, 191-207, doi:10.1016/j.apgeochem.2008.11.019.

Obenholzner. J.H., Schroettner, H. Golob, P., Delgado, H., 2003, Particles From the plume of Popocatepetl volcano, Mexico - the FESEM/EDS approach. Geological Society (UK) Special Publication, 213, 1, 123-148.

Owen T.C., 1992, The composition and early history of the atmosphere of Mars. In: Kieffer HH, Jakosky BM, Snyder CW, Matthews MS (eds) Mars. University of Arizona Press, Tucson, pp. 818-834.

Pabalan, R.T., Pitzer, K.S., 1987, Thermodynamics of concentrated electrolyte mixtures and the prediction of mineral solubilities to high temperatures for mixtures in the system Na-K-Mg-Cl-SO_4-OH-H_2O. Geochim. Cosmochim. Acta, 51 (9), 2429-2443.

Pfeiffer, S. and Nohlen, C., 2000, Pyritverwitterung und Gewässerversauerung – ein irreversibler Vorgang? Rundgespräche der Kommission für Ökologie, Bd. 20, Bergbau-Folgeschäden und Ökosysteme, Verlag Dr. Friedrich Pfeil, München, 15–28.

Piper, A.M., 1944, A graphic procedure in the geochemical interpretation of water analyses. Trans. Amer. Geophys. Union, 25, 914-928.

Pritchett, B.N., Elwood Madden, M.E., Madden, A.S., 2012, Jarosite dissolution rates and maximum lifetimes in high salinity brines: Implications for Earth and Mars. Earth Planet. Sci. Lett., 357-358, pp. 327-338.

Ptacek, C., Blowes, D., 2000, Predicting sulfate-mineral solubility in concentrated waters. In: Sulfate Minerals: Crystallography, Geochemistry, and Environmental Significance, Rev. Mineral. Geochem., Vol. 40, edited by C. N. Alpers, J. L. Jambor, and D. K. Nordstrom, pp. 513 – 540, Mineral. Soc. of Am., Washington, D. C.

Pytkowicz, R.M., 1965, Rates of inorganic calcium carbonate precipitation. J. Geol., 73, p. 196 – 199.

Ragan, D.M., 1963, Emplacement of the Twin Sisters Dunite, Washington, Am. J. Sci., 261, 549-565.

Railsback, L. Bruce, 1993, A geochemical view of weathering and the origin of sedimentary rocks and natural waters: J. Geol. Educ., v. 41, p. 404-411.

Railsback, L. Bruce, 1999, Patterns in the compositions, properties, and geochemistry of carbonate minerals: Carbonates Evaporites, v. 14, p. 1-20.

Rollinson, H., 1993, Using geochemical data: evaluation, presentation, interpretation. Longman Scientific and Technical, Essex, pp. 352.

Romanek, C.S., Grady, M.M., Wright, I.P., Mittlefehldt, D.W., Socki, R.A., Pillinger, C.T., Gibson, E.K., 1994, Record of fluid-rock interactions on Mars from the meteorite ALH84001. Nature, 372, p. 655-657.

Rossbacher, L.A., Judson, S., 1981, Ground ice on Mars: Inventory, distribution and resulting landforms. Icarus, 45, 39-59.

Rossi, A.P., Neukum, G., Pondrelli, M., van Gasselt, S., Zegers, T., Hauber, E., Chicarro, A., Foing, B., 2008, Large-scale spring deposits on Mars? J. Geophys. Res. (Planets) 113, E8.

Saper, L., Mustard, J.F., 2013, Extensive linear ridge networks in Nili Fossae and Nilosyrtis, Mars: implications for fluid flow in the ancient crust. Geophys. Res. Lett., 40, 245-249.

Scheffer, F., Schachtschabel, P., 2010, Lehrbuch der Bodenkunde. Springer, Heidelberg, pp. 569.

Schonfeld, E., 1979, Origin of Valles Marineris. 10th Lunar Planet. Sci., 3031-3038.

Schorn, R.A., Spinrad, H., Moore, R.C., Smith, H.J., Giver, L.P., 1967, High-dispersion spectroscopic observations of Mars II. The water-vapor variations. Astrophys. J., 147, 74—752.

Schulz, H.D., Zabel, M., 2000, Marine geochemistry. 2nd rev., Springer, Heidelberg, pp. 574.

Schwertmann, U., 1970, Der Einfluss einfacher organischer Anionen auf die Bildung von Goethit und Hämatit aus amorphem Fe(III)-Hydroxid. Geoderma, 3, 207-214.

Schwertmann, U. and Fischer, W.R., 1973, Natural „amorphous“ ferric hydroxide. Geoderma, 10, 237-247.

Seelos, F.P., Morgan, M. F., Taylor, H. W., Murchie, S. L., Humm, D. C., Seelos, K. D., Barnouin, O. S., Viviano, C. E., and The CRISM Team, 2012, CRISM Map Projected Targeted Reduced Data Records (MTRDRs) – High level analysis and visualization data products. Planetary data: A workshop for users and software developers, Flagstaff, AZ.

Seyfried, W.E. Jr., Ding, K., 1995, The hydrothermal chemistry of fluoride in seawater. Geochim. Cosmochim. Acta, 59, 1063-1071.

Sharp, R. P., 1973a, Mars: Troughed Terrain. J. Geophys. Res., 78, 4063-4072.

Seyfried, W.E. and M.J. Mottl, 1982, Hydrothermal alteration of basalt by seawater under seawater-dominated conditions. Geochim. Cosmochim. Acta, 46, pp. 985-1002.

Smith, D.E., Zuber, M.T., Frey, H.V., Garvin, J.B., Head, J.W., Muhleman, D.O., Pettengill, G.H., Phillips, R.J., Solomon, S.C., Zwally, H.J., Banerdt, W.B., Duxbury, T.C., Golombek, M.P., Lemoine, F.G., Neumann, G.A., Rowlands, D.D., Aharonson, O., Ford, P.G., Ivanov, A.B., Johnson, C.L., McGovern, P.J., Abshire, J.B., Afzal, R.S., Sun, X., 2001, Mars Orbiter Laser Altimeter: Experiment summary after the first year of global mapping of Mars. J. Geophys. Res. 106, E10, 23689-23722, 10.1029/2000JE001364

Smith, D.E., Neumann, G.A., Arvidson, R., Guinness, E., Slavney, S., 2003, Mars Global Surveyor Laser Altimeter Mission Experiment Gridded Data Record. MGS-M-MOLA-5-MEGDR-L3-V1.0 ed., NASA Planetary Data System.

Snow, J.E., Dick, H.J.B., 1995, Pervasive magnesium loss by marine weathering of peridotite. Geochim. Cosmochim. Acta, 59, 4219-4235.

Sonnenfeld, P., 1984, Brines and evaporites. Academic Press Inc., Orlando, San Diego, New York, London, Toronto, Montreal, Sydney, Tokyo, pp. 613.

Sowe, M., 2009. Interior Layered Deposits in chaotic terrains on Mars. PHD Thesis, Freie Universität Berlin, Berlin, pp. 174.

Spencer, R.J., Eugster, H.P., Jones, B.F., 1985, Geochemistry of Great Salt Lake, Utah II: Pleistocene-Holocene evolution. Geochim. Cosmochim. Acta, 49, pp. 739-747.

Spencer, J.R., Fanale, F.P., 1990, New models for the origin of Valles Marineris closed depressions. J. Geophys. Res., 95, 14,301-14,313.

Spencer, R.J., 2000, Sulfate minerals in evaporite deposits. In Sulfate Minerals: Crystallography, Geochemistry, and Environmental Significance, Rev. Mineral. Geochem., Vol. 40, edited by C. N. Alpers, J. L. Jambor, and D. K. Nordstrom, pp. 173 – 192, Mineral. Soc. of Am., Washington, D. C.

Squyres, S., Kasting, J.F., 1994, Early Mars: How warm and how wet? Science, 265, 744-749.

Squyres, S., 1979, The distribution of lobate debris aprons and similar flows on Mars. J. Geophys. Res., 84, 8087-8096.

Squyres, S. ., Arvidson, R.E., Bollen, D., Bell, J.F., Bruckner, J., Cabrol, N.A., Calvin, W.M., Carr, M.H., Christensen, P.R., Clark, B.C., Crumpler, L., Des Marais, D.J., d'Uston, C., Economou, T., Farmer, J., Farrand, W.H., Folkner, W., Gellert, R., Glotch, T.D., Golombek, M., Gorevan, S., Grant, J.A., Greeley, R., Grotzinger, J., Herkenhoff, K.E., Hviid, S., Johnson, J.R., Klingelhofer, G., Knoll, A.H., Landis, G., Lemmon, M., Li, R., Madsen, M.B., Malin, M.C., McLennan, S.M., McSween, H.Y., Ming, D.W., Moersch, J., Morris, R.V., Parker, T., Rice, J.W., Richter, L., Rieder, R., Schroder, C., Sims, M., Smith, M., Smith, P., Soderblom, L.A., Sullivan, R., Tosca, N.J., Wanke, H., Wdowiak, T., Wolff, M. and Yen, A., 2006, Overview of the Opportunity Mars Exploration Rover mission to Meridiani Planum: Eagle crater to Purgatory ripple. J. Geophys. Res., Planets 111, E12S12.

Stevens, A.H., Patel, M.R., Lewis, S.R., 2015, Numerical modelling of the transport of trace gases including methane in the subsurface of Mars. Icarus, 250, 587-594, doi:10.1016/j.icarus.2014.12.033.

Stoiber, R., Rose, W. Jr., 1974, Fumarole incrustations at active Central American volcanoes. Geochim. Cosmochim. Acta, 38, 495-516.

Streckeisen, A.L., 1974, Classification and nomenclature of plutonic rocks. Recommendations of the IUGS subcommission on the systematics of igneous rocks. Geologische Rundschau. Internationale Zeitschrift für Geologie. Stuttgart, 63, 773-785.

Stumm, W., Morgan, J.J., 1981, Aquatic chemistry. 3rd edition. Wiley & Sons, New York, pp. 780.

Summerson, I., Greshake, A., Fritz, J., Reimold, W.U., 2013, High-pressure phases in a melt pocket within an olivine macrocyst in the Tissint martian meteorite. 44th Lunar Planet. Sci., Vol. 44, The Woodlands, Tx, abs.#1974.

Tanaka, K.L., Skinner, J.A. Jr., Dohm, J.M., Irwin, R.P., Kolb, E.J., Fortezzo, C.M., Platz, T., Michael, G.G., Hare, M., 2014, Geologic Map of Mars: U.S. Geological Survey Scientific Investigations Map 3292, scale 1:20,000,000, pamphlet 43 p., http://dx.doi.org/10.3133/sim3292.

Thornber, C.R., Sherrod, D.R., Siems, D.F., Heliker, C.C., Meeker, G.P., Oscarson, R.L. & Kauahikaua, J.P., 2002, Whole-rock and glass major-element chemistry of Kilauea Volcano, Hawaii, near-vent eruptive products: September 1994 through September 2001. US Geological Survey Open File Report 02-17 (http://geopubs.wr.usgs.gov/open-file/of02-017).

Tosca, N.J., McLennan, S.M., Lindsley, D.H., Schoonen, A.A., 2004, Acid-sulfate weathering of synthetic Martian basalt: The acid fog model revisited. J. Geophys. Res., 109, 1-29, E05003, doi:10.1029/2003JE002218.

Tosca, N.J., McLennan, S.M., Clark, B.C., Grotzinger, J.P., Hurowitz, J.A., Knoll, A.H., Schröder, C., Squyres, S.W., 2005, Geochemical modeling of evaporation processes on Mars: Insight from the sedimentary record at Meridiani Planum. Earth Planet. Sci. Lett., 240, 122-148, doi:10.1016/j.epsl.2005.09.042.

Tosca, N.J., McLennan, S.M., 2006, Chemical divides and evaporite assemblages on Mars. Earth Planet. Sci. Lett., 241, 21-31, doi:10.1016/j.epsl.2005.10.021.

Usiglio, J. 1849, Zusammensetzung des Wassers des mittelländischen Meeres an den französischen Küsten. Annalen der Chemie (heute Journal für praktische Chemie), 46, p. 106-109.

van Gasselt, S., 2007, Cold-climate landforms on Mars. PhD thesis, Freie Universität Berlin, Berlin, pp. 264.

Vaniman, D.T., Bish, D.L., Ming, D.W., Bristow, T.F., Morris, R.V., Blake, D.F., Chipera, S.J., Morrison, S.M., Treiman, A.H., Rampe, E.B., Rice, M., Achilles, C.N., Grotzinger, J.P., McLennan, S.M., Williams, J., Bell III, J.F., Newsom, H.E., Downs, R.T., Maurice, S., Sarrazin, P., Yen, A.S., Morookian, J.M., Farmer, J.D., Stack, K., Milliken, R.E., Ehlmann, B.L., Sumner, D.Y., Berger, G., Crisp, J.A., Hurowitz, J.A., Anderson, R., Des Marais, D.J., Stolper, E.M., Edgett, K.S., Gupta, S., Spanovich, N. and the MSL Science Team, 2014, Mineralogy of a mudstone at Yellowknife Bay, Gale crater, Mars. Science, 343, 124380-1, doi: 10.1126/science. 124380.

Viviano-Beck, C.E., Murchie, S.L., 2014, Hydrothermally altered stratigraphy in the walls of Valles Marineris. 45th Lunar Planet. Sci., Vol. 45, The Woodlands, Tx, abs.#1963.

Walter, R., 1995, Geologie von Mitteleuropa. 5th edn. Schweizerbart, Stuttgart, pp. 1-566.

Warren, J.K., 2000, Dolomite: occurrence, evolution and economically important associations. Earth-Science Reviews, 52, pp. 1-81.

Warren, J.K., 2006, Evaporites – Sediments, Resources and Hydrocarbons. Springer, Berlin – Heidelberg, pp. 1036.

Webster, C.R., Mahaffy, P.R., Atreya, S.K., Flesch, G.J., Mischna, M.A., Meslin, P.-Y., Farley, K.A., Conrad, P.G., Christensen, L.E., Pavlov, A.A., Martin-Torres, J., Zorzano, M.-P., McConnochie, H., Owen, T., Eigenbrode, J.L., Glavin, D.P., Steele, A., Malespin, C.A., Archer Jr., P.D., Sutter, B., Coll, P., Freissinet, C., McKay, C.P., Moores, J.E., Schwenzer, S.P., Bridges, J.C., Navarro-Gonzalez, R., Gellert, R., Lemmon, M.T., the MSL Science Team, 2015, Mars methane detection and variability at Gale crater. Science, 347, 415-417, doi:101126/science.1261713.

Weitz, C. M., Milliken, R. E., Grant, J. A., McEwen, A. S., Williams, R. M. S., Bishop, J. L., 2008, Light-toned strata and inverted channels adjacent to Juventae and Ganges Chasmata, Mars. Geophys. Res. Lett., 35, L19202, doi:10.1029/2008GL035317.

Weitz, C. M., Milliken, R. E., Grant, J. A., McEwen, A. S., Williams, R. M. S., Bishop, J. L., Thomson, B. J., 2009, Mars Reconnaissance Orbiter observations of light-toned layered deposits and associated fluvial landforms on the plateaus adjacent to Valles Marineris. Icarus, doi:10.1016/j.icarus.2009.1004.1017.

Weitz, C. M., Bishop, J.L., Thollot, P., Mangold, N., Roach, L.H., 2011, Diverse mineralogies in two throughs of Noctis Labyrinthus, Mars. Geology, 39 (10), 899-902, doi: 10.1130/G32045.1.

Weitz, C.M., Bishop, J.L., Baker, L.L., Berman, D.C., 2015, Fresh exposures of hydrous Fe-bearing amorphous silicates on Mars. Geophys. Res. Lett., 41, 8744-8751, doi: 10.1002/2014GL062065.

Wendt, L., Combe, J.-P., McGuire, P.C., Bishop, J.L. and Neukum, G., 2009, Linear spectral unmixing of near-infrared hyperspectral data from Juventae Chasma, Mars. Image and Signal Processing for Remote Sensing XV, edited by Bruzzone, L., Notarnicola, C., and Posa, F., Proceedings of SPIE Vol. 7477 (SPIE, Bellingham, WA, 2009), 7477 0M.

Wendt, L., 2012, Phyllosilicates and Sulfates on Mars. PhD thesis, Freie Universität Berlin, Berlin, pp. 160.

Wolery, T.J., 1983, EQ3NR, a computer program for geochemical aqueous speciationsolubility calculations: users guide and documentation. UCRL-53414. Lawrence Livermore National Laboratory, Livermore, Calif.

Wolery, T., 1992, EQ3/6: Software package for geochemical modeling of aqueous systems: package overview and installation guide (version 7.0). Report UCRL-MA- 210662. Lawrence Livermore National Laboratory, Livermore, Calif.

Zahnle, K., Freedman, R.S., Catling, D.C., 2011, Is there methane on Mars? Icarus, 212, 493-503, doi:10.1016/j.icarus.2010.11.027.

Zurek, R.W., 1992, Comparative aspects of the climate of Mars: An introduction to the current atmosphere. In: Kieffer HH, Jakosky BM, Snyder CW, Matthews MS (eds) Mars. University of Arizona Press, Tucson, pp. 799-817.

Appendix

Appendix 1: Sample images

Appendix 2: X-ray fluorescence analyses

Appendix 3: Diffractograms

Appendix 4: Measured data of the pH 1.3 and pH 3 solution samples

Appendix 5: Input scipts for GWB

Appendix 6: Mineral assemblages in cm^3

Appendix 1: Sample images

Figure 1.1: Olivine

Figure 1.2: Plagioclase-Bytownite

Figure 1.3: Xhenolith

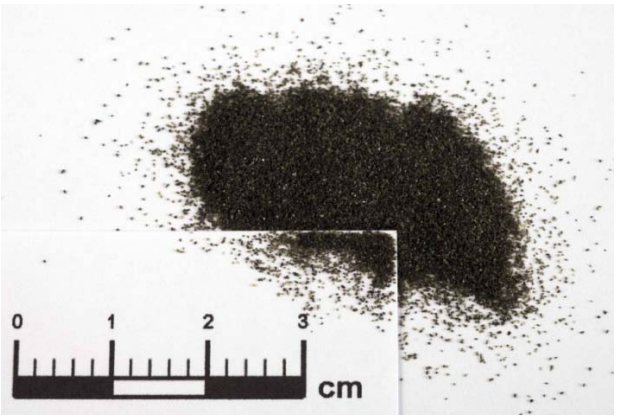

Figure 1.4: Clinopyroxene

Appendix 1: Sample images

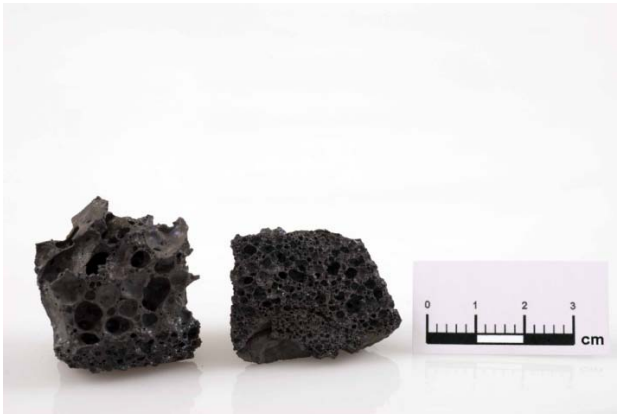

Figure 1.5: Volcanic glass

Figure 1.6: Orthopyroxene

Figure 1.7: 1-komatiite

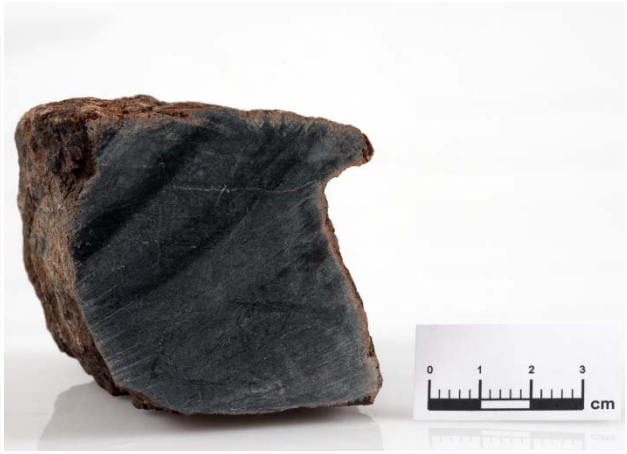

Figure 1.8: s-komatiite

Appendix 1: Sample images

Figure 1.9: BIR-1a & DTS-2b

Figure 1.10: Tissint

Appendix 2: X-ray fluorescence analyses of mafic to ultramafic rocks, minerals and the martian meteorite Tissint.

Sample ID	SiO_2 (%)	TiO_2 (%)	Al_2O_3 (%)	FeO (%)	MnO (%)	MgO (%)	CaO (%)	Na_2O (%)	K_2O (%)	P_2O_5 (%)	H_2O (%)	CO_2 (%)	Σ (%)	Ba (ppm)	Cr (ppm)	Ga (ppm)	Nb (ppm)	Ni (ppm)	Rb (ppm)	Sr (ppm)	V (ppm)	Y (ppm)	Zn (ppm)	Zr (ppm)
Tissint	44.5	0.673	5.3	22.8	0.504	16.84	6.86	0.03	<0.01	0.51	bld	bdl	97.99	110	5307	11	26	264	117	44	229	19	78	27
Olivine	40.5	0.010	0.1	10.2	0.131	48.52	0.11	<0.01	<0.01	<0.01	0.04	0.05	99.70	10	253	<10	<10	2715	11	<10	<10	<10	55	13
Clinopyroxene	48.0	1.631	6.1	7.4	0.102	13.40	22.28	0.42	0.14	0.04	0.14	0.09	99.69	134	493	10	<10	120	28	146	282	11	23	95
Orthopyroxene	49.2	0.441	6.1	19.5	0.265	22.14	1.80	0.04	<0.01	0.01	0.24	0.07	99.82	26	671	10	<10	175	16	<10	298	<10	154	18
Plagioclase	49.0	0.045	31.8	0.5	<0.01	0.07	15.23	2.42	0.07	<0.01	0.54	0.25	99.89	57	<10	17	<10	<10	13	473	<10	<10	<10	19
Volcanic Glass	48.6	2.063	11.2	12.9	0.166	12.84	9.34	1.70	0.38	0.21	0.18	0.05	99.58	201	680	17	12	459	22	320	247	21	98	152
1-komatiite	41.0	0.249	2.3	12.6	0.180	31.37	1.89	<0.01	<0.01	0.03	9.38	0.12	99.12	64	4542	<10	<10	1867	16	11	82	<10	68	28
s-komatiite	43.4	0.354	4.1	12.3	0.171	26.43	5.21	0.08	0.01	0.03	7.32	0.08	99.43	29	2235	<10	<10	1510	18	23	127	<10	70	30
Xenolith	44.6	0.027	1.8	8.0	0.114	41.73	1.37	0.08	<0.01	0.02	1.43	0.14	99.34	<10	2801	<10	<10	2267	10	23	39	<10	47	23
BIR-1a	47.8	0.974	15.3	11.5	0.172	9.54	13.12	1.65	0.01	0.02	0.29	0.07	100.51	<10	383	17	<10	169	16	111	330	14	75	27
DTS-2b	39.4	0.012	0.4	7.9	0.103	49.07	0.11	0.01	<0.01	<0.01	0.87	0.15	97.95	11	14829	<10	<10	3708	<10	<10	28	<10	57	15

.% = weight percent; ppm = mg/kg; bdl = below detection limit.

Appendix 3: Diffractograms

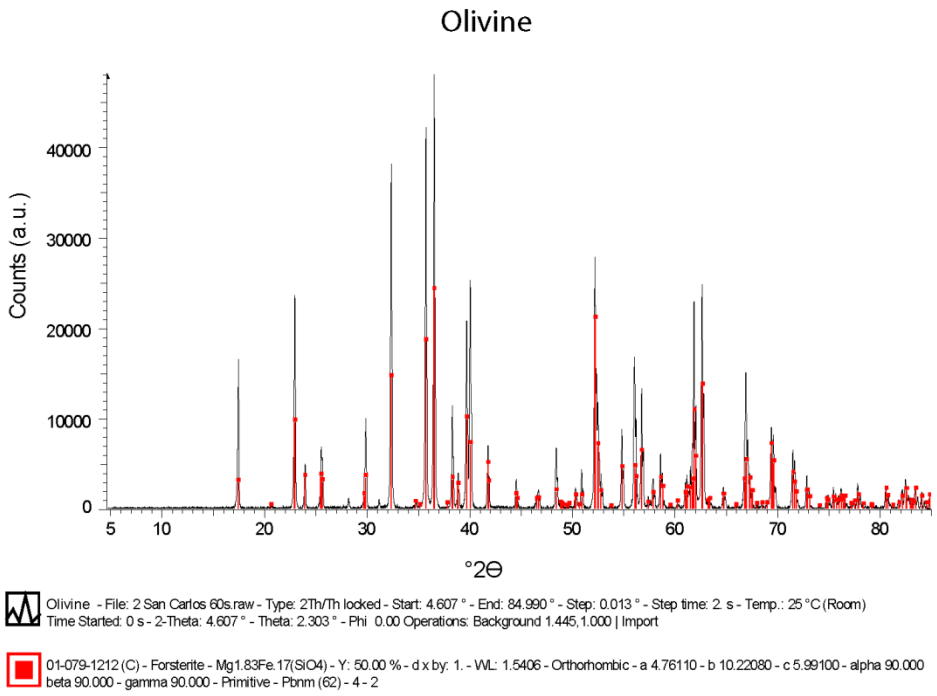

Figure 3.1: Diffractogram of the olivine sample showing the end-member forsterite.

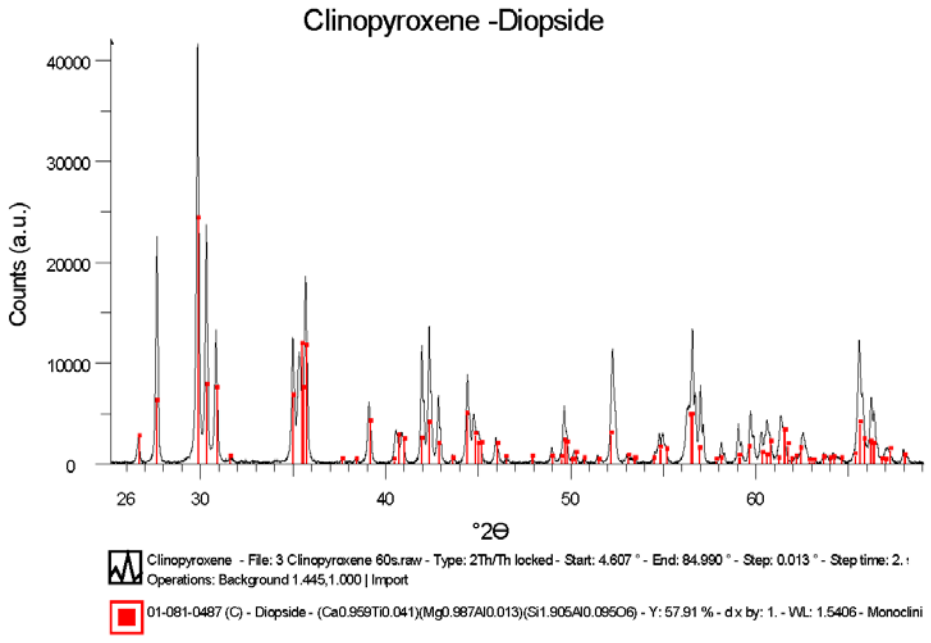

Figure 3.2: Diffractogram of the cpx sample.

Appendix 3: Diffractograms

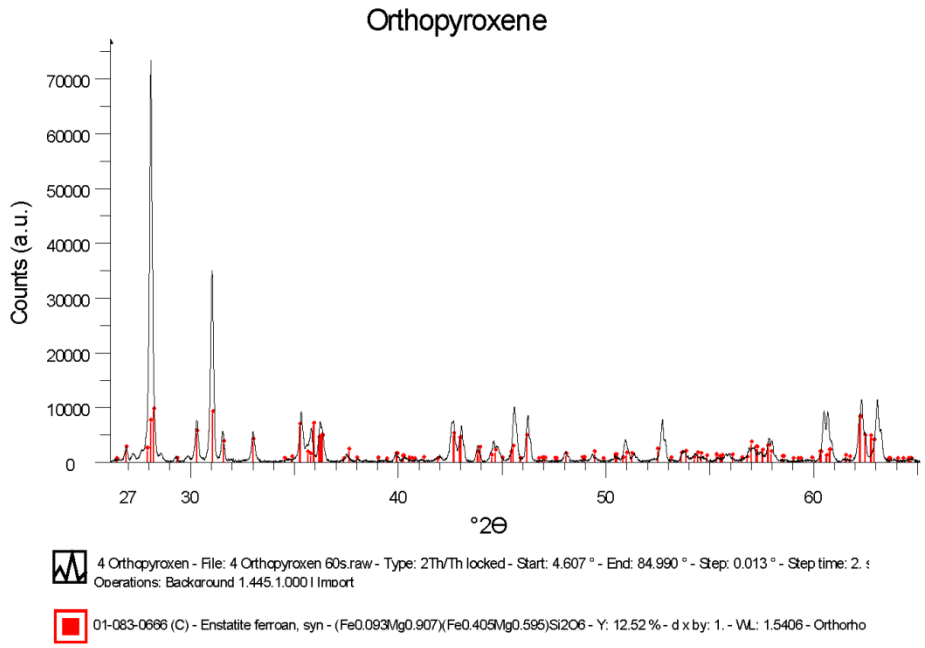

Figure 3.3: Diffractogram of the opx sample.

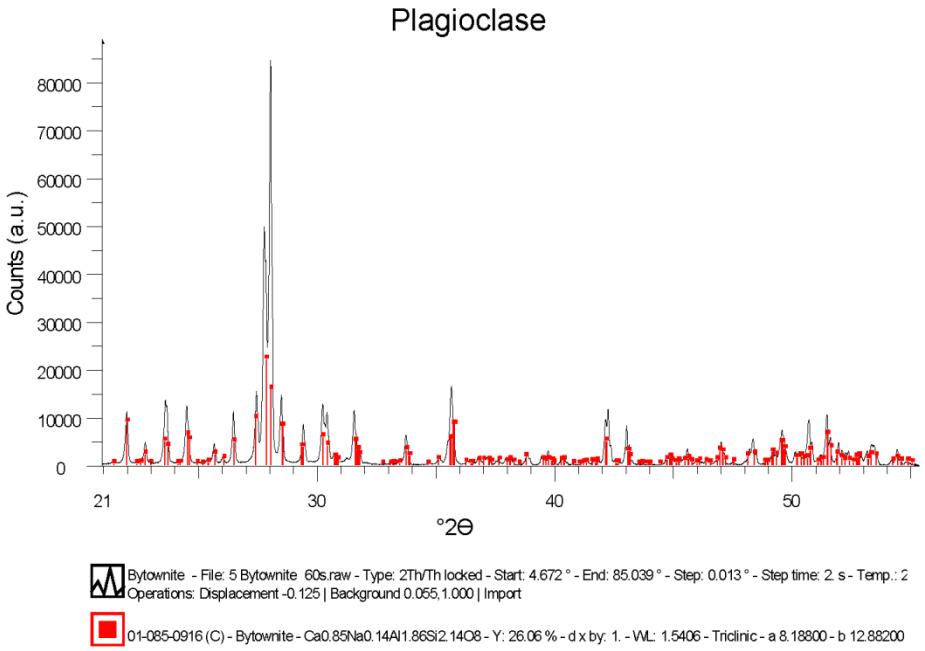

Figure 3.4: Diffractogram of the plagioclase sample.

Appendix 3: Diffractograms

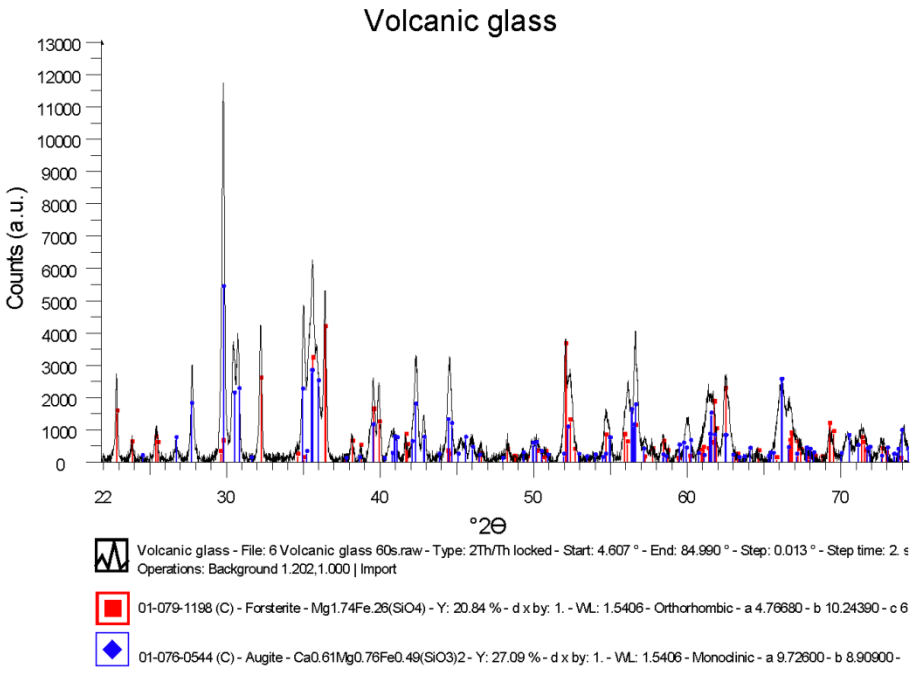

Figure 3.5: Diffractogram of the volcanic glass sample containing forsterite and augite.

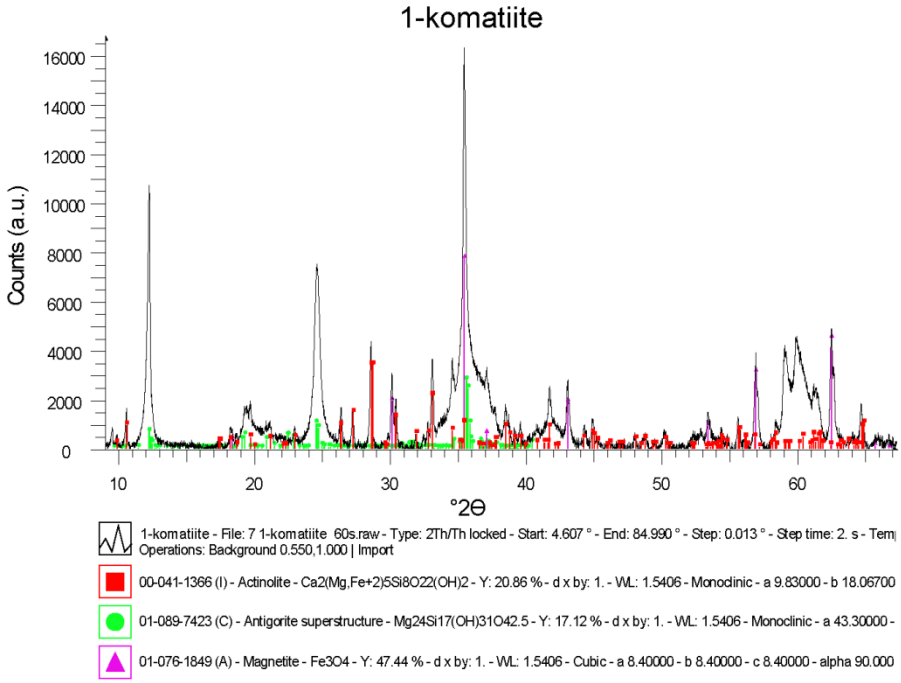

Figure 3.6: Diffractogram of the 1-komatiite sample containing actinolite, antigorite, and magnetite.

Appendix 3: Diffractograms

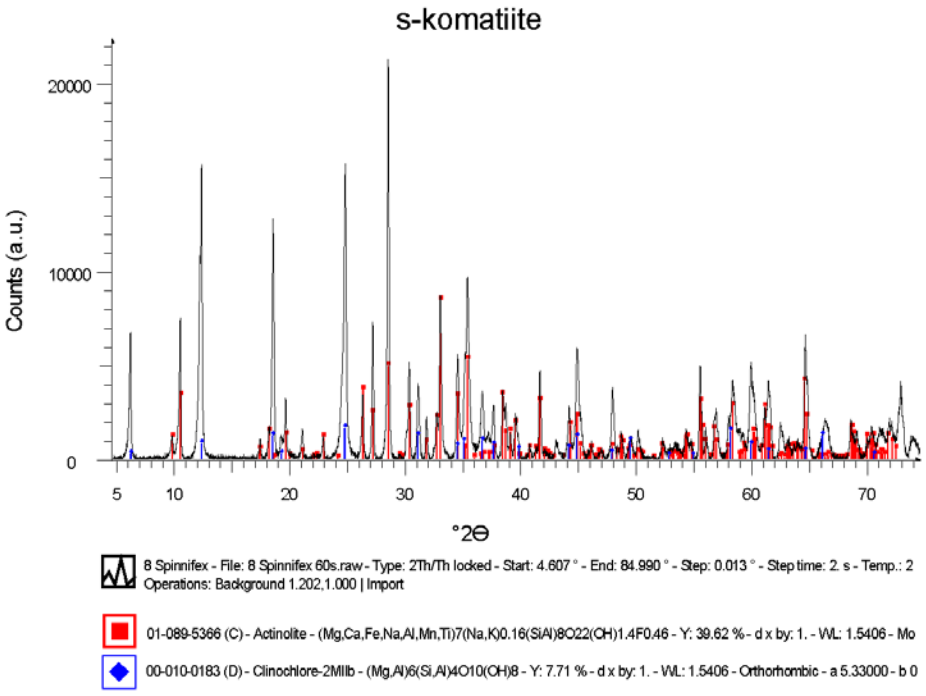

Figure 3.7: Diffractogram of the s-komatiite sample containing actinolite and clinochlore.

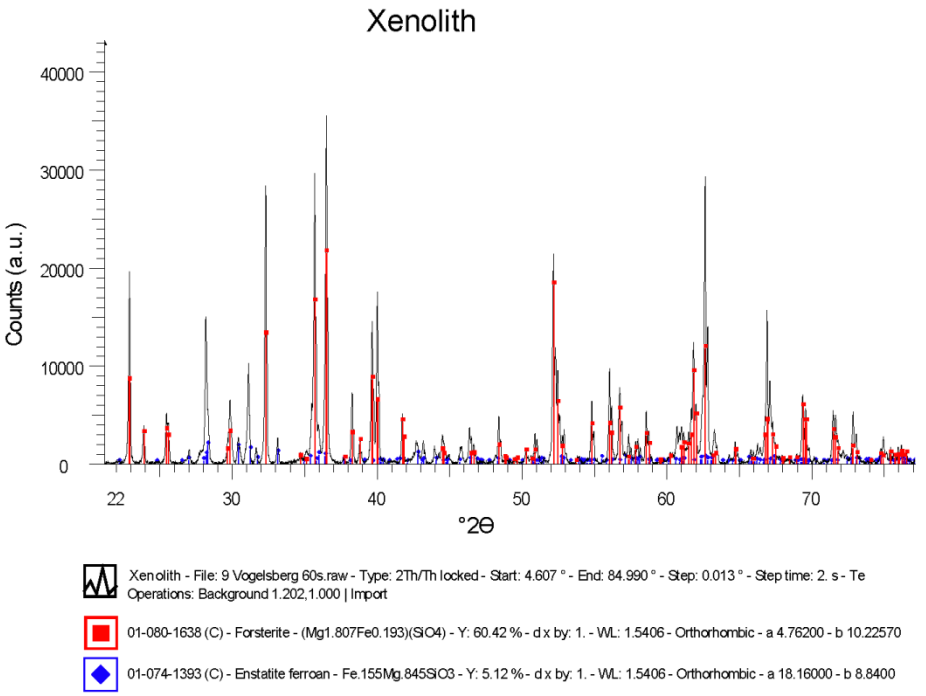

Figure 3.8: Diffractogram of the xenolith sample containing forsterite and enstatite.

Appendix 4: Measured data of the pH 1.3 solution samples

ICP-results of the pH 1.3-samples [mg/L]

Samples/Ions	Na	K	Ca	Mg	Mn	Fe	Al	CL	SO4
1a	13.5	13.9	62.6	39.4	1.1	42.1	12.2	17	455
1b	12.4	0.5	60.9	37	1.1	39	11.3	6.6	425
1c	14.1	0.6	64.7	43.1	1.2	44.6	16.9	6.8	509
1 mean value	13.33	5	62.73	39.83	1.13	41.9	13.47	10.13	463
1 value-BM	3.93	4.7	55.93	38.13	1.13	41.84	13.38	0.23	
2a	5.1	0.1	3.9	85.6	0.3	7.8	0.1	6.2	340
2b	5.5	0.1	3.8	86.1	0.3	7.6	0.05	7.4	345
2c	5.6	0.2	4.4	119	0.4	15.1	0.1	7.8	485
2 mean value	5.4	0.13	4.03	96.9	0.33	10.17	0.08	7.13	390
2 value-BM	-4	-0.17	-2.77	95.2	0.33	10.11	-0.01	-2.77	
3a	13.1	7.6	39.1	22.3	0.3	10.1	18.9	9.2	342
3b	11.8	7.5	40	22.9	0.27	10.6	19	8.2	353
3c	11.5	7.6	37.9	21.9	0.27	9.9	18.5	8.6	340
3 mean value	12.13	7.57	39	22.37	0.28	10.2	18.8	8.67	345
3 value-BM	2.73	7.27	32.2	20.67	0.28	10.14	18.71	-1.23	
4a	7.9	0.3	8.6	20.8	0.23	21.1	8.1	8.2	355
4b	5.4	0.2	7.2	21.4	0.24	25.8	8.6	6.6	360
4c	7.7	0.3	9.3	21.7	0.23	24.8	8.5	8.1	354
4 mean value	7	0.27	8.37	21.3	0.23	23.9	8.4	7.63	356.33
4 value-BM	-2.4	-0.03	1.57	19.6	0.23	23.84	8.31	-2.27	
5a	18.7	0.3	39.4	1.3	0.006	0.71	43.2	8.7	360
5b	18	0.2	40.1	1.2	0.006	0.7	43.6	8.6	370
5c	17.6	0.2	39.3	1.2	0.006	0.7	43.6	7.7	357
5 mean value	18.1	0.23	39.6	1.23	0.006	0.70	43.47	8.33	362.33
5 value-BM	8.7	-0.07	32.8	-0.47	0.006	0.64	43.38	-1.57	
6a	14	1	24.4	51.2	0.5	28.3	11.1	8.6	390
6b	11.3	1	25	52.7	0.5	28.9	11.7	7.5	400
6c	10.4	1	22.6	49.8	0.5	27.7	10.9	7.8	370
6 mean value	11.9	1	24	51.23	0.5	28.3	11.23	7.97	386.67
6 value-BM	2.5	0.7	17.2	49.53	0.5	28.24	11.14	-1.93	
7a	6	0.2	9.3	73	0.8	6.4	5.3	7.2	362
7b	6.6	0.1	10.4	74.2	0.8	6.4	5.3	7.6	362
7c	5.2	0.1	8.3	74.4	0.8	6.6	5.4	7	362
7 mean value	5.93	0.13	9.33	73.87	0.8	6.47	5.33	7.27	362
7 value-BM	-3.47	-0.17	2.53	72.17	0.8	6.41	5.24	-2.63	
8a	7.7	0.5	10.7	62.9	0.5	9.7	10.3	9.4	363
8b	6	0.5	9.9	64.5	0.5	9.9	10.9	7.7	365
8c	5.3	0.4	9.3	63.3	0.5	10.1	11.1	6.8	362
8 mean value	6.33	0.47	9.97	63.57	0.5	9.9	10.77	7.97	363.33
8 value-BM	-3.07	0.17	3.17	61.87	0.5	9.84	10.68	-1.93	
9a	6.3	0.4	7.8	83.3	0.3	1.6	0	8.7	334
9b	7.9	0.5	9.1	88.5	0.3	0.6	0	8	360
9 mean value	7.1	0.45	8.45	85.9	0.3	1.1	0	8.35	347
9 value-BM	-2.3	0.15	1.65	84.2	0.3	1.04	-0.09	-1.55	
10a	11.5	0.2	36.8	8.8	0.1	7.1	40	9.1	370
10b	13.4	0.2	37.3	8.1	0.1	6.5	38.4	9.6	360
10c	12.8	0.2	37.4	7.8	0.1	5.8	37.1	9.1	350
10 mean value	12.57	0.2	37.17	8.23	0.1	6.47	38.5	9.27	360
10 value-BM	3.17	-0.1	30.37	6.53	0.1	6.41	38.41	-0.63	
11a	7.4	0.1	5.8	94.8	0.08	0	0	9.5	362
11b	7.6	0.2	5.7	92.3	0.07	0	0	8.9	355
11c	8.7	0.1	6.1	96.4	0.07	0	0	9.7	364
11 mean value	7.9	0.13	5.87	94.5	0.07	0	0	9.37	360.33
11 value-BM	-1.5	-0.17	-0.93	92.8	0.07	-0.06	-0.09	-0.53	
B1	9.4	0.3	6.8	1.7	0	0.06	0.09	9.9	356

B1=blank value-BM=value-blank

1=Tissint, 2=olivine, 3=cpx, 4=opx, 5=plagioclase, 6=volcanic glass, 7=1-komatiite, 8=s-komatiite, 9=xenolith, 10=Bir-1a, 11=DTS-2b

Appendix 4: Measured data of the pH 3 solution samples

ICP-results of the pH 3-samples [mg/L]

Samples/Ions	Na	K	Ca	Mg	Mn	Fe	Al	Cl	SO4	NO3
1a	10.2	22.1	16.3	6.9	0.1	0.01	0	27	62	0
1 value-BM	5.15	21.95	12	6	0.1	-0.025	0	22.9		-0.45
2a	11	0.8	6.3	12.8	0.01	0.3	0	7	60	0
2b	12.7	0.7	7	12.7	0.01	0.33	0	8	61	0
2c	14.1	0.6	7.1	12.2	0.009	0.13	0	9.5	61	0
2 mean value	12.60	0.70	6.80	12.57	0.01	0.25	0.00	8.17	60.67	0.00
2 value-BM	7.550	**0.550**	**2.500**	**11.667**	**0.010**	**0.218**	**0.000**	**4.067**	**-0.333**	**-0.450**
3a	8.1	2.1	12.8	5.4	0.06	0.002	0	5	60	0
3b	13.1	2.3	11.1	3.9	0.05	0.5	0.06	7	60	0
3c	10.6	2.3	10.7	3.8	0.06	0.8	0.7	6	60	0
3 mean value	10.60	2.23	11.53	4.37	0.06	0.43	0.25	6.00	60.00	0.00
3 value-BM	5.55	2.08	7.23	3.47	0.06	0.40	0.25	1.90	-1.00	-0.45
4a	9	0.5	6.8	7.6	0.1	2.2	0.07	6	60	0
4b	9.2	0.3	6.3	7.8	0.1	2.2	0.08	6	60	0
4c	8.2	0.6	5.9	7.8	0.1	3	0.1	6	60	0
4 mean value	8.80	0.47	6.33	7.73	0.10	2.47	0.08	6.00	60.00	0.00
4 value-BM	3.75	0.32	2.03	6.83	0.10	2.43	0.08	1.90	-1.00	-0.45
5a	4.6	0.1	9.4	0.5	0.003	0.2	4.3	2	57	6.5
5b	4.5	0.2	7.9	0.5	0.003	0.1	5.3	2.5	57	7.4
5c	4.4	0.2	7.6	0.4	0.003	0.1	5.4	3	58	6.3
5 mean value	4.50	0.17	8.30	0.47	0.00	0.13	5.00	2.50	57.33	6.73
5 value-BM	-0.55	0.02	4.00	-0.43	0.00	0.10	5.00	-1.60	-3.67	6.28
6a	10.3	0.4	8.5	7.5	0.08	0.2	0	5.5	60	0
6b	11.8	0.6	9	7.6	0.08	0.3	0	7	60	0
6c	12.6	0.5	9.3	7.2	0.07	0.4	0.02	7	60	0
6 mean value	11.57	0.50	8.93	7.43	0.08	0.30	0.01	6.50	60.00	0.00
6 value-BM	6.52	0.35	4.63	6.53	0.08	0.27	0.01	2.40	-1.00	-0.45
7a	6.7	0.4	5.4	14.5	0.02	0.02	0	5	61	0
7b	10.8	0.3	7.9	12.1	0.007	0.02	0	7	63	0
7c	8.6	0.3	7.2	12.9	0.007	0.02	0	6.5	63	0
7 mean value	8.70	0.33	6.83	13.17	0.01	0.02	0.00	6.17	62.33	0.00
7 value-BM	3.65	0.18	2.53	12.27	0.01	-0.02	0.00	2.07	1.33	-0.45
8a	0.1	0.3	2.9	15.4	0	0.01	0	1	58	13.7
8b	1.6	0.3	4.8	15.1	0.003	0.02	0	2	61	7.7
8c	1.7	0.3	3.6	15.4	0	0.008	0	2	58	8.7
8 mean value	1.13	0.30	3.77	15.30	0.00	0.01	0.00	1.67	59.00	10.03
8 value-BM	-3.92	0.15	-0.53	14.40	0.00	-0.02	0.00	-2.43	-2.00	9.58
9a	1.4	0.5	5	15.9	0	0	0	2	58	10.3
9b	1.5	0.5	4.8	15.7	0	0	0	2	58	13
9c	2	0.6	5.7	15.9	0	0	0	2	59	14
9 mean value	1.63	0.53	5.17	15.83	0.00	0.00	0.00	2.00	58.33	12.43
9 value-BM	-3.42	0.38	0.87	14.93	0.00	-0.04	0.00	-2.10	-2.67	11.98
10a	3.2	0.2	7.8	2.3	0.06	1	4.2	2	58	5.8
10b	2.6	0.15	7.9	2.3	0.06	1.1	4.2	1	57	6.2
10c	2.9	0.15	7.9	2.3	0.06	1	4.1	2	58	10
10 mean value	2.90	0.17	7.87	2.30	0.06	1.03	4.17	1.67	57.67	7.33
10 value-BM	-2.15	0.02	3.57	1.40	0.06	1.00	4.17	-2.43	-3.33	6.88
11a	5.1	0.2	3.9	17.1	0	0	0	4	59	0
11b	9.3	0.5	5.8	15.7	0	0	0	7	61	0
11c	7	0.4	4.8	17.2	0	0	0	5.6	60	0
11 mean value	7.13	0.37	4.83	16.67	0.00	0.00	0.00	5.53	60.00	0.00
11 value-BM	2.08	0.22	0.53	15.77	0.00	-0.04	0.00	1.43	-1.00	-0.45
B1	5.2	0.2	3.7	0.9	0	0.05	0	4.4	61	0.5
B2	4.9	0.1	4.9	0.9	0	0.02	0	3.8	61	0.4
mean B	5.05	0.15	4.3	0.9	0	0.035	0	4.1	61	0.45

B=blank value-BM=mean value-blank

1=Tissint, 2=olivine, 3=cpx, 4=opx, 5=plagioclase, 6=volcanic glass, 7=1-komatiite, 8=s-komatiite, 9=xenolith, 10=Bir-1a, 11=DTS-2b

Appendix 5: Input scripts for Geochemist's Workbench (GWB)

Chemical formula of minerals in LLNL (Lawrence Livermore National Laboratories) Database provided by GWB

Suppressed minerals:

Arcanite	K_2SO_4
Artinite	$Mg_2CO_3(OH)_2{:}3H_2O$
Brucite	$Mg(OH)_2$
Dolomite	$CaMg(CO_3)_2$
Hydromagnesite	$Mg_5(CO_3)_4(OH)_2{:}4H_2O$
Magnesite	$MgCO_3$
Na-Sulfate	$Na_3H(SO_4)_2$
Nesquehonite	$Mg(HCO_3)(OH){:}2H_2O$
Rhodochrosite	$MnCO_3$
Siderite	$FeCO_3$

Tissint pH 1.3

```
data = "C:\Program Files\Gwb\Gtdata\thermo.dat" verify
temperature = 25 C
decouple Fe+++
H2O = 1 free kg
Fe+++ = 41.84 mg/l
Ca++ = 55.93 mg/l
balance on Ca++
Cl- = .23 mg/l
Mg++ = 38.13 mg/l
Na+ = 3.93 mg/l
K+ = 4.7 mg/l
SO4-- = 463 mg/l
Al+++ = 13.38 mg/l
Mn++ = 1.13 mg/l
pH = 3.55
swap CO2(g) for HCO3-
CO2(g) = -2.2 log fugacity
react -999.9 g of H2O
suffix _TissintpH1_3
delxi = 1e-4 linear
```

Tissint pH 3

```
data = "C:\Program Files\Gwb\Gtdata\thermo.dat" verify
temperature = 25 C
H2O = 1 free kg
Ca++ = 12 mg/l
Mg++ = 6 mg/l
Na+ = 5.15 mg/l
K+ = 21.95 mg/l
SO4-- = 62 mg/l
Cl- = 22.9 mg/l
balance on Cl-
Fe++ = .01 mg/l
Mn++ = .1 mg/l
pH = 6.54
swap CO2(g) for HCO3-
CO2(g) = -2.2 log fugacity
react -999.9 g of H2O
fix fugacity of CO2(g)
suffix _TissintpH3
delxi = 1e-5 linear
```

Appendix 5: Input scripts for Geochemist's Workbench (GWB)

Olivine pH 1.3

```
data = "C:\Program Files\Gwb\Gtdata\thermo.dat" verify
temperature = 25 C
decouple Fe+++
H2O = 1 free kg
Mg++ = 95.2 mg/l
SO4-- = 390 mg/l
Fe+++ = 10.11 mg/l
balance on Fe+++
pH = 4.1
swap CO2(g) for HCO3-
CO2(g) = -2.2 log fugacity
react -999.9 g of H2O
suffix _olivinepH1_3
delxi = 1e-5 linear
```

Olivine pH 3

```
data = "C:\Program Files\Gwb\Gtdata\thermo.dat" verify
temperature = 25 C
 H2O = 1 free kg
Ca++ = 2.5 mg/l
Mg++ = 11.67 mg/l
Na+ = 7.55 mg/l
balance on Na+
K+ = .55 mg/l
SO4-- = 60.67 mg/l
Cl- = 4.067 mg/l
Fe++ = .218 mg/l
Mn++ = .01 mg/l
pH = 7.51
swap CO2(g) for HCO3-
CO2(g) = -2.2 log fugacity
react -999 g of H2O
suffix _olivinepH3
delxi = 1e-5 linear
```

Clinopyroxene pH 1.3

```
data = "C:\Program Files\Gwb\Gtdata\thermo.dat" verify
temperature = 25 C
decouple Fe+++
H2O = 1 free kg
Ca++  = 32.2 mg/l
balance on Ca++
Mg++ = 20.67 mg/l
Na+ = 2.73 mg/l
K+ = 7.27 mg/l
SO4-- = 345 mg/l
Al+++ = 18.71 mg/l
Fe+++  = 10.14 mg/l
pH = 2.75
swap CO2(g) for HCO3-
CO2(g) = -2.2 log fugacity
react -999.9 g of H2O
suffix _ClinopyroxenepH1_3
delxi = 1e-5 linear
```

Clinopyroxene pH 3

```
data = "C:\Program Files\Gwb\Gtdata\thermo.dat" verify
temperature = 25 C
H2O = 1 free kg
Ca++  = 7.23 mg/l
Mg++ = 3.47 mg/l
Na+ = 5.55 mg/l
balance on Na+
K+ = 2.08 mg/l
swap CO2(g) for HCO3-
CO2(g) = -2.2 log fugacity
SO4-- = 60 mg/l
Cl- = 1.9 mg/l
Al+++ = .25 mg/l
Fe++ = .4 mg/l
Mn++ = .06 mg/l
pH = 4.18
react -999.9 g of H2O
suffix _ClinopyroxenepH3
delxi = 1e-5 linear
```

Appendix 5: Input scripts for Geochemist's Workbench (GWB)

Orthopyroxene pH 1.3

```
data = "C:\Program Files\Gwb\Gtdata\thermo.dat" verify
temperature = 25 C
decouple Fe+++
H2O = 1 free kg
Ca++ = 1.57 mg/l
Mg++ = 19.6 mg/l
SO4-- = 356.3 mg/l
balance on SO4--
Al+++ = 8.31 mg/l
Fe+++ = 23.84 mg/l
pH = 2.17
swap CO2(g) for HCO3-
CO2(g) = -2.2 log fugacity
react -999.9 g of H2O
suffix _OrthopyroxenepH1_3
delxi = 1e-5 linear
```

Orthopyroxene pH 3

```
data = "C:\Program Files\Gwb\Gtdata\thermo.dat" verify
temperature = 25 C
H2O = 1 free kg
Ca++ = 2.03 mg/l
Mg++ = 6.83 mg/l
balance on Mg++
Na+ = 3.75 mg/l
K+ = .32 mg/l
swap CO2(g) for HCO3-
CO2(g) = -2.2 log fugacity
SO4-- = 60 mg/l
Cl- = 1.9 mg/l
Al+++ = .08 mg/l
Fe++ = 2.43 mg/l
Mn++ = .1 mg/l
pH = 4.13
react -999.9 g of H2O
suffix _OrthopyroxenepH3
delxi = 1e-5 linear
```

Plagioclase pH 1.3

```
data = "C:\Program Files\Gwb\Gtdata\thermo.dat" verify
temperature = 25 C
decouple Fe+++
H2O = 1 free kg
Ca++        = 32.8 mg/l
balance on Ca++
Na+ = 8.7 mg/l
SO4-- = 362.3 mg/l
Al+++ = 43.38 mg/l
Fe+++ = .64 mg/l
Mn++ = .06 mg/l
pH = 3.75
swap CO2(g) for HCO3-
CO2(g) = -2.2 log fugacity
react -999.9 g of H2O
suffix _PlagioclasepH1_3
delxi = 1e-4 linear
```

Plagioclase pH 3

```
data = "C:\Program Files\Gwb\Gtdata\thermo.dat" verify
temperature = 25 C
H2O = 1 free kg
Ca++ = 4 mg/l
balance on Ca++
K+ = .02 mg/l
swap CO2(g) for HCO3-
CO2(g) = -2.2 log fugacity
SO4-- = 57.33 mg/l
Al+++ = 5 mg/l
Fe++ = .1 mg/l
pH = 4.21
react -999.9 g of H2O
suffix _PlagioclasepH3
delxi = 1e-5 linear
```

Appendix 5: Input scripts for Geochemist's Workbench (GWB)

1-komatiite pH 1.3

```
data = "C:\Program Files\Gwb\Gtdata\thermo.dat" verify
temperature = 25 C
decouple Fe+++
H2O = 1 free kg
Ca++ = 2.5 mg/l
Mg++ = 72.17 mg/l
balance on Mg++
SO4-- = 362 mg/l
Al+++ = 5.24 mg/l
Fe+++ = 6.41 mg/l
Mn++ = .8 mg/l
pH = 2.81
swap CO2(g) for HCO3-
CO2(g) = -2.2 log fugacity
react -999.9 g of H2O
suffix _11-102KomatiitepH1_3
delxi = 1e-5 linear
```

1-komatiite pH 3

```
data = "C:\Program Files\Gwb\Gtdata\thermo.dat" verify
temperature = 25 C
H2O = 1 free kg
Ca++ = 2.53 mg/l
Mg++ = 12.27 mg/l
Na+ = 3.65 mg/l
balance on Na+
K+ = .18 mg/l
swap CO2(g) for HCO3-
CO2(g) = -2.2 log fugacity
SO4-- = 62.33 mg/l
Cl- = 2.07 mg/l
Mn++ = .01 mg/l
pH = 6.28
react -999.9 g of H2O
suffix _11-102KomatiitepH3
delxi = 1e-5 linear
```

s-komatiite pH 1.3

```
data = "C:\Program Files\Gwb\Gtdata\thermo.dat" verify
temperature = 25 C
decouple Fe+++
H2O = 1 free kg
Ca++ = 3.17 mg/l
Mg++ = 61.87 mg/l
balance on Mg++
K+ = .17 mg/l
SO4-- = 363.3 mg/l
Al+++ = 10.68 mg/l
Fe+++ = 9.84 mg/l
Mn++ = .5 mg/l
pH = 2.95
swap CO2(g) for HCO3-
CO2(g) = -2.2 log fugacity
react -999.9 g of H2O
suffix _S-KomatiitepH1_3
delxi = 1e-5 linear
```

s-komatiite pH 3

```
data = "C:\Program Files\Gwb\Gtdata\thermo.dat" verify
temperature = 25 C
H2O = 1 free kg
Mg++ = 14.4 mg/l
balance on Mg++
K+ = .15 mg/l
swap CO2(g) for HCO3-
CO2(g) = -2.2 log fugacity
SO4-- = 59 mg/l
pH = 6.83
react -999.9 g of H2O
suffix _S-KomatiitepH3
delxi = 1e-5 linear
```

Appendix 5: Input scripts for Geochemist's Workbench (GWB)

Volcanic glass pH 1.3

```
data = "C:\Program Files\Gwb\Gtdata\thermo.dat" verify
temperature = 25 C
decouple Fe+++
H2O = 1 free kg
Ca++ = 17.2 mg/l
Mg++ = 49.53 mg/l
Na+ = 2.5 mg/l
K+ = .7 mg/l
SO4-- = 386.7 mg/l
balance on SO4--
Al+++ = 11.14 mg/l
Fe+++ = 28.24 mg/l
Mn++ = .5 mg/l
pH = 3.6
swap CO2(g) for HCO3-
CO2(g) = -2.2 log fugacity
react -999.9 g of H2O
suffix _VolcanicGlasspH1_3
delxi = 1e-5 linear
```

Volcanic glass pH 3

```
data = "C:\Program Files\Gwb\Gtdata\thermo.dat" verify
temperature = 25 C
H2O = 1 free kg
Ca++ = 4.63 mg/l
balance on Ca++
Mg++ = 6.53 mg/l
Na+ = 6.52 mg/l
K+ = .35 mg/l
swap CO2(g) for HCO3-
CO2(g) = -2.2 log fugacity
SO4-- = 60 mg/l
Cl- = 2.4 mg/l
Al+++ = .01 mg/l
Fe++ = .27 mg/l
Mn++ = .08 mg/l
pH = 4.66
react -999.9 g of H2O
suffix _VolcanicGlasspH3
delxi = 1e-5 linear
```

Xenolith pH 1.3

```
data = "C:\Program Files\Gwb\Gtdata\thermo.dat" verify
temperature = 25 C
H2O = 1 free kg
Ca++ = 1.65 mg/l
balance on Ca++
Mg++ = 84.2 mg/l
K+ = .15 mg/l
SO4-- = 347 mg/l
pH = 4.56
Fe++ = 1.04 mg/l
swap CO2(g) for HCO3-
CO2(g) = -2.2 log fugacity
react -999.9 g of H2O
suffix _XenolithpH1_3
delxi = 1e-4 linear
```

Xenolith pH 3

```
data = "C:\Program Files\Gwb\Gtdata\thermo.dat" verify
temperature = 25 C
H2O = 1 free kg
Ca++ = .87 mg/l
Mg++ = 14.93 mg/l
balance on Mg++
K+ = .38 mg/l
swap CO2(g) for HCO3-
CO2(g) = -2.2 log fugacity
SO4-- = 58.33 mg/l
pH = 7.88
react -999.9 g of H2O
suffix _XenolithpH3
delxi = 1e-6 linear
```

Appendix 5: Input scripts for Geochemist's Workbench (GWB)

DTS-2b pH 1.3

```
data = "C:\Program Files\Gwb\Gtdata\thermo.dat" verify
temperature = 25 C
H2O = 1 free kg
Mg++ = 92.8 mg/l
SO4-- = 360.3 mg/l
balance on SO4--
pH = 5.81
swap CO2(g) for HCO3-
CO2(g) = -2.2 log fugacity
react -999.9 g of H2O
suffix _DTS2bpH1_3
delxi = 1e-5 linear
```

DTS-2b pH 3

```
data = "C:\Program Files\Gwb\Gtdata\thermo_hmw.dat" verify
temperature = 25 C
H2O = 1 free kg
Ca++ = .53 mg/l
Mg++ = 15.77 mg/l
balance on Mg++
Na+ = 2.08 mg/l
K+ = .22 mg/l
swap CO2(g) for HCO3-
CO2(g) = -2.2 log fugacity
SO4-- = 60 mg/l
Cl- = 1.43 mg/l
pH = 8.88
react -999.9 g of H2O
suffix _ DTS2bpH3
delxi = 1e-5 linear
```

Bir-1a pH 1.3

```
data = "C:\Program Files\Gwb\Gtdata\thermo.dat" verify
temperature = 25 C
decouple Fe+++
H2O = 1 free kg
Ca++ = 30.37 mg/l
balance on Ca++
Mg++ = 6.53 mg/l
Na+ = 3.17 mg/l
SO4-- = 360 mg/l
Al+++ = 38.41 mg/l
Fe+++ = 6.41 mg/l
Mn++ = .1 mg/l
pH = 3.79
swap CO2(g) for HCO3-
CO2(g) = -2.2 log fugacity
react -999.9 g of H2O
suffix _BIRpH1_3
delxi = 1e-5 linear
```

Bir-1a pH 3

```
data = "C:\Program Files\Gwb\Gtdata\thermo.dat" verify
temperature = 25 C
H2O = 1 free kg
Ca++ = 3.57 mg/l
balance on Ca++
Mg++ = 1.4 mg/l
K+ = .02 mg/l
SO4-- = 57.67 mg/l
Al+++ = 4.14 mg/l
Fe++ = 1 mg/l
Mn++ = .06 mg/l
pH = 4.43
swap CO2(g) for HCO3-
CO2(g) = -2.2 log fugacity
react -999.9 g of H2O
suffix _BIR1apH3
delxi = .001 linear
```

Appendix 6: Calculated mineral assemblages of the pH 1.3 sample solutions in cm^3

Sample/Temperature (°C)	Minerals	Volume (cm^3)	Total volume (cm^3)
Tissint$_{(pH\ 1.3)}$ (25°C)	jarosite-K	0.01744	
	gypsum	0.1015	
	hematite	0.000436	0.1194
Tissint$_{(pH\ 1.3)}$ (75°C)	jarosite-K	0.01685	
	anhydrite	0.07195	
	hematite	0.006147	0.09495
Tissint$_{(pH\ 1.3)}$ (100-200°C)	kieserite	0.02161	
	anhydrite	0.06671	
	alunite	0.037	
	hematite	0.01189	0.1372
olivine$_{(pH\ 1.3)}$ (25°C)	epsomite	0.05894	
	hematite	0.001685	0.06063
olivine$_{(pH\ 1.3)}$ (75°C)	hexahydrite	0.5326	
	hematite	0.0002483	0.5329
olivine$_{(pH\ 1.3)}$ (100-200°C)	kieserite	0.2146	
	hematite	0.002785	0.2174
cpx$_{(pH\ 1.3)}$ (25°C)	mercallite	0.01076	
	mirabilite	0.01288	
	epsomite	0.5159	
	gypsum	0.0108	0.5503
cpx$_{(pH\ 1.3)}$ (75°C)	anhydrite	0.03779	
	szomolnokite	0.001983	0.03978
cpx$_{(pH\ 1.3)}$ (100-200°C)	anhydrite	0.0386	
	alunite	0.003221	0.04182
opx$_{(pH\ 1.3)}$ (25°C)	epsomite	0.4893	
	gypsum	0.00289	0.4922
opx$_{(pH\ 1.3)}$ (75°C)	anhydrite	0.001692	0.001692
opx$_{(pH\ 1.3)}$ (100-200°C)	anhydrite	0.00135	0.00135
plagioclase$_{(pH\ 1.3)}$ (25°C)	mirabilite	0.02924	
	gypsum	0.07838	
	hematite	0.0001713	0.1078
plagioclase$_{(pH\ 1.3)}$ (75°C)	anhydrite	0.05507	
	gibbsite	0.01456	
	hematite	0.0001778	0.0698
plagioclase$_{(pH\ 1.3)}$ (100-200°C)	anhydrite	0.05954	
	gibbsite	0.05091	
	hematite	0.0001817	0.1106
1-komatiite$_{(pH\ 1.3)}$ (25°C)	epsomite	1,349	
	gypsum	0.004601	1,354
1-komatiite$_{(pH\ 1.3)}$ (75°C)	hexahydrite	0.1156	
	anhydrite	0.002893	0.1185
1-komatiite$_{(pH\ 1.3)}$ (100-200°C)	kieserite	0.0211	
	anhydrite	0.002893	0.02399

Sample/Temperature (°C)	Minerals	Volume (cm^3)	Total volume (cm^3)
s-komatiite$_{(pH\ 1.3)}$ (25°C)	mercallite	9.889E-5	
	epsomite	1,244	
	gypsum	0.005816	1,250
s-komatiite$_{(pH\ 1.3)}$ (75°C)	hematite	0.1611	0.1611
s-komatiite$_{(pH\ 1.3)}$ (100-200°C)	kieserite	0.05127	
	anhydrite	0.003746	
	alunite	0.0001125	0.05513
volcanic glass$_{(pH\ 1.3)}$ (25°C)	jarosite-Na	0.02058	
	mirabilite	0.006959	
	epsomite	1,365	
	jarosite-K	0.002709	
	gypsum	0.03166	1,427
volcanic glass$_{(pH\ 1.3)}$ (75°C)	thenardite	0.001641	
	hexahydrite	0.3091	
	jarosite-K	0.002813	
	anhydrite	0.02022	
	hematite	0.00257	0.3363
volcanic glass$_{(pH\ 1.3)}$ (100-200°C)	kieserite	0.1155	
	anhydrite	0.02064	
	alunite	0.005508	
	hematite	0.00773	0.1493
DTS-2b$_{(pH\ 1.3)}$ (25°C)	epsomite	2,296	2,296
DTS-2b$_{(pH\ 1.3)}$ (75°C)	hexahydrite	0.5175	0.5175
DTS-2b$_{(pH\ 1.3)}$ (100-200°C)	kieserite	0.174	
	MHSH($Mg_{1.5}$)	0.02585	0.1998
Bir-1a$_{(pH\ 1.3)}$ (25°C)	epsomite	0.004488	
	gypsum	0.08042	
	hematite	0.0001597	0.08507
Bir-1a$_{(pH\ 1.3)}$ (75°C)	anhydrite	0.05772	
	hematite	0.001773	0.05949
Bir-1a$_{(pH\ 1.3)}$ (100-200°C)	kieserite	0.01489	
	$Al_2(SO_4)_3 \cdot 6\ H_2($	°--	
	anhydrite	0.06326	
	gibbsite	0.004072	
	hematite	0.001821	0.08404
xenolith$_{(pH\ 1.3)}$ (25°C)	mercallite	0.0002159	
	melanterite	0.01064	
	epsomite	2,100	
	gypsum	0.008213	2,119
xenolith$_{(pH\ 1.3)}$ (75°C)	melanterite	0.004538	
	hexahydrite	0.468	
	anhydrite	0.00462	0.4772
xenolith$_{(pH\ 1.3)}$ (100-200°C)	szomolnokite	0.0005524	
	kieserite	0.2028	
	anhydrite	0.00346	0.2068

Appendix 6: Calculated mineral assemblages of the pH 3 sample solutions in cm^3

Sample/Temperature (°C)	Minerals	Volume (cm^3)	Total volume (cm^3)
Tissint$_{(pH\ 3)}$ (25°C)	gypsum	0.01418	
	calcite	0.003839	0.01802
Tissint$_{(pH\ 3)}$ (75°C)	anhydrite	0.01195	
	calcite	0.001694	0.01365
Tissint$_{(pH\ 3)}$ (100-200°C)	kieserite	0.004161	
	MHSH($Mg_{1.5}$)	0.005425	
	anhydrite	0.01442	0.024
olivine$_{(pH\ 3)}$ (25°C)	calcite	0.002267	0.002267
olivine$_{(pH\ 1.3)}$ (75°C)	calcite	0.002359	0.002359
olivine$_{(pH\ 1.3)}$ (100-200°C)	MHSH($Mg_{1.5}$)	0.01748	
	calcite	0.002415	0.0199
cpx$_{(pH\ 3)}$ (25°C)	mirabilite	0.03662	
	gypsum	0.01324	0.04986
cpx$_{(pH\ 3)}$ (75°C)	thenardite	0.0006265	
	anhydrite	0.008471	
	alunite	0.0002987	0.009396
cpx$_{(pH\ 3)}$ (100-200°C)	thenardite	0.005672	
	kieserite	0.007682	
	anhydrite	0.008685	
	alunite	0.0009505	0.02299
opx$_{(pH\ 3)}$ (25°C)	epsomite	0.06319	
	gypsum	0.003666	0.06686
opx$_{(pH\ 3)}$ (75°C)	anhydrite	0.00236	0.00236
opx$_{(pH\ 3)}$ (100-200°C)	szomolnokite	0.0008205	
	kieserite	0.02305	
	anhydrite	0.002437	
	alunite	0.0003042	0.02661
plagioclase$_{(pH\ 3)}$ (25°C)	gypsum	0.02163	0.02163
plagioclase$_{(pH\ 3)}$ (75°C)	anhydrite	0.0184	
	alunite	0.000154	
	gibbsite	0.001644	0.0202
plagioclase$_{(pH\ 3)}$ (100-200°C)	anhydrite	0.02138	
	alunite	0.0001574	
	gibbsite	0.004076	0.02561

Sample/Temperature (°C)	Minerals	Volume (cm^3)	Total volume (cm^3)
1-komatiite$_{(pH\ 3)}$ (25°C)	epsomite	0.1536	
	mirabilite	0.03007	
	gypsum	0.002504	
	calcite	0.001038	0.1872
1-komatiite$_{(pH\ 3)}$ (75°C)	anhydrite	0.002946	0.002946
1-komatiite$_{(pH\ 3)}$ (100-200°C)	thenardite	0.001407	
	kieserite	0.02444	
	MHSH($Mg_{1.5}$)	0.003047	
	anhydrite	0.003039	0.03193
s-komatiite$_{(pH\ 3)}$ (25°C)	epsomite	0.2633	0.2633
s-komatiite$_{(pH\ 3)}$ (75°C)	hexahydrite	0.01389	0.01389
s-komatiite$_{(pH\ 3)}$ (100-200°C)	kieserite	0.02455	
	MHSH($Mg_{1.5}$)	0.01043	0.03499
volcanic glass$_{(pH\ 3)}$ (25°C)	mirabilite	0.01077	
	gypsum	0.01666	0.02743
volcanic glass$_{(pH\ 3)}$ (75°C)	anhydrite	0.01051	0.01051
volcanic glass$_{(pH\ 3)}$ (100-200°C)	thenardite	0.001403	
	kieserite	0.0152	
	alunite	3.802E-5	
	anhydrite	0.01051	0.02715
DTS-2b$_{(pH\ 3)}$ (25°C)	calcite	0.0004855	0.0004855
DTS-2b$_{(pH\ 3)}$ (75°C)	calcite	0.000502	0.000502
DTS-2b$_{(pH\ 3)}$ (100-200°C)	MHSH($Mg_{1.5}$)	0.03531	
	calcite	0.0005125	0.03582
Bir-1a$_{(pH\ 3)}$ (25°C)	gypsum	0.0213	0.0213
Bir-1a$_{(pH\ 3)}$ (75°C)	anhydrite	0.01897	
	alunite	0.000154	
	gibbsite	0.00242	0.02154
Bir-1a$_{(pH\ 3)}$ (100-200°C)	szomolnokite	0.0001532	
	alunite	0.0001574	
	anhydrite	0.02136	
	gibbsite	0.004891	0.02656
xenolith$_{(pH\ 3)}$ (25°C)	epsomite	0.2572	
	calcite	0.0007911	0.258
xenolith$_{(pH\ 3)}$ (75°C)	hexahydrite	0.01563	
	calcite	0.0008212	0.01645
xenolith$_{(pH\ 3)}$ (100-200°C)	kieserite	0.02399	
	anhydrite	0.001044	
	MHSH($Mg_{1.5}$)	0.009193	0.03423